



Doctoral Thesis

Integration of Luminescent Chemical Sensors into Miniaturized Devices

Birgit Ungerböck

2014

Zur Erlangung des akademischen Grades
„Doktorin der technischen Wissenschaften“
eingereicht an der
Technischen Universität Graz

Supervisor

Ass.Prof. Dipl.-Chem. Dr.rer.nat. Univ.-Doz. Torsten Mayr
Institute of Analytical Chemistry and Food Chemistry
Graz University of Technology

*„Am Ziele deiner Wünsche
wirst du jedenfalls eines vermissen:
dein Wandern zum Ziel.“*

Marie von Ebner-Eschenbach

STATUTORY DECLARATION

I declare that I have authored this thesis independently, that I have not used other than the declared sources / resources, and that I have explicitly marked all material which has been quoted either literally or by content from the used sources.

Date

Signature

Acknowledgement

Before I start a new chapter of my life it is time to pause for a moment and thank all the people, who have helped me to keep pursuing my goals throughout the last years.

First of all, I want to thank my supervisor Torsten Mayr. He handled the challenging task of facing my questions and my criticism in our manifold discussions, which helped me to find my path in the scientific world. Furthermore I want to thank Torsten for enabling the financial support throughout my thesis.

A huge “thank-you” also goes to the whole sensor group, the best research group I can imagine. Although it is sometimes hard to stop me talking, it is hard for me now to find the right words about what our working atmosphere, our lunch, cake and coffee breaks, and your professional and – sometimes even more important – psychological support meant to me during the last years. I don’t want to highlight any of you personally, but maybe you find yourselves in one of my following truly unforgettable memories: the Christmas parties (official and unofficial part), the Friday song, the Friday experiments, Gangnam Style dance sessions in our office, frozen bottoms in Stockholm and subsequent unfreezing vodka experiences, endless (skype-)conversations and coffee breaks on the terrace, barbecue parties, sensor man and his friends, after-work beer sessions, an awesome bike trip in Barcelona, a trip to the Hochseilklettergarten, the Lasertron-“Gemetzl”, a great ASCOS experience in Cork, exciting vierfarben-evenings, international guests and dinner parties, and so on.

Special thank goes to my “helping hands”, the bachelor and project lab students I worked with: Jan Senn, Hanna Dahlgren, Siegfried Fellinger, Bianca Frauscher, Philipp Sulzer and Bernhard Müller. Although I had to learn a lot concerning my supervising skills, you were sufficiently patient and kept being motivated even when my instructions were confusing or impossible to realize. The work with you not only yielded publishable results, but also was an exciting challenge in terms of learning how to handle the difficult task of supervising.

A huge part of my thesis was based on cooperations with companies, universities and other research institutions. That’s why I also want to mention these people, who worked with me on different publications, provided me with an endless number of microfluidic chips for my experiments or supported me with theoretical calculations. The work in international and interdisciplinary teams strengthened my interest to work in such teams, leading to a broadening of my personal competences.

Last but not least I want to thank my friends and my family – especially my mother - for their love, their support but also their patience, when time was too short to spend it with them. Knowing that you are there for me, even in hard times, helped me to face the challenges I had to face, always knowing that in cases of emergency I have a strong safety net in you.

Graz, 17th April 2014

Abstract

Microfluidic systems offer important advantages over traditionally applied technologies, but also evoke a number of new scientific challenges, which are due to their miniaturization. One of these challenges is the application of analytical tools, which have to be scalable to smaller dimensions, should provide sufficient sensitivity and selectivity, be rather low-cost and not consume the analyte under investigation.

The integration of luminescence-based sensors into miniaturized systems represents a promising tool to obtain analytical information from miniaturized or microfluidic systems. Oxygen and pH rank among the most commonly measured analytes for optical luminescent sensors and are very important analytes to be measured in a range of applications.

The scope of this thesis is to optimize and evaluate luminescent sensors for oxygen and pH regarding their applicability in microfluidic devices. For this purpose high performance sensor materials have been integrated into miniaturized devices in different sensor formats – sensor layers, nano sensor particles and magnetic sensor particles - and combined with different read-out methods. The sensor set-ups were developed and discussed concerning the specific measurement requirement, comprising a simple and relatively cheap ratiometric oxygen imaging set-up using the color channels of a color CCD camera for cell culture monitoring or dispersed nano sensor particles combined with oxygen lifetime imaging for validation of mathematical models, which describe transport and reaction phenomena inside microfluidic channels. Furthermore, nano sensor particles with an additional magnetic functionality were integrated into microfluidic devices to generate *in-situ* sensor spots and their general applicability and combination with different read-out methods were evaluated. We also report on the use of nano sensor particles for pH in microfluidic channels exhibiting 2D read-out by a color CCD-camera and the application of ring-shaped organic photodiodes, directly integrated into microfluidic chips.

Kurzfassung

Mikrofluidische Systeme bieten wichtige Vorteile gegenüber traditionell angewandten Technologien, bedingen aber auch eine Reihe neuer wissenschaftlicher Herausforderungen, die sich auf eben diese Miniaturisierung zurückführen lassen. Eine dieser Herausforderungen ist die Anwendung analytischer Werkzeuge, die eine Reihe von Eigenschaften aufweisen müssen: sie sollten auf kleinere Dimensionen skalierbar sein, ausreichende Empfindlichkeit und Selektivität aufweisen, kostengünstig sein und den untersuchten Analyten nicht verbrauchen.

Die Integration von lumineszenz-basierten Sensoren in miniaturisierte Systeme stellt ein vielversprechendes Werkzeug dar, um analytische Informationen aus miniaturisierten oder mikrofluidischen Systemen zu erhalten. Sauerstoff und pH zählen hierbei zu den am häufigsten durch optische lumineszente Sensoren gemessenen Analyten und sind in einer Reihe von Anwendungen als wichtige Analyten bekannt.

Diese Arbeit umfasst die Optimierung und Evaluierung lumineszenter Sensoren für Sauerstoff und pH bezüglich ihrer Anwendbarkeit in mikrofluidischen Elementen. Zu diesem Zweck wurden leistungsstarke Sensormaterialien in miniaturisierte Objekte in Form verschiedener Sensorformate integriert – Sensorschichten, Nanosensorpartikel und magnetische Sensorpartikel – und mit verschiedenen Auslesemethoden kombiniert. Die Sensorsetups wurden unter Berücksichtigung der jeweiligen Messanforderung entwickelt und optimiert, zum Beispiel in Form eines einfachen und relativ günstigen ratiometrischen bildgebenden Verfahrens zur Bestimmung von Sauerstoff unter Verwendung der Farbkanäle einer CCD-Farbkamera zur Kontrolle von Zellkulturen oder in Form suspendierter Nanosensorpartikel kombiniert mit lebenszeitbasierten bildgebenden Verfahren zur Validierung mathematischer Modelle, die Transport- und Reaktionsgegebenheiten in mikrofluidischen Kanälen beschreiben. Weiters wurden Nanosensorpartikel mit zusätzlichen magnetischen Eigenschaften in mikrofluidische Systeme integriert um *in-situ* Sensorspots zu generieren und deren allgemeine Anwendbarkeit und Kombinierbarkeit mit unterschiedlichen Auslesemethoden wurde beurteilt. Weiters werden in dieser Arbeit pH-Nanosensorpartikel mit einem 2D CCD-Farbkamera-Auslesesystem in mikrofluidischen Kanälen und die Anwendung von direkt in mikrofluidische Bauteile integrierten ringförmigen organischen Photodioden beschrieben.

Table of Contents

1	Scope and outline of the thesis	1
2	Integration of Luminescent Chemical Sensors into Miniaturized Devices	3
2.1	Introduction	4
2.2	Background	5
2.2.1	Luminescent oxygen sensors	6
2.2.2	Fluorescent pH sensors	9
2.3	Integration of optical sensors into microfluidic devices – an optimization challenge.	12
2.3.1	Sensing chemistry	13
2.3.2	Optical Sensor Formats	17
2.3.3	Optical Measurement Systems	19
2.3.4	Optical sensors for pH and oxygen in microfluidic devices.....	22
2.4	Conclusion	34
2.5	References.....	35
3	Microfluidic Oxygen Imaging using Integrated Optical Sensor Layers and a Color Camera	41
3.1	Introduction	42
3.2	Methods	43
3.2.1	Materials	43
3.2.2	Preparation of sensor films.....	43
3.2.3	Spectral measurements	44
3.2.4	Integration of sensor films into microfluidic chips.....	44
3.2.5	Sensor characterization.....	44
3.2.6	Cell culture	45
3.2.7	Imaging setup and data evaluation.....	45
3.3	Results and discussion.....	46
3.3.1	Chip assembly.....	46
3.3.2	Sensor assembly.....	46
3.3.3	Characterization of sensor films.....	49
3.3.4	Versatility of Sensor Setup	51
3.3.5	2D oxygen information of microfluidic cell cultures	52
3.4	Conclusion	54
3.5	Notes	54
3.6	Acknowledgement	54
3.7	Notes and references	54
3.8	Electronic Supplementary Information.....	89

4	Online Oxygen Measurements inside a Microreactor with Modeling of Transport Phenomena	57
4.1	Introduction	58
4.2	Materials and methods	59
4.3	Optical measurements	60
4.3.1	Batch experiments with GOx	60
4.3.2	Diffusion-convection experiments	60
4.3.3	GOx experiments	61
4.3.4	Modeling and reaction kinetics	61
4.4	Results and discussion	63
4.4.1	Batch experiments with GOx	63
4.4.2	Diffusion-convection experiments	64
4.4.3	GOx experiments	67
4.5	Conclusions	70
4.6	Acknowledgment	70
4.7	References	70
5	Magnetic Optical Sensor Particles: A Flexible Analytical Tool for Microfluidics	73
5.1	Introduction	74
5.2	Materials and Methods	75
5.2.1	Materials	75
5.2.2	Sensing setup and data evaluation	75
5.2.3	Preparation of MOSePs	76
5.2.4	Sensor characterization	76
5.2.5	Microfluidic measurements	76
5.3	Results and Discussion	77
5.3.1	Concept of magnetic sensor particles in microfluidics	77
5.3.2	Separation speed and stability of <i>in-situ</i> sensor spots	80
5.3.3	Sensor read-out	81
5.3.4	Pre-treatment for microscopic imaging applications	83
5.3.5	Microfluidic measurements and further applications	84
5.4	Conclusion	87
5.5	Acknowledgements	88
5.6	References	88
6	Opto-chemical sensors based on integrated ring-shaped organic photodiodes: progress and applications	91
6.1	Introduction	92
6.2	Description of the sensor array chip and experimental data	92
6.2.1	The sensor array chip lay-out	92

6.2.2	Materials	93
6.2.3	Luminescence decay-time measurements.....	94
6.2.4	Preparation of micro-fluidic chip with integrated OPDs.....	94
6.3	Results	95
6.3.1	Measurement in liquid phase	96
6.3.2	Reproducibility of sensor performance between different sensor elements and sensor array chips.....	97
6.3.3	Luminescence life-time determination with OPDs	98
6.3.4	Microfluidic device with integrated organic photodiodes.....	99
6.4	Conclusion	100
6.5	Acknowledgement	100
6.6	References.....	100
7	Fluorescent materials for pH sensing and imaging based on novel 1,4-diketopyrrolo-[3,4-c]pyrrole dyes.....	103
7.1	Introduction	104
7.2	Results and discussion.....	104
7.2.1	Indicator syntheses	105
7.2.2	Indicator properties	105
7.2.3	pH-sensing materials.....	109
7.3	Conclusion	112
7.4	Experimental	113
7.4.1	Materials and Methods.....	113
7.4.2	Indicator synthesis	114
7.4.3	Preparation of planar sensors.....	115
7.4.4	Preparation of sensor nanoparticles.....	115
7.5	Acknowledgements.....	115
7.6	Notes and References	115
7.7	Electronic Supplementary Information.....	118
8	Summary and Conclusion	129
9	Appendix.....	131
9.1	Curriculum Vitae	133
9.2	List of publications	135
	Publications in peer-reviewed journals	135
	Conference Proceedings	135
	Presentations	136
	Poster contributions	136

1 Scope and outline of the thesis

Microfluidic systems offer important advantages over traditionally applied technologies, but also evoke a number of new scientific challenges, which are due to their miniaturization. One of these challenges is the application of analytical tools, which have to be scalable to smaller dimensions, should provide sufficient sensitivity and selectivity, be rather low-cost and not consume the analyte under investigation.

The integration of luminescence-based sensors into miniaturized systems represents a promising tool to obtain analytical information from miniaturized or microfluidic systems. Oxygen and pH count to the most commonly measured analytes by optical luminescent sensors and are very important analytes to be measured in a range of applications.

The scope of this thesis is to optimize and evaluate luminescent sensors for oxygen and pH regarding their applicability in microfluidic devices. For this purpose high performance sensor materials have been integrated into miniaturized devices in different sensor formats – sensor layers, nano sensor particles and magnetic sensor particles - and combined with different read-out methods. The sensor set-ups were developed and discussed concerning the specific measurement requirement.

First, oxygen sensor layers were integrated into microfluidic chips and combined with referenced oxygen imaging, applying a color CCD camera (chapter 3, page 41). This measurement setup allowed for accurate real-time 2D oxygen imaging with superior quality compared to intensity imaging. The sensor films were subsequently used to measure respiratory activity of human cell cultures (Hela carcinoma cells and normal human dermal fibroblasts) in a microfluidic system in cooperation with Verena Charwat from AIT. The sensor setup proved to be well suited for different applications from spatially and temporally resolving oxygen concentration inside microfluidic channels to parallelization of oxygen measurements.

Second, oxygen-imaging using an epifluorescent microscope was performed inside a microfluidic chip by utilizing nanosensor particles stained with an oxygen-sensitive luminescent dye (chapter 4, page 57). Dissolved oxygen concentrations were measured at various flow rates and microchannel dimensions. They served as validation of mathematical models, ranging from a full 3D description of transport phenomena, incorporating convection, diffusion and enzymatic reaction terms along with the parabolic velocity profile, to simplified less precise models, which all were developed by Andrej Pohar from University of Ljubljana. By comparison of oxygen measurements with model predictions of dissolved oxygen we tried to assess the required model complexity for achieving precise results and to depict the governing transport characteristics at the microscale.

Third, we evaluated magnetic optical sensor particles (MOSePs) with incorporated sensing functionality regarding their applicability in microfluidic devices (chapter 5, page 73). MOSePs can be separated from the surrounding solution to form *in-situ* sensor spots within microfluidic channels, while the read-out is accomplished outside the chip. These magnetic sensor spots exhibit benefits of sensor layers (high brightness, convenient usage) combined with the advantages of dispersed sensor particles (ease of integration). MOSePs were optimized regarding fiber optic and imaging read-out systems, and different referencing schemes were critically discussed on the example of oxygen sensors. Furthermore, new application possibilities were addressed, being enabled by the use of MOSePs. They can be used for microscopic oxygen imaging in any chip with optically transparent covers, can serve as flexible sensor spots to monitor enzymatic activity or can be applied to form fixed sensor spots inside microfluidic structures, which would be inaccessible to integration of sensor layers.

Fourth, an application of a monolithically integrated sensor platform based on ring-shaped organic photo detectors integrated in a microfluidic chip is presented (chapter 6, page 91). It is part of a publication, which includes the investigation of various sensing chemistries based on luminescence for the detection of a number of parameters such as oxygen, carbon dioxide, humidity and pH in gaseous and/or liquid phase, which were optimized to the requirements of the general sensor platform in cooperation with several research partners.

Fifth, a ratiometric sensor in the form of nanoparticles is also presented. It is suitable for RGB camera read-out, and its practical applicability for fluorescence imaging in microfluidic systems was demonstrated (chapter 7, page 103). It is part of a publication on new optical pH-sensors relying on 1,4-diketopyrrolo-[3,4-c]pyrroles (DPPs) as fluorescent pH-indicators by Daniel Aigner.

Finally, an unpublished review article gives a compact introduction into luminescent sensing of oxygen and pH, identifies new scientific challenges concerning sensor development and evaluates the overall suitability of luminescent sensors to be integrated into microfluidic devices (chapter 2, page 3). The review comprises an introduction giving an overview over working principle, state-of-the-art and current trends of luminescent oxygen and pH sensors and a main part, which focuses on the integration of luminescent sensors into microfluidic devices including optimization strategies for sensor materials (matrices and indicators), sensor formats and detection methods as well as an overview over existing applications of luminescent sensors in microfluidic devices. Finally, we conclude with the overall suitability of luminescent sensors for microfluidics and figure out the scientific challenges, which should be addressed to further improve luminescent sensing performance in miniaturized devices.

2 Integration of Luminescent Chemical Sensors into Miniaturized Devices

Abstract Microfluidic systems offer important advantages over traditionally applied technologies, but also evoke a number of new scientific challenges, which are due to their miniaturization. One of these challenges is the application of analytical tools, which have to be scalable to smaller dimensions, should provide sufficient sensitivity and selectivity, be rather low-cost and not consume the analyte under investigation.

The integration of luminescence-based sensors into miniaturized systems represents a promising tool to obtain analytical information from miniaturized or microfluidic systems. Oxygen and pH count to the most commonly measured analytes by optical luminescent sensors and are very important analytes to be measured in a range of applications.

The scope of the present review is to give a compact introduction into luminescent sensing of oxygen and pH, to identify new scientific challenges concerning sensor development and to evaluate the overall suitability of luminescent sensors to be integrated into microfluidic devices. For this purpose the review starts with an overview over working principle, state-of-the-art and current trends of luminescent oxygen and pH sensors. The main part of the review focuses on the integration of luminescent sensors into microfluidic devices. Optimization strategies for sensor materials (matrices and indicators), sensor formats and detection methods are presented as well as an overview over existing applications of luminescent sensors in microfluidic devices. Finally, we will conclude with the overall suitability of luminescent sensors for microfluidics and figure out the scientific challenges, which should be addressed to further improve luminescent sensing performance in miniaturized devices.

2.1 Introduction

Optical chemical sensing has gained increasing interest throughout the last decades. The rise of the research field, but also of commercially available sensing systems is not only due to the beneficial features of optical sensors, such as their applicability for non-invasive measurements, remote and online-sensing, high sensitivity and versatility, but also due to advances in optoelectronics, which enabled the production of low-cost and miniaturized light sources and photodetectors, and availability of high quality optical fibers.

The widely used Cambridge definition of a chemical sensor describes them as “*miniaturized devices that can deliver real time and on-line information on the presence of specific compounds or ions in even complex samples.*”¹ Basic elements of an optical chemical sensor include the sample/analyte, the transduction platform and the signal processing electronics to yield information on the analyte concentration of interest. Most optical sensors are based on reagents that change their optical properties upon interaction with the analyte and an optical transducer is used to convert the optical signal into electronic information. Absorption, fluorescence intensity and luminescence decay time rank among the most commonly measured properties, but also reflectance, refractive index, light scattering and polarization can be used to obtain analytical information.

Another technology which has faced enormous rise during the last two decades is the versatile field of microfluidics. This technology is defined by the small volume of fluid that is processed by these systems (commonly μL to fL) and has considerably evolved since its origin as a miniaturized gas chromatograph at Stanford University² and the more general miniaturized total analysis system³. Originally stemming from analytical applications, the technology of microfluidics has reached various research fields. The success of microfluidics can mainly be attributed to the advantages of miniaturized devices such as minimized reagent and sample consumption, increased automation possibility, high controllability and reproducibility and reduced manufacturing costs due to mass-production from inexpensive polymers. Many research fields can benefit from these advantages such as point-of-care testing, diagnostics, industrial and environmental monitoring, analytics, microreaction technology and pharmaceutical and life sciences. The goal in many cases is to generate “lab-on-a-chip”-like microfluidic devices with integration of all the necessary components onto one single chip or at least a small number of subsequent chips. One way to integrate necessary analytical steps into a microfluidic device is the application of smart and suitable detection tools, including sensing devices for various analytes and physical parameters. However, the integration of sensors into microfluidic devices poses miniaturization-specific challenges to researchers: first of all the reduced analysis volume leads to a decreased number of analyte molecules compared to bench-scale devices. The small number of molecules results in the need for highly sensitive sensing devices and the constraint that the analyte may not be changed in its concentration during measurement. Second, the sensing device must be scalable to smaller dimensions, which is not possible for all existing sensing technologies. Third, the costs play an important role concerning the usefulness of microfluidic devices as most of them are thought to serve as disposable tools.

Optical sensors provide a range of interesting features to handle the above-mentioned challenges: they are easy to miniaturize, highly sensitive, do generally not consume the analyte under investigation and are relatively low-cost devices. Especially luminescent sensors are

deemed considerably promising due to their even enhanced sensitivity compared to other optical methods. For instance, absorption based methods are difficult to perform in microfluidics because of low channel depths and resulting short optical pathlengths that decrease the sensitivity of these applications.

Nowadays a range of different parameters can be measured by luminescent chemical sensors, ranging from cations (H^+ , Li^+ , Na^+ , K^+ , Ca^{2+} , Mg^{2+} , Zn^{2+} , Pb^{2+} , Cd^{2+} , Al^{3+} , etc.) and anions (halide ions, citrates, carboxylates, phosphates, ATP, etc.) over neutral molecules (sugars, e.g. glucose, etc.) and gases (O_2 , CO_2 , NO , etc.) to physical parameters (e.g. temperature). Oxygen and pH belong to the most commonly probes investigated by luminescent sensors and also represent important analytes in a range of applications such as bioprocess monitoring, different kinds of cell culture and tissue engineering.

The suitability of luminescent sensors for microfluidic applications has already been recognized by various scientists and in recent years several publications reported on the successful integration of luminescent chemical sensors into miniaturized devices. Some reviews have already been published on this subject including the review by Grist et al.⁴, who surveyed previously proposed optical oxygen sensors and discussed their applicability in microfluidic cell culture. Other reviews have been focused on different main subjects such as oxygen transfer characteristics of bioreactors⁵ or the use of microbioreactors in fermentation process development⁶, but additionally provide an overview over state of the art on-line measurement techniques in microbioreactors.

The scope of the present text is restricted to the integration of luminescent oxygen and pH sensors into microfluidic devices due to the importance of oxygen and pH as measured parameters and because they are considered to be the most commonly measured analytes by optical sensors. However, several principles of sensor integration may be transferable to other analytes such as temperature or carbon dioxide, which can also be important parameters to be measured. Optical pH sensors based on absorption are excluded due to the fundamental better performance of fluorescent pH sensors, which allow the fabrication of thinner sensor layer thicknesses inside microfluidic channels.

The introduction starts with a background chapter, which introduces the reader into working principle, state-of-the-art and current trends of luminescent oxygen and pH sensors. The main part of the present text focuses on the integration of luminescent sensors into microfluidic devices. Optimization strategies for sensor materials (matrices and indicators), sensor formats and detection methods will be presented as well as an overview over existing applications of luminescent sensors in microfluidic devices. Finally, we will discuss the overall suitability of luminescent sensors for microfluidics and figure out the scientific challenges, which should be addressed to further improve luminescent sensing performance.

2.2 Background

Luminescent sensors rely on the use of luminescent dyes that change their optical properties upon interaction with the analyte of interest. Usually, these dyes are integrated into a suitable matrix. There is a variety of luminescent probes that can be used as recognition element for an optical sensing device and different sensing methods have been developed since the origin of luminescence sensing.

Nowadays, luminescent sensors for oxygen and pH exploit well established sensing methods. The following chapter gives an overview over commonly used sensing principles (kind of interaction between optical probe and analyte), sensing methods and state-of-the-art and key trends in oxygen and pH sensing.

2.2.1 Luminescent oxygen sensors

Oxygen is a very important parameter to be measured in a range of applications – most of them dealing with biological or biochemical issues. This is due to the fact that oxygen is a key metabolite for almost all living organisms. Thus it is no surprise that a range of methods to determine oxygen concentration exists with luminescent sensing being one of them. Several helpful reviews⁷⁻⁹ and books^{10,11} exist, which cover sensing principles and sensing methods. Other aspects including sensor materials¹²⁻¹⁵ and applications of oxygen sensors¹⁶⁻¹⁸ have also been carefully summarized. The following chapter gives a short introduction on basic principles of luminescent oxygen sensing.

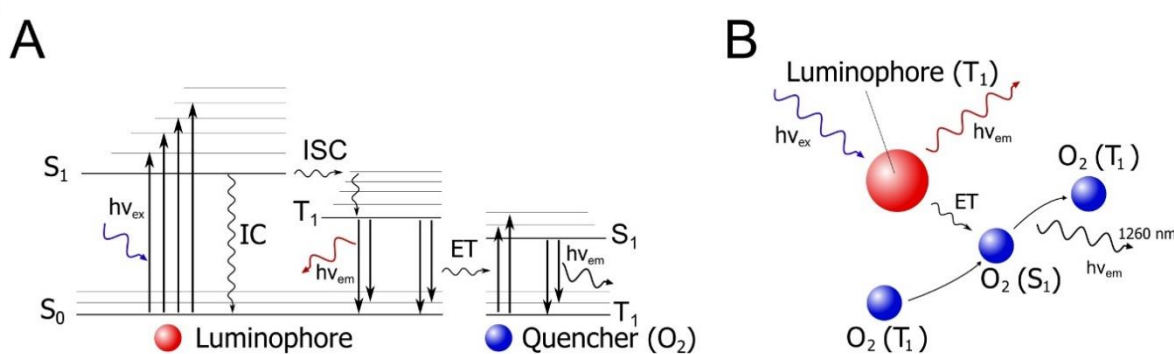


Figure 2.1. Basic principle of luminescent oxygen sensing. (A) Simplified Jablonski diagram displaying energetical transitions during the dynamic quenching process and (B) scheme of collisional quenching principle

2.2.1.1 Sensing principle

The majority of optical oxygen sensors is based on the use of luminescent probes, whose luminescence intensity and luminescence lifetime are quenched by molecular oxygen. During this quenching process excited-state energy from a phosphorescent indicator molecule is transferred to an oxygen molecule upon collision (Figure 2.1). This energy transfer (ET) leads to a decrease of both luminescence intensity and luminescence lifetime, which is proportional to the oxygen concentration. The impact of collisional quenching on luminescence intensity and luminescence lifetime is described by the linear Stern-Volmer equation (equation 2.1)

$$\frac{I_0}{I} = \frac{\tau_0}{\tau} = 1 + K_{SV} pO_2 \quad (2.1)$$

where I_0 and I are the luminescence intensities in absence and presence of the quencher, τ_0 and τ are the luminescence lifetimes in absence and presence of the quencher, K_{SV} is the Stern-Volmer quenching constant, which characterizes the quenching efficiency and therefore the sensitivity of the sensor and pO_2 is the partial pressure of oxygen.

However, many optical sensors do not exhibit a linear calibration curve – especially when luminescent probes are dissolved in microheterogeneous environments (e.g. in polymers). In such cases the so-called two-site model (equation 2.2) of Demas et al.¹⁹ is better suited to describe the behavior of an optical oxygen sensor.

$$\frac{I}{I_0} = \frac{\tau}{\tau_0} = \frac{f_1}{1 + K_{SV,1}pO_2} + \frac{f_2}{1 + K_{SV,2}pO_2} \quad (2.2)$$

Here, the parameters f_1 and f_2 describe different fractions of dye molecules, which are quenched with the respective K_{SV} . Note that $f_2 = 1 - f_1$. In many cases $K_{SV,2}$ can be set to zero, which simplifies equation 2.2.

2.2.1.2 Optical oxygen sensing methods

Luminescence quenching by molecular oxygen affects luminescence intensity and luminescence lifetime as described in the preceding chapter. Thus these are the parameters, which can be used to determine the pO_2 .

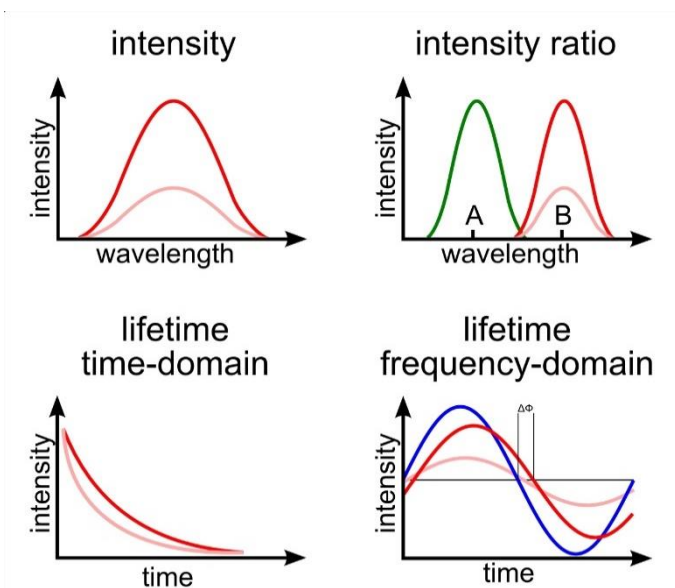


Figure 2.2. Measurement methods for luminescent oxygen sensors

The simplest method for sensing oxygen is the measurement of luminescence intensity. Unfortunately, this parameter is influenced by a variety of factors such as light source intensity, luminophore concentration, photobleaching or leaching of the luminophore, scattering, ambient light and detection efficiency. Several methods exist to overcome these potential sources of error for intensity-based measurements: ratiometric methods rely on the use of an oxygen-sensitive and a reference dye, which are excited by the same light source, but have different emission spectra. The presence of oxygen only influences the emission of the indicator dye, while the emission of the reference dye remains stable. Oxygen levels can be determined by the ratio between indicator and reference emission at two different wavelengths. The use of the ratio as oxygen-sensitive parameter helps to improve oxygen measurements in terms of stability to light source variations, scattering, detection efficiency and luminophore concentration, when intensity and reference dye

follow the same inhomogeneities as layer thickness. However, signal variations due to photobleaching or leaching of the luminophore, ambient light or wavelength-dependent scattering still influence the apparent oxygen concentration.

The measurement of luminescence lifetime is a possibility to overcome the remaining limitations of intensity-based methods. Luminescence lifetime can be detected using two different methods: the time-domain or the frequency-domain approach, both relying on a modulation of the light source. A square-shaped light pulse is generally used for excitation of the luminophore for the time-domain approach and the emission intensity is detected during the luminescence decay of the excited luminophore. This approach is most commonly used for imaging applications as the so-called “pulse-and-gate” method²⁰. A gated detector collects photons during two or more time gates. Assuming a single-exponential decay the ratio between these integrated gates A_1 and A_2 at different times t_1 and t_2 can be used to determine the luminescence lifetime of the indicator according to equation 2.3.

$$\tau = \frac{t_2 - t_1}{\ln\left(\frac{A_1}{A_2}\right)} \quad (2.3)$$

The frequency-domain method is the second method to determine the luminescence lifetime. This method involves excitation of the luminophore with sinusoidally modulated light and detection of the phase-shifted emission signal. The phase-shift (φ) between excitation and emission is oxygen-dependent and can be used to calculate luminescence lifetime τ according to equation 2.4.

$$\tau = \frac{\tan(\varphi)}{2\pi \cdot f} \quad (2.4)$$

where f is the modulation frequency.

2.2.1.3 Recent advances, key trends and perspectives

Several reviews report on recent advances in optical oxygen sensors. Quaranta et al.¹⁵ carefully reviewed indicators for optical oxygen sensors. They discussed promising classes of new indicator dyes such as NIR emitting dyes²¹ and dual wavelength emitting dyes^{22–25}. The longwave-shifted spectral properties of the former are especially promising for biological applications due to a reduction of scattering and autofluorescence generated by biological substances and deeper penetration depths into biological tissue. Moreover, they exhibit high luminescence brightness and photostability. The latter dye class, which possesses oxygen-sensitive phosphorescence and oxygen-insensitive fluorescence, represents promising candidates for ratiometric measurements. One intrinsically referenced dye can be used instead of using two different dyes with possibly different leaching or photobleaching behavior. Further recent advances in sensor material design have been made regarding covalent attachment of indicator dyes to silica gel²⁶ or polystyrene copolymers²⁷ to yield leaching-free sensors.

Other advances in optical sensing were made regarding multiple-analyte sensing methods, which have been critically reviewed by Stich et al.²⁸. Optical multisensors can be used for

simultaneous determination of analytes at exactly the same spot. This can be achieved via combination of different indicators and/or matrix polymers into either multi-layer or single-layer multisensory systems. Dual or triple sensors for most commonly oxygen and one or two other parameters such as temperature, carbon dioxide, pH and glucose have been realized in that way.

Apart from advances in sensor material development, considerable progress has been made regarding the application of optical oxygen sensors – with a strong focus on oxygen sensing for biological detection including enzymatic assays, analysis of respiration of mammalian and microbial cells, small organisms and plants, food and microbial safety, monitoring of oxygenation in cell cultures, live tissue measurements, bioreactors and fluidic chips. Papkovsky and Dmitriev reviewed recent developments in this area¹⁸.

Among other applications a growing field of application for optical oxygen sensors is their integration in microfluidic environments. Grist et al.⁴ reviewed previously proposed optical oxygen sensor methods, luminescent materials, sensor formats and measurement systems and discussed their applicability to microfluidic cell culture. They concluded that a variety of optical oxygen sensors is compatible with microfluidic environments and presented an overview of existing applications of these sensors in microfluidic cell culture. Seamless integration with existing microfluidic cell culture equipment was identified by Grist et al. to be part of future research.

A factor, which facilitates new applications of optical oxygen sensors is the commercial availability of sensor materials and systems. Nowadays there is a range of companies that develop and manufacture optical oxygen sensors, for instance Presens (www.presens.de), Ocean Optics (www.oceanoptics.com), PyroScience (www.pyro-science.com), Centec (www.centec.de), Oxsens (www.oxysense.com), Finesse (www.finesse.com) and Hach-Lange (www.hach-lange.de). Optical oxygen sensors are also sold by companies specialized in medical products as OptiMedical Systems (www.optimedical.com) and Terumo (www.terumo-cvs.com).

2.2.2 Fluorescent pH sensors

The need for pH measurement can be found in a broad range of applications such as environmental, industrial and biomedical. The measurement of pH is of high importance, because pH is of concern for synthesis, life sciences, food and beverage processing and marine and pharmaceutical research to only name a few.

Several reviews and book chapters have been published on different issues and cover issues such as sensing principles and methods and sensor materials. The following chapter gives a short introduction on these issues.

2.2.2.1 pH sensing principles

Fluorescent pH sensors are based on fluorescent indicator dyes, whose optical properties change upon reversible binding of a proton H^+ . Different sensing principles for fluorescent pH sensors exist. Most pH indicators are weak organic acids or bases exhibiting different fluorescence excitation and emission spectra related to their protonated (acidic) or deprotonated (basic) form. When the equilibrium between protonated and deprotonated form is shifted due to a change of H_3O^+ concentration, usually an alteration of the excitation as well as of the emission spectrum occurs. The spectral alteration of the emission spectra does not occur for indicators which undergo photoinduced proton transfer (PPT). The pK_a of the excited state of these indicators is

usually higher than the pK_a of the ground state. Only emission of the basic form can be observed due to deprotonation upon excitation, because these dyes are usually applied around the pK_a of the ground state.

Another class of pH indicators is based on the principle of photoinduced electron transfer (PET). These indicators consist of a fluorophore linked to an electron-donating group, which quenches the fluorophore's emission by energy transfer. Binding of a proton leads to an energetically shifted energy level and consequential prevention of the electron transfer and an increase of fluorescence intensity, while the deprotonated form shows low emission intensity due to the internal quenching. In this way only the quantum yield of these dyes and not excitation or emission spectra are changed upon a change of pH.

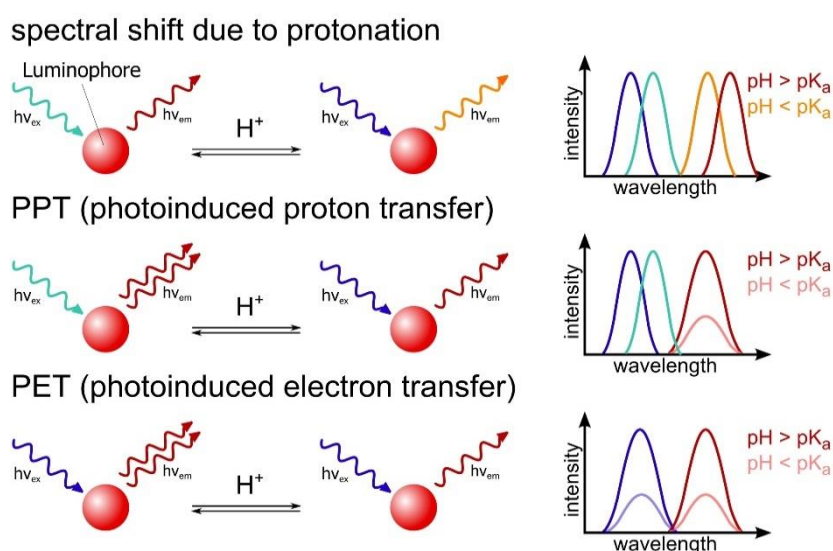


Figure 2.3. Basic principle of fluorescent pH indicators

In contrast to electrochemical determination of pH, optical methods are based on the determination of the concentration of the acidic, [A], and basic form, [B], of the indicator and follow the well-known Hendersson-Hasselbach equation

$$pH = pK_a + \log \frac{[B]}{[A]} \quad (2.5)$$

where pK_a is the negative logarithm of the acid dissociation constant K_a . Due to the definition of pH, which is the negative logarithm of the activity of protons H^+ (simplified notation for $H_3O_{aq}^+$), the H^+ activity has to be taken into account, leading to the following equation:

$$pH = pK + \log \frac{[B]}{[A]} + \log \frac{f_B}{f_A} \quad (2.6)$$

with f_B and f_A being the activity coefficients of the basic and the acidic form of the indicator. By comparison of equation 2.5 and equation 2.6 we yield

$$pK_a = pK + \log \frac{f_B}{f_A} \quad (2.7)$$

The pK_a therefore depends on the activity coefficients and all the factors, which influence the activity coefficients such as ionic strength or the interaction of the indicator dye with its microenvironment. Thus optical pH sensors show a cross-sensitivity towards ionic strength²⁹, which results in a shift of the calibration plot. However, the application of lowly charged indicator dyes in uncharged hydrogel matrices³⁰⁻³³ can be used to perform reliable pH measurements by optical sensing methods.

Another characteristic feature of optical pH measurements (in contrast to electrochemical detection) is the appearance of the calibration curve. Optical pH sensors exhibit a sigmoidal pH response with the highest signal change close to pK_a . The dynamic range of optical pH sensors is usually restricted to $pK_a \pm 1.5$, but its narrow leads to a high sensitivity around the pK_a . However, it has been shown, that an extension of the dynamic range can be achieved by using absorptiometric or fluorescent indicators with two pK_a values or by using several similar indicators with different pK_a values^{32,34-36}.

2.2.2.2 Optical pH sensing methods

As for optical oxygen sensors the simplest method for sensing pH is the measurement of luminescence intensity. We already discussed in chapter 2.2.1.2, that this parameter is influenced by a variety of factors such as scattering, ambient light or factors derived from temporal or spatial inhomogeneities of optical system or fluorophore concentration. Thus several methods for referenced pH sensing have been developed, ranging from ratiometric to time-resolved techniques.

Due to short lifetimes of fluorescent pH indicators, direct lifetime measurements require bulky and very expensive equipment. A phase modulation technique can be used to avoid the high costs, called dual lifetime referencing (DLR) as introduced for chloride sensors by Huber et al.³⁷. DLR makes use of two luminophores, which are simultaneously excited at the same wavelength. These dyes exhibit widely differing decay times, with one serving as phosphorescent reference dye and the other one being the fluorescent pH indicator. The change of the overall phase shift resulting from a pH dependent change of the intensity of the fluorescent pH indicator is used to determine the pH. Optical pH sensing by DLR is thereby independent of ambient light and of variations of luminophore concentration (as long as the concentration of both luminophores changes) or instability of light source and detector.

Nowadays, ratiometric methods are most widely applied for pH sensing. These methods can be used for either single pH indicator dyes or for dye combinations. Single indicator dyes exhibit a pH dependent ratio of fluorescent intensities, measured either at two excitation or at two emission wavelengths and require different spectral behavior of acidic and basic indicator form. Common pH indicators for these measurements are fluorescein, SNAFL dyes, SNARF dyes and HPTS. Ratiometric measurements for PET-based pH indicators are only possible applying dye combinations with one dye serving as reference dye (as already described for ratiometric oxygen measurements) due to the lacking spectral shift of acidic and basic form.

2.2.2.3 Recent advances, key trends and perspectives

Wencel et al.³⁸ summarized, that recent advances of luminescent pH sensing have been mainly based on synthesis of novel pH indicators and the development or investigation of new matrix materials such as novel polymer and sol-gel encapsulation matrices. Interesting progress includes the synthesis of long-wave-shifted absorption and emission spectra^{39,40}, which make them especially suited for biomedical applications as already discussed for oxygen indicators in 2.1.3. Important advances have also been achieved via covalent coupling of indicator dyes to sensor matrixes as reported by several publications^{39,41-45}. Other progress has been made regarding UV-patterning of sensor layers^{41,46} and overall development of matrix material⁴⁷.

Current trends and future perspectives were identified by Wencel et al. to comprise miniaturization, integration of pH sensors into miniaturized environments, the use of nano particles for their use in intracellular sensing as well as development of highly functional materials for pH sensing with improved sensitivity, selectivity and stability. Ongoing development further affects intracellular pH sensing and imaging as reviewed by Han and Burgess⁴⁸.

Further advances in optical sensing have been made regarding multiple-analyte sensing methods, which have been critically reviewed by Stich et al.²⁸ as already mentioned in chapter 2.1.3. Most publications report on multianalyte sensors comprising oxygen and pH indicators, but also methods for dual sensing of pH and temperature and triple sensors for pH, oxygen and temperature exist.

In contrast to oxygen sensors the commercial availability of optical pH sensors is still limited. While Ocean Optics sells colorimetric pH sensor patches, noninvasive sensor patches and microsensors, which are based on fluorescent pH indicators, are commercially available only from Presens (www.presens.de). Like optical oxygen sensors pH sensors are also sold by companies specialized in medical products as OptiMedical Systems (www.optimedical.com) and Terumo (www.terumo-cvs.com). pH optodes have been integrated in this area with blood gas analyzers.

2.3 Integration of optical sensors into microfluidic devices – an optimization challenge

Due to the fact that a variety of materials and methods for optical sensing of oxygen and pH already exists, there is no need to reinvent the “luminescent sensor wheel” for adjusting suitable sensing systems for microfluidic systems. Integration of luminescent sensors rather means an optimization and smart combination of different components, which have been previously proposed and optimized for optical sensing. The main decisions for an optical sensor set-up affect the sensing chemistry, comprising luminescent indicators and matrices (chapter 2.3.1), sensor format (chapter 2.3.2) and the optical sensor system, involving excitation sources, optical filters, detectors and detection methods (chapter 2.3.3). Due to the challenges that analysis in microfluidic devices entail, there is high demand for the use of high performance materials and methods. It is important to note, that the perfect sensing set-up does not exist, but the suitable sensing set-up has to be adapted to each specific analytical task in microfluidics. While some applications, for example, may be sufficiently covered by point measurements and allow a rather simple set-up with commercially available and glued-in sensor spots – connected with an optical fiber to a read-out unit, other applications might make it necessary to integrate whole sensor films with increased brightness for imaging applications – performed with rather expensive and

complicated imaging equipment. In other cases it might be necessary to use commercially available microfluidic chips without previously integrated sensing materials. Then another way has to be found to integrate sensor materials into the completed (and closed) microfluidic devices such as nano sensor particles or magnetic sensor particles.

The following chapter describes promising sensing materials, sensor formats and optical measurement systems and discusses their advantages and disadvantages concerning their integration into microfluidic devices. The final chapter on published microfluidic sensing set-ups (chapter 2.3.4) will provide an overview of successfully applied luminescent optical oxygen and pH sensors in microfluidic structures.

2.3.1 Sensing chemistry

Most luminescent sensors use a luminescent indicator integrated into a suitable sensing matrix. The optical properties of that luminescent dye change, when the analyte in the environment changes. The sensing chemistry affects important properties of the final optical sensor, as it determines dynamic range, brightness, spectral properties, photo- and chemical stability and biocompatibility.

2.3.1.1 Choice of luminescent indicator

State of the art of luminescent oxygen indicators¹⁵ and of fluorescent pH indicators⁴⁸ have been summarized elsewhere. Here criteria for the choice of luminescent indicators are generally discussed and especially promising features of luminescent indicators for microfluidics are highlighted.

Important criteria for the choice of an appropriate indicator are:

- spectral properties
- brightness
- luminescence decay time
- chemical stability and photostability
- cross-sensitivity
- toxicity
- commercial or synthetic availability

Spectral properties. Generally a large Stoke's shift is preferable, because luminescent emission can be easily separated from excitation light by suitable optical filters. Spectral compatibility with available excitation sources and detectors also has to be considered for the choice of an appropriate indicator. Especially in microfluidics it may be advantageous to combine luminescence sensing with existing laboratory equipment, e.g. available microscope set-ups, to avoid high purchase costs for new optical equipment. Nowadays a trend towards long-wave shifted excitation and emission can be observed. This trend can be traced back to the fact that excitation in the UV part of the spectrum can lead to autofluorescence by biological substances. Additionally, UV light is known for having a perturbing impact on cell growth and viability. The wavelength is also important for tissue monitoring, where penetration depth of excitation light is relevant. Long-wave shifted light is less affected by absorption and scattering of cell material. Due to these reasons long-wave excitable and emissive indicators are strongly preferable. Promising indicators for such applications are NIR emitting probes such as Pt(II) and Pd(II) complexes with

π -extended benzo-naphthoporphyrins⁴⁹ as well as azabenzoporphyrins⁵⁰ for oxygen measurements and long-wave shifted pH indicators^{39,40}. The need for spectral compatibility of luminescent indicator with available optical equipment may, for example, contraindicate the use of NIR dyes, because CCD chips of microscope cameras as well as some photodetectors exhibit lower sensitivity in this spectral region.

Brightness. The brightness of a luminescent indicator depends on its molar absorption coefficient and the luminescence quantum yield. The use of particularly bright indicators is generally advantageous, because these dyes can be used in lower concentration within a polymeric matrix. Moreover they enable the application of thin-film optodes with short response time or lower concentration of nano particles. Owing to low channel depths of microfluidic devices these indicators can be especially beneficial to increase the amount of detectable light. Oxygen indicators, which are known for their high brightness, comprise Ir(III) coumarin complexes⁵¹ and NIR emitting Pt(II) benzoporphyrins. Also not extended Pt(II) porphyrins are known for their high brightness upon excitation in their Soret-band, which is located in the UV region.

A possibility to increase the brightness of moderately luminescent indicators is the application of light harvesting. This method is based on the application of two luminescent dyes, one serving as antenna dye by absorbing excitation light. The absorbed light energy is further partially transferred to an indicator dye via FRET⁵². The principle of light harvesting was already shown for reagent-mediated optical sensors using the example of oxygen and ammonia sensors by Mayr et al.⁵³, but was stated to also be applicable for other analytes such as pH, carbon dioxide or ions.

Luminescence decay time. The luminescence decay time plays a crucial role for oxygen sensing since the sensitivity of oxygen sensors is determined by the decay time of the indicator and the gas permeability of the sensor matrix. Thus it is mandatory to employ well-tuned combinations of a luminescent indicator and a sensor matrix adapted to the measuring range of oxygen.

Chemical stability and photostability. Due to the usual incorporation of luminescent indicators into a protective sensor matrix, the chemical stability of luminescent sensors is sufficient for application in many different processes, for example waste water treatment plants. However, several harsh conditions such as employed sterilization procedures or oxidizing agents, can affect the long-term stability of luminescence indicators. The stability of sensing materials towards sterilization techniques has been comprehensively studied⁵⁴. Also some solvent-resistant sensors have been published, which are based on the application of sol-gel matrices⁵⁵⁻⁵⁷.

In contrast to chemical stability the photostability of luminescent indicators is a very critical parameter for the application of luminescent sensors, in particular for long-term applications or for methods, where high excitation intensities are used, e.g. in microscopic applications. Unfortunately there is a lack of data comparing different classes of indicators. However, studies showed, that electron-withdrawing substituents in the indicator molecule can improve the photostability of the indicator due to a reduced sensitivity towards singlet oxygen, which is known to otherwise oxidize indicator molecules. Highly photostable indicators for oxygen sensing include Pt(II) and Pd(II) complexes of octaethylporphyrinketones (PtOEPK)⁵⁸ and the respective complexes of highly fluorinated pentafluorophenylporphyrins⁵⁹. Highly photostable pH indicators include HPTS, NIR emitting aza-BODIPYs⁴⁰ and some perylene bisimides⁶⁰.

Cross-sensitivity. Luminescent indicators can be cross-sensitive to other parameters. The most important parameters herein are temperature for oxygen sensing and ionic strength for pH sensing. Strategies to reduce the erroneously obtained results are to correct for known dependencies or to choose indicators, which are less cross-sensitive.

Toxicity. Toxicity of luminescent dyes is not only caused by the dye itself, but also by production of singlet oxygen, which by definition happens during the dynamic quenching process of oxygen sensors. Compared to the toxicity due to generated singlet oxygen, the toxicity due to the dye plays a secondary role, because the dye is encapsulated in a sensing matrix and thus excluded from direct contact with the investigated biological material. Singlet oxygen, however, can diffuse through the matrix material and can negatively affect cell growth before it returns to its ground state again. Possible ways to reduce toxic effects of singlet oxygen are to decrease excitation light intensities or the dye loading - leading to a reduced production of singlet oxygen - or to increase diffusion pathlengths between sensing layer and biological material to increase the probability for singlet oxygen deactivation. Due to the fact that microfluidic applications often deal with biological or medical applications, the toxicity of the integrated sensor materials plays an important role for considering the ideal sensing setup.

Commercial or synthetic availability. Although a variety of different luminescent dyes exists, the commercial or synthetic availability of a luminescent dye represents a key factor for deciding which indicator to choose. This is especially important for microfluidic labs facing a lack of synthetic equipment or qualified personnel for complex synthesis. The costs of the luminescent indicator might play a major role for industrial applications, for example for the production of microfluidics with integrated luminescent sensors, while prize issues are probably less important for research activities, because of low amounts of needed dye.

2.3.1.2 Selection of sensor matrix

The selection of an appropriate sensor matrix is a critical step for sensor development. It serves as a solid support for the indicator dye and can help to improve the sensor performance or to reduce the cross-sensitivity to other analytes as it determines several fundamental characteristics of an optical sensor such as selectivity, sensitivity, response time, appearance of the calibration curve, mechanical and chemical stability, flexibility and covalent linkage of luminescent indicators. The following section tries to explain and to sum up the considerations for selecting an appropriate matrix in general including considerations concerning microfluidics. Additional information can be found in one of the reviews, which have described the impact of the sensor matrix on the performance of oxygen sensors¹² and of pH sensors^{38,61} in detail¹³.

Selectivity. The selectivity of a luminescent sensor can be improved by choosing a matrix that is permeable for the analyte while rejecting as far as possible other species, which may also interact with the luminophore. Typical oxygen sensor matrices exhibit hydrophobicity and gas permeability and therefore the selectivity of oxygen sensors is straightforward, while the cross-sensitivity of pH sensors to ionic strength still appears to be a topic to current research. Matrices for pH sensing should be hydrophilic to allow proton diffusion. However, only a few specific matrices, such as uncharged hydrogels seem to yield optical pH sensors with negligible cross-sensitivity to ionic strength³⁰⁻³³.

Sensitivity and response time. The permeability of an oxygen sensor matrix not only affects its selectivity, but also its sensitivity, thus the initial slope of the calibration plot, which is described by K_{SV} for oxygen sensors. For pH sensors the choice of the matrix affects the apparent pK_a of the calibration curve. Furthermore the response time of an optical sensor is affected by the permeability of the sensor matrix, because it determines the time for achieving the equilibrium between sample and sensor.

Appearance of the calibration curve. With the appearance of the calibration curve we refer to the linearity of the calibration curve. Unlike the pH electrode, optical pH sensors show linear behavior only over a limited pH range, mostly restricted to several pH units, whose position in the whole pH range is determined by the matrix as already mentioned. For oxygen sensors the properties of the matrix affect the linearity of the calibration curve. It was already mentioned in chapter 2.2.1.1, that heterogeneous microenvironments for a luminescent dye can be created by entrapment of the luminophore, for example, into a polymer. Thus linearity of the calibration curve can be achieved by choosing an appropriate sensing matrix.

Mechanical and chemical stability. As already mentioned in chapter 2.3.1.1, chemical and mechanical stability of the indicator is usually achieved via embedding the respective indicator into a protective host material. This means, that the stability mostly depends on the stability of this host material towards chemical or mechanical stress. Due to the solvability of many polymers in organic solvents, most optical sensors exhibit low chemical stability in non-aqueous measurement environments. However, a few sensing set-ups for solvent-resistant sensing exist, which are based on the application of sol-gel matrices⁵⁵⁻⁵⁷. Mechanical stability of sensor materials is of less importance than chemical stability for microfluidic applications due to the lack of mechanical stress in these environments. However, adhesion properties of the sensor matrix to the microfluidic channel represent an important parameter due to the high shear stress prevailing in microfluidics, which may detach sensor layers from channel walls.

Flexibility. Flexibility in the context of matrix material notably means the accessibility to different preparation techniques for sensor formats (e.g. dip-coating, spin-coating, screen printing, spray coating, inkjet-printing or knife coating to generate sensor layers, but also techniques to achieve sensor particles such as precipitation or solvent evaporation). Particularly the generation of sensor layers inside microfluidic channels is a challenging task and one may be restricted to certain deposition techniques.

Covalent linkage of luminescent indicators. Apart from the characteristics of an optical sensor caused by the sensor matrix, other considerations concern immobilization strategies of the luminophore inside the sensing matrix. Generally a luminophore can be physically or covalently immobilized in a suitable matrix material. In recent years, there has been an increasing interest in covalent immobilization of sensor dyes via direct grafting onto matrix materials for oxygen sensors as well as for pH sensors^{26,27}. These studies revealed that the resulting sensors with covalent linkage feature improved sensor performance and are not affected by dye leaching compared to sensors, which use physical entrapment methods. Nevertheless, physical entrapment is most possibly going to succeed in many cases comparing the effort and required expertise for applying these different immobilization strategies to yield optical sensors with acceptable sensing

features. However, covalent immobilization might be indispensable in certain applications where dye leaching plays a major role.

2.3.2 Optical Sensor Formats

The possibility to use different sensor formats makes optical sensors be a very versatile platform to be integrated into microfluidics. The format should be chosen – coordinated with the detection method - according to the respective measurements requirements, e.g. the requirement for single-point measurements or laterally resolved information. The particular choice of a microfluidic device is also important, meaning the application of commercially available microfluidic devices or self-constructed microfluidics.

Basically different sensor formats include sensor layers, optical fiber sensors, and micro/nanoparticles. Although soluble probes should not be referred to as sensors, they are included in this chapter, because they have been used in microfluidics. A schematic overview over different sensor formats is presented in Figure 2.4. All these formats are described and discussed regarding their applicability in microfluidics throughout the next section, whereas the application of different sensor formats in microfluidics is presented in chapter 2.3.4.

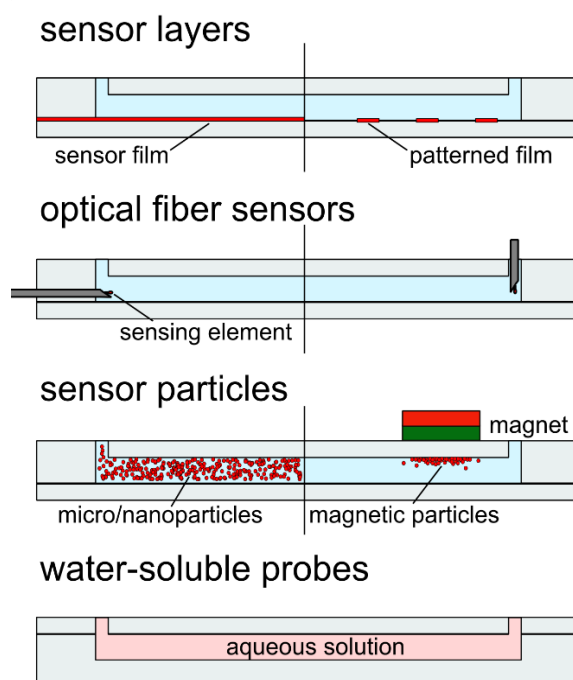


Figure 2.4. Different sensor formats for sensor integration into microfluidic devices

2.3.2.1 Sensor layers

Sensor layers represent the most commonly used format of optical sensors in microfluidics. They can be deposited from a so-called “sensor cocktail” (matrix material, indicator and additives dissolved in a suitable solvent) onto a substrate by spin-coating, screen printing, spray coating, knife coating, inkjet or pin-printing. Subsequently the applied wet film is allowed to dry, polymerize or cure. The layers can be used either as un-patterned films or as patterned films. The latter can be fabricated by either coating only small areas or by completely coating a substrate and

a subsequent lift-off process. Another possibility to create patterned sensors is to apply a photolithographic curing process of photopatternable matrices.

The use of sensing layers entails several advantages and disadvantages: an advantageous feature of sensor layers is that they do not require additional effort once they are integrated into a microfluidic device and can then simply be used for single-point measurements or for imaging applications. Moreover, the fabrication of layers is generally compatible with microfabrication techniques, which might facilitate their use. However, layer integration means an additional step in chip fabrication and until now no satisfactory techniques to integrate sensor layers into ready-made devices have been developed. Thus, only those laboratories are able to use sensor layers, which produce microfluidic chips by themselves. Additionally, the fix integration of sensing layers means, that photobleaching and leaching may limit the long-term stability of a sensor chip.

2.3.2.2 Optical fiber sensors

Optical fiber sensors are another frequently used sensor format as they enable remote sensing at poorly accessible sites or in harsh or hazardous environments. Several reviews have summarized fabrication and application of fiber optic chemical sensors or biosensors⁶²⁻⁶⁷. Optical fiber sensors consist of the sensing element (matrix material and indicator) attached to an optical fiber, which serves as waveguide and carries excitation and emission light from the light source to the sensing element and from the sensing element to the detector respectively. The sensing element is usually attached to the fiber via dip-coating from a sensor cocktail and sometimes covered by layers of black silicone providing optical isolation from ambient light.

Due to the use of the optical fiber the lateral resolution of this sensor format is limited by the size of the fiber. Although imaging applications are excluded for fiber optic sensing, gradients can be measured by using arrays of sensors⁶⁸.

Although the direct integration of fiber optic sensors into microfluidic chips is rarely used, many publications report on contactless optical fiber measurements, which means that a sensor spot is integrated into a microfluidic device and an optical fiber is used for coupling light to and from the sensor spot. Another interesting application is to use the waveguiding principle without the need for integration of an optical fiber.

2.3.2.3 Micro/nanoparticles

Sensor beads derive from the demand to create a sensing platform, which is as flexible as dissolved indicators regarding their integration into different systems, but which also exhibits the advantages of indicator encapsulation into a suitable matrix. Due to that versatility several reviews addressed the fabrication and application of sensor particles⁶⁹⁻⁷¹. Various preparation procedures have been reported, such as adsorbing indicator molecules to particle surfaces, polymerization, precipitation or grinding indicator-loaded matrix bulk materials.

Sensor particles represent a simple and versatile tool also for their application in microfluidic environments. They can simply be added to the fluid, which is pumped through microfluidic channels and therefore mean no additional effort of chip development. Moreover photobleaching behavior plays a minor role due to the fact, that the sensing element is not static, but permanently exchanged⁷². However, new challenges arise concerning the brightness of the applied sensor particles. Reduced channel depths lead to insufficient emission intensities, because the amount of sensor material is limited by the small volume. A method to circumvent this disadvantage of most

sensor particles is the use of magnetic sensor particles⁶⁹. The combination of both magnetic and sensing properties allows to combine advantageous features of nano sensor particles and sensor layers: they are easy to integrate into any microfluidic device, while their separation from surrounding solution allows the generation of magnetic sensor spots with increased brightness compared to nano particle dispersions.

2.3.2.4 Water-Soluble/Macromolecular probes

Water-soluble probes are another possibility to integrate a sensing functionality into a microfluidic device, although in a strict sense free probes should not be referred to as sensors and are only mentioned here for the sake of completeness. Interference with their environment is a drastic limitation of sensing performance, because of the lack of an encapsulation matrix. Moreover certain parameters such as sensitivity and selectivity can not be adjusted by selection of a suitable matrix. A way to overcome these severe drawbacks is the covalent linkage to other molecules, wherein the dendritic encapsulation of the luminophore into a cage of branched molecules (dendrimers) is one of the most promising techniques⁷³.

2.3.3 Optical Measurement Systems

The applied measurement system is an important step in microfluidic sensor development. A range of different excitation light sources, detectors and other optical components such as lenses or optical filters exist and have to be chosen according the specific measurement requirements.

Basically there are two approaches to combine optical components with microfluidic devices: the off-chip approach, where macro-scale excitation and detection techniques are coupled to micro-scale detection areas, and the on-chip approach, which aims at direct integration of miniaturized excitation and/or detection techniques into microfluidic devices as discussed in a review by Kuswandi et al⁷⁴. Both approaches entail their specific advantages and disadvantages: the off-chip approach employs commonly used sensing techniques, which have been developed for macro-scale sensing and thus are well established methods with low levels of background signals. The on-chip approach is based on utilizing recent developments in micro-optical electromechanical systems (MOEMS). These micro-optical technologies aim at replacing bulky, large and expensive macro-scale optical components. Thus their integration represents a promising possibility to obtain portable instrumentation based on microfluidic systems.

Aside from a distinction into different approaches of integration the optical measurement system has to be adapted to other considerations regarding spatial resolution, compatibility with optical sensing methods (e.g. lifetime measurements) and costs for sensor setups. Regarding the costs for sensor setups it is important to note, that it makes sense to consider the application of optical equipment already in use in microfluidic labs, such as fluorescent microscopes or other optical equipment.

The following chapter discusses different light sources, detectors and other (passive) optical components such as optical filters and microlenses regarding their applicability in microfluidic optical sensing.

2.3.3.1 Light sources

The emission of the excitation light source has to be spectrally compatible with the excitation spectrum of the luminescent indicator. Lifetime measurements need excitation sources that can

be modulated either sinusoidally or by a square-shaped light pulse for applying frequency domain or time domain lifetime methods, respectively.

Generally laser excitation, light-emitting diodes (LEDs) or filtered broad-spectrum excitation lamps can be used for indicator excitation. Laser excitation sources offer the possibility of light-source modulation, are well-suited to focus on very small detection volumes and high light densities with a narrow wavelength range can be obtained. Lamp-based excitation sources, such as xenon or mercury lamps, on the other hand, cover a broad spectral compatibility with different indicators, which makes them be a more flexible alternative, which is less expensive than laser excitation sources. Moreover, most microscope set-ups employ these lamps, whereby the acquisition costs remain low, because most microfluidic labs already possess this equipment, which can be easily adapted to sensing purposes. However, lamp-based excitation sources are limited in application due to their lack of modulation possibility.

LED sources are commonly used as excitation sources for optical sensors, because they represent low-cost tools, which can be pulsed or sinusoidally modulated. Moreover, they are almost monochromatic emitters, which are available in a broad range of excitation wavelengths, ranging from UV to IR excitation. Their compact design and their power-effectiveness make them be perfectly suited for integration into microfluidic devices. The last decades have seen interesting development in the field of organic light-emitting diodes (OLEDs), which are considered to be especially promising for integration into microfluidics due to their flat film-like shape. However, their broad emission spectra make the additional integration of optical filters in most cases indispensable.

2.3.3.2 Detectors

The detector has to exhibit compatibility with the emission wavelength of the luminescent indicator and with the required measurement method (lifetime detection, ratiometric detection, etc.). Moreover, the detector determines, if the analyte concentration is measured at single spots or if the analyte concentration can be spatially resolved. Several detection methods are well-established in optical pH and oxygen sensing and have been summarized in various recommendable books^{10,11}. Commonly used detectors include on the one hand point detectors, such as photomultiplier tubes (PMTs) and photodiodes, which are advantageous due to their simplicity and fast response time, and on the other hand charge-coupled devices (CCDs) for two-dimensional mapping of the analyte concentration.

The combination of high gain, low noise and fast response has PMTs made a frequently used detector for optical sensing. The sensitivity of PMTs covers the whole UV-VIS spectrum and also PMTs with increased sensitivity in the NIR are commercially available. Photodiodes generally represent a less sensitive alternative to PMTs in the visible range, but they are advantageous for applications in the NIR. Moreover, they are promising devices to be combined with microfluidic applications due to their small size, low costs, robustness and their need for low voltage. These features of photomultiplier tubes and photodiodes have made them well-suited for optical sensing set-ups and especially dedicated for lifetime detection.

However, spatial resolution of the analyte concentration can only be obtained using arrays of these detectors. CCDs or CMOS are usually used for these imaging purposes instead. These CCDs can be used for parallelization of optical measurements when used in macroscopic imaging set-ups or for a more detailed look into a microfluidic channel, when combined with microscope

optics. However, imaging set-ups enabling lifetime imaging are very high prized. Thus, the use of ratiometric imaging, using the different channels of a color CCD chip or simple intensity imaging seems to be more adequate to be combined with microfluidic optical sensing.

2.3.3.3 Other optical components

While light sources and detectors are absolutely necessary to perform optical sensing, additional optical components such as optical filters, lenses and waveguides are helpful to improve the performance of an optical sensing set-up. Optical filters selectively transmit light of certain wavelengths and are used for cutting disturbing excitation light from spectrally broad emitting light sources (excitation filters) or for reduction of ambient light, background fluorescence or other luminescence emission light without analytical information. Lenses may be used to focus excitation light on small detection volumes or to collect emission light to focus it on a suitable detector. Finally, waveguides can be used to guide excitation or emission light to or from a microfluidic channel.

Macroscopic optical components, which can be used for off-chip sensing approaches, are commercially available from several providers and are not discussed in this context. Recent effort, however, has focused on the integration of passive optical functions directly into microfluidic devices. These functions can be fabricated by standard micromachining technologies and thus are deemed considerably promising for their combination with chip fabrication processes.

Microlenses have been fabricated directly into microfluidic chips by melting pieces of photoresist into hemispherical shapes⁷⁵, or by a process including photolithography and deep reactive ion etching to achieve multiple 2D microlenses⁷⁶. In another approach an insertion channel for an optical fiber was integrated into a microfluidic PDMS chip⁷⁷. The interface between insertion channel and microfluidic channel was curved in the form of a lens to focus the excitation light guided through the optical fiber. In all these cases the integration of microlenses increased luminescence signal intensities, enabled to reduce sensing spot sizes and improved detection limits.

Another publication reported on the integration of optical long-pass filters by incorporating dye molecules into the microfluidic chip material⁷⁸. The filters only showed slight bleaching after extensive illumination and negligible dye leaching in aqueous solutions. Also waveguides have been applied in several publications^{79,80} to guide excitation light to and from the microfluidic channel.

These individual optical components can be combined to yield microfluidic devices exhibiting all the features needed for optical sensing. Such a device has for example been realized by Balslev et al.⁸¹ and is presented in Figure 2.5.

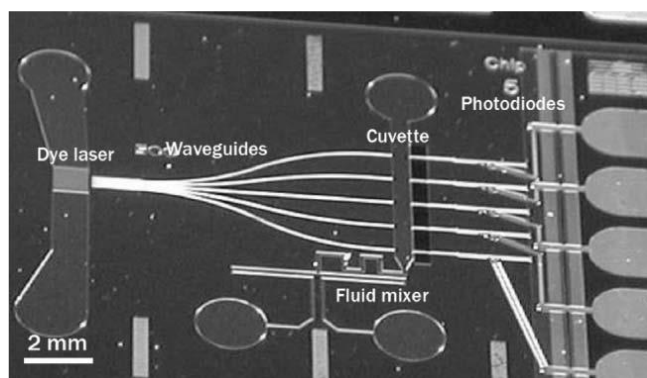


Figure 2.5. Photograph of a lab-on-a-chip device with integrated microfluidic dye laser, optical waveguides, microfluidic network and photodiodes. Reproduced by permission of the Royal Society of Chemistry from Balslev et al.⁸¹

2.3.4 Optical sensors for pH and oxygen in microfluidic devices

In recent years there has been an increasing amount of publications, which reported on successfully integrated optical sensors for oxygen and pH into microfluidics. As already stated in the introduction a few reviews have already been published on this subject – some of them focusing directly on optical sensors in microfluidics, others focusing on a different main subject, such as oxygen transfer characteristics of bioreactors or the use of microbioreactors in fermentation process development. In the following chapter, we summarize and critically discuss existing microfluidic oxygen and pH sensing set-ups and want to highlight particularly promising set-ups and specifically interesting applications.

2.3.4.1 Optical oxygen sensors in microfluidics

Single point measurements. The first approach of miniaturized sensor integration into a cuvette-based microbioreactor was reported in 2001 by Kostov et al.⁸², who attached a ruthenium-based sensor, $\text{Ru}(\text{diphenylphenanthroline})_3^{2+}$ immobilized in silicone rubber and covered by a layer of black silicone, to the cuvette wall. Sensor read-out was performed using lifetime detection in the frequency domain applying a blue LED and an avalanche photodiode module with suitable optical filters. The optical detection system, which included continuous monitoring of dissolved oxygen (DO), pH and optical density (OD), were used for a compact and low-cost system enabling high-throughput bioprocessing. Kostov et al. concluded, that the applied sensors and actuators allowed for an even further decrease of reactor volume.

The described development led to the first application of optical oxygen sensors in a microfluidic cell culture analog device by Sin et al.⁸³, which was designed to serve as an *in vitro* supplement to animal studies by culturing mammalian cells in interconnected chambers, which represented lung, liver and other compartments of human tissue (Figure 2.6 (A)). This device contained an oxygen sensing chamber, which was fabricated by machining a 150 μm deep recess into the bottom of the Plexiglas chip housing for integration of the oxygen sensing patch, consisting of $\text{Ru}(\text{diphenylphenanthroline})_3^{2+}$ immobilized onto resin particles, which were encapsulated in a PDMS matrix. The partially cured PDMS-particle mixture was filled into the recess and fully cured for several days at 60°C. Sin et al. used a read-out system similar to that of Kostov et al., applying

a blue LED, suitable optical filters and a photodiode module, connected to a lock-in amplifier for phase measurements. Despite this referencing technique a sensor drift was observed, which was traced back to drifts of the electronic equipment. However, the integrated oxygen sensor was successfully used to monitor the adequacy of oxygen supply into the system (Figure 2.6 (B)). They concluded that appropriate sensors enable online monitoring of microfluidic cell cultures and could also be used for investigating the physiological cell status in pharmacological testing. The results of this study revealed the feasibility of optical sensor integration and that optical oxygen sensors are a promising tool to monitor oxygen in microfluidic systems, while a task for future research would be to improve sensor performance in terms of read-out stability and sensor spot thickness (150 μm) and therefore response time (20 s).

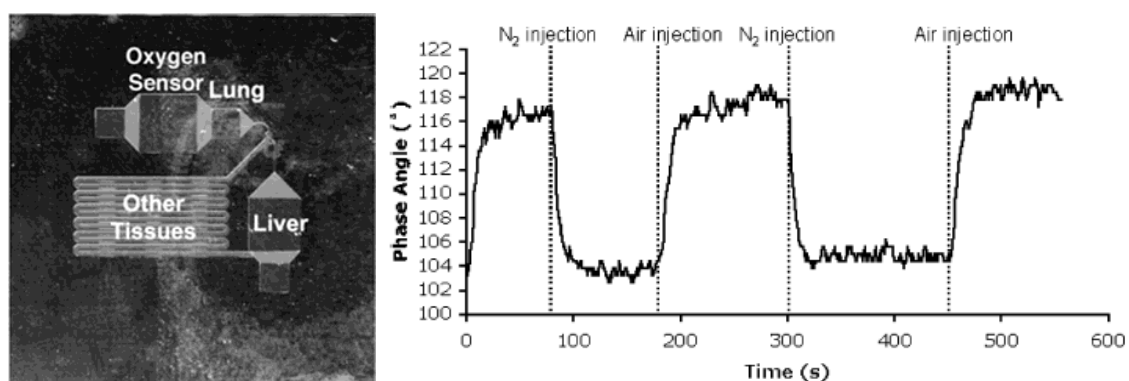


Figure 2.6. (A) Photograph of the fabricated microfluidic cell culture analog device and (B) Actual response of an integrated oxygen sensor, when input is alternate between gaseous nitrogen and air. Reproduced by permission of the American Chemical Society from Sin et al.⁸³

Several other publications reported on the successful integration of self-made oxygen sensor spots into microfluidics. Lee et al. developed an integrated array of microbioreactors providing bubble-free oxygenation with a closed loop control over oxygen and pH⁸⁴. The microbioreactor device consisted of four growth wells, each one being equipped with optical sensor spots for DO, pH and OD. The applied oxygen sensor spots were fabricated by deposition of a platinum-octaethyl-porphyrine (PtOEP)/polystyrene (PS) sensor cocktail in toluene onto a previously roughened glass slide. After evaporation of the solvent the sensor spots were integrated into the microbioreactor array PDMS base layer during molding. The sensor spots were excited by a LED at 380 nm and read-out was accomplished by photodiodes at 650 nm measuring the phase shift of the luminescence. Excitation and emission light were guided to and from the spots by optical fiber bundles equipped with color glass filters.

The same working group tried to enhance the performance of the previously described microbioreactor by introducing polymer waveguide backplanes for interfacing the optical sensor⁸⁵. The sensing chemistry was changed compared to the previously used oxygen sensor spots by exchanging PtOEP with the more photostable PtOEPK⁵⁸, which exhibits longwave-shifted excitation and emission maxima at 592 nm and 759 nm, respectively. The aim of directly integrating passive optical components into the chip design was to improve alignment tolerances with external optical elements and also to increase system design flexibility by replacing the optical fiber bundles used in the previous publication. The waveguides were designed to excite

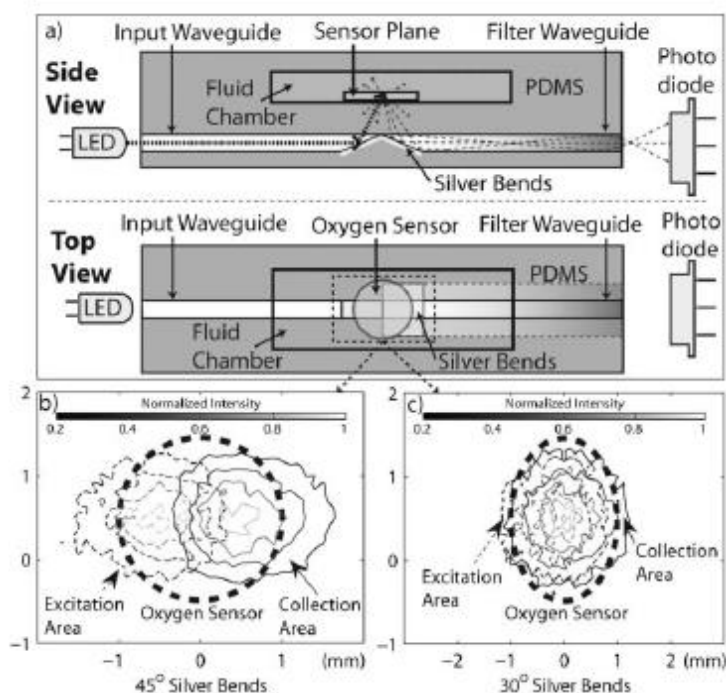


Figure 2.7. (a) A side and top view of the integrated oxygen sensor chip is shown. The waveguides are designed to excite and collect luminescence from the sensor located 1 mm above the silvered bends. (b,c) Ray tracing simulations of the intensity distribution for the input waveguide excitation and point source collection efficiency of the output waveguide at the sensing plane for 45° bends and 30° bends, respectively. Reproduced by permission of the Royal Society of Chemistry from Lee et al.⁸⁵

and collect luminescence from the oxygen sensor located 1 mm above the fabricated waveguides (Figure 2.7). Silver blends were used as vertical couplers to guide the excitation light to and the emission light from the sensing spot. The waveguides were fabricated by filling hollow channels in PDMS (cladding material) with a polyurethane core material containing an organic dye with an absorption maximum at 600 nm in the emission waveguide for replacement of optical emission filters. The phase shift measuring set-up consisted of 590 nm fiber-coupled LEDs interfacing the excitation waveguides and silicon photodiodes interfacing the emission waveguides. Lee et al. concluded that the on-chip integration of polymer waveguide backplanes led to a sensing set-up, which allows the application of off-chip optical components (LEDs and photodiodes) with reduced complexity and costs.

A last publication of the same working group should be mentioned in this context, which brought no advances in sensor development, but which points out the importance of oxygen sensors in microfluidics. Lee et al. developed a microfluidic device capable of controlling oxygen levels, pH, flow rate and temperature for dynamic continuous cell culture experiments⁸⁶. They described such experiments to possibly be important for characterizing biological behavior such as genetic switches, environmental shock responses, directed evolution, co-metabolism, and co-culture dynamics.

Another interesting publication by Mayr et al. reported on a monolithically integrated sensor array based on ring-shaped organic photodiodes into microfluidics⁸⁷. Several sensing chemistries for the simultaneous detection of various parameters such as oxygen, carbon dioxide, humidity

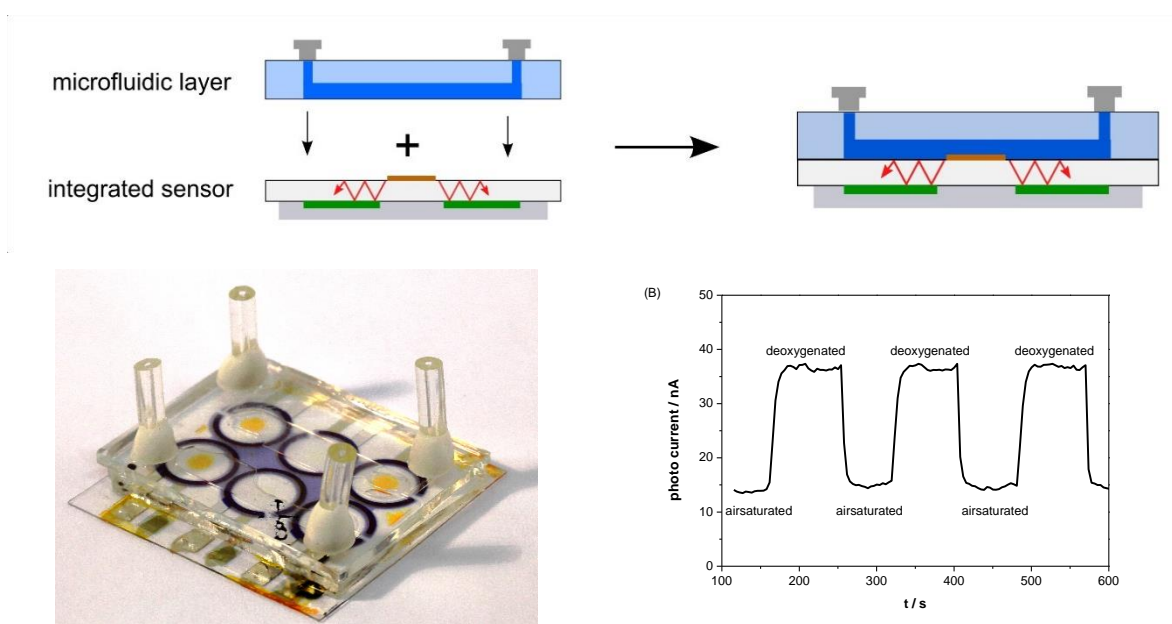


Figure 2.8. (A) Schematic of the preparation of the microfluidic device with integrated sensor spots and photodetectors ; (B) a microfluidic chip with integrated sensor spots for oxygen and organic photo-diodes and (C) Response of the sensor to air-saturated and deoxygenated solutions injected with a syringe pump. Reproduced by permission of the American Chemical Society from Mayr et al.⁸⁷

and pH in gaseous and/or liquid phase were investigated and optimized and different methods for referenced sensor read-out were evaluated. Finally they showed the suitability of the sensor platform to be integrated into a microfluidic chip taking the example of oxygen sensors (Figure 2.8).

The application of commercially available sensor spots is an alternative to developing and optimizing self-made sensor spots. This alternative has been applied by several working groups, who only have to care about how to attach the sensor spot to the walls of the microfluidic device and to care for the interface between light source, sensor spot and detector. Read-out is usually accomplished by phasemodulated lifetime fluorometry using LEDs, bifurcated fiberbundles, suitable optical filters and a lock-in amplifier. Due to the similarity of optical oxygen sensor set-ups, we only describe mentionable differences of these set-ups and applications of oxygen sensing. Zanzotto et al. integrated sensors for optical density (OD), DO and pH into a microbioreactor with a volume of 50 μl , which is used for highly reproducible high-throughput bioprocessing⁸⁸. The oxygen sensor, which was embedded in the bottom layer of the bioreactor, served to experimentally validate theoretical models, which describe the oxygen transfer characteristics of the microbioreactor and growth and oxygen consumption of bacteria during a fermentation process.

A 50 μl microbioreactor with integrated sensors for OD, DO and pH for fermentation monitoring was also used by Boccazzi et al.⁸⁹ to combine high-throughput growth physiology and global gene expression data analysis to enable rapid screening of metabolic and genomic data of *E. coli*. The same set-up was also applied by Zanzotto et al.⁹⁰, who combined oxygen monitoring with *E. coli* reporter strains, which exhibit bioluminescence upon specific environmental stresses (e.g. absence of oxygen). Zhang et al. further developed the microbioreactor by integrating a small

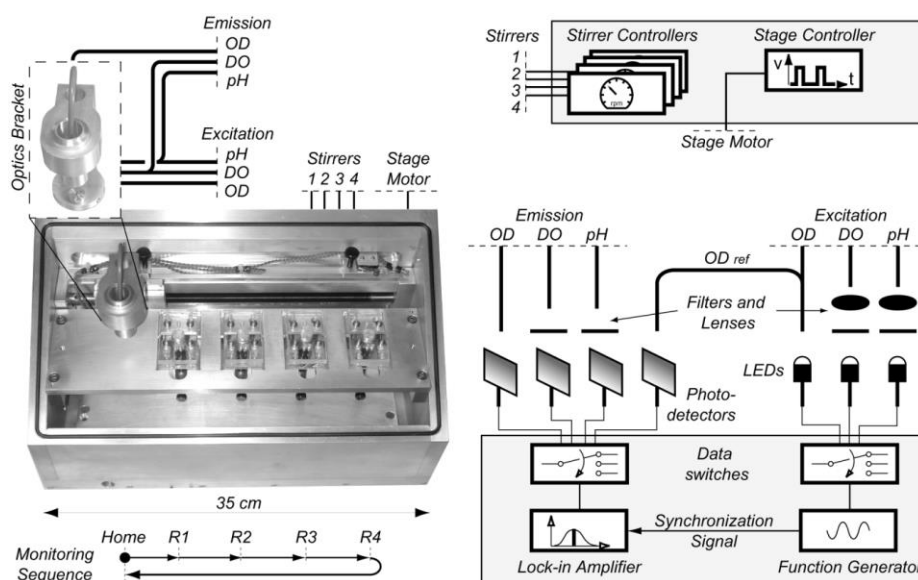


Figure 2.9. Photograph of the multiplexed microbioreactor system embedded in a schematic of the instrumentation. The multiplexed system is loaded with four stirred microbioreactors made out of PMMA and PDMS. The optics bracket (detailed photographic view) contains the optical fibers for monitoring of the fermentation parameters OD600, DO, and pH. Reproduced by permission of the American Chemical Society from Szita et al.⁹³

stirring bar into a 150 μ l reactor chamber to operate it under oxygenated and well-mixed conditions. A similar reactor was applied to serve as a microchemostat, a reactor, where microbial cell cultures reach a steady state, at which cell mass production, substrate and product concentration remain constant⁹¹ and for combination of high-throughput growth physiology and global gene expression data analysis of *S. cerevisiae*⁹².

Subsequent development by Szita et al. led to a multiplexed microbioreactor system (Figure 2.9) for parallel operation of multiple microbial fermentations⁹³. Apart from multiplexing, they also incorporated magnetic spin bars into the reactor chambers. An “optical bracket” holding the bifurcated optical fibers was used to scan over the microbioreactors in stop-and-go sequences with adjustable fiber z-position above and below the single reactors to increase signal intensity. The system was capable of simultaneous and reproducible operation of up to eight microbioreactors, with process parameters being monitored and recorded in each reactor. However, the number of parallelizable reactors was still limited by the scanning speed of the optical bracket. Thus subsequent advancement by Zhang et al. was achieved by integrating microlenses and optical connectors into the device⁹⁴. This approach enabled the use of plastic fibers instead of the previously used expensive, customer-made bifurcated optical fibers and the moving optical bracket could be avoided. It was reported, that a higher light-coupling efficiency was achieved by focusing by the microlenses compared to butt-end coupling techniques, even for slight misalignments of the optical fibers.

Schäpper et al. followed a similar approach, yet trying a new microreactor design for cultivation of *S. cerevisiae* with a relatively low complexity and cost, but high flexibility⁹⁵. In this case a LED and a silicon detector were used, both connected to a lock-in amplifier, getting by without optical fibers for optically interfacing the sensor spot.

The integration of a commercially available implantable oxygen microsensor into a 100 μl stirred microreactor was shown by van Leeuwen et al.⁹⁶. The sensor was mounted in the 1 cm thick bottom layer, 0.5 mm below the bottom surface of the reactor. The reactor was developed to serve as a pressure based system capable of the quantification of gas consumption or production in a nmol/min range. The oxygen consumption rate was measured by means of the pressure controlled oxygen supply system, while the optical oxygen sensor was used to confirm the carried out pressure measurements.

The use of commercially available sensor spots or optical fiber sensors represents a simple possibility to integrate optical oxygen sensors into microfluidic devices. However, as soon as the design changes to smaller dimension, e.g. narrow microfluidic channel networks, or when sensor integration should be combined with microfabrication techniques, the integration of whole sensor spots by hand may not be valuable any more. On this account, several publications reported on the direct integration of micro-patterned sensor layers into microfluidic structures.

Chang-Yen and Gale for example employed alternately charged polyion layers to selectively cover a SU-8 waveguide surface with the oxygen sensitive dye tris(2,2A-bipyridyl-dichloro-ruthenium)-hexahydrate ($\text{Ru}(\text{bpy})$)⁷⁹. They used an interesting method combining two manufacturing steps, namely waveguide fabrication and fiber-optic interfacing, into a single process with the fiber optic interface enabling simple waveguide interfacing by hand. The dye was excited by the 450 nm LED source, and the emitted fluorescence intensity at 615 nm was detected by an USB spectrometer. The evanescent interaction with the dye molecules along the waveguide length allowed highly sensitive luminescence detection compared to previous work using the same dye without that arrangement.

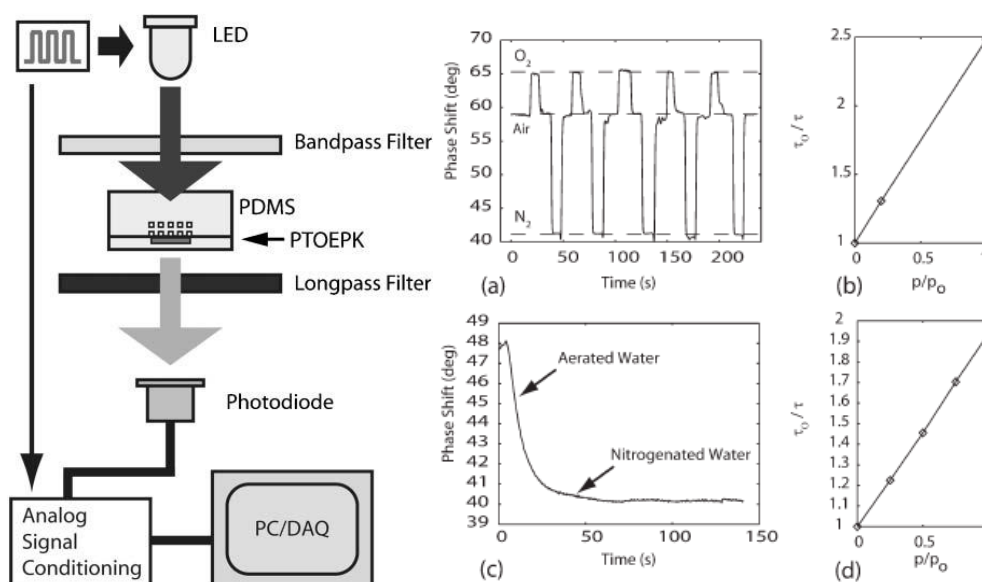


Figure 2.10. (A) Optical and electrical components and alignment in excitation/detection system. (B) (a) Dynamic sensor response (phase shift) for detection of gaseous oxygen. (b) Stern–Volmer calibration curve for detection of gaseous oxygen. (c) Dynamic sensor response (phase shift) for detection of dissolved oxygen. (d) Stern–Volmer calibration curve for detection of dissolved oxygen. Reproduced by permission of the American Chemical Society from Vollmer et al.⁹⁷

Vollmer et al. applied selectively etched glass surfaces and micropipetting for fabrication of patterned PtOEPK/PS spots⁹⁷. Luminescence lifetime detection was performed applying phase-shift measurements with a LED, a silicon photodiode and suitable optical filters (

Figure 2.10). The sensor was subsequently used to determine the convective mass-transfer characteristics of a multilayer PDMS microfluidic oxygenator, exhibiting excellent agreement between experiment and theoretical convection model.

Subsequent publications of the same group used the same patterning technique to integrate sensor patterns of PtOEPK in PS into a microfluidic oxygenator, which was used to investigate mammalian and bacterial cell response to different oxygen levels^{98,99}. Oxygen gradients were generated by a network of mixing gas channels with two inlets for N₂ and O₂, inducing different, but repeatable DO concentrations in an array of parallel microchannels containing aqueous media. The integrated oxygen sensors with a film thickness of 2 - 4 μm enabled real-time monitoring of the DO levels in culture media within the microchannels.

While the above mentioned publications all performed single point measurements, it may be useful in other cases to obtain spatially resolved information on analyte concentrations. Spatially resolved measurements are usually performed using CCD cameras, yielding 2D oxygen images. The thereby obtained information can be used for detecting oxygen gradients, but also as means for parallelized measurements.

Microfluidic Imaging. Sud et al. were the first to perform oxygen imaging inside a PDMS microreactor applying fluorescence lifetime imaging (FLIM) of the dissolved oxygen indicator ruthenium (tris(2,2'-dipyridyl) dichloride hexahydrate (RTDP))¹⁰⁰. The bioreactor contained C2C12 mouse myoblasts, which led to decreased oxygen levels at high cell densities. Mehta et al., from the same group, studied heterogeneous mammalian cell development along a microfluidic channel length correlated to oxygen gradients inside these channels¹⁰¹. They performed intensity as well as FLIM measurements using rapid lifetime determination (RLD) on an inverted fluorescence microscope of RTDP dissolved in buffer. These measurements, which agreed with a mathematical model, showed a decreased downstream oxygen concentration with increased cell density and decreased flow rate through the microfluidic channels. It is important to note, that the information obtained by oxygen imaging was the same as for performing single point measurements in upstream and downstream regions, such as performed by Vollmer et al.⁹⁷. Moreover, state-of-the-art of optical sensing usually involves luminescent indicators dissolved in a suitable matrix, which could on the one hand eliminate toxic interaction of indicator and cells and could on the other hand also have improved the performed oxygen measurements. Actually in a subsequent publication¹⁰² simple lifetime measurements were performed, using LEDs and silicon photodiodes connected to a fluorescence microscope instead of the former used expensive imaging set-up.

The first group, which applied oxygen imaging in microfluidic devices, and took full advantage of the imaging technology, were Nock et al., who integrated patterned sensor layers into microfluidic structures and performed intensity imaging of these patterned layers^{103,104}. These sensor patterns were fabricated by spin-coating a PtOEPK/PS sensor layer onto glass-substrates with subsequent reactive ion etching applying PDMS stamps for spatially selective shielding to yield sensor patterns exhibiting a minimum feature size of 25 μm (Figure 2.11). A simple digital camera was mounted to a fluorescent microscope and operated in "Nightshot" mode for

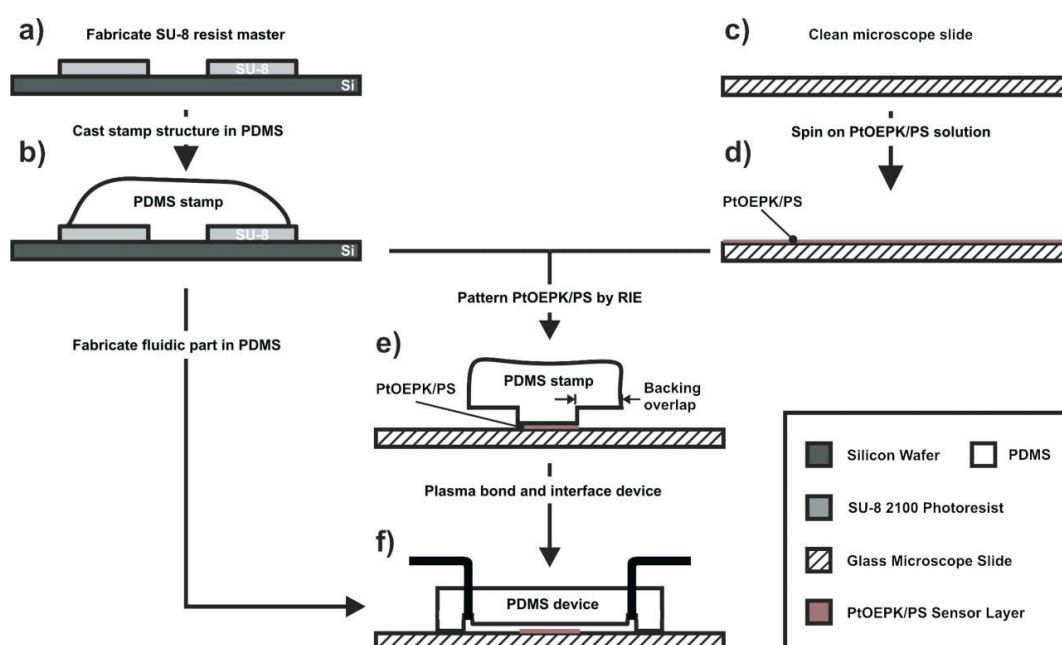


Figure 2.11. Schematic of the sensor fabrication process depicting stamp fabrication in PDMS (a,b), spin-coating of the sensor layer (c,d), pattern transfer into the sensor layer by RIE (e), and integration with a PDMS microfluidic device by plasma bonding (f). Reproduced by permission of the Royal Society of Chemistry from Nock et al.¹⁰³

intensity image acquisition. The described sensing set-up was used to detect laterally varying oxygen gradients inside microfluidic devices and also for subsequent publications^{105,105}, one of them describing a simplified fabrication process for even smaller ($3\ \mu\text{m}$) arbitrarily shaped sensor structures¹⁰⁵. These publications report on important progress regarding sensor layer integration into microfluidic devices. However, the implementation of the whole sensing set-up could be improved regarding the read-out system. Simple intensity imaging was used, which limits the applicability regarding image section misalignment without the need for recalibration.

Laterally varying oxygen levels inside microfluidic devices were also studied by Thomas et al.¹⁰⁶, who demonstrated a new method for on-chip oxygen control. Oxygen levels inside a microfluidic chamber were regulated by using pre-equilibrated aqueous solutions in gas-control channels. A $24\ \mu\text{m}$ thick PDMS-based sensor layer with alternate layers of Teflon AF and PDMS, containing the oxygen indicator PtTFPP, was spin-coated onto microscope slides and used for oxygen monitoring to achieve a better understanding of oxygen diffusion through microfluidic systems. Sensor read-out was accomplished using a fluorescence microscope, equipped with a color CCD camera for performing intensity imaging as described in a previous publication¹⁰⁷.

Intensity oxygen imaging in microfluidics was also performed by Gitlin et al., who successfully integrated inherently homogeneous sensing layers into a microfluidic structure. The specific improvement of their work involved localized generation of PtTFPP/PS sensor layers directly onto even complex, inert glass microstructures. Despite the homogeneity of their sensor layers, the remaining inhomogeneities caused signal read-out variations of 10% at the channel borders.

A possibility to overcome the drawbacks of pure intensity imaging was applied by Ungerböck et al.¹⁰⁸ and Ochs et al.¹⁰⁹. Both publications performed ratiometric oxygen imaging of planar sensor

foils, which were integrated into microfluidic devices. The former applied a self-made sensing film of PtTFPP and MFY in PS, employing the principle of light harvesting, to further increase signal intensity and a color CCD camera for relatively simple and low-cost yet reliable signal read-out. The sensing set-up was used to monitor spatially varying oxygen levels of microfluidic human cell cultures. The latter publication used commercially available sensor foils combined with a commercially available imaging device to verify a mathematical model capable of estimating the cellular respiratory activity in microfluidic devices.

Microfluidic oxygen imaging can also be used for performing parallelized measurements to reduce the need for multiple optical components. Such an application was for example used by Lin et al., who integrated oxygen and glucose sensors along the length of a microfluidic channel. Oxygen sensors consisted of $\text{Ru}(\text{dpp})_3\text{Cl}_2$ dissolved in PDMS, which was filled into microtrenches within the microfluidic channel wall. A matrix-assisted layer-by-layer (LbL) coating technique was used for encapsulation of the sensors. Signals were read-out on a fluorescence microscope by intensity imaging, at which the single pixel intensity values were only used for obtaining an average signal of each sensor. Oxygen and glucose sensors were used to study concentration gradients along a microfluidic channel, which was filled with a transgenic insulin-secreting cell line derived from mice.

Parallelized oxygen measurement were also performed by Molter et al.¹¹⁰ and Etzkorn et al.¹¹¹, who applied micro-patterned sensor rings to study single-cell oxygen consumption rates in microwell arrays. Molter et al. used commercially available microspheres, which were added to each microwell before drying of the bead dispersion, under which the rings in the microwells were formed, and a subsequent annealing step to generate adhesion of the microspheres by slightly melting them. Etzkorn et al. fabricated the sensor rings by dispersing a dendron-modified Pt(II) porphyrin indicator into the photopatternable resin SU8 and exposure to UV light. In both publications oxygen data were obtained by an imaging technique called optimized rapid lifetime determination (ORLD), applying an inverted microscope equipped with LEDs, suitable optical filters and a gateable high-speed camera.

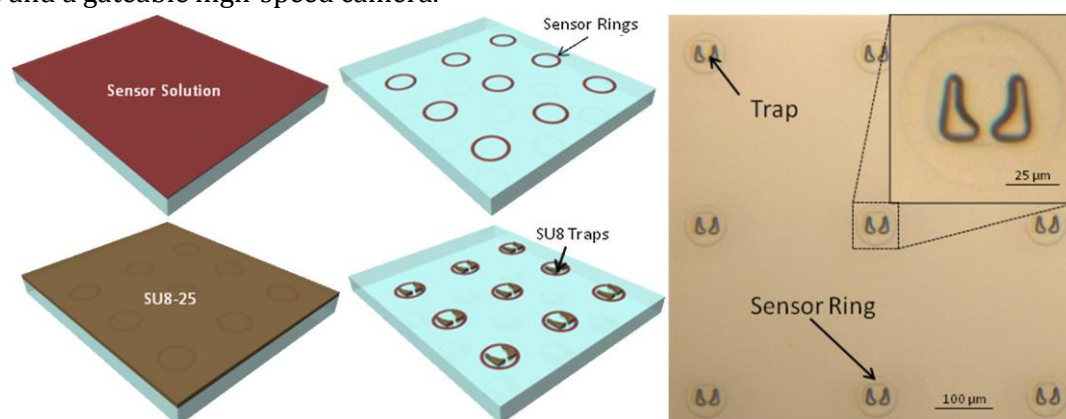


Figure 2.12 (A) Glass template fabrication. (A) Sensor solution spread across the entire wafer. (B) Oxygen sensor patterned in a 3×3 array of rings. (C) SU8-25 covered entire wafer, including sensor rings. (D) Patterned SU8 traps in the center of each sensor ring. (E) Microfabrication results showing an optical microscope image of a 3×3 array of single-cell self-assembly traps encircled by an oxygen sensor embedded in SU8 rings with an insert of a magnified image of a trap and sensor ring. Reproduced by permission of the IOP Science from Etzkorn et al.¹¹¹

Alternative Sensor Formats. Although the majority of integrated oxygen sensors entailed the use of sensor layers, also alternative formats of oxygen sensors have been used for performing oxygen measurements inside microfluidic channels. For example, Ungerböck et al. used nano sensor particles, stained with $\text{IrCs}_2(\text{acac})^{112}$ to monitor the oxidation reaction of b-D-glucose to hydrogen peroxide and d-D-gluconolactone by molecular oxygen in the presence of glucose oxidase inside microreactors with Y-shaped microchannels¹¹³. Oxygen imaging was performed on an epifluorescent microscope equipped with an LED, optical filters and a gateable camera applying RLD imaging. These experimental results were compared to mathematical models to assess the required model complexity for an accurate description of reagent transport and reaction inside the microchannels. Another and more complex application of sensor beads inside microfluidics was described by Ungerböck et al, where they evaluated multifunctional optical sensor particles (MOSePs)¹¹⁴ with incorporated magnetic and sensing functionalities regarding their applicability in microfluidic devices¹¹⁵. The magnetic properties of these particles served to separate the particles from the surrounding solution to form *in-situ* sensor spots within microfluidic channels, while read-out was accomplished outside the chip. These magnetic sensor spots exhibited advantageous features of sensor layers (high brightness, convenient usage) combined with the benefits of dispersed sensor particles (ease of integration). Different read-out methods were evaluated and critically discussed, including fiber optic as well as 2D read-out using RLD and RGB imaging.

To summarize, luminescent oxygen sensors have already been integrated into microfluidic devices in various formats. On the one hand the use of hand-made or commercially available sensor spots represents a straightforward approach as long as the size of the devices allow for sensor integration into microreactors. On the other hand suitable processes for direct integration and even complex patterning of sensor layers into microfluidics have been developed and also alternative sensor formats have been successfully applied. Also different read-out systems have been combined with microfluidic sensor read-out. The respective measurement method should be considered carefully. While fiber optic read-out is generally accomplished using lifetime methods via phase-shift measurements, oxygen imaging is usually performed by intensity imaging due to the availability and simplicity of the technical equipment compared to lifetime imaging. An interesting alternative between intensity imaging and the expensive lifetime imaging is the application of ratiometric CCD read-out employing the color channels of a RGB camera.

2.3.4.2 Optical pH sensors in microfluidics

While the integration of luminescent oxygen sensors has arrived microfluidics, only few groups have reported the integration of fluorescent pH sensors. This can probably be traced back to the fact, that the use of optical pH sensors is still limited and further development of high performance materials with increased photostability, sensitivity and selectivity remains a challenging scientific task to yield pH sensors with sufficient long-term stability. Moreover referenced pH sensor read-out is far more difficult to perform than referenced oxygen sensor read-out due to the lack of cheap equipment for short-lifetime measurements. However, some publications have already reported on the successful integration of luminescent pH sensors into microfluidics, which will be described in the following section.

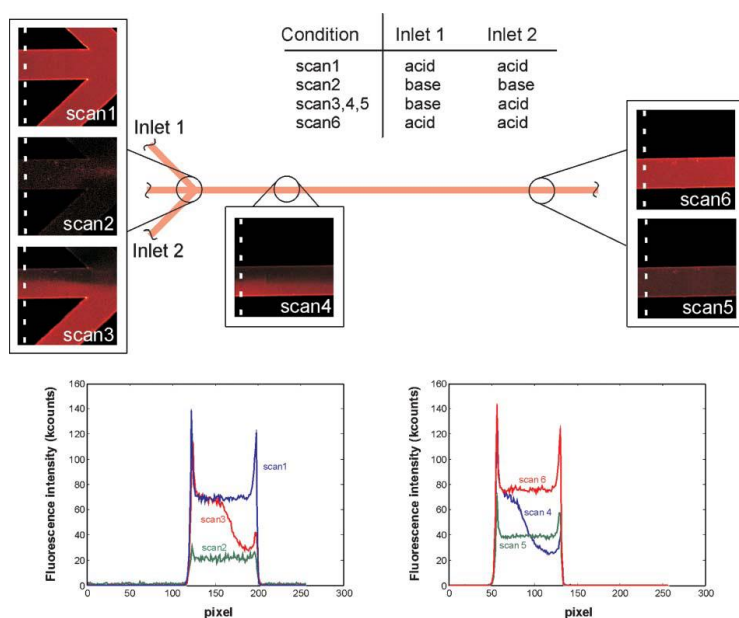


Figure 2.13. Confocal microscopy images of the RhB-functionalized microfluidics chip at different positions along the channel, using various conditions (see included table), and mean fluorescence intensity profiles for each scan averaged over 10 scan lines. Reproduced by permission of the Royal Society of Chemistry from Mela et al¹¹⁶

The first integration of an optical pH sensor into microfluidic channels was reported in 2005 by Mela et al.¹¹⁶, who covalently bound the fluorescent pH indicators Rhodamine B and an Oregon Green dye derivative to self-assembled monolayers. The integrated sensing layers served to measure the acidity of the surrounding solution in organic solvents (Rhodamin B) and the pH in aqueous solutions (Oregon Green derivative). Fluorescence intensity read-out was accomplished by a home-built laser scanning confocal microscopy set-up, consisting of an Ar:Kr laser as excitation source, suitable optical filters and two glass fibers, which served as pinholes and guided the emission light to two avalanche photo diodes. The presented sensing set-ups enabled pH imaging of diffusion controlled mixing of acidic and basic solutions with uniform intensity values throughout the whole device (Figure 2.13). Only the edges of the channel exhibited higher intensity values, which was explained by the presence of fluorescent molecules at the channel wall, but may also be due to light diffraction.

A simpler alternative to integrate pH sensors into microfluidics is – as already explained for oxygen sensors – the attachment of commercially available sensor spots into microfluidic devices. This approach has been applied by several working groups to monitor pH in microbioreactors^{84,86,88–95} with mostly cell culture monitoring applications already explained in chapter 2.3.4.1. The amount of literature published on the use of commercially available sensor spots reveals, that that this is a simple-to-realize method to perform single point pH monitoring as long as the microreactor is big enough for such a sensor spot. Thus, it is useful to invent more flexible solutions for pH sensor integration.

Sebra et al., for example used a previously published living radical photografting technique [Zitát Hutchison] to generate pH sensitive surfaces from poly(ethylene glycol) acrylate succinyl fluorescein in a fully polymeric microfluidic device¹¹⁷. The spatially controlled photografting

process yielded patterned pH sensor layers and the pH dependent fluorescence intensity was read out using a 2D fluorometer exhibiting a dynamic range from pH 6 to 11.

Lee et al. also reported on the fabrication of a patterned microarray sensor, which was used for pH and oxygen measurements using a compact fluorescent imaging system¹¹⁸. The detection system consisted of an ultra-bright blue diode source, coupling optics, interference filters and a monochrome CCD camera. A modified fluorescein based compound (BCECF-dextran) was used as pH indicator, incorporated into a PEG matrix, which was cured from a precursor solution by a photolithographic procedure. Fluorescence intensity between pH 6 and 8 was read out by an optical set-up, which was described as being compact and inexpensive – dispensing a complicated microscopic system. The oxygen and pH microarray was integrated into a microfluidic flow cell and coupled to a bioreactor for cell culture monitoring.

Another approach to integrate fluorescent pH sensing layers was presented by Jezierski et al., who used a similar process as Lee et al. to photopolymerize BCECF-dextran in a hydrogel precursor mixture⁴⁶. The sensor layers were integrated into a microfluidic free-flow electrophoresis chip to enable localized pH monitoring during isoelectric focusing. Microscopic read-out was performed using an inverted fluorescence microscope equipped with suitable optical filters and a CCD camera. A calibration curve for a BCECF-dextran in the PEG-DA sensor layer in an FFE microchip showed an apparent pK_a of 6.23.

A method for high throughput optical sensor patterning should be mentioned in this context, which was developed by Zhu et al. and is based on polymerization of monomeric oxygen and pH optical probes with 2-hydroxyethyl methacrylate (HEMA) and acrylamide (AM) on fused silica wafers and a subsequent reactive ion etching step with an etch mask layer to partially remove the sensor layers¹¹⁹. The patterning process yielded *inter alia* micron-sized pH sensor spots, which exhibited pH sensitivity between pH 2 and 10, yet with a decreased sensitivity compared to unpatterned sensor films. Although the integration of the patterned sensor films has not been shown in this publication, a further development of the method using more gentle patterning processes could lead to promising miniaturized optical sensor systems to be applied in microfluidic systems.

As already discussed for oxygen, also alternative formats of pH sensors have been used for performing pH measurements inside microfluidic channels. Klauke et al. used micron sized beads, modified with fluorescent dyes, as noninvasive sensors to probe the local changes in pH¹²⁰. For this purpose amine-modified polystyrene beads were functionalized with a SNARF pH indicator and trapped at defined positions within a microchannel, using optical tweezers. A mercury arc lamp, optical filters and an intensified CCD camera were mounted to a fluorescence microscope with optical tweezer facility to perform intensity imaging, while ratiometric read-out was accomplished by exchange of the CCD camera with two PMTs. The optical tweezer manipulation of the beads allowed spatially resolved pH measurements of the pH gradient, generated electrolytically around a given microelectrode.

Funfak et al. used polymer microparticles with a covalently grafted pH indicator for cell cultivation monitoring in droplet-based microfluidics¹²¹. A flow-through fluorometer equipped with a LED, optical filters and a photon counting module was developed to perform fluorescence intensity read-out of the HPTS/p-HEMA beads of 3 μm size suspended in the cell culture medium.

The set-up was used to monitor metabolic activity of the organisms by measuring the time-dependent pH development.

Sensor particles have also been used by Aigner et al. for ratiometric pH imaging in microfluidic channels⁷². They applied finely dispersed nano sensor particles, which were obtained by a simple precipitation method of RL 100 with a pH indicator and a reference dye incorporated into the matrix. The optical system consisted of LEDs as excitation source, optical filters and a RGB camera for ratiometric read-out, where the pH dependent signal was detected by the red channel and the green channel served as reference channel. Microscopic as well as macroscopic pH imaging was performed in microfluidic devices.

As already mentioned at the beginning of the chapter, the application of fluorescent pH sensors is still in its very early stages, although such sensors have already been successfully integrated and applied in microfluidic devices. Ongoing development of pH sensor materials might help to improve the long-term stability of pH sensors, which is especially important for harsh patterning methods or critical measurements concerning photobleaching, for example microscopic observations of integrated pH sensors.

2.4 Conclusion

The integration of analytical tools into miniaturized devices is a challenging scientific task due to several reasons: the need of the sensing device to be scalable to smaller dimensions, the importance of overall costs of microfluidic devices and a reduced analysis volume and consequentially a small number of analyte molecules. Optical on-chip sensors, and especially luminescent sensors, provide a range of interesting features to handle the above-mentioned challenges: they are easy to miniaturize, highly sensitive, do generally not consume the analyte under investigation and are relatively low-cost devices. However, microfluidic sensing with luminescent sensors remains a specifically challenging task and sensing devices have to be adapted to these new challenges.

On the one hand a smart combination of sophisticated sensing chemistry, sensor format and the optical measurement system is required. On the other hand ongoing development regarding highly photostable luminescent indicators with increased brightness, sterilizable and stable sensing matrices, new application procedures of sensor cocktails and simple and cheap measurement systems are going to advance useful applications of luminescent sensors in microfluidics.

To date various publications have already reported on the successful integration and application of oxygen and pH sensors in miniaturized devices. The promising results reveal that microfluidic systems with integrated luminescent sensors provide a powerful tool particularly for biological applications such as monitoring of cell cultures or (bio-)catalytic process optimization. The information obtained through all these sensor applications might help to gain a deeper understanding of cellular behavior and general microfluidic processes.

2.5 References

1. Cammann, K., Guibault, E. A., Hall, H., Kellner, R. & Wolfbeis, O. S. The Cambridge Definition of Chemical Sensors.
2. Terry, S. C., Jerman, J. H. & Angell, J. B. A gas chromatographic air analyzer fabricated on a silicon wafer. *Electron Devices IEEE Trans. On* **26**, 1880–1886 (1979).
3. Manz, A., Graber, N. & Widmer, H. M. Miniaturized total chemical analysis systems: A novel concept for chemical sensing. *Sens. Actuators B Chem.* **1**, 244–248 (1990).
4. Grist, S. M., Chrostowski, L. & Cheung, K. C. Optical Oxygen Sensors for Applications in Microfluidic Cell Culture. *Sensors* **10**, 9286–9316 (2010).
5. Kirk, T. V. & Szita, N. Oxygen transfer characteristics of miniaturized bioreactor systems. *Biotechnol. Bioeng.* **110**, 1005–1019 (2013).
6. Schäpper, D., Alam, M., Szita, N., Eliasson Lantz, A. & Gernaey, K. Application of microbioreactors in fermentation process development: a review. *Anal. Bioanal. Chem.* **395**, 679–695 (2009).
7. Ramamoorthy, R., Dutta, P. K. & Akbar, S. A. Oxygen sensors: Materials, methods, designs and applications. *J. Mater. Sci.* **38**, 4271–4282 (2003).
8. Mills, A. Optical Oxygen Sensors. *Platin. Met. Rev.* **41**, 115–127 (1997).
9. Demas, J. N., DeGraff, B. A. & Coleman, P. B. Peer Reviewed: Oxygen Sensors Based on Luminescence Quenching. *Anal. Chem.* **71**, 793A–800A (1999).
10. Lakowicz, J. R. *Principles of Fluorescence Spectroscopy*. (Springer, Berlin, 2006).
11. Valeur, B. *Molecular Fluorescence: Principles and Applications*. (Wiley-VCH, 2001).
12. Amao, Y. Probes and Polymers for Optical Sensing of Oxygen. *Microchim. Acta* **143**, 1–12 (2003).
13. Wolfbeis, O. S. Materials for fluorescence-based optical chemical sensors. *J. Mater. Chem.* **15**, 2657–2669 (2005).
14. Demchenko, A. P. Nanoparticles and nanocomposites for fluorescence sensing and imaging. *Methods Appl. Fluoresc.* **1**, 022001 (2013).
15. Quaranta, M., Borisov, S. M. & Klimant, I. Indicators for optical oxygen sensors. *Bioanal. Rev.* **4**, 115–157 (2012).
16. Ast, C., Schmäzlin, E., Löhmansröben, H.-G. & van Dongen, J. T. Optical Oxygen Micro- and Nanosensors for Plant Applications. *Sensors* **12**, 7015–7032 (2012).
17. Wolfbeis, O. S. Sensor Paints. *Adv. Mater.* **20**, 3759–3763 (2008).
18. Papkovsky, D. B. & Dmitriev, R. I. Biological detection by optical oxygen sensing. *Chem. Soc. Rev.* (2013). doi:10.1039/C3CS60131E
19. Demas, J. N., DeGraff, B. A. & Xu, W. Modeling of Luminescence Quenching-Based Sensors: Comparison of Multisite and Nonlinear Gas Solubility Models. *Anal. Chem.* **67**, 1377–1380 (1995).
20. Liebsch, G., Klimant, I., Frank, B., Holst, G. & Wolfbeis, O. S. Luminescence Lifetime Imaging of Oxygen, pH, and Carbon Dioxide Distribution Using Optical Sensors. *Appl. Spectrosc.* **54**, 548–559 (2000).
21. Borisov, S. M. *et al.* Photophysical properties of the new phosphorescent platinum(II) and palladium(II) complexes of benzoporphyrins and chlorins. *J. Photochem. Photobiol. Chem.* **206**, 87–92 (2009).
22. Zhang, G., Palmer, G. M., Dewhurst, M. W. & Fraser, C. L. A dual-emissive-materials design concept enables tumour hypoxia imaging. *Nat. Mater.* **8**, 747–751 (2009).
23. Zhang, G. *et al.* Multi-Emissive Difluoroboron Dibenzoylmethane Polylactide Exhibiting Intense Fluorescence and Oxygen-Sensitive Room-Temperature Phosphorescence. *J. Am. Chem. Soc.* **129**, 8942–8943 (2007).
24. Yoshihara, T., Yamaguchi, Y., Hosaka, M., Takeuchi, T. & Tobita, S. Ratiometric Molecular Sensor for Monitoring Oxygen Levels in Living Cells. *Angew. Chem. Int. Ed.* **51**, 4148–4151 (2012).
25. Wu, W. *et al.* Tuning the emission properties of cyclometalated platinum(II) complexes by intramolecular electron-sink/arylethynylated ligands and its application for enhanced luminescent oxygen sensing. *J. Mater. Chem.* **20**, 9775–9786 (2010).
26. Borisov, S. M., Lehner, P. & Klimant, I. Novel optical trace oxygen sensors based on platinum(II) and palladium(II) complexes with 5,10,15,20-meso-tetrakis-(2,3,4,5,6-pentafluorophenyl)-porphyrin covalently immobilized on silica-gel particles. *Anal. Chim. Acta* **690**, 108–115 (2011).
27. Koren, K., Borisov, S. M. & Klimant, I. Stable optical oxygen sensing materials based on click-coupling of fluorinated platinum(II) and palladium(II) porphyrins—A convenient way to eliminate dye migration and leaching. *Sens. Actuators B Chem.* **169**, 173–181 (2012).
28. Stich, M. I. J., Fischer, L. H. & Wolfbeis, O. S. Multiple fluorescent chemical sensing and imaging. *Chem. Soc. Rev.* **39**, 3102–3114 (2010).
29. Janata, J. Do optical sensors really measure pH? *Anal. Chem.* **59**, 1351–1356 (1987).

30. Weidgans, B. M., Krause, C., Klimant, I. & Wolfbeis, O. S. Fluorescent pH sensors with negligible sensitivity to ionic strength. *Analyst* **129**, 645–650 (2004).
31. Schröder, C. R., Weidgans, B. M. & Klimant, I. pH Fluorosensors for use in marine systems. *Analyst* **130**, 907–916 (2005).
32. Vasylevska, A. S., Karasyov, A. A., Borisov, S. M. & Krause, C. Novel coumarin-based fluorescent pH indicators, probes and membranes covering a broad pH range. *Anal. Bioanal. Chem.* **387**, 2131–2141 (2007).
33. Borisov, S. M., Gatterer, K. & Klimant, I. Red light-excitable dual lifetime referenced optical pH sensors with intrinsic temperature compensation. *Analyst* **135**, 1711–1717 (2010).
34. Lin, J. & Liu, D. An optical pH sensor with a linear response over a broad range. *Anal. Chim. Acta* **408**, 49–55 (2000).
35. Dong, S., Luo, M., Peng, G. & Cheng, W. Broad range pH sensor based on sol-gel entrapped indicators on fibre optic. *Sens. Actuators B Chem.* **129**, 94–98 (2008).
36. Chauhan, V. M., Burnett, G. R. & Aylott, J. W. Dual-fluorophore ratiometric pH nanosensor with tuneable pKa and extended dynamic range. *Analyst* **136**, 1799–1801 (2011).
37. Huber, C., Klimant, I., Krause, C. & Wolfbeis, O. S. Dual Lifetime Referencing as Applied to a Chloride Optical Sensor. *Anal. Chem.* **73**, 2097–2103 (2001).
38. Wencel, D., Abel, T. & McDonagh, C. Optical Chemical pH Sensors. *Anal. Chem.* (2013). doi:10.1021/ac4035168
39. Aigner, D., Borisov, S. M., Petritsch, P. & Klimant, I. Novel near infra-red fluorescent pH sensors based on 1-aminoperylene bisimides covalently grafted onto poly(acryloylmorpholine). *Chem. Commun.* **49**, 2139–2141 (2013).
40. Jokic, T. *et al.* Highly Photostable Near-Infrared Fluorescent pH Indicators and Sensors Based on BF₂-Chelated Tetraarylazadipyrromethene Dyes. *Anal. Chem.* **84**, 6723–6730 (2012).
41. Ma, Q.-J. *et al.* A fluorescent sensor for low pH values based on a covalently immobilized rhodamine-naphthalimide conjugate. *Sens. Actuators B Chem.* **166–167**, 68–74 (2012).
42. Kriltz, A., Löser, C., Mohr, G. J. & Trupp, S. Covalent immobilization of a fluorescent pH-sensitive naphthalimide dye in sol-gel films. *J. Sol-Gel Sci. Technol.* **63**, 23–29 (2012).
43. Ge, X., Kostov, Y., Tolosa, L. & Rao, G. Study on low-cost calibration-free pH sensing with disposable optical sensors. *Anal. Chim. Acta* **734**, 79–87 (2012).
44. Tian, Y. *et al.* A fluorescent colorimetric pH sensor and the influences of matrices on sensing performances. *Sens. Actuators B Chem.* **188**, 1–10 (2013).
45. Ferrari, L., Rovati, L., Fabbri, P. & Pilati, F. Disposable Fluorescence Optical pH Sensor for Near Neutral Solutions. *Sensors* **13**, 484–499 (2012).
46. Jezierski, S., Belder, D. & Nagl, S. Microfluidic free-flow electrophoresis chips with an integrated fluorescent sensor layer for real time pH imaging in isoelectric focusing. *Chem. Commun.* **49**, 904–906 (2013).
47. Wencel, D., Barczak, M., Borowski, P. & McDonagh, C. The development and characterisation of novel hybrid sol-gel-derived films for optical pH sensing. *J. Mater. Chem.* **22**, 11720–11729 (2012).
48. Han, J. & Burgess, K. Fluorescent Indicators for Intracellular pH. *Chem. Rev.* **110**, 2709–2728 (2010).
49. Niedermair, F. *et al.* Tunable Phosphorescent NIR Oxygen Indicators Based on Mixed Benzo- and Naphthoporphyrin Complexes. *Inorg. Chem.* **49**, 9333–9342 (2010).
50. Borisov, S. M., Zenkl, G. & Klimant, I. Phosphorescent Platinum(II) and Palladium(II) Complexes with Azatetrabenzoporphyrins—New Red Laser Diode-Compatible Indicators for Optical Oxygen Sensing. *ACS Appl. Mater. Interfaces* **2**, 366–374 (2010).
51. Borisov, S. M. & Klimant, I. Ultrabright Oxygen Optodes Based on Cyclometalated Iridium(III) Coumarin Complexes. *Anal. Chem.* **79**, 7501–7509 (2007).
52. Förster, T. Zwischenmolekulare Energiewanderung und Fluoreszenz. *Ann. Phys.* **437**, 55–75 (1948).
53. Mayr, T. *et al.* Light Harvesting as a Simple and Versatile Way to Enhance Brightness of Luminescent Sensors. *Anal. Chem.* **81**, 6541–6545 (2009).
54. Zajko, S. Comprehensive Study of the Effects of Different Sterilization Procedures on the Optical Sensors. (2012).
55. Valencia-Gonzalez, M. J. & Diaz-Garcia, M. E. Enzymic Reactor/Room-Temperature Phosphorescence Sensor System for Cholesterol Determination in Organic Solvents. *Anal. Chem.* **66**, 2726–2731 (1994).
56. Costa-Fernández, J. M., Diaz-García, M. E. & Sanz-Medel, A. Sol-gel immobilized room-temperature phosphorescent metal-chelate as luminescent oxygen sensing material. *Anal. Chim. Acta* **360**, 17–26 (1998).

57. Díaz-García, M. E., Noval Gutiérrez, B. & Badía, R. Tailoring room-temperature phosphorescent ormosil particles for oxygen recognition in organic solvents. *Sens. Actuators B Chem.* **110**, 66–72 (2005).
58. Papkovsky, D. B., Ponomarev, G. V. & Wolfbeis, O. S. Longwave luminescent porphyrin probes. *Spectrochim. Acta. A. Mol. Biomol. Spectrosc.* **52**, 1629–1638 (1996).
59. Lee, S.-K. & Okura, I. Photostable Optical Oxygen Sensing Material: PlatinumTetrakis(pentafluorophenyl)porphyrin Immobilized in Polystyrene. *Anal. Commun.* **34**, 185–188 (1997).
60. Rademacher, A., Märkle, S. & Langhals, H. Lösliche Perylen-Fluoreszenzfarbstoffe mit hoher Photostabilität. *Chem. Ber.* **115**, 2927–2934 (1982).
61. Lin, J. Recent development and applications of optical and fiber-optic pH sensors. *TrAC Trends Anal. Chem.* **19**, 541–552 (2000).
62. Wolfbeis, O. S. Fiber-Optic Chemical Sensors and Biosensors. *Anal. Chem.* **72**, 81–90 (2000).
63. Wolfbeis, O. S. Fiber-Optic Chemical Sensors and Biosensors. *Anal. Chem.* **74**, 2663–2678 (2002).
64. Wolfbeis, O. S. Fiber-Optic Chemical Sensors and Biosensors. *Anal. Chem.* **76**, 3269–3284 (2004).
65. Wolfbeis, O. S. Fiber-Optic Chemical Sensors and Biosensors. *Anal. Chem.* **78**, 3859–3874 (2006).
66. Wolfbeis, O. S. Fiber-Optic Chemical Sensors and Biosensors. *Anal. Chem.* **80**, 4269–4283 (2008).
67. Wang, X.-D. & Wolfbeis, O. S. Fiber-Optic Chemical Sensors and Biosensors (2008–2012). *Anal. Chem.* **85**, 487–508 (2013).
68. Holst, G., Glud, R. N., Köhl, M. & Klimant, I. A microoptode array for fine-scale measurement of oxygen distribution. *Sens. Actuators B Chem.* **38**, 122–129 (1997).
69. Mistlberger, G. & Klimant, I. Luminescent magnetic particles: structures, syntheses, multimodal imaging, and analytical applications. *Bioanal. Rev.* **2**, 61–101 (2010).
70. Borisov, S. M., Mayr, T., Mistlberger, G. & Klimant, I. in *Adv. Fluoresc. Report. Chem. Biol. II* (Demchenko, A. P.) 193–228 (Springer Berlin Heidelberg, 2010). at http://link.springer.com/chapter/10.1007/978-3-642-04701-5_6
71. McShane, M. in *Optochemical Nanosensors 2012* **1458**, 99–118 (Taylor & Francis, 2012).
72. Aigner, D. *et al.* Fluorescent materials for pH sensing and imaging based on novel 1,4-diketopyrrolo-[3,4-c]pyrrole dyes. *J. Mater. Chem. C* **1**, 5685–5693 (2013).
73. Vinogradov, S. A., Lo, L.-W. & Wilson, D. F. Dendritic Polyglutamic Porphyrins: Probing Porphyrin Protection by Oxygen-Dependent Quenching of Phosphorescence. *Chem. – Eur. J.* **5**, 1338–1347 (1999).
74. Kuswandi, B., Nuriman, Huskens, J. & Verboom, W. Optical sensing systems for microfluidic devices: A review. *Anal. Chim. Acta* **601**, 141–155 (2007).
75. Roulet, J.-C. *et al.* Performance of an Integrated Microoptical System for Fluorescence Detection in Microfluidic Systems. *Anal. Chem.* **74**, 3400–3407 (2002).
76. Seo, J. & Lee, L. P. Disposable integrated microfluidics with self-aligned planar microlenses. *Sens. Actuators B Chem.* **99**, 615–622 (2004).
77. Camou, S., Fujita, H. & Fujii, T. PDMS 2D optical lens integrated with microfluidic channels: principle and characterization. *Lab. Chip* **3**, 40–45 (2003).
78. Hofmann, O. *et al.* Monolithically integrated dye-doped PDMS long-pass filters for disposable on-chip fluorescence detection. *Lab. Chip* **6**, 981–987 (2006).
79. Chang-Yen, D. A. & Gale, B. K. An integrated optical oxygen sensor fabricated using rapid-prototyping techniques. *Lab. Chip* **3**, 297–301 (2003).
80. Mazurczyk, R., Vieillard, J., Bouchard, A., Hannes, B. & Krawczyk, S. A novel concept of the integrated fluorescence detection system and its application in a lab-on-a-chip microdevice. *Sens. Actuators B Chem.* **118**, 11–19 (2006).
81. Balslev, S. *et al.* Lab-on-a-chip with integrated optical transducers. *Lab. Chip* **6**, 213–217 (2006).
82. Kostov, Y., Harms, P., Randers-Eichhorn, L. & Rao, G. Low-cost microbio reactor for high-throughput bioprocessing. *Biotechnol. Bioeng.* **72**, 346–352 (2001).
83. Sin, A. *et al.* The Design and Fabrication of Three-Chamber Microscale Cell Culture Analog Devices with Integrated Dissolved Oxygen Sensors. *Biotechnol. Prog.* **20**, 338–345 (2004).
84. Lee, H. L. T., Boccuzzi, P., Ram, R. J. & Sinskey, A. J. Microbio reactor arrays with integrated mixers and fluid injectors for high-throughput experimentation with pH and dissolved oxygen control. *Lab. Chip* **6**, 1229–1235 (2006).
85. Lee, K. S., Lee, H. L. T. & Ram, R. J. Polymer waveguide backplanes for optical sensor interfaces in microfluidics. *Lab. Chip* **7**, 1539–1545 (2007).

86. Lee, K. S., Boccazzi, P., Sinskey, A. J. & Ram, R. J. Microfluidic chemostat and turbidostat with flow rate, oxygen, and temperature control for dynamic continuous culture. *Lab. Chip* **11**, 1730–1739 (2011).
87. Mayr, T. *et al.* Opto-chemical sensors based on integrated ring-shaped organic photodiodes: Progress and applications. in *Proc. SPIE - Int. Soc. Opt. Eng.* **8479**, (2012).
88. Zanzotto, A. *et al.* Membrane-aerated microbioreactor for high-throughput bioprocessing. *Biotechnol. Bioeng.* **87**, 243–254 (2004).
89. Boccazzi, P. *et al.* Gene expression analysis of *Escherichia coli* grown in miniaturized bioreactor platforms for high-throughput analysis of growth and genomic data. *Appl. Microbiol. Biotechnol.* **68**, 518–532 (2005).
90. Zanzotto, A. *et al.* In situ measurement of bioluminescence and fluorescence in an integrated microbioreactor. *Biotechnol. Bioeng.* **93**, 40–47 (2006).
91. Zhang, Z. *et al.* Microchemostat—microbial continuous culture in a polymer-based, instrumented microbioreactor. *Lab. Chip* **6**, 906–913 (2006).
92. Boccazzi, P. *et al.* Differential Gene Expression Profiles and Real-Time Measurements of Growth Parameters in *Saccharomyces cerevisiae* Grown in Microliter-Scale Bioreactors Equipped with Internal Stirring. *Biotechnol. Prog.* **22**, 710–717 (2006).
93. Szita, N. *et al.* Development of a multiplexed microbioreactor system for high-throughput bioprocessing. *Lab. Chip* **5**, 819–826 (2005).
94. Zhang, Z. *et al.* Microbioreactors for Bioprocess Development. *J. Assoc. Lab. Autom.* **12**, 143–151 (2007).
95. Schäpper, D., Stocks, S. M., Szita, N., Lantz, A. E. & Gernaey, K. V. Development of a single-use microbioreactor for cultivation of microorganisms. *Chem. Eng. J.* **160**, 891–898 (2010).
96. Van Leeuwen, M. *et al.* A system for accurate on-line measurement of total gas consumption or production rates in microbioreactors. *Chem. Eng. Sci.* **64**, 455–458 (2009).
97. Vollmer, A. P., Probst, R. F., Gilbert, R. & Thorsen, T. Development of an integrated microfluidic platform for dynamic oxygen sensing and delivery in a flowing medium. *Lab. Chip* **5**, 1059–1066 (2005).
98. Lam, R. H. W., Kim, M.-C. & Thorsen, T. A Microfluidic Oxygenator for Biological Cell Culture. in *Solid-State Sens. Actuators Microsyst. Conf. 2007 TRANSDUCERS 2007 Int.* 2489–2492 (2007). doi:10.1109/SENSOR.2007.4300676
99. Lam, R. H. W., Kim, M.-C. & Thorsen, T. Culturing Aerobic and Anaerobic Bacteria and Mammalian Cells with a Microfluidic Differential Oxygenator. *Anal. Chem.* **81**, 5918–5924 (2009).
100. Sud, D. *et al.* Optical imaging in microfluidic bioreactors enables oxygen monitoring for continuous cell culture. *J. Biomed. Opt.* **11**, 050504–050504–3 (2006).
101. Mehta, G. *et al.* Quantitative measurement and control of oxygen levels in microfluidic poly(dimethylsiloxane) bioreactors during cell culture. *Biomed. Microdevices* **9**, 123–134 (2007).
102. Mehta, G. *et al.* Hard Top Soft Bottom Microfluidic Devices for Cell Culture and Chemical Analysis. *Anal. Chem.* **81**, 3714–3722 (2009).
103. Nock, V., Blaikie, R. J. & David, T. Patterning, integration and characterisation of polymer optical oxygen sensors for microfluidic devices. *Lab. Chip* **8**, 1300–1307 (2008).
104. Nock, V., Blaikie, R. J. & David, T. Micro-patterning of polymer-based optical oxygen sensors for lab-on-chip applications. in *BioMEMS Nanotechnol. III* **6799**, 67990Y–10 (SPIE, 2007).
105. Nock, V., Alkai, M. & Blaikie, R. J. Photolithographic patterning of polymer-encapsulated optical oxygen sensors. *Microelectron. Eng.* **87**, 814–816 (2010).
106. Thomas, P. C., Raghavan, S. R. & Forry, S. P. Regulating Oxygen Levels in a Microfluidic Device. *Anal. Chem.* **83**, 8821–8824 (2011).
107. Thomas, P. C. *et al.* A Noninvasive Thin Film Sensor for Monitoring Oxygen Tension during in Vitro Cell Culture. *Anal. Chem.* **81**, 9239–9246 (2009).
108. Ungerböck, B., Charwat, V., Ertl, P. & Mayr, T. Microfluidic oxygen imaging using integrated optical sensor layers and a color camera. *Lab. Chip* (2013). doi:10.1039/C3LC41315B
109. Ochs, C. J., Kasuya, J., Pavesi, A. & Kamm, R. D. Oxygen levels in thermoplastic microfluidic devices during cell culture. *Lab. Chip* (2013). doi:10.1039/C3LC51160J
110. Molter, T. W. *et al.* A microwell array device capable of measuring single-cell oxygen consumption rates. *Sens. Actuators B Chem.* **135**, 678–686 (2009).
111. Etzkorn, J. R. *et al.* Using micro-patterned sensors and cell self-assembly for measuring the oxygen consumption rate of single cells. *J. Micromechanics Microengineering* **20**, 095017 (2010).
112. Borisov, S. M., Mayr, T. & Klimant, I. Poly(styrene-block-vinylpyrrolidone) beads as a versatile material for simple fabrication of optical nanosensors. *Anal. Chem.* **80**, 573–582 (2008).

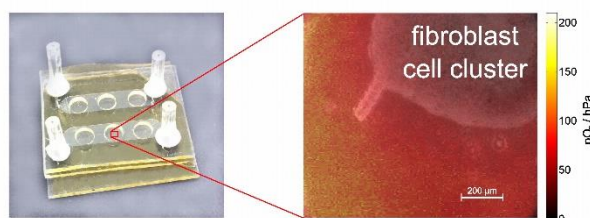
113. Ungerböck, B., Pohar, A., Mayr, T. & Plazl, I. Online oxygen measurements inside a microreactor with modeling of transport phenomena. *Microfluid. Nanofluidics* (2012). doi:10.1007/s10404-012-1074-8
114. Mistlberger, G. *et al.* Multifunctional Magnetic Optical Sensor Particles with Tunable Sizes for Monitoring Metabolic Parameters and as a Basis for Nanotherapeutics. *Adv. Funct. Mater.* **20**, 1842–1851 (2010).
115. Ungerböck, B., Fellingner, S., Sulzer, P., Abel, T. & Mayr, T. Magnetic Optical Sensor Particles: A Flexible Analytical Tool for Microfluidics. *Analyst* (2014). doi:10.1039/C4AN00169A
116. Mela, P. *et al.* Monolayer-functionalized microfluidics devices for optical sensing of acidity. *Lab. Chip* **5**, 163–170 (2005).
117. Sebra, R. P., Kasko, A. M., Anseth, K. S. & Bowman, C. N. Synthesis and photografting of highly pH-responsive polymer chains. *Sens. Actuators B Chem.* **119**, 127–134 (2006).
118. Lee, S., Ibey, B. L., Coté, G. L. & Pishko, M. V. Measurement of pH and dissolved oxygen within cell culture media using a hydrogel microarray sensor. *Sens. Actuators B Chem.* **128**, 388–398 (2008).
119. Zhu, H. *et al.* Micro-patterning and characterization of PHEMA-co-PAM-based optical chemical sensors for lab-on-a-chip applications. *Sens. Actuators B Chem.* **173**, 817–823 (2012).
120. Klauke, N., Monaghan, P., Sinclair, G., Padgett, M. & Cooper, J. Characterisation of spatial and temporal changes in pH gradients in microfluidic channels using optically trapped fluorescent sensors. *Lab. Chip* **6**, 788 (2006).
121. Funfak, A., Cao, J., Wolfbeis, O., Martin, K. & Köhler, J. Monitoring cell cultivation in microfluidic segments by optical pH sensing with a micro flow-through fluorometer using dye-doped polymer particles. *Microchim. Acta* **164**, 279–286 (2009).

3 Microfluidic Oxygen Imaging using Integrated Optical Sensor Layers and a Color Camera

Birgit Ungerböck,^a Verena Charwat,^b Peter Ertl^b and Torsten Mayr^{*a}

Published by the Royal Society of Chemistry in Lab on A Chip, January 2013, Volume 13, pp 1593-1601
DOI: 10.1039/C3LC41315B

Abstract In this work we present a high resolution oxygen imaging approach, which can be used to study 2D oxygen distribution inside microfluidic environments. The presented setup comprises a fabrication process of microfluidic chips with integrated luminescent sensing films combined with referenced oxygen imaging applying a color CCD-camera. Enhancement of the sensor performance was achieved by applying the principle of light harvesting. This principle enabled for ratiometric imaging employing the red and the green channel of a color CCD-camera. The oxygen sensitive emission of platinum(II)-5,10,15,20-tetrakis-(2,3,4,5,6-pentafluorophenyl)-porphyrin (PtTFPP) was detected by the red channel, while the emission of a reference dye was detected by the green channel. This measurement setup allowed for accurate real-time 2D oxygen imaging with superior quality compared to intensity imaging. The sensor films were subsequently used to measure respiratory activity of human cell cultures (Hela carcinoma cells and normal human dermal fibroblasts) in a microfluidic system. The sensor setup is well suited for different applications from spatially and temporally resolving oxygen concentration inside microfluidic channels to parallelization of oxygen measurements and paves the way to novel cell based assays, e.g. in tissue engineering, tumor biology and hypoxia reperfusion phenomena.



3.1 Introduction

Oxygen concentration is an immensely important factor in cellular studies¹. Important physiological processes and cell culture applications where O₂ supply plays a prime role include tumor biology and vascularization, hypoxia-reperfusion phenomena, tissue engineering and stem cell differentiation^{2,3}. Oxygen is fundamental in cellular activities, because it is required for aerobic metabolism of carbon compounds, a very basic cellular function. A lack of oxygen therefore has a huge impact on cell behavior including alterations of the cellular metabolism⁴, physiological pathways⁵, tissue remodeling and growth of new capillaries, increased tumor resistance to therapy⁶ as well as necrotic cell death. An excess of oxygen on the other hand can damage cells because of oxidative stress.

Because of the high importance of oxygen for cell cultivation, different approaches to define and control oxygen concentrations in bulk applications are commercially available, such as incubators with O₂ control (in addition to CO₂), cell culture flasks with integrated O₂ sensors or motorized sensor tips⁷. These devices provide single spot measurements and do not consider oxygen gradients within a culture vessel. However, many biological questions require information about oxygen distribution rather than a single averaged value: Tumor biology is one well known example for the importance of spatially varying oxygen concentration. Many studies have been conducted to investigate the effects of oxygen gradients in solid tumors⁸⁻¹⁰. Oxygen supply becomes a limiting factor and eventually leads to necrosis of cells in the inner tumor mass while at the same time promoting tumor vascularization for tissue thicknesses greater than 100 μm ¹¹. To investigate such phenomena assay formats that aim at the creation of a biological niche have been developed. For example co-culture models, 3D tissue analogues or micro-patterned and microfluidic devices have been established to provide physiologically relevant environments. In these assay formats culture conditions are varying over the entire area or volume. Thus it is of prime importance to obtain spatially resolved information on concentration gradients and distribution of parameters of interest such as temperature, cytokines or dissolved gases including oxygen. Literature examples of suitable devices to study oxygen gradients include oxygen sensitive scaffolds¹², microparticles¹³ or sensor foils¹⁴ for tissue cross sections.

In the case of microfluidic devices a variety of integrated optical oxygen sensors for cell analysis have been developed¹⁵. Some of the publications report on point measurements^{16,17}, while others present 2D read out systems¹⁸⁻²³. While the former measurements assume average cultivation conditions over the entire sensor area, 2D measurements allow a more detailed look at oxygen levels and gradients inside microbioreactors²⁰⁻²³. All methods apply oxygen sensitive luminescent dyes based on the well-known collisional luminescence quenching sensing scheme. These dyes exhibit high luminescence intensity (I) and luminescence lifetime (τ) under oxygen-free conditions, while the presence of oxygen molecules leads to a decrease of I and τ . This decrease is a result of energy transfer from the energetically excited dye to oxygen, which is transferred into its excited singlet state, while the excited oxygen indicator returns to its ground state by radiation-free deactivation.

Luminescence-based imaging applications have been realized in different formats using for example dissolved oxygen sensitive luminescent dyes^{19,24}, sensor beads^{13,20} or sensor layers^{14,18,21-23,25}. Also different read out methods have been developed and applied in microfluidic imaging setups. Intensity imaging^{18,21-23,26} for example can be easily implemented in laboratories working

with fluorescence microscopy equipment. This method, however, has the disadvantage of unwanted signal variations due to defects in the optical system such as inhomogeneities of the light source, inhomogeneous sensitivity of the detection system or inhomogeneous distribution of the fluorescent probes in the sensing matrix. These issues limit the accuracy of the obtained oxygen images. Fluorescence life-time imaging (FLIM)^{20,27} on the other hand gives highly accurate results, but requires expensive and specialized instrumentation that is not commonly available in cell biological laboratories and consequently limits its application.

In the presented work we therefore implemented two-wavelength ratiometric imaging²⁸⁻³⁰ to combine low-cost and easily available imaging equipment with high resolution imaging. A color CCD camera measures the intensity at two different wavelengths of the sensor's emitted light by using the different color channels of the camera – one channel providing the oxygen sensitive intensity image, the other one providing a so called reference image. Through calculation of the ratio between these images (red image/green image) the obtained ratiometric image is independent of the previously listed inhomogeneities.

The sensor setup was used to combine ratiometric 2D oxygen imaging and microfluidic cell culturing. The microfluidic system with integrated sensor layers is simple to fabricate. The technology can be used in laboratories working with microfluidic cell cultures to better control and optimize cultivation conditions. This opens the way for novel microfluidic cell based assays in many fields of tissue engineering, tumor biology and hypoxia reperfusion phenomena.

3.2 Methods

3.2.1 Materials

Platinum(II)-5,10,15,20-tetrakis-(2,3,4,5,6-pentafluorophenyl)-porphyrin (= PtTFPP) was purchased from Frontier Scientific (www.frontiersci.com); polystyrene (= PS; M = 250 000) was obtained from Fischer Scientific (www.fishersci.com); 3 (5 chlorobenzooxazol-2-yl)-7-(diethylamino)-coumarin (CO) "Macrolex fluorescent yellow" (= MFY) was bought from Simon and Werner GmbH (www.simon-und-werner.de); All the solvents and α -D-glucose monohydrate were obtained from Roth (www.carl-roth.de); glucose oxidase from *Aspergillus niger* (211 U/mg) was purchased from Sigma Aldrich (www.sigmaaldrich.com). Polydimethylsiloxan soft polymer Sylgard 184 (= PDMS) was purchased from Dow Corning Germany (www.dowcorning.com); SU-8 2050 negative photoresist was purchased from MicroChem Corp. (www.microchem.com).

3.2.2 Preparation of sensor films

1, 2, or 4 mg PtTFPP, 4 mg MFY, and 200 mg of PS were dissolved in 4.00 g of chloroform to obtain the sensor "cocktails" for optimization experiments of the sensor films. 200 μ L of these cocktails were knife-coated onto dust-free microscope slides (www.carl-roth.de) by using a bar film applicator (1 mil, www.byk.com) and the solvent was allowed to evaporate under ambient air to result in a \sim 2.5 μ m sensor film. Sensor cocktails for optimized sensor films in microfluidic chips contained 4 mg MFY, 2 mg PtTFPP and 200 mg of PS dissolved in 4.00 g of chloroform.

3.2.3 Spectral measurements

Emission spectra were acquired on a Hitachi F-7000 fluorescence spectrometer (www.inula.at) equipped with a red-sensitive photomultiplier tube (PMT) R 928 from Hamamazu (www.hamamatsu.com). The emission spectra were corrected for the sensitivity of the PMT.

3.2.4 Integration of sensor films into microfluidic chips

The microfluidic channels were fabricated from PDMS. First, an SU-8 mold featuring the negatives of two 3 mm wide and 50 μm high channels was prepared on a silicon wafer by standard lithography processes. Then liquid PDMS (mixed 1:10 with curing agent) was poured on the structures to cast a 1.5 mm thick PDMS sheet featuring the microchannels. After thermal curing at 60°C for 4 h, a section of solidified PDMS layer, 2.0 \times 2.5 cm^2 , was cut and peeled from the mold. Three holes (3 mm diameter) were punched into each of the channels to form cell cultivation chambers with low shear force. A 1 mm thick glass cover with holes drilled for fluidic connection was permanently bonded on top of the microfluidic layer using oxygen plasma surface activation (femto plasma cleaner, diener electronic: 40% power, 0.5 min, 45°C, 0.8 mbar). Then the fluidic layer was assembled with the sensor layer: 2.5 \times 2.5 cm^2 glass substrates with sensor films were spin-coated (5 min at 2500 rpm) with a thin (10 μm) PDMS film in order to protect the sensor layer (prevention of scratches or delamination) and to promote adhesion of the fluidic layer. The fluidic layer was placed on the sensor layer and then the PDMS film was cured and served as glue. Finally, a piece of tygon tubing (length 1 cm, inner tubing diameter 0.51 mm, SC0029, Ismatec) was glued to the glass cover to create the fluidic interface. Figure 3.1 shows a schematic cross section and a photograph of the microfluidic chip with integrated oxygen sensor layer.

In order to promote cell attachment the channels were activated by 1 min plasma exposure and then coated with 1 $\mu\text{g}/\text{mL}$ fibronectin (F4759, Sigma-Aldrich) right before use. For operation the chip was mounted on a 37°C heated microscope stage and connected to a syringe pump (KD Scientific) to rinse the system with fresh (air saturated) medium.

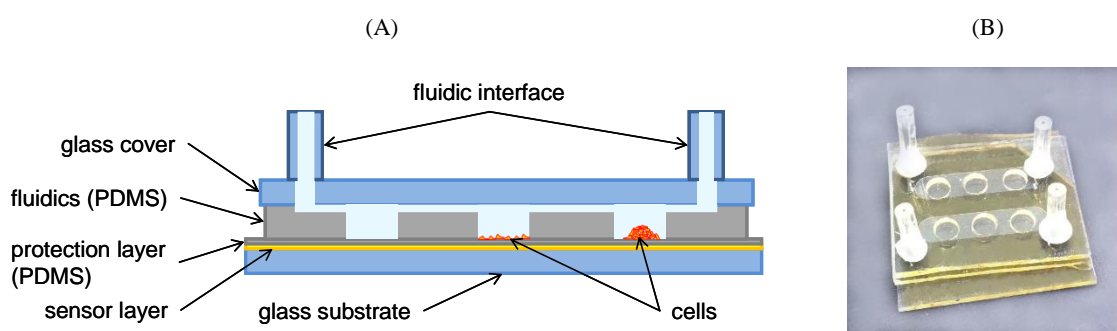


Figure 3.1. Microfluidic oxygen sensor chip; A) Schematic cross section of the chip assembly showing components of the sensor and fluidic layer (not to scale). The 3 cultivation wells illustrate a cell-free control chamber, a cell monolayer on fibronectin coated PDMS and a cell aggregate on uncoated PDMS. B) Photo of the actual cell-chip device with 2 individually addressable microfluidic channels and three O_2 -sensitive cell cultivation chambers on each side.

3.2.5 Sensor characterization

Full calibration of the sensor films was performed inside the microfluidic chip by flushing it with gaseous air-nitrogen mixtures. The ratio R of red and green channel was determined for deaerated (R_0) and fully air-saturated (R_{air}) conditions in water at 37°C. Full calibration of each chip was then

obtained by adapting the gaseous calibration data to R_0/R_{air} obtained from their determination in water. Deaerated water was obtained by deoxygenation reaction of glucose (10 mg/mL) with oxygen in the presence of glucose oxidase (0.05 mg/mL).

3.2.6 Cell culture

Two different cell types (a cancer cell line and a normal (non-immortalized) cell strain) that are widely used for cell-based assay were selected to demonstrate the performance of the newly developed oxygen sensitive cell culture device. HeLa carcinoma cells were cultivated in RPMI-1640 medium (R 00883, Sigma-Aldrich) supplemented with 10% FCS and 4 mM L-glutamine (M11-004, PAA) and normal human dermal fibroblasts (NHDF, PromoCell C-12300) were cultivated in DMEM high glucose medium with stable glutamine (PAA, E15-883) supplemented with 10% fetal calf serum (FCS) from PAA (A15-101). For cell loading of the sensor chip, cells were first enzymatically removed from the culture flask using 0.25% trypsin EDTA (fisher scientific) and suspended in fresh medium. The cell suspension was then injected into the chip through the fluidic interface using 1 mL syringes or pipette tips. Cells gravimetrically separated from the slowly flowing medium and accumulated in the cultivation chambers. Fresh cell suspension was added until desired cell coverage of the chambers was achieved. Then the medium flow was stopped and depending on the experiment cells were allowed to either form a monolayer (on fibronectin coated PDMS) or aggregate to cell clusters (on untreated PDMS). Monolayers consisted of about 50 000 (NHDF) to 150 000 (HeLa) cells/cm² or ca. 3 500 (NHDF) to 10 000 (HeLa) cells/well. Cell clusters consisted of similar total cell numbers, but cells aggregated to 5 to 8 layers resulting in about 100 μm thickness (75 to 150 μm). During experimentation medium flow of 10 $\mu\text{L}/\text{min}$ was applied to provide the cells with oxygenated medium and flow was stopped to monitor respiratory cell activity.

3.2.7 Imaging setup and data evaluation

Microscopic oxygen imaging was performed using a Hund Wilovert AFL 40 Phako inverse microscope equipped with a hot stage to regulate the temperature of the microfluidic chips. A HBO 100 (100-watt high-pressure mercury plasma arc-discharge lamp) was used as excitation source. All these components, a Zeiss objective A-Plan 10x/0.25 Ph1 and the FITC filter set consisting of an excitation filter (450-490 nm), a dichroic mirror (510 nm) and a long-pass emission filter (520 nm) were purchased from Werner Jülich (www.juelich-bonn.com).

For image acquisition an Olympus XC10 color camera was connected to the microscope via a c-mount 0.5x adapter. The camera uses the Sony ICX 285 AQ image sensor with relative sensitivities of the color channels shown in Figure 3.2. This image sensor is commonly used in different camera types (as Leica, Olympus, Allied Vision Technologies, etc.). Image acquisition was performed with the software Olympus Cell[^]D (www.olympus-europa.com).

Macroscopic oxygen imaging was performed using a 458 nm high-power 10 W LED array (www.led-tech.de) as excitation source. The filter set consisting of the excitation filter BG12 (350-470 nm) and the long-pass emission filter OG515 (515 nm) was purchased from Schott (www.schott.com). An AVT Marlin F-201C color camera equipped with a Xenoplan 1.4/23 objective lense (<http://www.schneiderkreuznach.com>) was used for image acquisition. The camera also uses the Sony ICX 285 AQ image sensor. Image acquisition was performed with the software AVT SmartView (<http://www.alliedvisiontec.com>).

Matlab R2008a (www.mathworks.com) was used for image processing. The color channels of the obtained images were separated and the ratiometric image R was obtained by dividing the red by the green channel. pO_2 images were calculated using the adapted calibration data. Fitting was performed using OriginLab 8.6 (www.originlab.com).

3.3 Results and discussion

3.3.1 Chip assembly

The microfluidic oxygen sensor chips consist of a glass substrate, a sensor layer with a protection film, the fluidic part made from PDMS and a glass cover as can be seen in Figure 3.1. One important aspect of our chip design was protection of the oxygen sensor to increase mechanical stability. While the dry sensor layer shows good adhesion to the glass substrate, it can peel off more easily in a liquid environment. If tiny scratches or other small defects are present in the sensor layer, liquid films can form under the polystyrene and lift it from the glass substrate. In order to protect the sensor layer, we spin coated it with a thin (10 μm) PDMS layer. Due to the high gas permeability of PDMS oxygen diffusion from the cell chambers to the sensor took only ~ 10 s, which is fast enough for most biological applications. Additionally, the thin PDMS coating served as glue for the fluidic layer. This is a convenient way of assembly for PDMS(microfluidics) and polystyrene (sensor layer), which are otherwise difficult to bond permanently. In order to limit oxygen diffusion into the system the whole fluidic device was covered with a glass slide (see Figure 3.1). The glass cover (and glass substrate) restricted oxygen ingress through the thick channel side walls (ca. 5 mm). Sensor devices fabricated in the described manner showed long usability without loss of performance.

It is important to note that our oxygen sensor layer is integrated in the bottom of the cell cultivation device sensing the oxygen concentration almost directly underneath the cell layer. This is a big advantage compared to other sensing methods where oxygen sensitive probes are placed in the medium surrounding the cells. In the presented device distance of the sensing layer to the cells is well defined and reproducible. Furthermore the minimal distance and location underneath the cells ensures that we measure oxygen concentrations, the cells are really surrounded by instead of less relevant information on oxygen in the bulk medium.

3.3.2 Sensor assembly

3.3.2.1 Choice of dye system, imaging setup and polymer matrix

The purpose of the current study was to provide a luminescent sensor for microfluidics, which combines high resolution oxygen imaging with a low-cost and easily available setup for detection, namely a color CCD camera used in fluorescence microscopy applications.

Demands for the sensor chemistry were:

- a) oxygen sensitive emission in one color channel and a reference emission in another channel of the camera
- b) excitation at one wavelength
- c) avoidance of UV light, because UV light can lead to background luminescence from media or cell material. It is also known for having a negative impact on cell growth and viability.

To solve the need for matching two different color channels by using one excitation wavelength and to overcome the use of UV light, the principle of FRET³¹ was chosen and applied as a so-called light harvesting system³². MFY with its excitation and emission maxima at $\lambda_{\max, EX} = 450$ nm and $\lambda_{\max, EM} = 490$ nm, the antenna dye of the system, collects blue light and transfers a part of its energy to the Q-bands of the oxygen sensitive indicator dye PtTFPP with its emission maximum at $\lambda_{\max} = 650$ nm.

The use of the light harvesting system allows the usage of the two-wavelength referencing method and sensor signals can be read out by a color CCD camera. Figure 3.2 (A) shows the working principle of the presented sensor setup. The oxygen sensitive emission of PtTFPP is detected by the red channel of the Sony ICX 285 AQ CCD-chip (frequently used in color CCD cameras for fluorescence microscopy), while the reference emission of MFY matches the green reference channel. Temporal and/or spatial inhomogeneities of the light source, inhomogeneous sensitivity of the detection system or concentration gradients of the luminescent probes influence the emission of both dyes equally, while changes in oxygen concentration alter only PtTFPP emission. Therefore, the ratio of the two channels depends only on the pO_2 , while it is robust against common drawbacks of intensity imaging such as inhomogeneities in the sensor layer. Further advantages of the light harvesting system are increased signal intensity, decreased risk of background luminescence and an extended Stokes Shift, which leads to a better separability of excitation and emission light.

To form sensor layers both dyes were dissolved in PS, a sensor polymer matrix, which provides good oxygen permeability, bio-compatibility and low auto fluorescence. PS sensor cocktails were applied onto microscope slides by blade coating. This method led to sensor layers with sufficient homogeneity to perform ratiometric imaging. In general, spin coating is also possible and results in homogenous layers. However, we preferred blade coating, because less sensor material is wasted during the coating process compared to spin coating.

Figure 3.2 (B) shows a response curve of an integrated sensor film inside a microfluidic chip, which was flushed alternately with air-saturated and deaerated water, recorded with ratiometric imaging. The oxygen sensitive signal is detected in the red channel, while the intensity of the green channel remains stable. From these intensities the referenced ratiometric image R was calculated, which was then transformed into the pO_2 image. The curves show data averaged over a region of interest of the channel area.

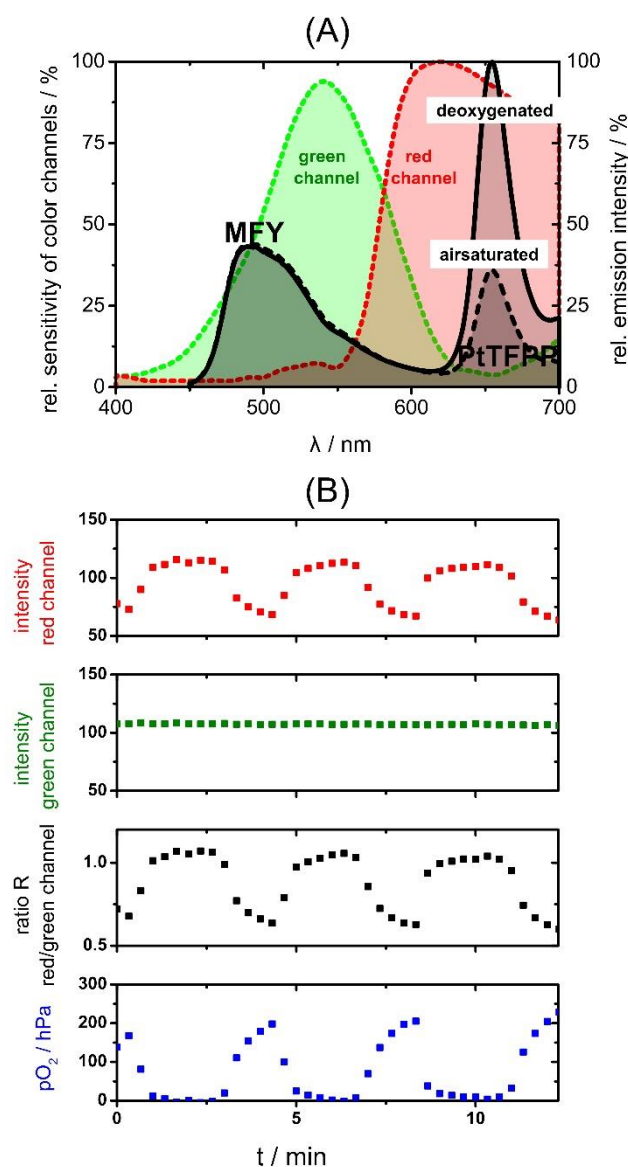


Figure 3.2. (A) Emission spectra of the two-wavelength ratiometric oxygen sensor under air saturated and deoxygenated conditions and relative sensitivities of the color channels of the color camera; the red channel detects the oxygen sensitive emission of PtTFPP while the green emission of MFY acts as green reference channel. (B) Response curve of a microfluidic chip with integrated sensor film read out by a CCD color camera; from the intensities of red and green images the referenced ratiometric images were calculated, which were then transformed into pO_2 images. The curves show data averaged over a region of interest (0.045 mm^2) of the channel area.

3.3.2.2 Optimization of sensor films for color camera

One important parameter describing the sensor performance is the ratio R , calculated as the division of red and green channel. Best sensor performances can be achieved with R around 1 with R_{air} (air saturated conditions) below 1 and R_0 (oxygen depleted conditions) above 1). This is due to the fact that the noise of the ratiometric image can only be reduced by increasing the intensity of both channels used for detection, because the signal-to-noise ratio of the channel with lower intensity determines the quality of the ratiometric image. However, intensities cannot be

increased infinitely. The upper limit of intensity increase is determined by the channel with higher intensity, when it reaches saturation.

R can easily be changed by changing the concentration of one of the used dyes of the light harvesting system. Our studies showed that the dye ratio also affects the parameter R_0/R_{air} , which determines the sensitivity of oxygen sensors (see chapter sensor calibration). This is due to spectral overlapping of the color channels. When the signal intensity of the green channel is too high, the reference signal is also detected in the red channel, which contributes to the oxygen sensitive red channel as background signal. This lowers R_0/R_{air} and thus the sensitivity of the sensor calibration.

Optimization concerning the ratio R and R_0/R_{air} was performed by changing the concentration of the oxygen indicator PtTFPP. A change of the concentration of the antenna dye MFY was not studied as the principle of light harvesting is to use the antenna dye in excess³¹. Table 1 compares the results of the optimization. The sensor films with 2% (w/w) MFY and 1% (w/w) PtTFPP showed the best performance with a ratio between 0.62 (H_2O_{air}) and 1.56 (H_2O_{deox}). The ratio R_0/R_{air} of this combination is 2.50. Higher concentration of PtTFPP led to a higher value for R_0/R_{air} (see Table 1), which would be worth pursuing in terms of the sensor's sensitivity, but was unsuitable in terms of the ratio R ($R_{\text{air}} = 1.16$, $R_0 = 4.41$). Moreover, these sensor films showed inhomogeneous ratiometric images, which can be traced back to the fact, that high dye concentration leads to inhomogeneously dissolved dyes in the sensor matrix.

Table 1 Optimization of the sensor films for imaging applications by variation of the concentration of the oxygen sensitive dye PtTFPP. The films contained 2% (w/w) MFY in PS

PtTFPP [% (w/w)]	R_{air}	R_0	R_0/R_{air}
0.5	0.42 ± 0.04	0.77 ± 0.01	1.84 ± 0.20
1	0.62 ± 0.01	1.56 ± 0.05	2.50 ± 0.08
2	1.16 ± 0.05	4.41 ± 0.08	3.80 ± 0.19

3.3.3 Characterization of sensor films

3.3.3.1 Ratiometric Imaging as high quality alternative to intensity imaging

As mentioned before the luminescence intensity within one image can be inhomogeneous due to varying film thickness of sensor films, heterogeneous light fields and /or contamination of the used optics. These inhomogeneities can be referenced out by the use of fluorescence lifetime imaging (FLIM), which requires complex and expensive equipment. Another possibility of referencing is ratiometric imaging, which is also capable of referencing the mentioned inhomogeneities while less complex and less expensive equipment can be used.

Figure 3.3 compares an intensity image with a ratiometric image obtained by division of the red by the green channel. Looking at the intensity response shown in Figure 3.3 (A) it is obvious, that the pure intensity image cannot be calibrated by using only one calibration function, but requires the use of multiple calibration functions (one per pixel). While this is possible for one position of the microfluidic chip, the use of multiple calibration functions is very cumbersome and inefficient, when the chip is moved to another position. In case of referenced ratiometric imaging (Figure 3.3 (B)) a single calibration function is sufficient to adequately describe the whole sensing area of one chip. Thereby the ratiometric imaging approach enables considerably

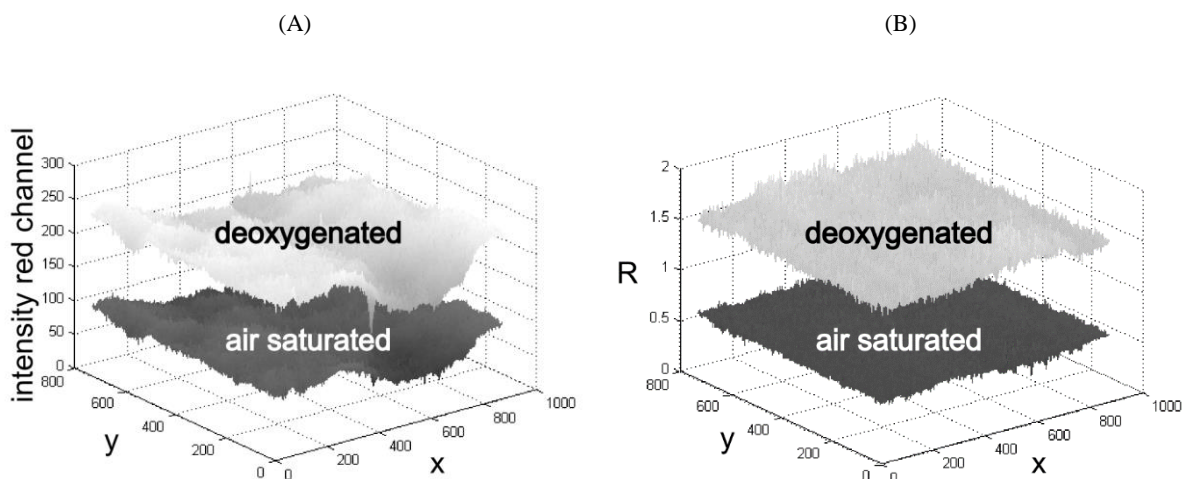


Figure 3.3. (A) Intensity response (red channel) of the oxygen sensor and (B) ratiometric (referenced) image obtained by division of the red by the green channel

easier handling of oxygen imaging inside microfluidics and offers the possibility for high accuracy imaging.

Table 2 shows a qualitative comparison of intensity imaging and ratiometric imaging. The values in brackets display the relative standard deviations of the obtained intensity or referenced signal within one image. With the ratiometric imaging approach the error was decreased to less than the half of the intensity imaging standard deviation.

Table 2 Quality comparison of intensity imaging (red channel) and ratiometric imaging

pO_2 [hPa]	intensity (red) image [a.u.]	ratiometric image R [a.u.]
0	219 ± 17 ($\pm 7.7\%$)	1.588 ± 0.049 ($\pm 3.1\%$)
210	92 ± 10 ($\pm 10.7\%$)	0.631 ± 0.023 ($\pm 3.6\%$)

3.3.3.2 Sensor calibration

A Stern-Volmer calibration curve of a microfluidic sensor chip calibrated with gaseous oxygen is shown in

Figure 3.4. The experimental data points show the typical non-linearity, which is also known for many other optical sensors described in literature³³. An adapted version of the two-site model of Demas et al³⁴ was used to fit the calibration data.

$$\frac{I}{I_0} = \frac{R}{R_0} = \frac{f_1}{1 + K_{SV} pO_2} + f_2 \quad (3.1)$$

I and I_0 are emission intensities, I_0 being the unquenched (deoxygenated) emission intensity. The parameter K_{SV} characterizes the quenching efficiency and therefore the sensitivity of the sensor. In our case I/I_0 was replaced by R/R_0 , where R is the ratio of red and green channel at the respective pO_2 . The parameters f_1 and f_2 describe different fractions of dye molecules, with f_1 being the fraction of dyes, which is quenched with a certain K_{SV} ($K_{SV} = 11.5 \cdot 10^{-3} \text{ hPa}^{-1}$) and f_2 as a non-quenchable fraction ($K_{SV} = 0 \text{ hPa}^{-1}$). These parameters were determined to be $f_1 = 0.785$ and

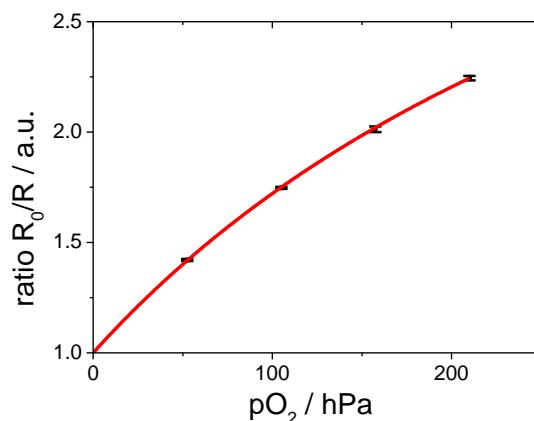


Figure 3.4. Calibration plot of the used sensor showing the nonlinear fit (simplified two-site-model). The black dots and error bars show experimental data from 3 independent calibration measurements.

$f_2 = 1 - f_1 = 0.215$. The red line in Figure 3.4 shows the fitting result, which accurately describes experimental values (black dots with error bars).

3.3.4 Versatility of Sensor Setup

Oxygen imaging using the presented microfluidic chips with integrated sensor layers not only enabled microscopic oxygen imaging but also “macroscopic” imaging. Here macroscopic refers to parallelized measurements with basically the same sensor setup, where one image shows multiple microfluidic channels. Both, the microscopic and the macroscopic approach were performed with basically the same sensor setup and equally benefit from the use of ratiometric imaging, as they are usually subject to inhomogeneous illumination and detection efficiencies. Figure 3.5 shows a

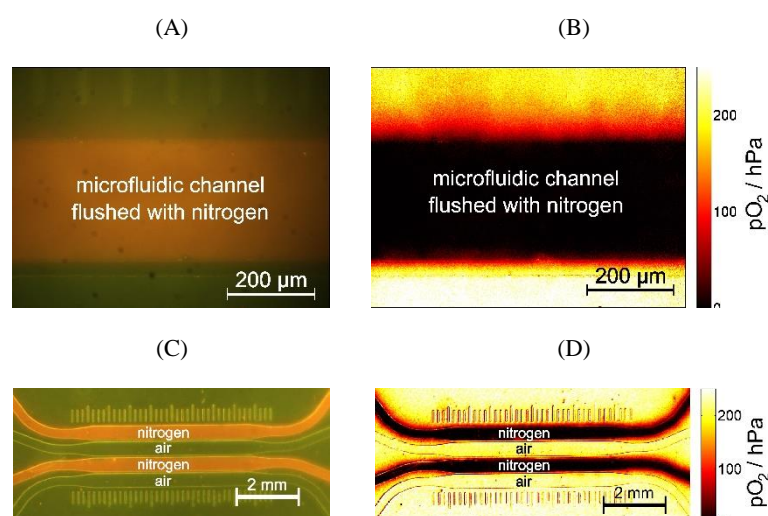


Figure 3.5. (A) Microscopic color (original) image and (B) calculated oxygen image of one channel a microfluidic chip, which is flushed with nitrogen. (C) Macroscopic color (original) image and (D) calculated oxygen image of four channels of the same microfluidic chip; the first and the third channel were flushed with nitrogen, while the other channels contained air.

color and an oxygen image. Choosing suitable camera lenses and excitation sources allows for performing microscopic imaging to resolve oxygen concentration within one microfluidic channel (Figure 3.5 (A) and (B)) and for macroscopic and parallelized measurements (Figure 3.5 (C) and (D)) within one image.

3.3.5 2D oxygen information of microfluidic cell cultures

As was mentioned in the introduction, 2D measurements allow a more detailed look at oxygen levels and gradients inside microbioreactors. This chapter assesses the importance of these measurements, especially when oxygen consumption of complex cell clusters is observed.

Figure 3.6 shows how oxygen gradients can be resolved in a cell culture microenvironment. (A) and (D) show phase contrast images of (A-C) a Hela cell monolayer and (D-F) fibroblasts forming a cell cluster. (B) and (E) show the corresponding pO_2 images. While the oxygen level of the monolayer is rather homogeneous, oxygen gradients can clearly be seen in case of the cell cluster. Towards the center of the cell cluster oxygen concentration is significantly lower compared to the edge of the cluster or even cell free areas. Figure 3.6 (C) and (F) compare the pO_2 gradients taken from a horizontal line in the images to the mean pO_2 , which would be obtained by a single point measurement of a fiber optic sensor with $d = 1 \text{ mm}^2$. In case of the Hela cell monolayer, the pO_2 gradient over the image is fairly constant and can be approximated by the mean pO_2 without loss of relevant information. Here, a single point measurement would be a sufficiently good alternative

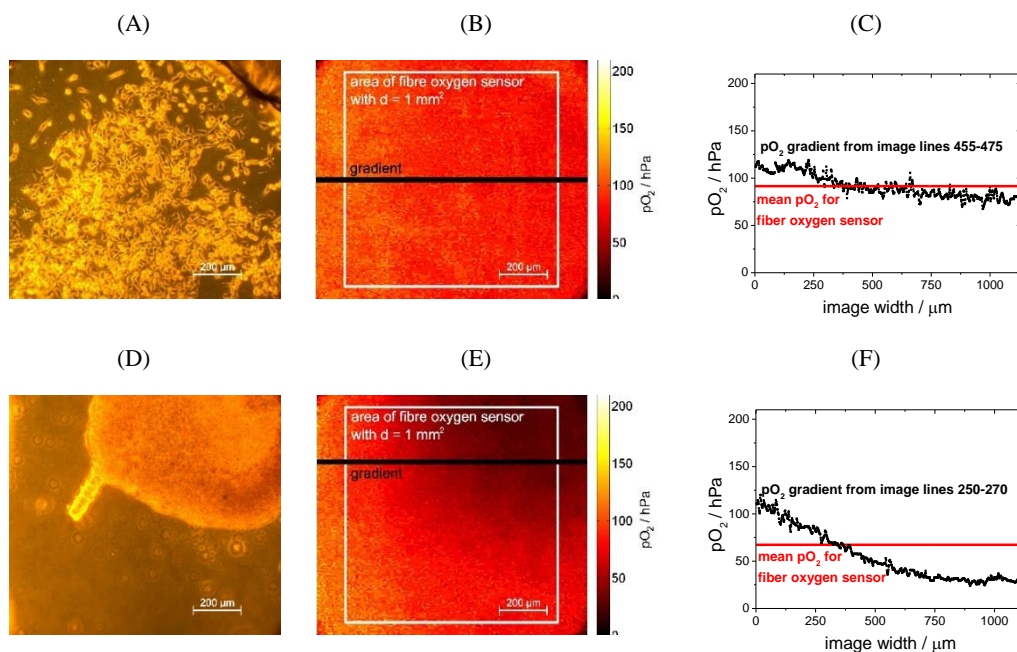


Figure 3.6. (A) Phase contrast and (B) pO_2 image of Hela cells forming a monolayer with marks for regions of interest for data evaluation. After overnight cell adhesion, the chip was rinsed with medium to replenish oxygen. Then the flow was stopped and after 1 h the images were taken to show cellular oxygen consumption. (C) shows the pO_2 gradient of image lines 445-475 of image (B); mean pO_2 over image area covering the area of an optical fiber is 91.5 hPa, while the detailed gradient from lines 455-475 ranges from 67.3 to 119.0 hPa; (D) phase contrast and (E) pO_2 image of fibroblasts forming a cell cluster with marks for regions of interest for data evaluation. The images were taken 13 h after seeding the chip with fibroblasts (F) shows the pO_2 gradient of image lines 250-270 of the pO_2 image; mean pO_2 over image area covering the area of an optical fiber is 67.3 hPa, while the detailed gradient ranges from 24.0 to 120.0 hPa.

for 2D information. The cell cluster in Figure 3.6 (D) to (F) however, shows an example of a clear pO_2 gradient. Some areas of the cell cluster almost face hypoxic conditions, while the mean pO_2 displays sufficient oxygen supply. Since oxygen tension impacts basic metabolic functions, it is important to know that cells in some areas were exposed to low oxygen concentration. Here oxygen imaging can serve as a tool to observe the heterogenous oxygen distribution during experimentation in cellular assays.

In addition to spatial information on oxygen distribution, for many applications also temporal resolution is of interest. For example, it can be important to follow the metabolic activity of cells during pharmaceutical drug screening or environmental monitoring. In Figure 3.7 oxygen changes in a microfluidic chip containing a Hela cell aggregate were monitored over time. A region of interest (red square, $250 \times 250 \mu m^2$) was selected in the center of the cell cluster and the mean pO_2 values of this region was extracted from the oxygen images.

Oxygen sensing was started after overnight formation of the cell cluster without medium flow resulting in low initial oxygen concentrations. First the microfluidic channel was flushed with medium ($v = 1 \mu L/min$) for 23 min. During the first minutes no change in oxygen concentration was observed. This can easily be explained by the fluidic dead volume. After the volume of the cell chambers was exchanged with fresh air saturated medium an increase in oxygen levels was observed. However, this increase was not very rapid, because it was counteracted by the cells' oxygen consumption. The balance between oxygen supply and cellular respiration resulted in an overall constant increase of pO_2 . After 23 min the medium flow was stopped. Oxygen supply was therefore limited to diffusion through the medium and consequently the increase in oxygen concentrations became slower and eventually reached a plateau. Then (after 57 min) the medium flow was started again ($t = 57$ min), but this time 0.4% Triton X was added to the medium. Triton X is a detergent that rapidly kills cells by destroying their membranes. When the Triton X containing medium reached the cells ($t = 70$ min), a clear and fast increase of pO_2 was observed. This strong increase indicates reduced oxygen consumption as a result of cell death. Importantly, at this point also oxygen levels became almost constant over the entire image area. The experiment showed that oxygen imaging allows for time resolved information on oxygen levels

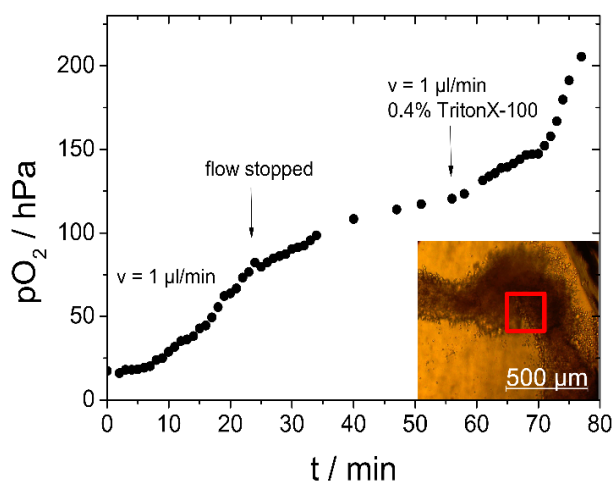


Figure 3.7 oxygen imaging of Hela cells over time; the microfluidic chip was flushed with 0.4% Triton X in media. The curve shows the average pO_2 of a region of interest (red square, $250 \times 250 \mu m^2$) with high cell density.

within a microfluidic device with high sensitivity by selecting a highly sensitive region of interest with high cell densities. The method enables to monitor respiration rates as indicator of metabolic activity for instance during pharmaceutical drug screening.

3.4 Conclusion

In this work we adapted a fabrication process of microfluidic chips for integration of luminescent sensing films and implemented ratiometric oxygen imaging inside microfluidic environments. This ratiometric approach allows for improved read outs compared to intensity imaging because of data normalization to a non-oxygen sensitive reference dye. Ratiometric imaging yielded less than half the standard deviation compared to intensity imaging. The non-linear two-site model was used to accurately describe the experimental calibration curve. The applied sensor setup allowed for performing temporally and spatially resolved measurements inside microfluidic environments ranging from microscopic to macroscopic and parallelized oxygen imaging.

The sensitivity of the selected sensor setup showed to be sufficiently accurate to monitor 2D oxygen levels in human cell culture devices. The technology can be used in laboratories working with microfluidic cell cultures to better control and optimize cultivation conditions and opens the way for novel cell based assays in the highly relevant fields of tissue engineering, tumor biology and hypoxia reperfusion phenomena.

3.5 Notes

Birgit Ungerböck and Verena Charwat contributed equally to this work.

3.6 Acknowledgement

Financial support by the Austrian Research Promotion Agency (FFG) in the framework of the Austrian Nano Initiative (Research Cluster 0700-ISOTEC) and by the European Union FP7 Project BIOINTENSE – Mastering Bioprocess integration and intensification across scales (Grant Agreement Number 312148) is gratefully acknowledged.

3.7 Notes and references

^a Applied Sensors, Institute of Analytical Chemistry and Food Chemistry, Graz University of Technology, Stremayrgasse 9/3, 8010 Graz, Austria. Fax: +43 (0) 316 873 32502; Tel: +43 (0) 316 873 32504; E-mail: torsten.mayr@tugraz.at

^b BioSensor Technologies, AIT Austrian Institute of Technology GmbH, Muthgasse 11/2, 1190 Vienna, Austria. Fax: +43(0) 50550 4450; Tel: +43(0) 50550 4469; E-mail: peter.ertl@ait.ac.at

1. S. M. Grist, L. Chrostowski, and K. C. Cheung, *Sensors*, 2010, **10**, 9286–9316.
2. M. Csete, *Ann. N. Y. Acad. Sci.*, 2005, **1049**, 1–8.
3. M. C. Simon and B. Keith, *Nat. Rev. Mol. Cell. Biol.*, 2008, **9**, 285–296.
4. S. Lahiri, *J Appl Physiol*, 2000, **88**, 1467–1473.
5. M. Radisic, J. Malda, E. Epping, W. Geng, R. Langer, and G. Vunjak-Novakovic, *Biotechnol. Bioeng.*, 2006, **93**, 332–343.
6. M. Höckel and P. Vaupel, *JNCI J. Natl. Cancer Inst.*, 2001, **93**, 266–276.
7. E. O. Pettersen, L. H. Larsen, N. B. Ramsing, and P. Ebbesen, *Cell Prolif.*, 2005, **38**, 257–267.
8. C. Yeom, Y. Goto, Y. Zhu, M. Hiraoka, and H. Harada, *Int. J. Mol. Sci.*, 2012, **13**, 13949–13965.
9. G. L. Semenza, *Cancer Metastasis Rev.*, 2000, **19**, 59–65.
10. D. Fan, L. R. Morgan, C. Schneider, H. Blank, S. Roy, Y. F. Wang, and S. Fan, *J. Cancer Res. Clin. Oncol.*, 1985, **110**, 209–215.

11. O. Trédan, C. M. Galmarini, K. Patel, and I. F. Tannock, *JNCI J. Natl. Cancer Inst.*, 2007, **99**, 1441–1454.
12. Y. Liu and S. Wang, *Colloids Surf., B*, 2007, **58**, 8–13.
13. M. A. Acosta, P. Ymele-Leki, Y. V. Kostov, and J. B. Leach, *Biomaterials*, 2009, **30**, 3068–3074.
14. K. Kellner, G. Liebsch, I. Klimant, O. S. Wolfbeis, T. Blunk, M. B. Schulz, and A. Göpferich, *Biotechnol. Bioeng.*, 2002, **80**, 73–83.
15. D. Schäpper, M. Alam, N. Szita, A. Eliasson Lantz, and K. Gernaey, *Anal. Bioanal. Chem.*, 2009, **395**, 679–695.
16. R. H. W. Lam, M.-C. Kim, and T. Thorsen, *Anal. Chem.*, 2009, **81**, 5918–5924.
17. A. P. Vollmer, R. F. Probst, R. Gilbert, and T. Thorsen, *Lab Chip*, 2005, **5**, 1059–1066.
18. V. Nock, R. J. Blaikie, and T. David, *Lab Chip*, 2008, **8**, 1300–1307.
19. D. Sud, G. Mehta, K. Mehta, J. Linderman, S. Takayama, and M.-A. Mycek, *J. Biomed. Opt.*, 2006, **11**, 050504.
20. B. Ungerböck, A. Pohar, T. Mayr, and I. Plazl, *Microfluid Nanofluid*, 2012.
21. V. Nock and R. J. Blaikie, *Sensors*, 2010, **10**, 1813–1819.
22. V. Nock and R. J. Blaikie, in *2009 IEEE Sensors*, 2009, pp. 1248–1251.
23. P. C. Thomas, S. R. Raghavan, and S. P. Forry, *Anal. Chem.*, 2011, **83**, 8821–8824.
24. G. Mehta, K. Mehta, D. Sud, J. Song, T. Bersano-Begey, N. Futai, Y. S. Heo, M.-A. Mycek, J. Linderman, and S. Takayama, *Biomed. Microdevices*, 2007, **9**, 123–134.
25. H. Zhu, X. Zhou, F. Su, Y. Tian, S. Ashili, M. R. Holl, and D. R. Meldrum, *Sensor Actuat. B-Chem.*, 2012, **173**, 817–823.
26. Z. Lin, T. Cherng-Wen, P. Roy, and D. Trau, *Lab Chip*, 2009, **9**, 257–262.
27. G. Liebsch, I. Klimant, B. Frank, G. Holst, and O. S. Wolfbeis, *Appl. Spectrosc.*, 2000, **54**, 548–559.
28. M. I. J. Stich, S. M. Borisov, U. Henne, and M. Schäferling, *Sensor Actuat. B-Chem.*, 2009, **139**, 204–207.
29. Y. Feng, J. Cheng, L. Zhou, X. Zhou, and H. Xiang, *Analyst*, 2012, **137**, 4885–4901.
30. M. Larsen, S. M. Borisov, B. Grunwald, I. Klimant, and R. N. Glud, *Limnol. Oceanogr-Meth.*, 2011, **9**, 348–360.
31. T. Förster, *Ann. Phys.*, 1948, **437**, 55–75.
32. T. Mayr, S. M. Borisov, T. Abel, B. Enko, K. Waich, G. Mistlberger, and I. Klimant, *Anal. Chem.*, 2009, **81**, 6541–6545.
33. E. R. Carraway, J. N. Demas, and B. A. DeGraff, *Anal. Chem.*, 1991, **63**, 332–336.
34. J. N. Demas, B.A. DeGraff, and W. Xu, *Anal. Chem.*, 1995, **67**, 1377–1380.

4 Online Oxygen Measurements inside a Microreactor with Modeling of Transport Phenomena

Birgit Ungerböck^a, Andrej Pohar^b, Torsten Mayr^a and Igor Plazl^{b*}

Published in Microfluidics and Nanofluidics, March 2013, Volume 14, Issue 3-4, pp 565-574

With kind permission from Springer Science and Business Media

DOI: 10.1007/s10404-012-1074-8

Abstract Oxygen-imaging using an epifluorescent microscope was performed inside a microfluidic chip by utilizing nanosensor particles stained with oxygen-sensitive luminescent dye. The oxidation reaction of β -D-glucose to hydrogen peroxide and δ -D-gluconolactone by molecular oxygen in the presence of glucose oxidase from *Aspergillus niger* inside microreactors with Y-shaped microchannels was followed with this measuring technique. This reaction is widely used in diagnostics and biotechnology. Dissolved oxygen concentrations were measured at various flow rates and microchannel dimensions. Additional batch experiments and microreactor experiments with a reaction-free set-up were conducted. Mathematical models, ranging from a full 3D description of transport phenomena, incorporating convection, diffusion and enzymatic reaction terms along with the parabolic velocity profile, to simplified less precise models were developed to simulate the concentration of dissolved oxygen inside the microchannels, in order to assess the required model complexity for achieving precise results and to depict the governing transport characteristics at the microscale.

4.1 Introduction

Glucose oxidase (GOx) (β -D-glucose:oxygen 1-oxido-reductase, EC 1.1.3.4) is an oxido-reductase, which catalyzes the oxidation of β -D-glucose to hydrogen peroxide and δ -D-gluconolactone by a variety of oxidizing substrates, including molecular oxygen (Leskovac et al. 2005). It is a useful tool for selective glucose determination and is of interest in analytical chemistry, biochemistry, food, beverages and clinical chemistry, as well as in the development of microreactor systems (Raba and Mottola 1995, Wang et al. 2010). There has been increased demand in recent years due to novel applications and for the integration of biosensors with enzymatic microreactors, an area which becomes wider every year (Baronas et al. 2009).

Most microdevices are designed and fabricated by trial and error so proper modeling and simulation methods are indispensable for shortening their design period (Brand et al. 2006). Modeling provides insight into reaction mechanisms, allows for parameter sensitivity analyses, and is a valuable tool for process optimization, data interpretation, for the determination of kinetic parameters and for the evaluation of transport phenomena. Microreactors are an ideal platform for studying such processes due to the precisely controllable operating conditions, and simulations are used to optimally design microreactors under various constraints (Brand et al. 2006).

Song et al. (2011) conducted measurements of dissolved oxygen in a microchannel using phosphorescence and concluded that it could be a useful tool for investigating dissolved oxygen concentrations in various microfluidic devices. Similarly, Nock et al. (2009) measured oxygen concentrations by means of fluorescence, but no modeling was involved in the two works. In a later work, Nock et al. (2010) validated their results with a 2D computational fluid dynamics code, obtaining a good agreement with their experimental data.

There have been numerous models employed for modeling processes inside microreactors, only a few relevant to this work are presented. Gaseous flows inside microchannels of simple geometry have been modeled extensively using 1D plug flow models, which assume uniform process properties in the cross-sectional directions, and were proven to be sufficient in providing reliable results (Kaisare et al. 2005, Alfadhel and Kothare 2005, Deshmukh et al. 2004, Choi and Stenger 2003, Park et al. 2006). Chein et al. (2010) showed that the prediction of a 1D model for a packed-bed microreactor with gaseous flows was in good agreement with experimental results and Constales et al. (2001) showed that a 1D model for a packed-bed microreactor is valid for aspect ratios length/radius > 3.5 . For the case of more complex structured microreactors 2D modeling is required, which improves the accuracy of the steady-state solution (Deshmukh et al. 2004).

For the case of liquid flows, Jovanović et al. (2005) developed a 2D model containing convection, diffusion, and reaction terms. The model could be reduced to the ideal plug-flow model. They also recognized that the small length scale of microreactors reduces transport limitations, giving nearly gradientless conditions desirable for the determination of intrinsic reaction kinetics. Tišma et al. (2009) successfully described the reaction diffusion dynamics inside a microreactor with a 2D model. Žnidaršič-Plazl and Plazl (2009) found good agreement with experimental data by using a 3D model for modeling transport phenomena under parallel flow conditions, but the possible sufficiency of a 2D model was not addressed.

Several analytical models were developed for only convection and diffusion of species considering various simplifications (Holden et al. 2003, Wang et al. 2006, Wu et al., 2004, Lam et

al. 2005, Beard 2001). The most extensive analytical model was derived for three dimensions by Song et al. (2012), which only neglected axial diffusion.

In this work, dissolved oxygen concentration profiles inside microchannels were measured with a novel method under forced convection conditions and a detailed description of the transport phenomena and chemical reaction dynamics by means of mathematical modeling was presented, which provided insight into the concentration profiles of all reacting species.

4.2 Materials and methods

Microreactor chips experimented on were custom ordered from Micronit Microfluidics B.V. (Enschede, The Netherlands). They were made of optically transparent borosilicate glass, which allowed for the visualization of the inner microchannels. These were of rectangular geometry, and were curved to facilitate their total length of 66.4 cm. Two microreactors with different channel geometries were used, the first had a $220 \times 50 \mu\text{m}$ channel cross-section (width to depth), and the second a $440 \times 50 \mu\text{m}$ channel cross-section. Their corresponding hydraulic diameters were $81.5 \mu\text{m}$ and $89.8 \mu\text{m}$ respectively. They had two inlet channels, which merged in parallel to form a central channel, and one outlet channel. They were positioned inside a stainless steel housing and connected with PEEK tubes to high performance syringe pumps (Harvard Apparatus, Holliston, USA) equipped with steel syringes (8 mL). The syringe pumps ensured precise, highly controllable flow rates, which could be as low as $0.5 \mu\text{L}/\text{min}$.

The oxygen sensitive dye $\text{Ir}(\text{Cs})_2(\text{acac})$ (Borisov and Klimant 2007) was synthesized in our lab. Glucose oxidase from *Aspergillus niger* was obtained from Sigma Aldrich (211 U/mg) and α -D-glucose monohydrate was obtained from Roth; both were of analytical grade. The preparation of luminescent poly(styrene-block-vinylpyrrolidone) nanobeads (PSPVP nanobeads) containing 1.5% (w/w) $\text{Ir}(\text{Cs})_2(\text{acac})$ was reported elsewhere (Borisov and Klimant 2007, 2009, Borisov et al. 2008). The nanobeads had an average size of 245 nm in aqueous media; their size distribution has been specified in an article by Borisov et al. (2008). For measurements in the microfluidic chips, PSPVP nanoparticles 1% (w/w) were used dispersed in water. The viscosity of the nanoparticle dispersion was measured with a Cannon-Fenske viscometer at room temperature and the density was measured with a 10 mL picnometer.

Oxygen lifetime imaging was performed on a Zeiss Axiovert 25 CFL (Zeiss, Gottingen, Germany) by using a PCO SensiCam (PCO, Kehlheim, Germany) for Rapid lifetime determination (RLD) as described by Moser et al. (2006). A blue ultrabright LED with emission maximum at $\lambda = 450 \text{ nm}$ (Luxeon lambert emitter, blue, 5 W) was applied as the triggered excitation light source for fluorescence lifetime imaging and combined with a filter set-up consisting of Linos DT blue/Linos DC blue/Schott OG 515 (LINOS Photonics, Göttingen, Germany; Schott, Mainz, Germany) as the excitation filter/dichromatic mirror/barrier filter, respectively. Full calibration of the sensor particles was performed outside the chip by flushing the particle suspension with gaseous air-nitrogen mixtures. For each measurement they were recalibrated by determining τ_0 and τ_{air} under deoxygenated and fully air saturated conditions inside the microfluidic chip. As the calibration function shows slightly nonlinear behavior, the full calibration was then adapted to τ_0/τ_{air} obtained from the recalibration.

4.3 Optical measurements

4.3.1 Batch experiments with GOx

In order to get an insight into the kinetics of the reaction between β -D-glucose and molecular oxygen, batch experiments were performed beforehand. Sensor spots (Pyro Science, Germany) were placed at the bottom of 5 mL vials. PSPVP-nanosensor particles (2 % (w/w)) were dispersed in a water/glucose solution (20 g/L). 2.5 mL of the solution were added to the vials and saturated with air through a tube fitted to an air tank and closed with a septum. As soon as the glucose solution was saturated with air, 2.5 mL of a GOx/water solution were quickly added and the vials were shaken to overcome mass transfer limitations. A pH of 5.6 was presumed for the water equilibrated with air, which is normal for an air saturated solution due to the CO₂ content (Kamei and Ohmoto 2000). It was assured that no air was left inside the vial. Sensor signals were read out from outside using a miniaturized phase fluorimeter (Firesting, Pyro Science, Germany). Three experiments with the following GOx concentrations were performed: 0.05 g/L (2.69×10^{-7} M), 0.01 g/L (5.38×10^{-8} M), and 0.005 g/L (2.69×10^{-8} M). The molar mass of the enzyme was 1.86×10^5 g/mol. The measured dissolved oxygen concentrations were followed for 160 seconds and plotted against time.

4.3.2 Diffusion-convection experiments

Diffusion-convection experiments were performed in order to test the performance of the optical nanosensor particles and to evaluate the diffusion of oxygen. The microreactor with the $220 \times 50 \mu\text{m}$ microchannel cross-section was used. One syringe was filled with an air saturated PSPVP-dispersion, while the other with an oxygen-free dispersion (formerly purged with nitrogen), which was also pumped through deoxygenated silicon tubes. Local oxygen concentrations were followed through image acquisition, performed on a Zeiss epifluorescent microscope (10 \times objective) using a monochrome, gateable camera (Sensicam; 480×640 pixels; lifetime-imaging), as shown on Figure 4.1. Image processing was performed using Matlab. Flow rates from 0.5 to 5 $\mu\text{L}/\text{min}$ on each syringe were experimented with.

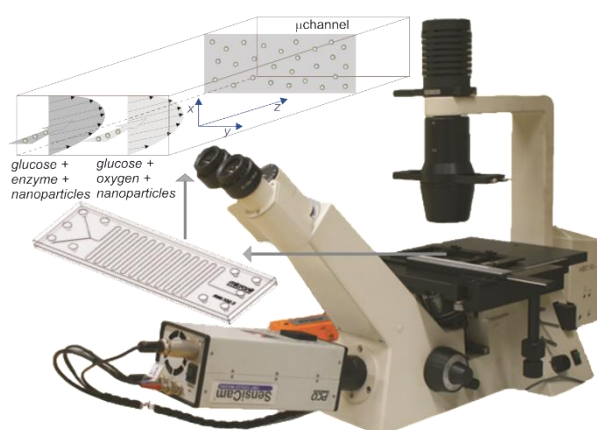


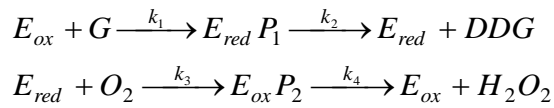
Figure 4.1. The experimental set-up for the microreactor experiments. The Zeiss epifluorescent microscope, the microreactor chip used in the study, and the microreactor domain in question are presented. The diffusion-convection experiments were performed without the enzyme.

4.3.3 GOx experiments

The reaction between β -D-glucose and molecular oxygen with GOx as the catalyst was performed in a similar manner as the diffusion-convection experiments. β -D-glucose (final concentration 10 g/L) and PSPVP nanosensor particles stained with oxygen-sensitive luminescent dye were added to both syringes. GOx was added to the oxygen-free syringe (0.05 g/L); the other syringe was purged with air and closed. The microreactor with $440 \times 50 \mu\text{m}$ microchannel cross-section was used. Measurements were taken at the following distances from the inlet: 14.2, 153.7, 286.2, 418.7, 551.2, and 657.1 mm.

4.3.4 Modeling and reaction kinetics

The commonly accepted mechanism for β -D-glucose oxidation in the presence of oxygen is the Ping Pong Bi Bi mechanism comprising of two half-reactions. When β -D-glucose and O_2 are the substrates of the enzyme the reactions are irreversible (Bright and Porter, 1975). The reaction scheme is:



where E_{ox} is the enzyme in its oxidized form, E_{red} in its reduced form, $E_{red}P_1$ and $E_{ox}P_2$ are the enzyme intermediates, G is β -D-glucose, O_2 , H_2O_2 and DDG are molecular oxygen, hydrogen peroxide and δ -D-gluconolactone. The rate equations for the reaction mechanism therefore read:

$$\begin{aligned} r_{E_{ox}} &= -k_1 c_{E_{ox}} c_G + k_4 c_{E_{ox}P_2} \\ r_G &= -k_1 c_{E_{ox}} c_G \\ r_{E_{red}P_1} &= k_1 c_{E_{ox}} c_G - k_2 c_{E_{red}P_1} \\ r_{E_{red}} &= k_2 c_{E_{red}P_1} - k_3 c_{E_{red}} c_{O_2} \\ r_{O_2} &= -k_3 c_{E_{red}} c_{O_2} \\ r_{E_{ox}P_2} &= k_3 c_{E_{red}} c_{O_2} - k_4 c_{E_{ox}P_2} \\ r_{H_2O_2} &= k_4 c_{E_{ox}P_2} \\ r_{DDG} &= k_2 c_{E_{red}P_1} \end{aligned} \tag{4.1}$$

and the mass balance for the batch experiments is:

$$\frac{dc_i}{dt} = -r_i \tag{4.2}$$

with appropriate initial conditions as specified in the section: Batch experiments with GOx. Index i represents the appropriate chemical specie. The kinetic parameters used for the simulations

were taken from literature; k_1 , k_3 and k_4 for the reaction at 25 °C and pH = 5.6 from Bright and Gibson (1967), while k_2 was taken from Leskovac et al. (2005):

$$\begin{aligned} k_1 &= 13158 \text{ M}^{-1} \text{ s}^{-1} \\ k_2 &= 6000 \text{ s}^{-1} \\ k_3 &= 1.8 \times 10^6 \text{ M}^{-1} \text{ s}^{-1} \\ k_4 &= 1440 \text{ s}^{-1} \end{aligned}$$

The mathematical description of the reaction-diffusion dynamics was described with partial differential equations containing a convection, a diffusion and a reaction term at steady-state conditions. Diffusion was considered in all three spatial directions:

$$v(x, y) \frac{\partial c_i(x, y, z)}{\partial z} = D_i \left(\frac{\partial^2 c_i(x, y, z)}{\partial x^2} + \frac{\partial^2 c_i(x, y, z)}{\partial y^2} + \frac{\partial^2 c_i(x, y, z)}{\partial z^2} \right) - r_i \quad (4.3)$$

with the following boundary conditions:

$$\begin{aligned} c_i(x, y, 0) = c_{i0} \quad \frac{\partial c_i(x, y, L)}{\partial z} = 0 \\ \frac{\partial c_i(0/H, y, z)}{\partial x} = 0 \quad \frac{\partial c_i(x, 0/W, z)}{\partial y} = 0 \end{aligned} \quad (4.4)$$

The reaction term facilitates the appropriate rate equation from eqs. 1 and is non-existent in the case of the diffusion experiments where no reaction took place. The steady-state velocity profile was obtained through simplified Navier-Stokes equations, considering no-slip boundary conditions (zero velocity at the wall), as already described (Stojkovič et al. 2011, Pohar et al. 2011). Due to the complex set of equations which have to be solved, an explicit approach was adopted and a time term added to the model equations, with the solution being obtained when the results converged to steady-state. Initial concentrations were used as the initial conditions inside the computational domain and a $22 \times 40 \times 42$ (depth \times width \times length) mesh was used, which was sufficient to provide accurate results.

Further models were made for comparison: 1D model, 2D plug flow without diffusion in the way of convection, 2D plug flow model, 3D model without diffusion in the way of convection, a 3D plug flow model and a model considering Michaelis-Menten kinetics. The kinetic constants for the Ping Pong mechanism, considering a nearly irreversible reaction of oxygen and glucose are (Leskovac et al. 2005):

$$v_{\max} = \frac{k_2 k_4}{(k_2 + k_4)} \quad K_a = \frac{v_{\max}}{k_1} \quad K_b = \frac{v_{\max}}{k_3} \quad (4.5)$$

The modeling was done with the finite difference method in Matlab. The following reasonable assumptions were made:

- (1) Gravitational effects were disregarded.
- (2) The microreactor operates under steady-state conditions.
- (3) Both inlet streams are of identical physical properties and there is no change in the flow due to the reaction.

The merging of the two flows is considered instantaneous since the length of the entire microchannel is much larger than the merging part.

4.4 Results and discussion

4.4.1 Batch experiments with GOx

The results of the batch model simulation, according to equation 2, showed excellent agreement with the measured dissolved oxygen concentrations (Figure 4.2). Therefore the parameters taken from literature were retained for modeling purposes and no further experiments regarding the enzyme activity were made. The equilibrium saturated oxygen concentration, under atmospheric conditions at 25 °C, of 8.3 mg/L was presumed.

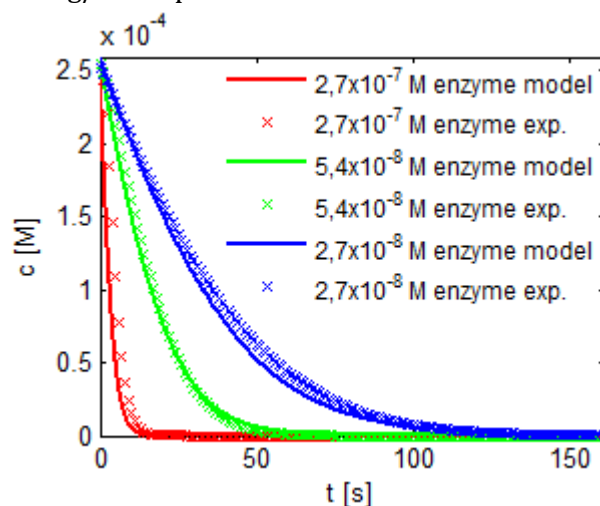


Figure 4.2. Batch model and experimental data at various enzyme concentrations. Dissolved oxygen concentrations are presented.

Upon the review of the concentration change of each species over time for the case of 2.69×10^{-8} M enzyme concentration (Figure 4.3), the following conclusions could be made. The first half-reaction reaction is instantaneous, which can be seen from the immediate substantial formation all enzyme forms. Dissolved oxygen concentration begins to lower at the very beginning, and δ -D-gluconolactone is formed (Figure 4.3a). After the first half-reaction takes place there is only minute δ -D-gluconolactone formed, since the enzyme concentration is approximately 4 orders of magnitude lower than then the concentration of oxygen and the final amount of δ -D-gluconolactone formed, so it is not visible on Figure 4.3a. The concentration of E_{ox} exhibits a rapid lowering, which would result in its total depletion if it was not for its further production in the second half-reaction. The formation of the reduced enzyme form (E_{red}) allows for the second-half

reaction to take place. Figure 4.3b presents the concentrations of all enzyme forms; their total concentration is always the initial enzyme concentration.

In the second half-reaction, the formed E_{red} reacts with oxygen, consequently returning the enzyme to its original oxidized form. Hydrogen peroxide is formed in the process. The newly produced E_{ox} can further react with the abundant glucose, again leading to the production of δ -D-gluconolactone and to the consumption of oxygen. Consequently, hydrogen peroxide and δ -D-gluconolactone are formed identically and at the same rate as oxygen is being consumed.

β -D-glucose was in high excess (0.0555 M) and there is hardly any drop in its concentration from the beginning to the end of the reaction, hence it is not presented. In summary, the whole oxygen consumption process is limited by the second reaction, awaiting the reformation of the original enzyme form.

From the simulation it was found that the biggest increase in the reaction rate could be achieved by raising k_3 , which implies that the reaction between the reduced enzyme form and oxygen is the rate limiting.

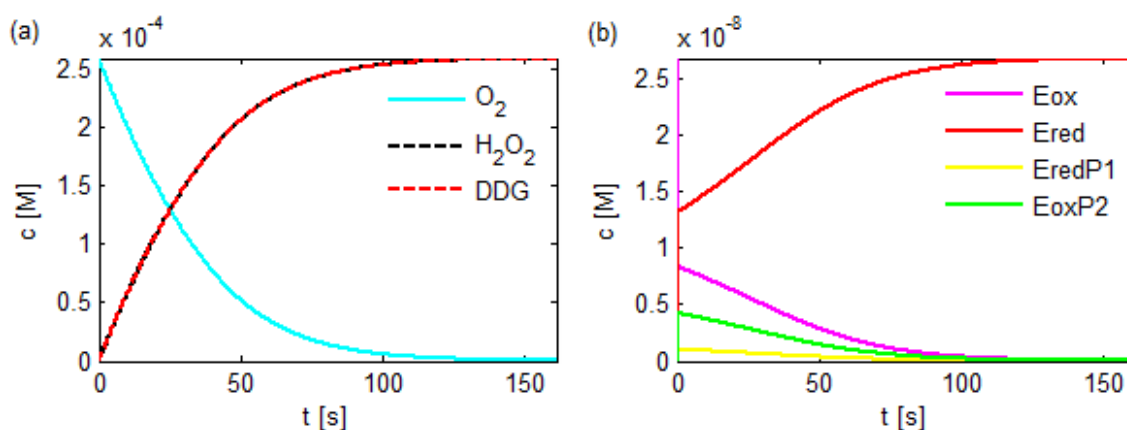


Figure 4.3. The time evolution of the species involved in the Ping Pong Bi Bi reaction mechanism for the case with 2.69×10^{-8} M enzyme concentration.

4.4.2 Diffusion-convection experiments

Under both microreactor geometries and flow rate conditions, the highest Reynolds number achieved was approximately 4, so all of the experiments were done at laminar flow conditions. The diffusion-convection experiments involved oxygen entering the central channel through one inlet and diffusing into the other part of the channel. The concentration distribution is dependent on the diffusion coefficient of oxygen and the flow rate. The diffusion coefficient for oxygen in a 10 g/L glucose solution (0.0555 M) was taken from literature (Jamnongwong et al. 2010) and was 1.97×10^{-9} m²/s. Figure 4.4 shows an intensity image taken through the epifluorescent microscope.

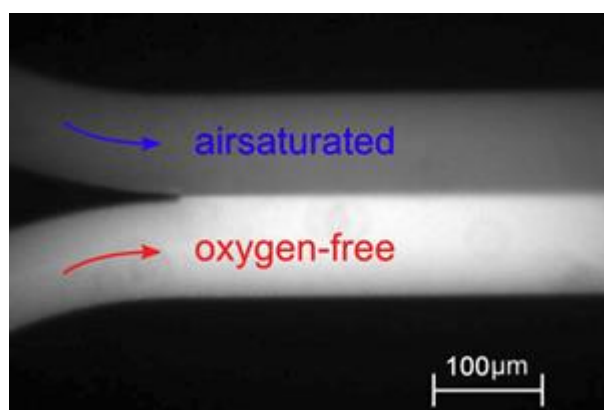


Figure 4.4. The intensity image of the $220 \times 50 \mu\text{m}$ channel taken through the epifluorescent microscope.

Figure 4.5 shows the experimental and the model results for comparison for the flow rate of $0.5 \mu\text{L}/\text{min}$ on each syringe at half-depth. The result for the smallest flow rate is presented since it displays the highest alteration in the concentration distribution compared to the entrance into the central channel. They show good agreement with the simulation, which confirms the accurate value of the diffusion coefficient of oxygen. The biggest discrepancies can be noticed near the channel walls, where the local concentration is measured higher than it is in reality. It is a consequence of light dissipation at the walls.

The measurement accuracy of the technique was estimated by calculating the standard deviation of the experimental data, compared to a curve fitted to that data. The value was 0.03.

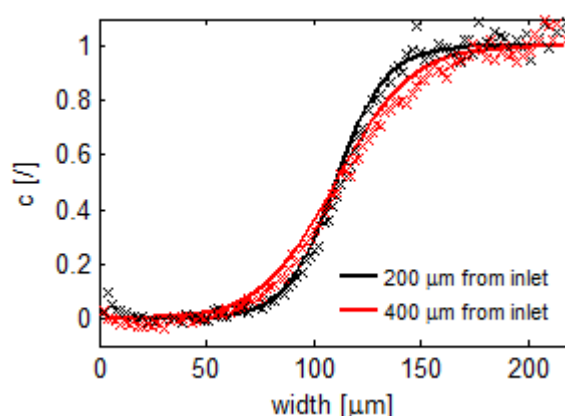


Figure 4.5 The concentration profile of dissolved oxygen at the cumulative flow rate of $1 \mu\text{L}/\text{min}$; $200 \mu\text{m}$ and $400 \mu\text{m}$ from the merging of the inlet channels (- model; \times experimental data). The concentration is normalized to the inlet dissolved oxygen concentration.

The Péclet number, for the case of mass transfer, is a dimensionless number defined as the ratio of the rate of advection of mass by the flow to the rate of diffusion. All experiments performed involved high Péclet numbers. The smallest Péclet number of 35 was calculated for the microreactor with the largest microchannel cross-section ($440 \times 50 \mu\text{m}$) at the slowest flow rate of $1 \mu\text{L}/\text{min}$. Simulations revealed that diffusion in the way of convection comes into effect at Péclet numbers less than 0.5, when discrepancies in the concentration profiles can be observed, if

it is not considered. This means that simulations for the majority of microfluidic studies, involving forced convection, can be done without considering diffusion in the way of convection. This simplifies the method of the finite difference solution, since with the absence of the second derivative of the concentration over space in the way of the flow, a simple explicit formulation can be applied.

The solution of the 3D model showed almost identical concentration profiles at every depth of the microchannel, which can be seen on Figure 4.6. There was only a small variation of the concentrations next to the walls of the microchannels, caused by the parabolic velocity profile. Molecules near the top and bottom of the microchannel diffuse further because of the longer residence time in these regions of the channel, resulting in a butterfly shaped concentration profile termed the “butterfly effect” (Song et al. 2012, Kamholz et al. 1999). For the microchannels under considerations, with high width/depth aspect ratios, rapid depth-wise diffusion causes the effect to be barely noticeable.

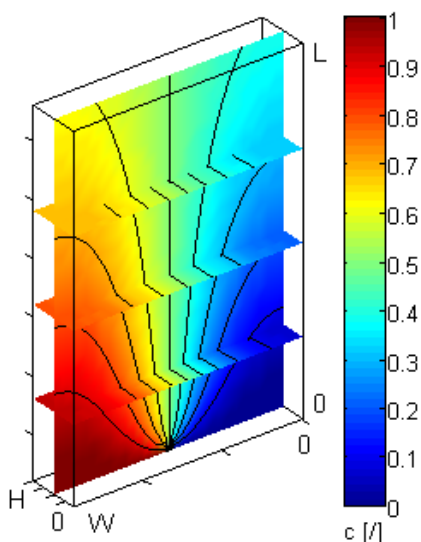


Figure 4.6 A 3D representation of oxygen distribution inside the $220 \times 50 \mu\text{m}$ ($W \times H$) channel to the length (L) of 6 mm at the flow rate of $1 \mu\text{L}/\text{min}$. The slices are positioned at $1/2$ depth, $1/4$ length, $1/2$ length, and $3/4$ length.

Michaelis-Menten kinetics was accurate in predicting the concentration profiles of the substrates, which shows that the underlying assumptions of Michaelis-Menten kinetics are valid for the studied reaction. The maximum deviation between elementary kinetics and Michaelis-Menten kinetics was less than $1 \times 10^{-3}\%$, which could also be a consequence of numerical uncertainty.

The concentration profiles of the 2D and 3D plug flow models were exactly the same. This is expected since there are no variations of any parameters depth-wise. Interestingly, the solution of the 3D model with the parabolic velocity profile showed very little variation from the plug flow models. The concentrations near the walls were only slightly lower. A 2D plug flow model, disregarding diffusion in the way of convection, has been proven to accurately describe the steady-state solution of the concentration distribution inside typical Y-shaped microchannels.

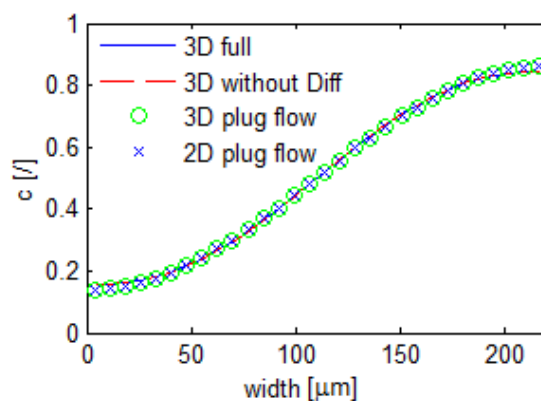


Figure 4.7 The normalized concentration profiles (to the inlet dissolved oxygen concentration) at the length of 8.8 mm (L) with the average velocity of 0.006 m/s. The model: *3D without Diff* disregards diffusion in the way of convection. The concentrations of the 3D models are presented as the average concentrations through the depth.

4.4.3 GOx experiments

The diffusion coefficient for GOx was taken from Swoboda and Massey (1965) and was $4.11 \times 10^{-11} \text{ m}^2/\text{s}$; the molar mass of GOx from *Aspergillus niger* was 186000 g/mol (from the provider's data sheet). The value of the diffusion coefficient for hydrogen peroxide was $1.37 \times 10^{-9} \text{ m}^2/\text{s}$ and the value for β -D-glucose of $5 \times 10^{-10} \text{ m}^2/\text{s}$ was taken from literature (Groebe et al. 1994); the same value was also used for δ -D-gluconolactone due to its similar structure and molar mass. The density of the 1 % (w/w) PSPVP-nanoparticle dispersion measured at room temperature (25 °C) was 1020.6 kg/m^3 and the viscosity was $1.1 \times 10^{-3} \text{ Pas}$.

The first syringe was filled with oxygen saturated PSPVP-dispersion and β -D-glucose, while the second contained the oxygen-free dispersion with GOx and β -D-glucose. The fast reaction between GOx and β -D-glucose immediately occurred in the second syringe, which means that the entire enzyme was converted to its reduced form, there was a slight lowering of the β -D-glucose concentration, and some δ -D-gluconolactone was produced. Similarly to the batch experiment, the concentration of δ -D-gluconolactone was very low compared to the amount formed once the second reaction took place.

All the concentration profiles of the molecules involved in the reaction are presented on Figure 4.8. The enzyme can be seen entering the central channel through one inlet in its reduced form (E_{red}) and due to its low diffusion coefficient it only partly diffused into the other part of the central channel. Oxygen entered through the other inlet and spread inside the microchannel. In the areas where it encountered the enzyme, it was consumed by the reaction and consequently $E_{ox}P_2$ was formed where the two met. $E_{ox}P_2$ decayed into E_{ox} and hydrogen peroxide; its ongoing production was fueled by the reaction between E_{ox} and glucose, which produced new E_{red} required for the second reaction. δ -D-gluconolactone had a similar concentration profile, since it was also being produced in the process (and not consumed). It was concentrated in the middle of the channel due to its lower diffusion coefficient, as compared to hydrogen peroxide. Both enzyme intermediates and E_{ox} had a similar shape due to the fact that they were always formed in the middle where their reactants met and all were being consumed in the two half-reactions. There was only a slight lowering of glucose concentration in the middle of the channel due to the excess amount used.

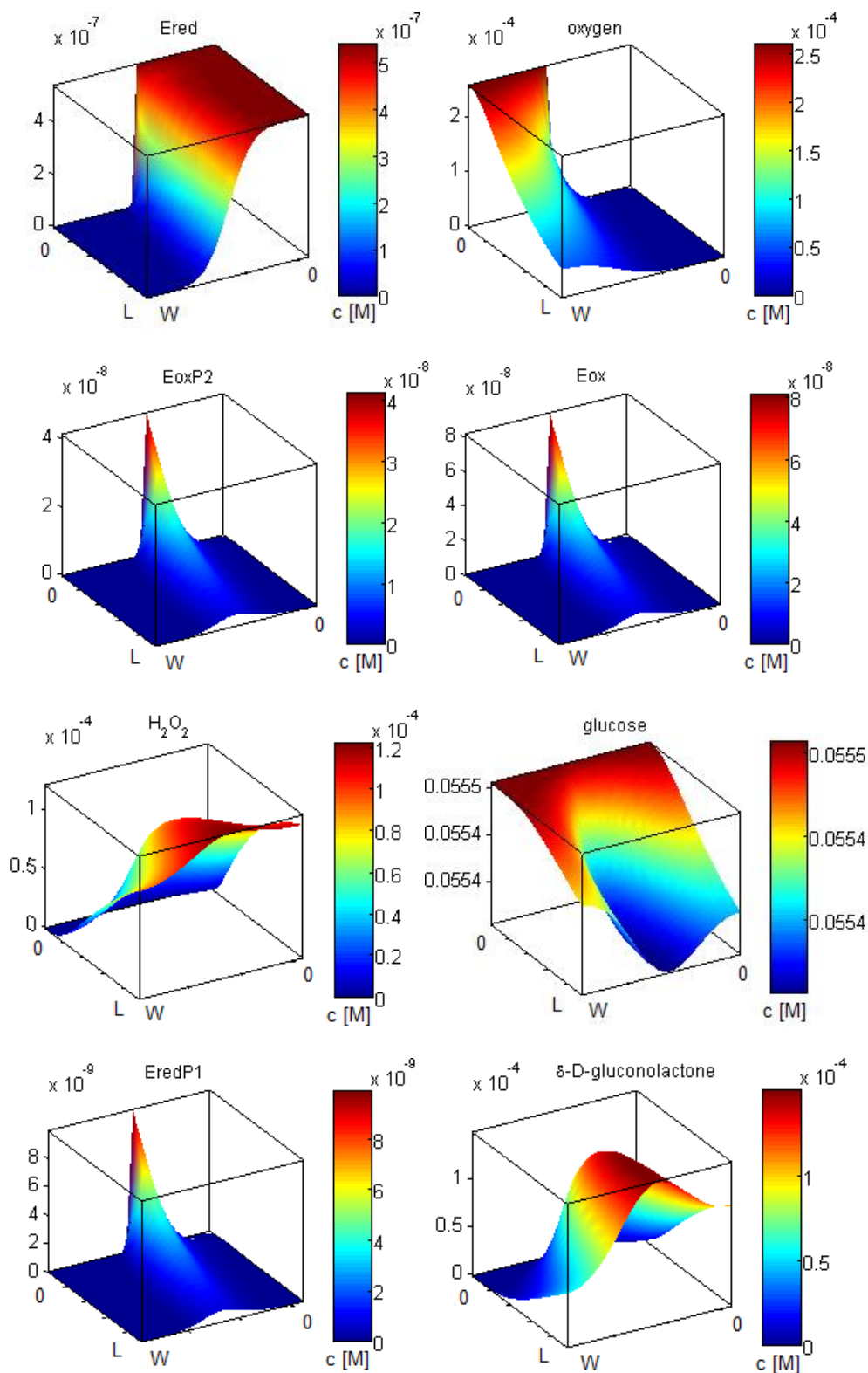


Figure 4.8 Concentration profiles of all species involved in the reaction for the flow rate of 15 $\mu\text{L}/\text{min}$ on each pump in the $440 \times 50 \mu\text{m}$ ($W \times H$) microchannel for the total length (L) of 66.4 cm.

The majority of the enzyme was in its reduced form throughout the channel and stayed in that form once all of the oxygen was consumed.

Figure 4.9 and 4.10 display the comparison between the model simulations and the experimental images at various residence times inside the microchannel. Once again, a 2D plug flow model, disregarding diffusion in the way of convection, produced the same results as the full 3D model, which can be attributed to the high width/depth ratio. The use of a one dimensional model is inappropriate, since it presumes homogenous distribution of components inside the channel and with that their ubiquitous availability for the reaction. Although a one-dimensional distribution of species would be an adequate approximation for reactors that have the characteristic length in the order of 100 μm (Mitsos and Barton 2009), a micromixer preceding the reaction channel would be required.

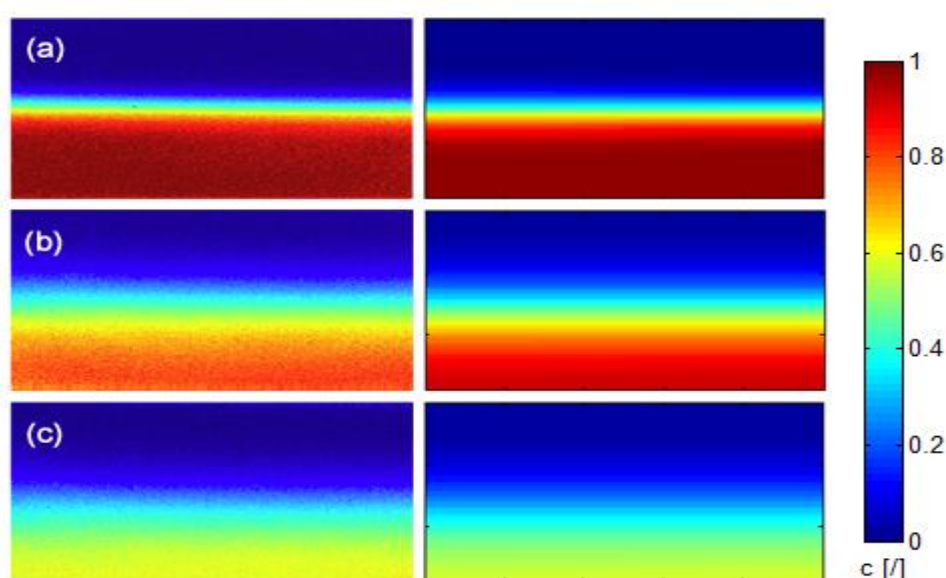


Figure 4.9 The experimental (left) and model (right) normalized concentration profiles at the following residence times: (a) 0.63 s; (b) 12.6 s; (c) 24.3 s.

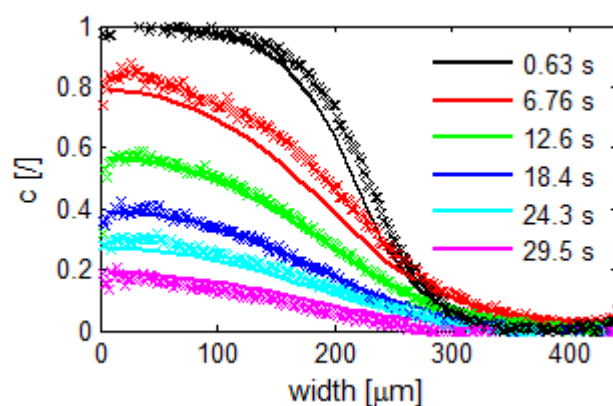


Figure 4.10 The concentration profiles at 1/2 depth for various residence times inside the microchannel (- model; \times experimental data).

4.5 Conclusions

The oxidation reaction of β -D-glucose by molecular oxygen in the presence of glucose oxidase was studied and the concentration profiles of oxygen were followed by means of the described novel oxygen-imaging technique, which gave results of high resolution. Modeling of the reaction mechanism in the microfluidic system provided an insight into concentration distributions of all reaction species. A good agreement without any fitting procedure was found between the model predictions and obtained experimental data for both channel geometries.

Models with simplifications commonly adopted by researchers were made in order to compare the results and to evaluate whether the assumptions were reasonable for modeling transport phenomena inside a microreactor of typical dimensions. Although two dimensional simulations assume an infinitely deep channel, they produced identical solutions as the 3D model. Similarly, the shape of the velocity profile did not influence the solution for the given conditions. Michaelis-Menten kinetics was proven to accurately predict the concentration distributions of the substrates. Finally, it was shown that for the majority of microfluidic studies, involving forced convection, modeling can be done without considering diffusion in the way of convection, which is in accordance with the Péclet number.

4.6 Acknowledgment

This work was supported by Österreichischer Austauschdienst (ÖAD) under the project number SI 15/2011. A. Pohar was supported through PhD Grant 1000-07-310011, provided by the Ministry of Higher Education, Science and Technology of the Republic of Slovenia. Further financial support by the Austrian Research Promotion Agency (FFG) in the framework of the Austrian Nano Initiative (Research Project Cluster 0700 – ISOTEC) is gratefully acknowledged.

4.7 References

- Alfadhel K, Kothare MV (2005) Modeling of multicomponent concentration profiles in membrane microreactors. *Ind Eng Chem Res* 44:9794–9804
- Baronas R, Ivanauskas F, Kulys J (2009) *Mathematical modeling of biosensors: An introduction for chemists and mathematicians*. Springer, New York
- Beard DA (2001) Response to 'Comment on Taylor dispersion of a solute in a microfluidic channel'. *J Appl Phys*, 90:6555–6556
- Borisov SM, Klimant I (2007) Ultrabright oxygen optodes based on cyclometalated iridium(III) coumarin complexes. *Anal Chem* 79:7501–7509
- Borisov SM, Klimant I (2009) Luminescent nanobeads for optical sensing and imaging of dissolved oxygen. *Microchim Acta* 164:7–15
- Borisov SM, Mayr T, Klimant I (2008) Poly(styrene-block-vinylpyrrolidone) beads as a versatile material for simple fabrication of optical nanosensors *Anal Chem* 80:573–582
- Brand O, Fedder GK, Hierold C, Korvink JG, Tabata O (2006) *Micro process engineering: Fundamentals, devices, fabrication, and applications*. Wiley-VCH, New Jersey
- Bright HJ, Gibson QH (1967) The oxidation of 1-deuterated glucose by glucose oxidase. *J Biol Chem* 242:994–1003
- Bright HJ, Porter DJT (1975) 7 Flavoprotein oxidases. *The enzymes*, Paul DB, Ed. Academic Press 12:421–505
- Chein RY, Chen YC, Chang CS, Chung JN (2010) Numerical modeling of hydrogen production from ammonia decomposition for fuel cell applications. *Int J Hydrogen Energy* 35:589–597
- Choi Y, Stenger HG (2003) Water gas shift reaction kinetics and reactor modeling for fuel cell grade hydrogen. *J Power Sources* 124:432–439
- Constales D, Yablonsky GS, Marin GB, Gleaves JT (2001) Multi-zone TAP-reactors theory and application: I. The global transfer matrix equation. *Chem Eng Sci* 56:1913–1923

- Deshmukh SR, Mhadeshwar AB, Lebedeva MI, Vlachos DG (2004) From density functional theory to microchemical device homogenization: Model prediction of hydrogen production for portable fuel cells. *Int J Mult Comp Eng* 2:221–238
- Deshmukh SR, Mhadeshwar AB, Vlachos DG (2004) Microreactor modeling for hydrogen production from ammonia decomposition on ruthenium. *Ind Eng Chem Res* 43:2986–2999
- Groebe K, Erz S, Mueller-Klieser W (1994) Glucose diffusion coefficients determined from concentration profiles in EMT6 tumor spheroids incubated in radioactively labeled L-glucose. *Adv Exp Med Biol* 361:619–644
- Holden MA, Kumar S, Castellana ET, Beskok A, Cremer PS (2003) Generating fixed concentration arrays in a microfluidic device. *Sensor Actuat B-Chem* 92:199–207
- Jamnongwong M, Loubiere K, Dietrich N, Hebrard G (2010) Experimental study of oxygen diffusion coefficients in clean water containing salt, glucose or surfactant: Consequences on the liquid-side mass transfer coefficients. *Chem Eng J* 165:758–768
- Jovanović GN, Žnidaršič-Plazl P, Sakrithichai P, Al-Khalidi K. (2005) Dechlorination of p-chlorophenol in a microreactor with bimetallic Pd/Fe catalyst. *Ind Eng Chem Res* 44:5099–5106
- Kaisare NS, Lee JH, Fedorov AG (2005) Hydrogen generation in a reverse-flow microreactor: 1. Model formulation and scaling. *AIChE J* 51:2254–2264
- Kamei G, Ohmoto H (2000) The kinetics of reactions between pyrite and O₂-bearing water revealed from in situ monitoring of DO, Eh and pH in a closed system. *Geochim Cosmochim Acta* 64:2585–2601
- Kamholz AE, Weigl BH, Finlayson BA, Yager P (1999) Quantitative analysis of molecular interaction in a microfluidic channel: The T-sensor. *Anal Chem* 71:5340–5347
- Lam YC, Chen X, Yang C (2005) Depthwise averaging approach to cross-stream mixing in a pressure-driven microchannel flow. *Microfluid Nanofluid* 1:218–226
- Leskovac V, Trivić S, Wohlfahrt G, Kandrač J, Peričin D (2005) Glucose oxidase from *Aspergillus niger*: the mechanism of action with molecular oxygen, quinones, and one-electron acceptors. *Int J Biochem Cell B* 37:731–750
- Mitsos A, Barton PI (2009) *Microfabricated power generation devices: Design and technology*. Wiley-VCH, New Jersey
- Moser C, Mayr T, Klimant I (2006) Microsphere sedimentation arrays for multiplexed bioanalytics. *Anal Chim Acta*, 558:102–109
- Nock V, Blaikie RJ (2009) Visualization and measurement of dissolved oxygen concentrations in hydrodynamic flow focusing. *Sensors*, 2009 IEEE
- Park HG, Malen JA, Piggott WT, Morse JD, Greif R, Grigoropoulos CP, Havstad MA, Upadhye R (2006) Methanol steam reformer on a silicon wafer. *J Microelectromech S* 15:976–985
- Pohar A, Lakner M, Plazl I (2011) Parallel flow of immiscible liquids in a microreactor: modeling and experimental study. *Microfluid Nanofluid* 12: 307–316
- Raba J, Mottola HA (1995) Glucose oxidase as an analytical reagent. *Cr Rev Anal Chem* 25:1–42
- Song D, Kim H, Kim K (2011) Measurement of dissolved oxygen concentration field in a microchannel using PtOEP/PS film. *J Visual* 14:295–304
- Song HJ, Wang Y, Pant K (2012) Cross-stream diffusion under pressure-driven flow in microchannels with arbitrary aspect ratios: a phase diagram study using a three-dimensional analytical model. *Microfluid Nanofluid* 12:265–277
- Stojković G, Plazl I, Žnidaršič-Plazl P (2011) L-Malic acid production within a microreactor with surface immobilised fumarase. *Microfluid Nanofluid* 10:627–635
- Swoboda BEP, Massey V (1965) Purification and properties of the glucose oxidase from *Aspergillus niger*. *J Biol Chem* 240:2209–2215
- Tišma M, Zelić B, Vasić-Rački Đ, Žnidaršič-Plazl P, Plazl I (2009) Modelling of laccase-catalyzed L-DOPA oxidation in a microreactor. *Chem Eng J*, 149:383–388
- Wang S, Su P, E H, Yang Y (2010) Polyamidoamine dendrimer as a spacer for the immobilization of glucose oxidase in capillary enzyme microreactor. *Anal Biochem* 405:230–235
- Wang Y, Mukherjee T, Lin Q (2006) Systematic modeling of microfluidic concentration gradient generators. *J Micromech Microeng* 16:2128–2137
- Wu Z, Nguyen NT, Huang X (2004) Non-linear diffusive mixing in microchannels: Theory and experiments. *J Micromech Microeng* 14:604–611
- Žnidaršič-Plazl P, Plazl I (2009) Modelling and experimental studies on lipase-catalyzed isoamyl acetate synthesis in a microreactor. *Proc Biochem* 44:1115–1121

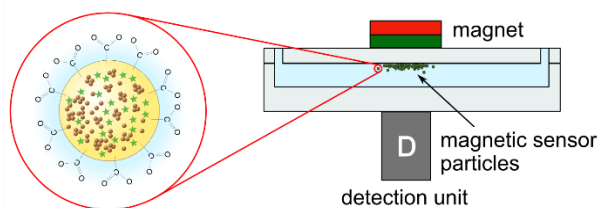
5 Magnetic Optical Sensor Particles: A Flexible Analytical Tool for Microfluidics

Birgit Ungerböck,^a Siegfried Fellingner,^a Philipp Sulzer,^a Tobias Abel^a and Torsten Mayr^{*a}

Published by The Royal Society of Chemistry in *Analyst*, February 2014, Volume 139, pp 2551-2559

DOI: 10.1039/C4AN00169A

Abstract In this study we evaluate magnetic optical sensor particles (MOSePs) with incorporated sensing functionality regarding their applicability in microfluidic devices. MOSePs can be separated from the surrounding solution to form *in-situ* sensor spots within microfluidic channels, while read-out is accomplished outside the chip. These magnetic sensor spots exhibit benefits of sensor layers (high brightness, convenient usage) combined with the advantages of dispersed sensor particles (ease of integration). The accumulation characteristics of MOSePs with different diameters were investigated as well as the *in-situ* sensor spot stability under varying flow rates. Magnetic sensor spots were stable under flow rates specific to microfluidic applications. Furthermore, MOSePs were optimized regarding fiber optic and imaging read-out systems, and different referencing schemes were critically discussed on the example of oxygen sensors. While the fiber optic sensing system delivered precise and accurate results for measurement in microfluidic channels, limitations due to analyte consumption were found for microscopic oxygen imaging. A compensation strategy is provided, which utilizes simple pre-conditioning by exposure to light. Finally, new application possibilities were addressed, being enabled by the use of MOSePs. They can be used for microscopic oxygen imaging in any chip with optically transparent covers, can serve as flexible sensor spots to monitor enzymatic activity or can be applied to form fixed sensor spots inside microfluidic structures, which would be inaccessible to integration of sensor layers.



5.1 Introduction

The integration of luminescent chemical sensors into microfluidics is deemed considerably promising due to their features, which are advantageous for their application in microfluidic environments: they are easy to miniaturize, can be highly sensitive, generally do not consume the analyte under investigation and are relatively low-cost devices compared to other sensing technologies.

A variety of microfluidic devices with integrated luminescent chemical sensors have already been developed. Commonly, the “off-chip-approach” is used, where microscale sensing materials are combined with macro-scale off-chip detection systems¹. The sensing material usually consists of a luminescent indicator dye immobilized in a polymer or sol-gel matrix, allowing adjustment of sensor performance and minimization of interferences with other components of the investigated sample. Due to the flexibility of the matrices, these sensing materials have been integrated into microfluidic environments in different formats such as sensor layers²⁻⁸ or sensor beads⁹⁻¹¹, each of these formats exhibiting advantages as well as disadvantages. Microfluidic chips with integrated sensor layers are user friendly and probably the most convenient way to measure an analyte concentration. However, their integration is an additional step for the microfluidic chip processing. Sensor particles exhibit the advantage of simply adding them to the fluid in the microfluidic channels and therefore their use is a possibility to avoid additional effort of chip development. However, they suffer from disadvantages like low light intensities at low channel depths.

Magnetic optical sensor particles, which have been published by Mistlberger et al.¹², represent a promising strategy to combine the advantages of sensor layers and sensor beads while reducing the disadvantages of each sensor format: on the one hand they can be simply added to the fluid in the microfluidic channels. On the other hand they can be collected inside a microfluidic channel from outside by a magnet, which allows the in-situ generation of sensor spots with brightness independent of microfluidic channel depths. They can be combined with oxygen sensing, biosensing and pH sensing functionalities or be used as magnetic photodynamic therapy agents or stimuli-responsive magnetic optical sensors.

The applicability of magnetic chemical sensor particles to microfluidic devices has not been studied yet, although magnetic forces are utilized in various microfluidic applications¹³ and several reviews have summarized technical approaches of particle trapping^{14,15} or the application of magnetic particles with biological sensing or catalyzing functionalities¹⁶ in microfluidics. One important feature for magnetic particle manipulation is the size of the applied particles: on the one hand, they should be as small as necessary to prevent blocking of microfluidic components and interference with microfluidic flow characteristics. On the other hand, adequate accumulation properties, which strongly depend on the particle size, are absolutely essential for generation and stability of in-situ sensor spots.

A further important evaluation criterion for the application of MOSePs is the reliability of the measurement method. This study investigates this aspect using the example of oxygen sensors. Although a variety of read-out methods for luminescent oxygen sensors exists, read-out of magnetic sensor particles has to be chosen carefully due to highly varying luminescence intensities between different magnetic sensor spots or even within one generated sensor spot. The measurement of luminescence lifetime τ is the most accurate method to reference for these

variations of luminescence intensity. Thus fiber optic read-out is usually performed using lifetime based methods. Imaging applications, however, have been realized applying different measurement methods, mainly for cost reasons. Meier et al. compared different imaging methods including intensity imaging, referenced intensity imaging, luminescence lifetime imaging and ratiometric RGB imaging¹⁷. They stated that lifetime imaging is the most accurate and precise method, while ratiometric imaging using the color channels of a RGB camera represents a less expensive read-out possibility, which is still adequate for certain sensor applications.

The aim of this study is to evaluate the applicability of MOSePs¹² to microfluidic devices. Important features like accumulation characteristics and measuring reliability are investigated. Read-out possibilities of MOSePs are discussed critically by the example of oxygen sensors. Furthermore, new application possibilities of luminescent sensors - enabled through the use of MOSePs - are addressed. Interesting applications of magnetic sensor particles include microscopic imaging in any chip with optically transparent covers, parallel monitoring of multiple analytes, flexible sensor spots or their application to form fixed sensor spots inside microfluidic structures, which would be inaccessible to integration of sensor layers.

5.2 Materials and Methods

5.2.1 Materials

PSMA93 (7% maleic anhydride; $M_w = 224\,000\text{ g}\cdot\text{mol}^{-1}$) and glucose oxidase from *Aspergillus niger* (211 U \cdot mg⁻¹) were obtained from Sigma Aldrich (www.sigmaaldrich.com); L-MNP (polymer-coated magnetite nanoparticles "EMG1300" from MNP-kit) were purchased from FerroTec GmbH (www.ferrotec-europe.de). THF and glucose were obtained from Carl Roth GmbH (www.carl-roth.de); Platinum(II)-5,10,15,20-tetrakis-(2,3,4,5,6-pentafluorophenyl)-porphyrin (PtTFPP), Macrolex Fluorescent Yellow (MFY) and Lumogen Red F300 (LR) were bought from Frontier Scientific (www.frontiersci.com), Simon and Werner GmbH (www.simon-und-werner.de) and Kremer Pigmente (kremer-pigmente.de), respectively; The oxygen-sensitive dyes PtTpTBPF18 and Ir(Cs)2(acac)¹⁹ were synthesized in our laboratory.

For investigation of formation and stability of in-situ generated sensor spots, microfluidic chips were custom ordered from ix-factory (ix-factory.de), each exhibiting one powder blasted microfluidic channel of 15 mm length and different depths and widths. Thin bottom flowcells from Micronit Microfluidics (www.micronit.com) were used for singlet oxygen experiments. Straight channel chips made from PMMA (product code: 01-0174-0138-01) were received from Microfluidic Chip Shop (www.microfluidic-chipshop.com).

NdFeB disc/cylinder and block magnets (material grade N38) were purchased from Chen-Yang Technologies (www.chenyang.de).

5.2.2 Sensing setup and data evaluation

Sensor signals of fiber optic measurements were read out using a Firesting oxygen meter (Firesting, <http://www.pyro-science.com>).

Microscopic oxygen imaging was performed on a Zeiss Axiovert 25 CFL (microscopy.zeiss.com). A blue ultrabright LED with emission maximum at $\lambda = 450\text{ nm}$ (Luxeon lambert emitter, blue, 5 W) was applied as excitation light source and combined with a filter set-up consisting of Linos DT blue, Linos DC blue and Schott OG 515 (www.qioptiq.de; www.schott.com) as the excitation filter,

dichromatic mirror and barrier filter, respectively. Image read-out was performed using a PCO SensiCam (www.pco.de) for rapid lifetime determination (RLD) as described by Moser et al.²⁰ or using an AVT Marlin F 201C color camera (www.alliedvisiontec.com) for ratiometric imaging as already published elsewhere⁴.

Fitting was performed using OriginLab 8.6 (www.originlab.com). Original images were processed to oxygen images by Matlab R2008a (www.mathworks.com) using the respective calibration data.

5.2.3 Preparation of MOSePs

Synthesis of MOSePs was performed via an optimized nano precipitation method described by Mistlberger et al.¹². In a typical synthesis PSMA93 (53.4 mg), L-MNP (10.7 mg) and dye (0.267 mg) were dissolved or dispersed in THF (5.0 mL). This “cocktail” was then added slowly (approximately $1 \text{ mL}\cdot\text{s}^{-1}$) to deionized water (10 mL) under vortexing (1200 min^{-1}). Under a stream of air, THF was evaporated from the mixture over a period of 25 min. Aggregates were removed by filtration through a syringe filter (Rotilabo, 0.8 mm). Different particle sizes were obtained by varying the polymer concentration from 0.2 – 1.2% (w/w) polymer/THF.

Generally particle suspensions were diluted 1:10 for application in microfluidics. Particle sizes were measured with a particle size analyzer Zetasizer Nano ZS.

5.2.4 Sensor characterization

Full calibration of the MOSePs was performed outside the chip by flushing the particle suspension with gaseous air-nitrogen mixtures. For each measurement, they were recalibrated by determining τ_0 and τ_{air} under deoxygenated and fully air-saturated conditions inside the microfluidic chip. As the calibration function shows slightly nonlinear behavior, the full calibration was then adapted to τ_0/τ_{air} obtained from the recalibration.

5.2.5 Microfluidic measurements

For operation under flow the chips were connected to a programmable syringe pump (TSE systems GmbH, www.tse-systems.com).

To study separation of different particle sizes from nano sensor dispersions, a custom ordered microfluidic chip from ix-factory (width: 4000 μm , depth: 300 μm) was filled with aqueous dispersions containing MOSePs with different particle diameters. Light intensities were observed during separation of the particles by a cylindrical magnet from outside the channel.

Separate luminescent spots were generated by using luminescent magnetic nano particles stained with Lumogen Red (3% (w/w) dye/polymer) and Macrolex Yellow (3% (w/w) dye/polymer). A microfluidic channel was filled with the first particle suspension, stained with Lumogen Red (LR), and particles were collected from outside by a magnet, which was placed next to the inlet. After removal of not-collected LR particles, a second magnet was placed next to the other inlet. Drops of a second particle dispersion, stained with Macrolex Yellow (MFY), were disposed at the second inlet to avoid accumulation of the MFY particles at the LR spot. Due to diffusion the particle suspension slowly seeped into the channel and MOSePs were collected by the second magnet. This procedure was repeated multiple times until sufficient luminescent intensity of the MFY spot was achieved ($\sim 10 \text{ min}$). Images of the spots were acquired applying the color camera to determine the quality of separation.

Investigations on application of flexible sensor spots to determine intensity loss during spot movement and to follow the oxidation reaction of β -D-glucose to hydrogen peroxide and δ -D-gluconolactone by molecular oxygen in the presence of glucose oxidase were performed inside a straight channel chip made from PMMA (width: 1000 μm , depth: 200 μm , cover lid thickness: 175 μm). MOSePs stained with PtTpFPTBP (0.5% (w/w)) were collected to form a magnetic sensor spot inside a microfluidic channel and read-out by a miniaturized phase fluorimeter. Two syringes containing a 20 $\text{g}\cdot\text{L}^{-1}$ glucose solution and a 0.05 $\text{g}\cdot\text{L}^{-1}$ GOX solution were mounted on syringe pumps (TSE systems; model 540060; <http://www.tse-systems.com/>) and connected to the microfluidic channel with a T-shaped connection piece. During fluid flow of 60 $\mu\text{L}\cdot\text{min}^{-1}$ (30 $\mu\text{L}\cdot\text{min}^{-1}$ per syringe) the magnetic sensor spot and the optic fiber were moved along the channel (Figure 5.1 E).

To integrate fixed sensor spots into a microfluidic channel made from glass, powder blasted microfluidic chips were filled with a MOSePs stained with PtTpFPTBP (0.5% (w/w)) mixed with THF (1:1). Different magnets were used to collect the swollen polymer particles. After several hours single sensor spots as well as sensor layers were formed. Full calibration of one sensor spot was performed inside the microfluidic chip by flushing it with gaseous air–nitrogen mixtures. For obtaining aqueous measuring curves the chip was flushed with deoxygenated and air-saturated water. Deaerated water was obtained by deoxygenation reaction of glucose (10 $\text{mg}\cdot\text{mL}^{-1}$) with oxygen in the presence of glucose oxidase (0.05 $\text{mg}\cdot\text{mL}^{-1}$).

5.3 Results and Discussion

5.3.1 Concept of magnetic sensor particles in microfluidics

The use of luminescence sensing methods in combination with magnetic bead manipulation paves the way for an advanced application of luminescence sensors in microfluidics. MOSePs can be separated from a magnetic particle dispersion to form *in-situ* sensor spots – including the possibility to generate multiple spots inside one device – or can be transported along a microfluidic channel.

The concept of MOSePs in microfluidics is presented in Figure 5.1. Magnetite nano particles and luminescent dye molecules are incorporated into a PSMA nano particle (Figure 5.1 (A)). These particles can be collected by a magnet, which is placed above a microfluidic channel, to form a magnetic sensor spot, while sensor signals are read-out from the opposite side of the chip (Figure 5.1 (B)). This assembly allows fiber optic as well as imaging sensor read-out. Fiber optic assemblies have also been realized with magnetic adapters, which allow read-out and separation from the same side²¹. However, for microfluidic applications it turned out to be more convenient to use the two-sided separation/read-out approach because of limited available space.

Figure 5.1 (C) shows a photo series of the separation of MOSePs from a homogeneous particle dispersion in water inside a microfluidic channel with a magnet placed underneath the chip. The particles are usually separated from the surrounding solution at zero fluid flow within 10 min. **In-situ** formed sensor spots exhibited around 10 times higher emission intensities than particle dispersions before separation was induced. After separation the surrounding solution showed no luminescence emission, indicating, that a negligible portion of the magnetic particles was lost during this process. The shape of a sensor spot can be adjusted by the choice of the magnet shape reaching from small single sensor spots to sensor lines or covering the whole channel area for

imaging applications. Particles are concentrated at regions of high magnet field density. Taking the added volume of the particles, an ellipsoidal shape of the generated spots and sphere packing into account, the height of the spots was calculated to range between 5 and 10 μm . Computational Fluid Dynamics simulation studies revealed that the formed sensing spots do not cause turbulences (†, S4).

MOSePs can also be used to form multiple sensor spots, e.g. for different analytes inside one microfluidic channel. Figure 5.1 (D) shows the successful generation of separate luminescent spots. Their color values were recorded applying the color camera to determine the quality of separation. These color values indicate very good separation of the two spots. In this way MOSePs can be used to generate magnetic sensor spots, which are sensitive to different analytes or which expand the dynamic range of optical sensors (e.g. pH or temperature sensing particles or particles with higher oxygen sensitivity).

Magnetic sensor spots can be used as flexible sensor spots, because these spots follow the movement of a magnet outside a microfluidic channel after particle separation (Figure 5.1 E). A cylindrical magnet was slowly moved along the channel length at the backside of the microfluidic chip (total duration around 3 s). This allows for example to study the concentration of an analyte along a microfluidic channel. The perpetuation of spot size and of measurable intensity is decreased with increasing velocity of spot movement. Figure 5.2 (A) presents the relative intensity loss, when a magnetic sensor spot is moved along a 5 cm distance in a microfluidic channel at varying spot movement velocities.

Through providing these interesting features MOSePs enlarge the application possibilities of luminescent sensors: they can be used inside an arbitrary microfluidic chip with optically transparent covers, enable the formation of multiple sensor spots inside microfluidics, can be used as flexible sensor spot inside one microfluidic channel or can be fixed after their integration to any position where information about a certain analyte is needed. Microfluidic applications of MOSePs will be discussed later.

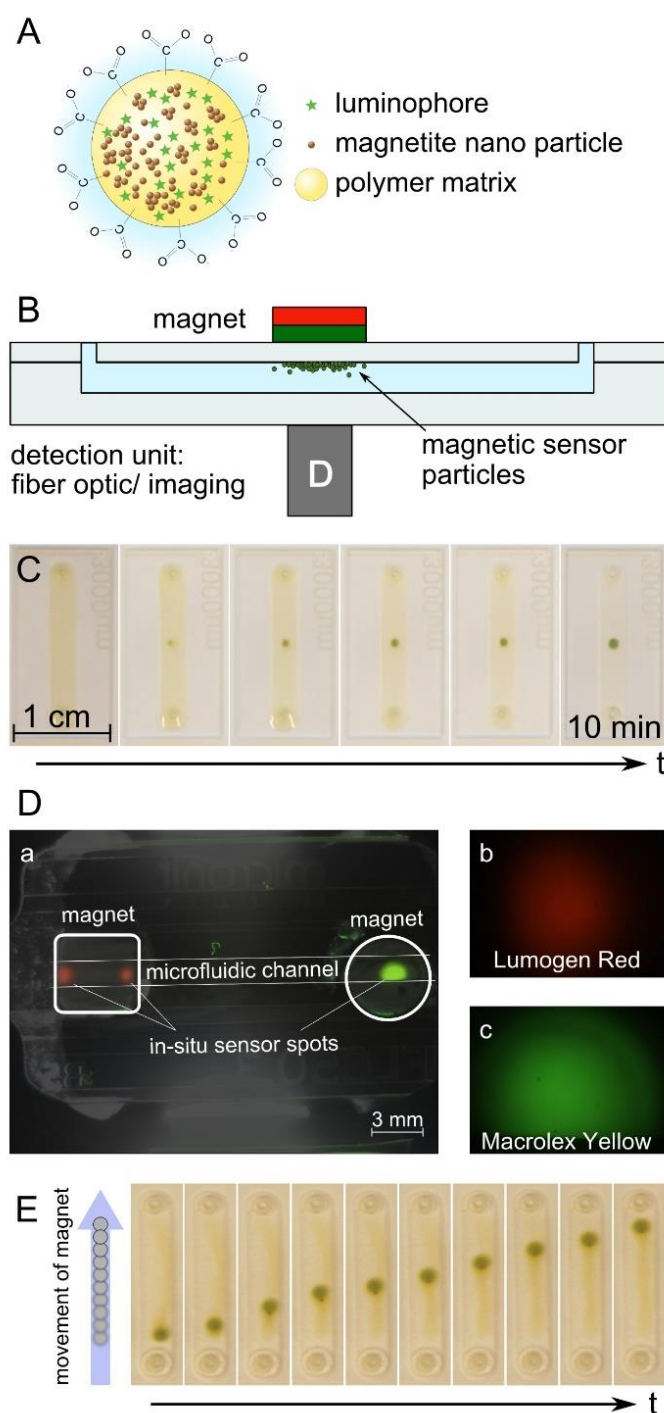


Figure 5.1. Concept of MOSePs in microfluidics. (A) Scheme of a magnetic particle with incorporated luminophores (adapted from Mistlberger et al.¹²). (B) Schematic cross section of a chip with separated MOSePs. (C) Time course of particle separation. (D) Formation of multiple nano particle spots inside one microfluidic channel. (E) Movement of a magnetic sensor spot along a microfluidic channel.

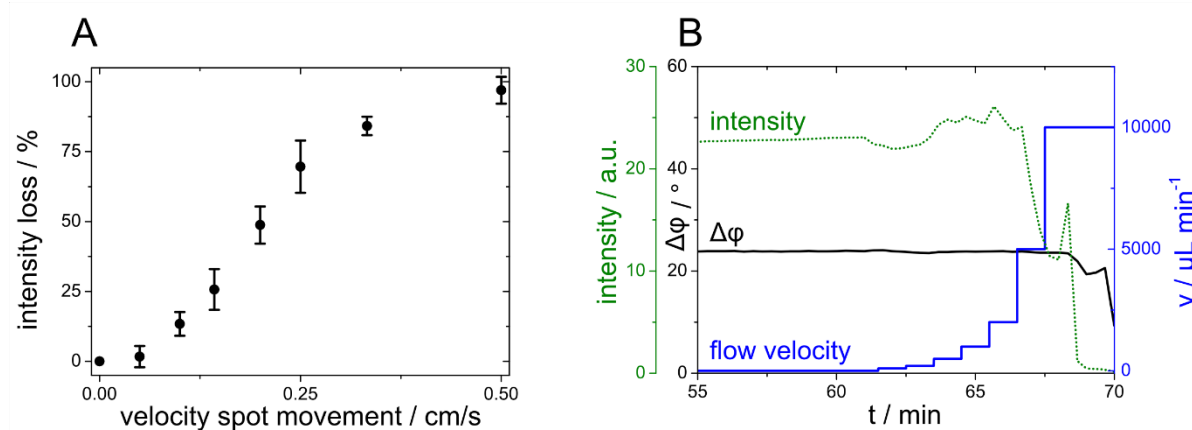


Figure 5.2. (A) Intensity loss during movement of a magnetic sensor spot along a 5 cm distance in a microfluidic channel at varying spot movement velocities. The error bars show standard deviations derived from 5 independent measurements. (B) Stability of a magnetic sensor spot to different flow velocities. The experiment showed reliably measurable phase shifts up to 5 ml·min⁻¹ (Δ 287 cm·min⁻¹).

5.3.2 Separation speed and stability of *in-situ* sensor spots

Separation speed and stability of *in-situ* sensor spots inside microfluidic channels play a critical role regarding their applicability in microfluidics, because these features determine the time for generating a magnetic sensor spot and influence the maximum flow velocity inside microfluidic channels.

5.3.2.1 Separation speed

Theoretically, separation behavior is governed, inter alia, by the diameter of such a particle due to the directly proportional relationship between the velocity of a magnetic particle and the volume of this particle.

To study separation of different particle sizes from nano sensor dispersions, a microfluidic channel was filled with aqueous dispersions containing MOSePs of different hydrodynamic diameters. Light intensities were observed during separation of the particles by a cylindrical magnet from outside the channel. As expected from theory, the velocity of particles showed to be proportional to the particle size. Particles with $z\text{-av} = 159$ nm showed higher separation speed than particles with $z\text{-av} = 110$ nm. Exemplary intensity curves illustrating the separation behavior of different particle sizes from a MOSeP dispersion are presented in the supporting information (†, S1).

This finding reveals that choosing a suitable particle size is an important factor leading to an optimized sensing set-up. On the one hand, adequate accumulation properties are absolutely essential for generation and stability of *in-situ* sensor spots. These properties can be enhanced by increasing the particle diameter. On the other hand, magnetic particles should be as small as necessary to prevent blocking of microfluidic components and interference with microfluidic flow characteristics. Also for imaging applications it is important to have particles with a size smaller than the resolution of the imaging set-up. For this study MOSePs with $z\text{-av} = 159$ nm were used for further application in microfluidic channels.

5.3.2.2 Stability of magnetic sensor spots

Magnetic sensor spots should be stable at flow rates typically applied in microfluidic applications ranging from $v = 6\text{--}60\text{ cm}\cdot\text{min}^{-1}$ ²². Otherwise sensor particles are washed out of the chip during measurements.

The in-situ formed sensor spots displayed suitable stability during investigation of different fluid velocities. In Figure 5.2 (B) a fluid flow with increasing flow velocity, starting from $100\text{ }\mu\text{L}\cdot\text{min}^{-1}$ ($\cong 5.74\text{ cm}\cdot\text{min}^{-1}$), was applied to a microfluidic channel with a magnetic sensor spot. The flow velocity was increased to $2\text{ mL}\cdot\text{min}^{-1}$ ($\cong 115\text{ cm}\cdot\text{min}^{-1}$) without loss of luminescence intensity – indicating excellent stability of the sensor spot. When fluid velocity was then further increased to $5\text{ mL}\cdot\text{min}^{-1}$ ($\cong 287\text{ cm}\cdot\text{min}^{-1}$), a drop of signal intensity was observed, whereas the measured phase shift $\Delta\varphi$ was still stable (discussed later in detail). Fluid flows of $10\text{ mL}\cdot\text{min}^{-1}$ ($\cong 574\text{ cm}\cdot\text{min}^{-1}$) led to complete elution of the in-situ-formed sensor spot.

It is important to note, that separation and sensor spot stability not only depend on particle size, but also on magnetic field strength. This parameter can be influenced by choice of the magnet and by the thickness of the microfluidic cover lid influencing the distance between magnet and formed sensor spot²³, but was not investigated in detail during this study.

5.3.3 Sensor read-out

Several considerations have to be addressed in finding the most suitable sensing set-up for the respective measurement requirement. First, in some cases information about averaged values inside a microfluidic channel, in other cases more detailed information about the spatial distribution of the analyte may be needed. Second, MOSePs have to be adapted to the respective measurement requirement through the choice of the indicator dye. Third, the measurement method has to be chosen carefully, because the use of MOSePs entails a particular challenge due to highly varying luminescence intensities between different magnetic sensor spots or even within one generated sensor spot. Other considerations include a specification concerning accuracy and precision and the prize of the sensor set-up. A variety of measurement methods for luminescent sensors exists: in general, the measurement of luminescence lifetime is the most reliable method to reference for variations of luminescence intensity. However, luminescence lifetime imaging systems are expensive. Alternatively, ratiometric imaging using the color channels of a color CCD-camera is less expensive, yet less accurate, read-out possibility. To show the flexibility of the presented analytical tool and to discuss different referencing schemes regarding their combination with MOSePs, magnetic particles for fiber optic read-out and imaging applications using different referencing possibilities were prepared and optimized in this study. Stern-Volmer plots and characteristic calibration data for different oxygen sensing systems are presented in the supporting information (†, S2 and S3).

5.3.3.1 Fiber optic read-out

The fiber optic read-out represents a straightforward method for automatable oxygen sensing without the need for spatial resolution of oxygen values in a microscopic range. A benzoporphyrine dye (PtTpFPTBP) was chosen for fiber optic read-out, which is known for high photostability and phosphorescence emission in the NIR spectrum¹⁸. It is compatible with a commercially available read-out system, which is based on lifetime measurement using the frequency domain method. The luminophore is excited by a sinusoidal modulated light source and

the phase shift $\Delta\phi$ between excitation and emission, depending on the oxygen concentration, is recorded. The measured phase shift remains stable even if luminescence intensity exhibits high fluctuations as already shown in Figure 5.2 (B). The spectral characteristics of benzo-porphyrine dyes (absorption of red light and emission in the NIR) especially fit the needs for biological applications because of the increased penetration depth in high scattering media such as cell cultures and because of reduced background due to lower scattering and autofluorescence.

5.3.3.2 Microfluidic imaging

High varying intensities within one sensing spot due to varying numbers of luminescent particles make intensity based imaging insufficient. Thus MOSePs were combined with well-established referencing schemes – rapid lifetime determination (RLD) imaging or ratiometric RGB imaging. While RLD imaging is characterized by its precision and insensitivity to disturbances like light scattering, inhomogenous illumination and dye bleaching, RGB imaging setups are incomparably cheap and simple, but limited to suppress certain interferences.

RLD imaging employing the indicator dye $(\text{Ir}(\text{Cs})_2(\text{acac}))^{19}$ is recommended for short-term application with the need for high emission intensities due to the exceptional brightness but low photostability of $\text{Ir}(\text{Cs})_2(\text{acac})$. Particles employing PtTFPP and MFY were chosen for long-term RLD or RGB imaging applications, providing an adequate photostability with still high brightness due to the principle of light harvesting²⁴. The characteristics of this sensor chemistry and the choice of the dye system have already been discussed elsewhere⁴.

In order to address the reliability of lifetime imaging and ratiometric imaging, a magnetic sensor spot was generated inside a microfluidic channel and investigated using lifetime imaging and ratiometric imaging. Figure 5.3 provides the results derived from this investigation. It is important to note, that after preconditioning the MOSePs as described later, the particles had to be recalibrated for both RLD (lifetime) imaging as well as RGB (ratiometric) imaging by determining

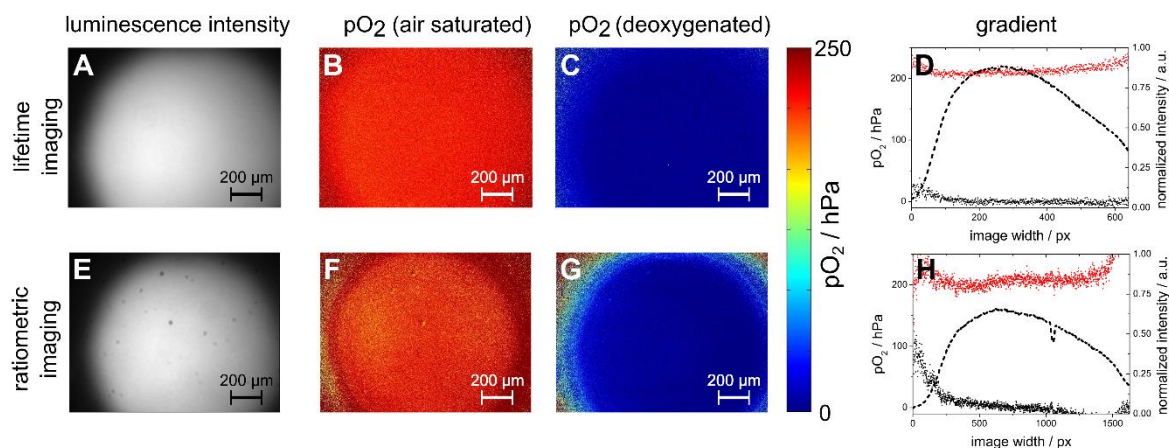


Figure 5.3. Comparison of referencing quality between lifetime imaging and ratiometric imaging; Images of a deoxygenated luminescent magnetic spot inside a microfluidic channel employing the principle of light harvesting were recorded using (A) - (D) RLD (lifetime) imaging and (E) - (H) RGB imaging. (A) and (E) show the intensity images, (B) and (F) the referenced air saturated images and (C) and (G) the referenced deoxygenated images. (D) and (H) display the horizontal image gradients of images (A) - (C) and (E) - (G) respectively.

τ_0 and τ . RLD (lifetime) imaging yielded homogeneous pO_2 images for air saturated and deoxygenated images. Only at regions with very low emission intensities stronger deviations from expected results can be observed (Figure 5.3 (D)). Ratiometric imaging yielded pO_2 images with stronger deviations than lifetime imaging over the image area (Figure 5.3 (H)). However, ratiometric imaging represents a simple and cheap method, which can be used in cases when the differences in oxygen levels are big enough to be determined by this method.

5.3.4 Pre-treatment for microscopic imaging applications

Reduced sample volume and hence low number of analyte molecules inside a microfluidic channel lead to important aspects for microfluidic sensing devices: as already stated in the introduction, optical sensors generally do not consume the analyte under investigation. However, highly reactive singlet oxygen is produced during the dynamic quenching process. Subsequent oxidation of sensor matrix components can lead to oxygen consumption severely affecting the oxygen concentration inside microfluidics. In our case this effect is further intensified by the high excitation light densities produced by the fluorescent microscope, leading to an increased production of singlet oxygen.

Actually, our investigations on oxygen consumption of a magnetic sensor spot employing the light harvesting system (PtTFPP and MFY) showed, that luminescence lifetime for air saturated DI water was 15 to 20 μs higher than expected from the calibration data recorded outside a microfluidic chip. It further increased during the measurement although no change of oxygen concentration was expected. Moreover, the lifetime images showed higher lifetimes in the middle of one image with decreasing lifetimes towards image areas with lower particle densities (Figure 5.4 (B)). When compared to particles homogeneously dispersed inside the microfluidic chip, the described effect was further intensified by concentrating the MOSePs to one sensor spot. A

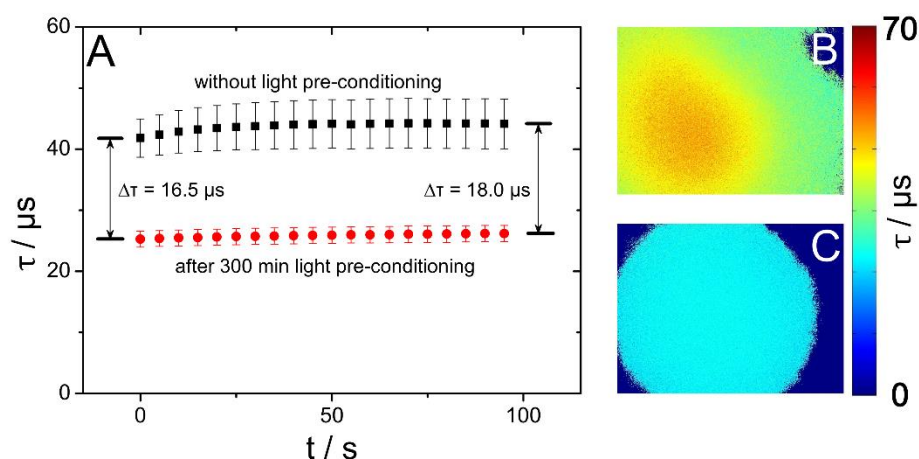


Figure 5.4. Oxygen depletion during microscopic oxygen imaging inside a microfluidic chip filled with air saturated DI water. (A) Magnetic sensor spots without pre-conditioning delivered unexpected high lifetimes ($\Delta\tau = 16.5 \mu\text{s}$), which further increased during the investigation. The error bars show the standard deviation of all pixel lifetimes of the image area. (B) Microscopic oxygen imaging of a magnetic sensor spot without pre-conditioning showed higher lifetimes in the middle of one image with decreasing lifetimes towards image areas with lower particle densities. (C) Microscopic oxygen imaging of a magnetic sensor spot with pre-conditioning delivered homogenous distributed lifetime images with invariant values over the whole sensing spot area.

possible explanation for this might be that the accumulation of particles leads to an increased local production of singlet oxygen as well as reduced diffusion of oxygen to the inner part of the collected spot.

Enko et al.²⁵ suggest to reduce oxygen consumption via deactivation of singlet oxygen by adding physical quenching additives. However, the high volatility and water solubility make additives useless for nano particles. To make magnetic particles applicable to microfluidic imaging, they were pre-conditioned by continuous irradiation with a blue LED in order to saturate reactive binding sites of the polymer. As a consequence singlet oxygen can no longer react with these binding sites and returns to its ground state again without being consumed. After 300 min pre-conditioning the same investigation showed stable luminescence lifetime values over time (Figure 5.4 (A)) and homogeneous lifetime images with invariant values over the whole sensing spot area (Figure 5.4 (C)). The pre-conditioning also led to a decreased sensing sensitivity of approximately 75% compared to calibration data before pre-conditioning presented in the supporting information (†, S2 and S3). This means, that a recalibration after this procedure is necessary.

One general issue, which emerges from these findings, is that microfluidic oxygen measurements should be conducted carefully with regard to these outcomes, especially when MOSePs are applied in microfluidic channels and under extreme conditions with high light intensities on a fluorescence microscope. Whenever possible, excitation time and intensity should be reduced to a necessary minimum value to reduce production of singlet oxygen and to prevent subsequent reaction of singlet oxygen.

5.3.5 Microfluidic measurements and further applications

5.3.5.1 Online monitoring inside microfluidic channels

Magnetic nano particles enable measurements inside any microfluidic chip with optically transparent covers. The performance of an in-situ formed sensor spot was investigated for fiber optic measurement in Figure 5.5 (A). A microfluidic chip equipped with a cylindrical magnet was first filled with a MOSeP dispersion. Magnetic particles were collected for 60 min. Then deoxygenated and air saturated DI water was pumped through the microfluidic chip alternately at different flow rates. Figure 5.5 (A) shows a measurement inside a microfluidic chip at $100 \mu\text{L}\cdot\text{min}^{-1}$ and $200 \mu\text{L}\cdot\text{min}^{-1}$. The response curve shows excellent signal reversibility. Calculated $p\text{O}_2$ levels are stable although the signal intensity showed high deviations. The relatively long apparent response time can be explained by the time needed to equilibrate the whole chip set-up, that means to exchange the whole liquid in the connection tubing and the microfluidic channel. Hence, the equilibration time decreases with an increasing flow rate. Figure 5.5 (B) presents the results obtained for microfluidic lifetime imaging at $100 \mu\text{L}\cdot\text{min}^{-1}$. The dots represent averaged values over the entire sensing spot area. The different apparent response time of Figure 5.5 (B) compared to Figure 5.5 (A) (left two peaks) can be traced back to different microfluidic set-ups including different chip geometries and connection tubing causing different adsorption of deoxygenizing reagents to channel and tubing walls.

In this context it should be emphasised, that the apparent response times in Figure 5.5 do not display the actual sensor particle or sensor spot response time. The response time of a particle spot to a rapid change in oxygen concentration was reported by Mistlberger et al.¹² to have a t_{90} of

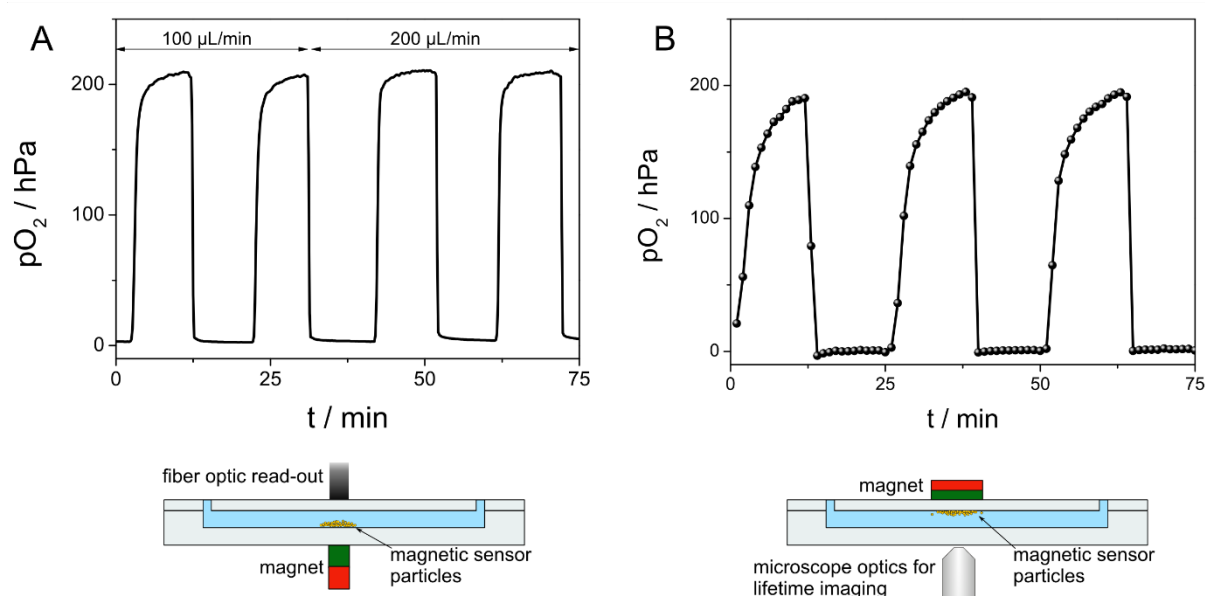


Figure 5.5. Measurement inside a microfluidic chip applying (A) fiber optic and (B) lifetime read-out. Magnetic sensor spots were formed before the measurement was started. Deoxygenated and air-saturated water was pumped through the microfluidic chip alternately. Different apparent response times were observed for fiber optic and imaging read-out due to different microfluidic set-ups.

1.4 s, while they assumed the response of single particles to be much faster. Thus magnetic sensor spots can be considered to respond in real-time.

5.3.5.2 Spatially resolved respiratory cell activity

MOSePs containing $\text{Ir}(\text{Cs})_2(\text{acac})$ as oxygen indicator were used for imaging of cell respirometry within a microfluidic chip. 20 μL magnetic particle suspension were inserted into the chip and collected by a magnet from outside before the chip was inoculated with *E. coli*. Luminescent signals were read out by application of lifetime imaging. Figure 5.6 (A) shows a microfluidic channel with a magnetic sensor layer. Dark spots at the luminescent intensity image inside the microfluidic channel (Figure 5.6 (A) inlay) mark areas of *E. coli* cell aggregates. The pO_2 image shows lowest oxygen levels at areas where cell aggregates are located.

5.3.5.3 Flexible sensor spots for use in microreactors

Flexible sensor spots can be used to study the concentration of an analyte along a microfluidic channel. This is especially interesting for microfluidic reactions, where the analyte is consumed over the channel length, with the channel length corresponding to reaction time.

Figure 5.6 (B) shows the principle of a flexible sensor spot applied in a microfluidic channel. When the magnet outside a microfluidic channel is moved along the channel length, the magnetic sensor spot follows the movement of the magnet inside the channel from one inlet to the other. The oxidation reaction of β -D-glucose to hydrogen peroxide and δ -D-gluconolactone by molecular oxygen in the presence of glucose oxidase was followed by measuring the pO_2 along the channel length by applying a flexible sensor spot. A glucose solution and a solution containing glucose oxidase were mixed short before the microfluidic inlet. Figure 5.6 (B) presents the obtained

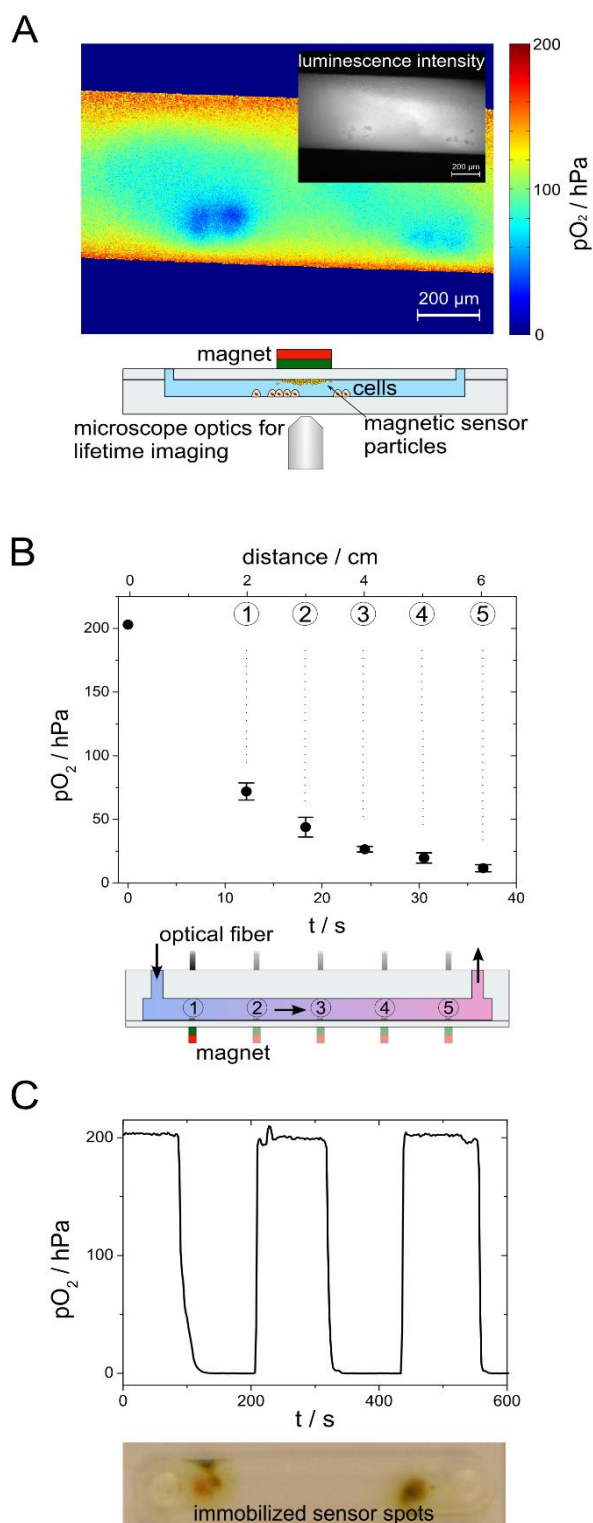


Figure 5.6. Applications of MOSePs in microfluidics; (A) pO_2 image of E.coli in a microfluidic channel of a PDMS chip applying luminescent magnetic nano sensor particles. (B) Application of flexible sensor spots with a concentration gradient along the channel length. The error bars show the standard deviation derived from 3 independent measurements (C) Response curve of an immobilized sensor spots inside a microfluidic device.

measured oxygen concentrations at distances $d = 2, 3, 4, 5$ and 6 cm from mixing area (\triangleq retention time of 12.2, 18.3, 24.4, 30.5 and 36.6 s).

5.3.5.4 Generation of fixed sensor spots

MOSePs can also be used to form fixed sensor spots inside microfluidic structures, which would be inaccessible to integration of sensor layers. This can be especially helpful, when microfluidic structures made of glass are used. The abrasive methods, which are used for microfluidic glass structuring or as bonding procedures, would destroy the sensing chemistry of sensor spots or layers integrated into microfluidic structures during fabrication of a microfluidic device.

Fixed sensor spots were integrated into a microfluidic channel made from powder blasted microfluidic glass chips. The addition of THF to a MOSeP suspension (1:1) leads to swelling of the particles. These particles are transferred into a microfluidic chip and magnetically separated. The magnetic force acting on soft particle shells leads to particle adhesion to the channel wall. Different magnets were used to form single sensor spots as well as sensor layers, which can then be used without magnetic support.

Fixed sensor spots showed to behave similar to flexible sensor spots. A measuring curve with air saturated and deoxygenated water was recorded (Figure 5.6 (C)), exhibiting shorter response times compared to diffusion limited magnetic sensor spots. Furthermore, fixed sensor spots were stable beyond flow velocities of $2\ 000\ \text{cm}\cdot\text{min}^{-1}$.

5.4 Conclusion

Magnetic separation of MOSePs leads to the generation of in-situ sensor spots with different shapes. These sensor spots can be moved along microfluidic channels following the position of a magnet outside the channel. An investigation of magnetic sensor spot stability towards different flow velocities showed reliable lifetime measurements up to flow velocities of $5\ \text{mL}\cdot\text{min}^{-1}$ ($\triangleq 287\ \text{cm}\cdot\text{min}^{-1}$). Summing up, the stability of in-situ formed sensor spots showed to be sufficiently stable at flow rates typically applied in microfluidic applications.

MOSePs can be easily adapted to the respective measurement requirement. They enable fiber optic as well as imaging read-out by adapting luminescent indicators and referencing schemes to the respective measurement requirement. Fiber optic oxygen measurements as well as oxygen imaging inside microfluidic channels turned out to be straightforward. The measurement of luminescence lifetime was shown to be the most accurate and precise methods to reference for these variations, while for imaging applications ratiometric imaging using the color channels of a RGB camera may be the less expensive but still adequate read-out possibility.

However, microscopic oxygen imaging with high excitation light intensities must be performed with caution paid to singlet oxygen production and subsequent reactions, which can lead to underestimated pO_2 levels. Nevertheless, microscopic oxygen imaging was also reliably performed after preconditioning of the particle dispersion by irradiation with light.

MOSePs were also demonstrated to serve as useful tool for a variety of new and flexible applications inside microfluidic devices. They can be used for microscopic oxygen imaging applied in microfluidic cell culture, to form multiple separated sensor spots, e.g. for different analytes inside one microfluidic channel, serve as flexible sensor spots to study analyte gradients along a

microfluidic channel or can be used to form fixed sensor spots inside microfluidic structures, which would otherwise be inaccessible to integration of sensor layers.

All these findings suggest that in general MOSePs are an interesting tool to be applied in microfluidic environments and can facilitate further integration and new applications of luminescent sensors in this research field.

5.5 Acknowledgements

Financial support by the European Union FP7 Project BIOINTENSE – Mastering Bioprocess integration and intensification across scales (Grant Agreement Number 312148) is gratefully acknowledged.

5.6 References

^a Applied Sensors, Institute of Analytical Chemistry and Food Chemistry, Graz University of Technology, Stremayrgasse 9/3, 8010 Graz, Austria. Fax: +43 (0) 316 873 32502; Tel: +43 (0) 316 873 32504; E-mail: torsten.mayr@tugraz.at

† Electronic Supplementary Information (ESI) available: See DOI: 10.1039/c4an00169a

- 1 B. Kuswandi, Nuriman, J. Huskens, and W. Verboom, *Anal. Chim. Acta*, 2007, **601**, 141–155.
- 2 V. Nock, R. J. Blaikie, and T. David, *Lab. Chip*, 2008, **8**, 1300–1307.
- 3 H. Zhu, X. Zhou, F. Su, Y. Tian, S. Ashili, M. R. Holl, and D. R. Meldrum, *Sens. Actuators B Chem.*, 2012, **173**, 817–823.
- 4 B. Ungerböck, V. Charwat, P. Ertl, and T. Mayr, *Lab. Chip*, 2013.
- 5 L. Gitlin, C. Hoera, R. J. Meier, S. Nagl, and D. Belder, *Lab. Chip*, 2013.
- 6 S. Jezierski, D. Belder, and S. Nagl, *Chem. Commun.*, 2013, **49**, 904–906.
- 7 A. P. Vollmer, R. F. Probst, R. Gilbert, and T. Thorsen, *Lab. Chip*, 2005, **5**, 1059–1066.
- 8 R. H. W. Lam, M.-C. Kim, and T. Thorsen, *Anal. Chem.*, 2009, **81**, 5918–5924.
- 9 M. A. Acosta, P. Yemele-Leki, Y. V. Kostov, and J. B. Leach, *Biomaterials*, 2009, **30**, 3068–3074.
- 10 B. Ungerböck, A. Pohar, T. Mayr, and I. Plazl, *Microfluid. Nanofluidics*, 2012.
- 11 D. Aigner, B. Ungerböck, T. Mayr, R. Saf, I. Klimant, and S. M. Borisov, *J. Mater. Chem. C*, 2013, **1**, 5685–5693.
- 12 G. Mistlberger, K. Koren, E. Scheucher, D. Aigner, S. M. Borisov, A. Zankel, P. Pölt, and I. Klimant, *Adv. Funct. Mater.*, 2010, **20**, 1842–1851.
- 13 N. Pamme, *Lab. Chip*, 2006, **6**, 24.
- 14 M. A. M. Gijs, *Microfluid Nanofluid*, 2004, **1**, 22–40.
- 15 J. Nilsson, M. Evander, B. Hammarström, and T. Laurell, *Analytica Chimica Acta*, 2009, **649**, 141–157.
- 16 M. A. M. Gijs, F. Lacharme, and U. Lehmann, *Chem. Rev.*, 2010, **110**, 1518–1563.
- 17 R. J. Meier, L. H. Fischer, O. S. Wolfbeis, and M. Schäferling, *Sens. Actuators B Chem.*, 2013, **177**, 500–506.
- 18 S. M. Borisov, G. Nuss, W. Haas, R. Saf, M. Schmuck, and I. Klimant, *J. Photochem. Photobiol. Chem.*, 2009, **201**, 128–135.
- 19 S. M. Borisov and I. Klimant, *Anal. Chem.*, 2007, **79**, 7501–7509.
- 20 C. Moser, T. Mayr, and I. Klimant, *Anal. Chim. Acta*, 2006, **558**, 102–109.
- 21 G. Mistlberger, P. Chojnacki, and I. Klimant, *J. Phys. Appl. Phys.*, 2008, **41**, 085003.
- 22 H. A. Stone, A. D. Stroock, and A. Ajdari, *Annu. Rev. Fluid Mech.*, 2004, **36**, 381–411.
- 23 P. Zhang, S. Park, and S. H. Kang, *Chem. Commun.*, 2013, **49**, 7298–7300.
- 24 T. Mayr, S. M. Borisov, T. Abel, B. Enko, K. Waich, G. Mistlberger, and I. Klimant, *Anal. Chem.*, 2009, **81**, 6541–6545.
- 25 B. Enko, S. M. Borisov, J. Regensburger, W. Bäuml, G. Gescheidt, and I. Klimant, *J. Phys. Chem. A*, 2013, **117**, 8873–8882.

5.7 Electronic Supplementary Information

S1

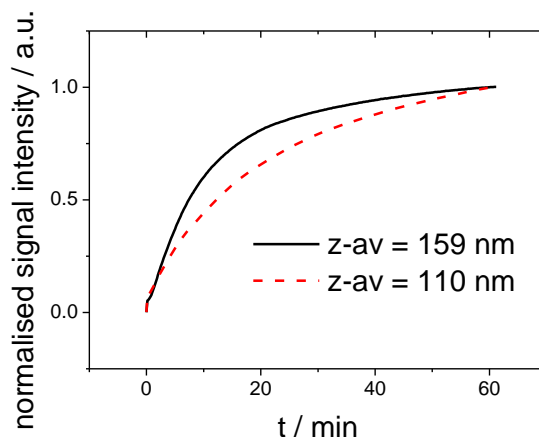


Figure S1. Separation behavior of different particle sizes from a MOSeP dispersion. The graph illustrates observed signal intensities of MOSePs of varying particle diameters.

S2

Figure S2 provides calibration data (Stern-Volmer plots) for four different oxygen sensing systems: (■) PtTpFPTBP (fiber optic read-out), (Δ) Ir(C_s)₂(acac) (lifetime imaging) (o) PtTFPP and MY (lifetime imaging) and (\blacktriangledown) PtTFPP and MY (RGB imaging). Table 1 summarizes characteristic calibration data, obtained by applying an adapted version of the two-site model of Demas et al.¹ for these sensing systems. Further information on sensor characterization can be found in previously published literature by Mistlberger et al.²

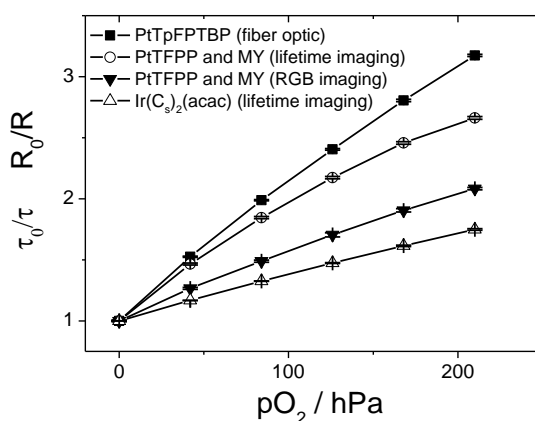


Figure S2. Calibration plots for MOSePs applying four different oxygen sensing systems for oxygen monitoring from 0-100% air saturation: (■) PtTpFPTBP (fiber optic read-out), (Δ) Ir(C_s)₂(acac) (lifetime imaging) (o) PtTFPP and MY (lifetime imaging) and (\blacktriangledown) PtTFPP and MY (RGB imaging). The error bars show experimental data from 3 subsequent measurements.

S3

Table 1 Calibration data of luminescent magnetic nano sensor particles for fiber optic read-out and imaging applications for oxygen monitoring from 0-100% air saturation.

read-out	sensor dye ([% (w/w)])	τ_0/τ / R_0/R_{air}	K_{SV} [hPa ⁻¹]	f_1
fiber optic	PtTpFPTBP (0.5)	3.17 ± 0.01	0.01408 ± 0.00018	0.916 ± 0.003
lifetime imaging	Ir(C _s) ₂ (acac) (1.5)	1.75 ± 0.01	0.00486 ± 0.00002	0.847 ± 0.002
lifetime imaging	PtTFPP (1.5) and MY (3)	2.66 ± 0.01	0.01506 ± 0.00037	0.824 ± 0.006
RGB imaging	PtTFPP (1.5) and MY (3)	2.08 ± 0.01	0.00769 ± 0.00015	0.842 ± 0.008

S4

Computational Fluid Dynamics simulation studies using ANSYS CFX® software and Solid works revealed that the formed sensing spots do not cause turbulences. Figure 3 shows the velocity profile inside a microchannel with integrated magnetic sensor spots ($d = 2$ mm) for sensor spot heights of (A) $10 \mu\text{m}$ (realistic dimension) and (B) $200 \mu\text{m}$ (for comparison). A sensing spot with $10 \mu\text{m}$ spot height exhibited homogeneous velocity profiles across the whole microfluidic channel length and width with minimal variations of flow velocity. Computational Fluid Dynamics simulation studies showed that the flow runs around the sensor spot smoothly even for sensor spots with $200 \mu\text{m}$ height, although the simulation revealed inhomogeneous velocity profiles across the microfluidic channel length and width.

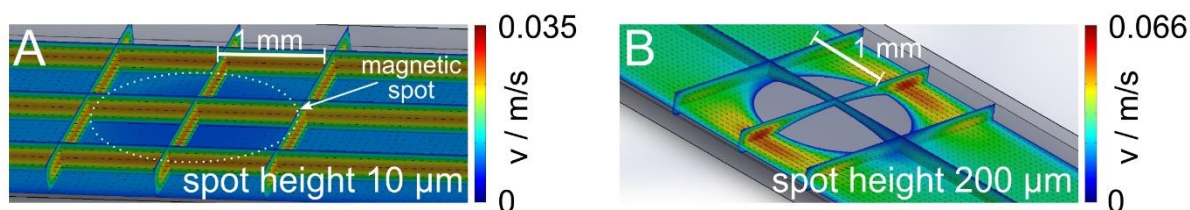


Figure S3. Simulation results for flow and velocity profiles in microfluidic channels (height = $300 \mu\text{m}$, width = 3 mm) at a fluid flow of $1 \text{ mL} \cdot \text{min}^{-1}$ with integrated magnetic sensor spots ($d = 2 \text{ mm}$) for sensor spot heights of (A) $10 \mu\text{m}$ and (B) $200 \mu\text{m}$.

References

- 1 J. N. Demas, B. A. DeGraff, and W. Xu, *Anal. Chem.*, 1995, **67**, 1377–1380.
- 2 G. Mistlberger, K. Koren, E. Scheucher, D. Aigner, S. M. Borisov, A. Zankel, P. Pötl, and I. Klimant, *Adv. Funct. Mater.*, 2010, **20**, 1842–1851.

6 Opto-chemical sensors based on integrated ring-shaped organic photodiodes: progress and applications

Torsten Mayr^a, Tobias Abel^a, Birgit Ungerböck^a, Martin Sagmeister^b, Verena Charwat^c, Peter Ertl^c, Elke Kraker^b, Stefan Köstler^b, Andreas Tschepp^b, Bernhard Lamprecht^b

Published in Proc. SPIE 8479, Organic Semiconductors in Sensors and Bioelectronics V, October 2012

DOI: 10.1117/12.932285

Abstract The recent advances on a monolithically integrated sensor platform based on ring-shaped organic photo detectors are presented. Various sensing chemistries based on luminescence for the detection of a number of parameters such as oxygen, carbon dioxide, humidity and pH in gaseous and/or liquid phase were investigated and optimized to the requirements of the sensor platform. Aiming on practical application, the need and methods to reference luminescence signals are evaluated including two wavelength rationing and lifetime measurements. Finally, we will discuss potential applications of the platform and present a microfluidic chip containing an array of integrated sensor spots and organic photodiodes.

6.1 Introduction

Optical chemical sensors have found wide-ranging applications in chemical, environmental, and biological analysis and clinical diagnostics.[1,2] An increasing trend goes towards monolithic integration of sensor systems, where optical, optoelectronic and electronic elements (e.g. light detectors and/or sources) are assembled into one functional unit fabricated on the same substrate in order to build “lab-on-a-chip” systems.[3] In this context organic semiconductors offer new possibilities of cheap and compact integration of organic electronics on a sensor chip such as integrating an organic light emitting diode (OLED)[4–6] as light source or organic photodiodes (OPDs) as integrated optical detectors.[7–9]

We have developed such an integrated sensor platform suitable for multi-analyte detection in an array format with integrated OPDs as detectors. Three different sensing principles can be realized with such OPDs, namely fluorescence, absorption, and surface plasmon resonance (SPR) sensing schemes.[10–14] The devices are produced with simple and cheap methods such as screen-printing, spin-coating, and vacuum deposition on either glass or polymer (e. g. PET) substrates.

In this contribution we will illustrate the possibility of multi-analyte measurements in an array format of the sensing platform. Herein, we focus on the luminescent sensor chemistries showing the most promising results and application potential. A sensor array chip for the simultaneous determination oxygen, carbon dioxide and relative humidity is presented. In addition the measurement of oxygen and pH in aqueous media is demonstrated. Calibrated systems based on intensity measurements achieved a good reproducibility between different devices.

Ideally, factory or calibration free systems are desirable. In order to realize such systems luminescence life-time measurements are favourable, because they are independent on changes of the intensity, due to e.g. bleaching of the indicators or fluctuations of the optical systems. However, response dynamics of organic photodiodes show nonlinear photocurrent transients on the timescale of tens of microseconds[15], which impair correct luminescence life-time measurements of optical sensors. By applying a positive we were able to resolve these transients and demonstrate the life-time measurements of oxygen sensors.

Moreover we combined the sensor array chip with a microfluidic chip suitable for measurement of dissolved oxygen.

6.2 Description of the sensor array chip and experimental data

6.2.1 The sensor array chip lay-out

The results presented in this paper are obtained on a versatile sensing platform, where three different sensing principles can be implemented (fluorescence, absorption, and SPR). All three different types of sensor systems can be produced on either glass or polymer substrates where six organic Tang-type photodiodes (pn-heterojunction device consisting of p-type conducting copper phthalocyanine (CuPc) and n-type perylene tetracarboxylic bisbenzimidazole (PTCBI)[16] as charge generating layers) are layer-by-layer vacuum deposited on one side of the substrate and protected by an Ormocer® protective layer, afterwards. An example for such a substrate with OPDs on its bottom side and fluorescent spots on the upper side can be seen in Figure 6.1a. The measurements of the photocurrent on the OPDs were achieved with a custom- made readout-

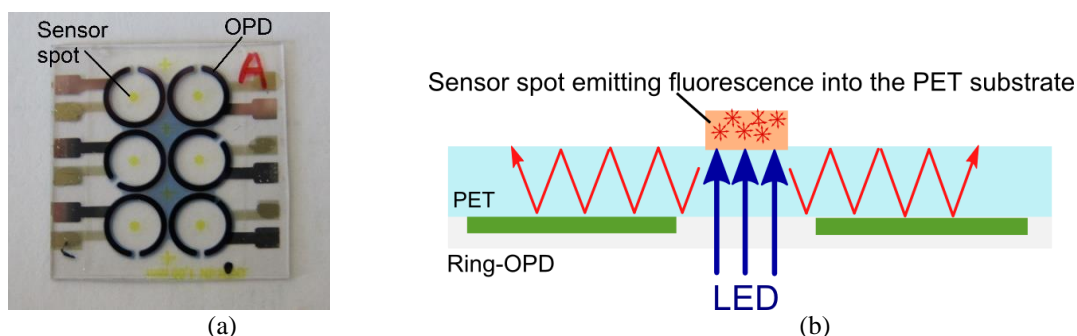


Figure 6.1. Pictures of a polymer or glass substrate with six OPDs and screen-printed fluorescence sensor spots (a) and b) a schematic drawing of the fluorescence sensor. The analyte-sensitive spot is illuminated by an LED and the emitted light waveguided through the substrate to be detected at the OPDs.

system with a mechanical fixture for the sensor device within a flow-through cell for various gases. The readout-system basically consists of a printed circuit board, commercial LEDs (460 nm) and an aperture for excitation, and the electronics for the signal acquisition from the OPDs. (Figure 6.1b). The measured current from the OPDs is pre-amplified and can be read-out digitally.

The fluorescence configuration, as shown in Figure 6.1b, requires no optical filters to differentiate between excitation and luminescence light. The geometry itself prefers the guiding of luminescent light directly to the detection unit. The LEDs illuminate exclusively the area of the sensing layer due to an aperture-like hole in the mount of the read-out unit beneath the chip. Luminescence is induced in the sensing layer and emitted isotropically. Because of the substrate's high refractive index, a predominant part of the emitted light is coupled in and subsequently guided in the substrate. The light spreads radially till it is absorbed by the ring-shaped OPD, giving a rise in the photo current. Non-absorbed excitation light passes through the sensing layer and is subsequently absorbed in the matte-black finish of the flow-through cell. A small part of the excitation light is coupled in due to scattering defects and polymer roughness, but this part was found to be insignificant.

6.2.2 Materials

Anisole, polystyrene (MW. 250000) (PS), were obtained from Acros Organics (Geel, Belgium). Ethyl cellulose (48% ethyloxy content) (EC) was purchased from Scientific Polymers Inc. (Ontario, NY, United States). Hydrogel D7 was obtained from CardioTech International Inc. (Wilmington, MA, United States). Tetra-N-octylammonium chloride (TOA+Cl⁻), tert-Octylimino-tris(dimethylamino) phosphorane (P₁-t-Oct), m-Cresol Purple (mCP), Coumarin 545 T or C545T, 8-hydroxypyrene-1,3,6-trisulfonic acid trisodium salt (HPTS-Na), tetra-N-octylammonium hydroxide (TOA+OH) (20% solution in methanol), were purchased from Sigma Aldrich Chemie GmbH (Steinheim, Germany). Hexadecyltrimethylammonium chloride (CTAC) was purchased from Fluka Chemie GmbH (Buchs, Switzerland). Teflon AF 1600 was from DuPont Fluoroproducts (Wilmington, DE, United States). Macrolex Fluorescent Yellow 10 GN (MFY) and Macrolex Fluorescent Red G (MFR) were purchased from Simon & Werner GmbH (Flörsheim am Main, Germany). Platinum (II) and palladium(II) 5,10,15,20-meso-tetrakis-(2,3,4,5,6-pentafluorophenyl)-porphyrin (PtTFPP and PdTFPP) were obtained by Frontier Scientific. Ir(Cs)₂(acac) and HPTS(DHA)₃ were synthesized in-house.

6.2.3 Luminescence decay-time measurements

In order to determine the lifetimes of the luminescent dyes a set-up a prototype printed circuit board (PCB) including a mount for the sensor chips and an electronic circuit to convert the nA current of the sensor into a voltage was developed. For the power supply of the amplifiers and the biasing of the OPDs two Dual Power Supply EL302RD units (TTi, Cambridgeshire, UK) were used. The excitation of the sensor spots was conducted through an aperture with an LED (470 nm, Roithner Laser Technik, Austria) driven by a Pulse Function Arbitrary Generator 81150A (Agilent Technologies, Santa Clara, USA). The electric potential provided by the transimpedance amplifier was recorded using an Infinii Vision MS07104A oscilloscope from Agilent Technologies. The data was then processed using OriginPro 8.1 Software (OriginLab Corporation, Northampton, USA).

6.2.4 Preparation of micro-fluidic chip with integrated OPDs

The microfluidic chip was prepared by assembling a PDMS layer with fluidic channels onto a substrate with processed OPDs and sensor spots (see Figure 6.2). The substrate consisted of polymeric material (Melinex®) to achieve a good adherence of the sensor spots. The microfluidic network is formed in a PDMS (Polydimethylsiloxane) layer as an imprint of a silicon master mold. The SU-8 based master mold is placed in a Petri dish and covered with a 3mm thick layer of liquid PDMS. Air inclusions are removed by repeated degassing in an evacuated exsiccator. After baking at 60°C for 4 hours, the PDMS containing microfluidic channels is cut and peeled off the mold. At in- and outlets of the fluidic holes are punched into the PDMS (dia. of approx. 500 μm). Finally a glass fluidic interface containing predrilled holes for the in- and outlets of the microfluidic channels is covalently bonded on top of the PDMS. Oxygen plasma is used for surface activation. Fluidic connections are assembled by attaching 1cm long pieces of TYGON tubes to the predrilled glass slides (2 component epoxy adhesive, Loctite 9492). The PDMS is then attached to the substrate with the integrated OPDs: A small amount of liquid PDMS (approximately 200 μL) is dropped onto a clean glass slide and a thin layer is generated by spinning the slide at 5000 U/min for 300 s. Then the fluidic is carefully dipped into the layer of liquid PDMS and transferred to the polymer substrate. The assembled chip is put into an oven (60°C for 4 hours) to harden the PDMS film.

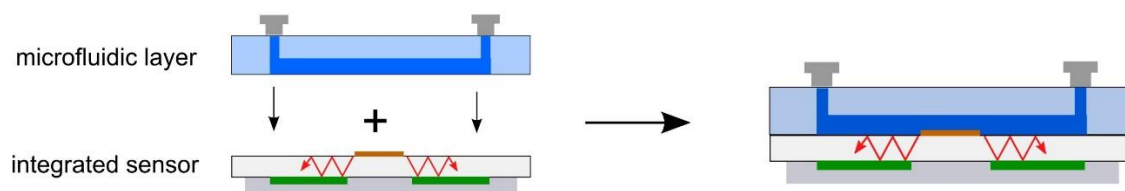


Figure 6.2. Schematic of the preparation of the microfluidic device with integrates sensor spots and photodetectors

6.3 Results

The feasibility of carrying out single- and multi-analyte measurement with the luminescence sensor chip in gaseous media was shown with following analytes: oxygen, carbon dioxide, and humidity.

Oxygen sensing was performed using PtTFPP as oxygen indicator. The brightness of PtTFPP was enhanced by using a Light Harvesting system [17], immobilizing them together with the antenna dyes MFY or C545T. They feature high molar absorption coefficient, high quantum yield, absorption spectra matching the excitation wavelength, and emission spectra overlapping to the absorption of PtTFPP. The carbon dioxide sensitive sensor layer is based on a dry chemistry approach by Mills [18]. The fluorescent indicator HPTS-TOA embedded in ethylcellulose as host polymer has been known as suitable for carbon dioxide sensing. Excess TOA·OH⁻ was added to improve the stability of the sensing layer. The sensing layer for relative humidity is derived from the functional principle of a carbon dioxide sensor. It was adapted by exchanging the counter cation (CTA) of the indicator dye HPTS to form a less sensitive carbon dioxide indicator and replacing the quaternary ammonium base TOA·OH⁻ with a neutral phosphazene compound. This neutral compound forms, together with water, a quaternary ammonium base, which consecutively deprotonates the indicator dye [19].

The sensor response and calibration of the carbon dioxide sensor showed results which are comparable to values reported from literature. The response curves of six carbon dioxide sensing elements on one array chip and six relative humidity sensing elements on one array chip are shown in Figure 6.3A and 6.3B. Both sensors show a cross-sensitivity, the carbon dioxide sensor toward relative humidity and vice versa. This performance is typical for gas-phase carbon dioxide sensing mechanisms based on pH indicators [19]. To overcome this drawback, both parameters have to be monitored to measure reliably. This is shown in Figure 6.3C showing the sensor response of a multi-analyte sensor array, based on oxygen, carbon dioxide and relative humidity. The sensor array chip consisted of six screen-printed spots, two spots each analyte. As a matter of course does the oxygen sensor not show any cross-sensitivity toward humidity or carbon dioxide, because it is based on dynamic luminescence quenching unlike the sensing schemes for the latter two analytes. The carbon dioxide sensor shows an increased sensitivity toward carbon dioxide at higher humidity (see Figure 6.3D). This illustrates that interference in response can be compensated between analytes by the sensor array chip arrangement.

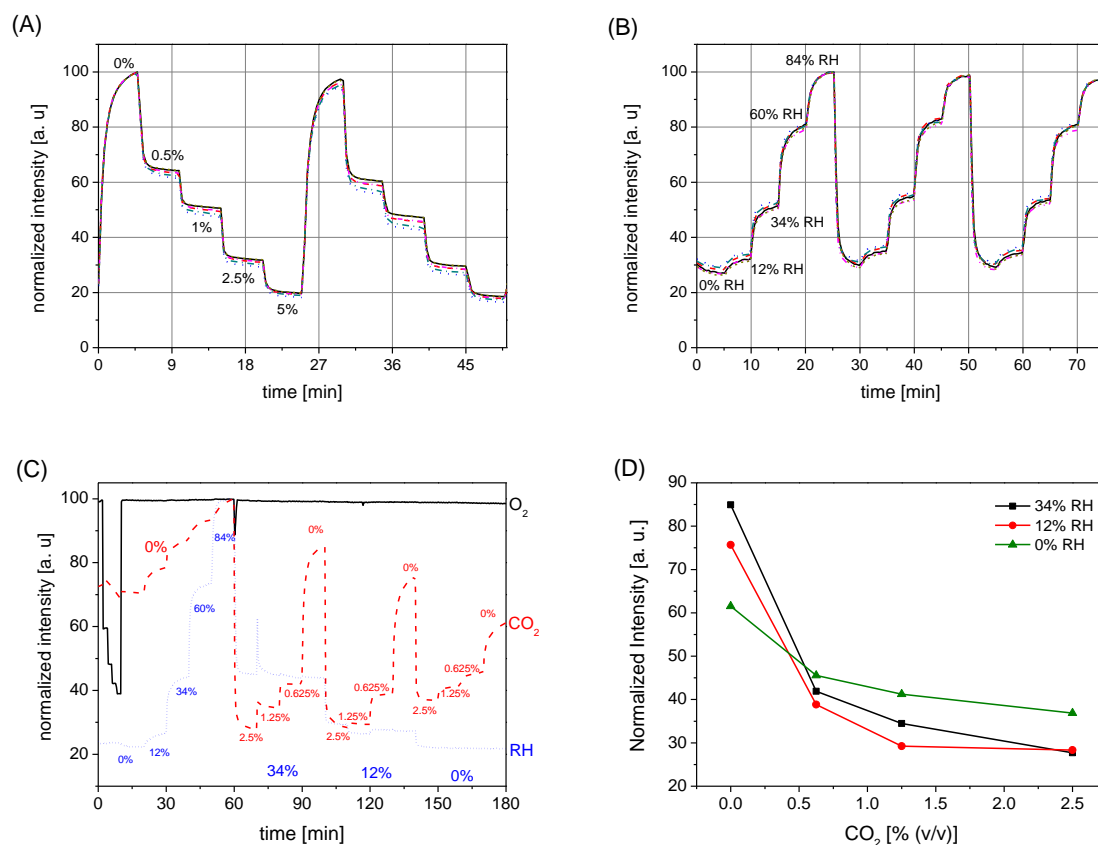


Figure 6.3. Response of the carbon dioxide sensor (A) and relative humidity sensor (B). Response of the multianalyte sensor chip for the determination of oxygen (black solid line), carbon dioxide (red dashed line) and relative humidity (blue dotted line) (C) and calibration curve of the carbon dioxide sensor at different relative humidity values (D).

6.3.1 Measurement in liquid phase

The sensing platform is also suitable for measurements in aqueous media. An average drop of the photocurrent of 44% at 200 hPa and 51% at 0 hPa was observed for an oxygen sensor compared with gas phase measurements. An explanation for the decrease in signal intensity is the higher refractive index of the aqueous media ($n=1.33$) instead of gaseous media ($n\sim 1.0$). As a consequence the critical angle of total reflection of the waveguide, on which the components are processed, is raised. This leads to less amount of guided light that can be detected by the integrated organic photodiode.

Figure 6.4A shows the response curve of an optical pH sensor based on a lipophilized derivative of HPTS immobilized in D7 hydrogel. The average response time t_{90} is 5 min. Figure 6b depicts the calibration gained by the response curves of Figure 6.4B. All sensor responses have been normalized to [0;1] resulting in an sigmoidal calibration characteristic. All four sensor responses show the same inflection point (pK_a) at 8.36 ± 0.015 and the same slope (0.46) when normalized.

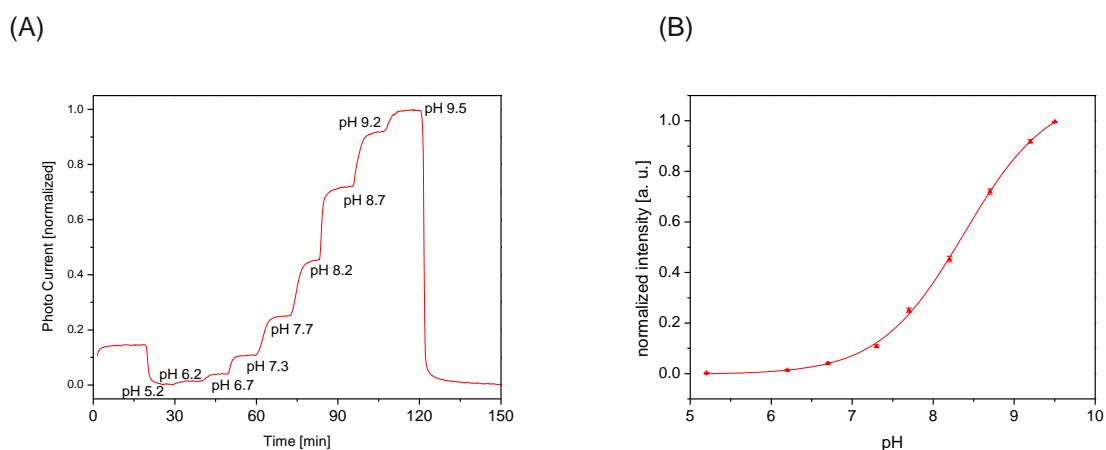


Figure 6.4. Response of the pH-sensor to various pH (A) and calibration plot of the average of six sensor elements (B)

6.3.2 Reproducibility of sensor performance between different sensor elements and sensor array chips

The reproducibility of the sensor performance based on calibrations curves was investigated. Figure 5 illustrates the variation of the luminescence intensity signal from spot to spot and between different sensor chips. Three different luminescence sensor chips have been coated with an oxygen sensitive layer and calibrated. The difference in signal derives mainly from 3 sources: a) variations in the light intensity of excitation source, b) variations in the OPD performance and c) reproducibility of the screen-printed sensor spots.

However, the calibration curves do not significantly change from one chip to another as shown in Figure 6.5 B. I_0/I_{200} (I_0 =intensity at 0 hPa O_2 , I_{200} =intensity at 200 hPa O_2). Values of these three sensor chips were determined to be 2.61 ± 0.03 for the first, 2.63 ± 0.01 for the second, and 2.63 ± 0.01 for the third sensor chip. The average I_0/I_{200} value for all three chips is 2.62 ± 0.03 . Calculated to oxygen pressure units yields in an absolute deviation of 6 hPa or relative deviation of 3% at 200 hPa, which is acceptable for many practical applications.

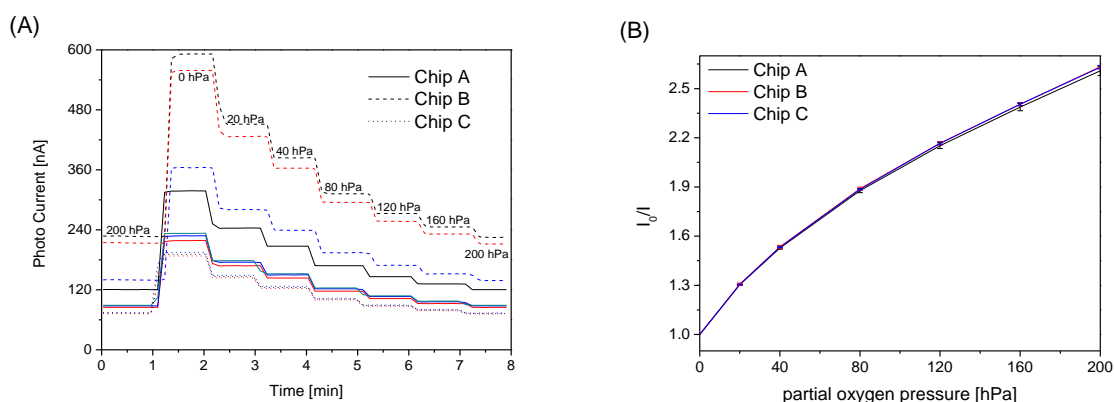


Figure 6.5. Response of curves of oxygen sensors spots on three different sensor array chips (A) and calibration curves of the average I_0/I value of the sensing spots of one sensor array chip (B).

6.3.3 Luminescence life-time determination with OPDs

The measurement of the luminescence decay time with organic photodiodes was investigated in the time domain. The electronics of the measurement set-up were arranged in a way that cross-talk between the excitation circuits and detection circuits was minimized.

First the response dynamics (see Figure 6.6A) of a ring-shaped OPD was recorded by applying a square light pulse on a fluorescent spot containing resonance energy pair C545T and MFR. Both dyes show fluorescence decay-times in the ns-range, which is much faster than the characteristics of the OPDs. A rapid exponential decay of the signal up to $<2 \mu\text{s}$, followed by a slower decay up to several $100 \mu\text{s}$ was observed. This long-lived tail is proposed to correspond to filled trap states that slowly detrapp after the illumination is switched off [15,20]. Negatively biasing the OPDs up to -300 mV did not change this behavior (Figure 6.6A), if higher negative bias was applied the OPDs degraded within a few seconds.

If a positive bias was applied (Figure 6.6B) the response characteristic does not change significantly up to 100 mV , in the range from 100 to 250 mV the amplitude the slow decay decline until it is barely noticeable, whereas the fast decay stays almost constant throughout this range. When biasing above 250 mV the amplitude of the first rapid decay decreases until the signal completely vanishes around 290 mV . This second decrease can be explained by the I-V characteristics of OPD (not shown) where the difference between dark and photo current and thus the on/off ratio decreases significantly around this biasing range. These behavior is explained by the assumption that the trapped charge carriers which normally slowly detrapp and migrate to the respective electrodes due to the built-in field of the diode do reach the electrodes if biased positive, because this bias decreases the built-in field and prevents the charges from leaving the OPD before they recombine within the material [21]. Above 250 mV biasing this long decay tail vanishes almost completely meaning the trapped charges do not significantly add to the signal.

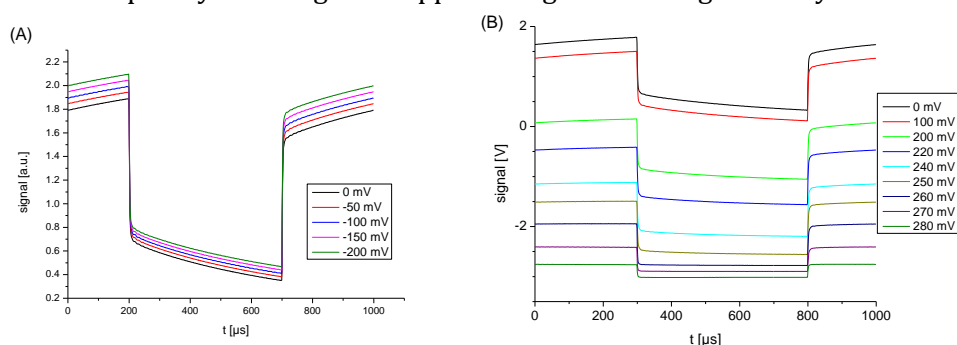


Figure 6.6. Photocurrent dynamics of an integrated OPD exposed to a square light pulse applying a negative (a) and positive bias (b)

These results above indicate that a positive bias suppresses the slow decay efficiently, thus enabling the detection of luminescence life-time of sensing layers with a lifetimes above $2 \mu\text{s}$. In order to prove this concept we employed oxygen sensing films based on $\text{Ir}(\text{Cs})_2(\text{acac})$ as oxygen indicator embedded in polystyrene. This sensing chemistry with a reported luminescence decay time of $\sim 5 \mu\text{s}$ in presence of 20% oxygen was chosen because we wanted to examine the limit of our system. The luminescence decay of the sensing film was recorded with an oscilloscope and the data were fitted with a single exponentials yielding in decay times comparable with data from the literature [22]. For the unquenched lifetime ($0\% \text{ O}_2$) the system delivers values slightly higher

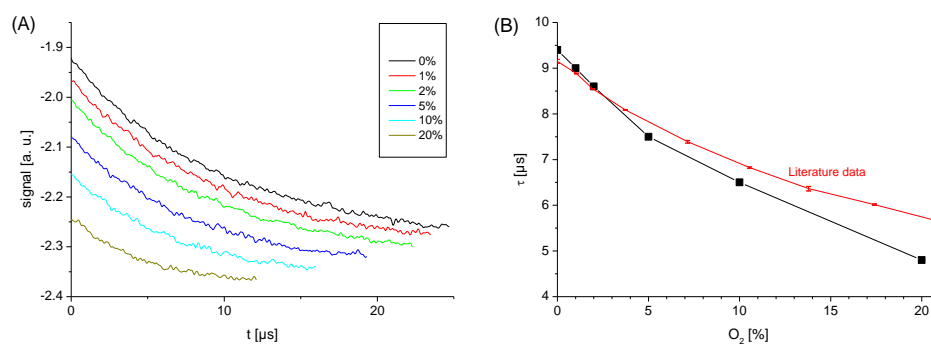


Figure 6.7 Decay curves of $\text{Ir}(\text{Cs})_2(\text{acac})$ sensor spots (left) and decay times of two different sensors (right) upon exposure to 0 to 20% O_2 in N_2 .

than expected, at 20% O_2 (in N_2) the lifetime is slightly underestimated. The latter could be explained by the influence of the background signal with a time constant of $1.6 \mu\text{s}$ that mixes with the decay signal of the oxygen indicator and makes the quenched lifetime appear to be shorter.

6.3.4 Microfluidic device with integrated organic photodiodes

The integrated sensor array chip process was combined with microfluidic layer made of PDMS. The chip contained two microfluidic channels positioned on top of OPDs. Each channel covered three sensor spots as shown in Figure 6.8A. The response of a sensor, when the channel was flushed with air-saturated and deoxygenated solution is shown in Figure 6.8B.

This preliminary result illustrates the potential of the combination of the sensor array platform with microfluidics. Potential applications of this device are monitoring of oxygen and pH-values in cell cultures for bioprocess optimization or toxicity tests for drug screening. The ability of non-invasive and continuous monitoring metabolic activities such as respiration and glycolysis of small cell populations is expected to significantly advance current cell-based assays where end point detection methods are used to provide information on the health status of cells.

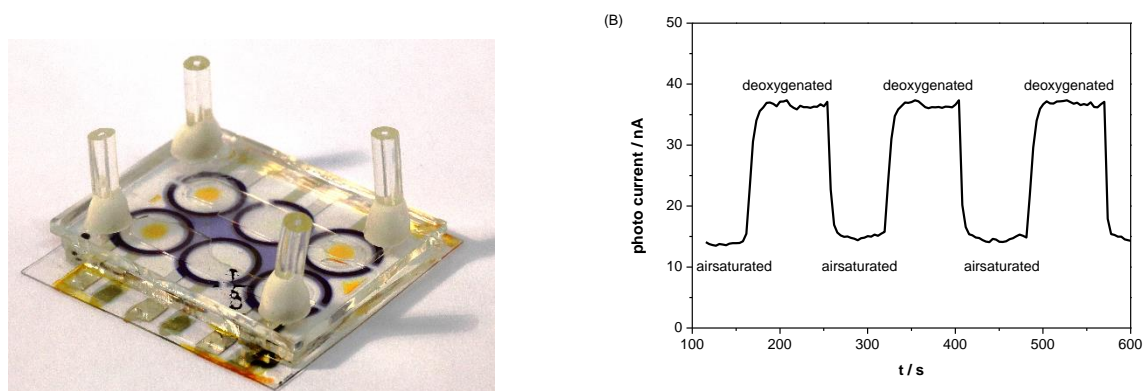


Figure 6.8. A micro-fluidic chip with integrated sensor spots for oxygen and organic photo-diodes (A). Response of the sensor to air-saturated and deoxygenated solutions injected with a syringe pump (B).

6.4 Conclusion

We present a multi-parameter sensor chip for the simultaneous measurement of oxygen, carbon dioxide and humidity based on luminescence. Hereby, it is demonstrated that the sensor chip can be used to compensate cross-sensitivity between different analytes. The sensor array chip is also suitable for measurement in aqueous media, illustrated by measurements of pH utilizing fluorescent sensor spots. The sensor chips show a good reproducibility between different sensor chips, when calibration routines are applied. The measurement of luminescence lifetimes in the μ -range in the time domain was also demonstrated yielding in lifetimes in good agreement with reported. The advantage of lifetime measurements is the possibility to enable factory calibration or even calibration free systems. However, the electronic system is more sophisticated and the elimination of electronic cross-talk of the excitation circuits and detection circuits is challenging and resulted in our case in a bulky instrumentation. In comparison, the electronic system of intensity based measurements can be kept simple, and the calculated accuracy of 3% is sufficient for many applications, when a two-point calibration is acceptable. We also present a microfluidic device with integrated sensor spots and photo-detectors. We plan to apply this adapt this microfluidic chip to monitor and control the viability of cells.

6.5 Acknowledgement

Financial support by the Austrian Research Promotion Agency (FFG) in the framework of the Austrian Nano Initiative (Research Project Cluster 0700 –Integrated Organic Sensor and optoelectronics Technologies) is gratefully acknowledged.

6.6 References

- [1] O. S. Wolfbeis, "Materials for fluorescence-based optical chemical sensors," *Journal of Materials Chemistry* **15**(27-28), 2657–2669 (2005).
- [2] C. McDonagh, C. S. Burke, and B. D. MacCraith, "Optical Chemical Sensors," *Chemical Reviews* **108**(2), 400–422 (2008) [doi:10.1021/cr068102g].
- [3] S. Vengasandra, Y. Cai, D. Grewell, J. Shinar, and R. Shinar, "Polypropylene CD-organic light-emitting diode biosensing platform," *Lab on a Chip - Miniaturisation for Chemistry and Biology* **10**(8), 1051–1056 (2010).
- [4] Y. Cai, R. Shinar, Z. Zhou, and J. Shinar, "Multianalyte sensor array based on an organic light emitting diode platform," *Sensors and Actuators B: Chemical* **134**(2), 727–735 (2008) [doi:10.1016/j.snb.2008.06.019].
- [5] R. Liu, Y. Cai, J.-M. Park, K.-M. Ho, J. Shinar, and R. Shinar, "Organic Light-Emitting Diode Sensing Platform: Challenges and Solutions," *Advanced Functional Materials* **21**(24), 4744–4753 (2011) [doi:10.1002/adfm.201101536].
- [6] J. Shinar and R. Shinar, "Organic light-emitting devices (OLEDs) and OLED-based chemical and biological sensors: an overview," *Journal of Physics D: Applied Physics* **41**(13), 133001 (2008).
- [7] A. Pais, A. Banerjee, D. Klotzkin, and I. Papautsky, "High-sensitivity, disposable lab-on-a-chip with thin-film organic electronics for fluorescence detection," *Lab on a Chip - Miniaturisation for Chemistry and Biology* **8**(5), 794–800 (2008).
- [8] O. Hofmann, P. Miller, P. Sullivan, T. S. Jones, J. C. deMello, D. D. C. Bradley, and A. J. deMello, "Thin-film organic photodiodes as integrated detectors for microscale chemiluminescence assays," *Sensors and Actuators B: Chemical* **106**(2), 878–884 (2005).

- [9] X. Wang, O. Hofmann, R. Das, E. M. Barrett, A. J. DeMello, J. C. DeMello, and D. D. Bradley, "Integrated thin-film polymer/fullerene photodetectors for on-chip microfluidic chemiluminescence detection," *Lab on a Chip - Miniaturisation for Chemistry and Biology* **7**(1), 58–63 (2007).
- [10] B. Lamprecht, T. Abel, E. Kraker, A. Haase, C. Konrad, M. Tscherner, S. Köstler, H. Ditlbacher, and T. Mayr, "Integrated fluorescence sensor based on ring-shaped organic photodiodes," *physica status solidi (RRL) - Rapid Research Letters* **4**(7), 157–159 (2010) [doi:10.1002/pssr.201004096].
- [11] B. Lamprecht, M. Sagmeister, E. Kraker, P. Hartmann, G. Jakopic, S. Köstler, H. Ditlbacher, N. Galler, J. Krenn, et al., "Integrated waveguide sensor platform utilizing organic photodiodes," *Proceedings of SPIE* **8234**(1), 82341H–82341H–9 (2012) [doi:10.1117/12.908432].
- [12] B. Lamprecht, E. Kraker, M. Sagmeister, S. Köstler, N. Galler, H. Ditlbacher, B. Ungerböck, T. Abel, and T. Mayr, "Integrated waveguide sensor utilizing organic photodiodes," *physica status solidi (RRL) - Rapid Research Letters* [doi:10.1002/pssr.201105300].
- [13] M. Sagmeister, B. Lamprecht, E. Kraker, A. Haase, G. Jakopic, S. Köstler, H. Ditlbacher, N. Galler, T. Abel, et al., "Integrated organic optical sensor arrays based on ring-shaped organic photodiodes," *Proceedings of SPIE* **8118**(1), 811805–811805–6 (2011) [doi:10.1117/12.893497].
- [14] T. Abel, M. Sagmeister, B. Lamprecht, E. Kraker, S. Köstler, B. Ungerböck, and T. Mayr, "Filter-free integrated sensor array based on luminescence and absorbance measurements using ring-shaped organic photodiodes," *Analytical and Bioanalytical Chemistry*, 1–9 [doi:10.1007/s00216-012-6175-4].
- [15] C. R. McNeill, I. Hwang, and N. C. Greenham, "Photocurrent transients in all-polymer solar cells: Trapping and detrapping effects," *Journal of Applied Physics* **106**(2), 024507 (2009) [doi:10.1063/1.3177337].
- [16] C. W. Tang, "Two-layer organic photovoltaic cell," *Appl. Phys. Lett.* **48**(2), 183–185 (1986) [doi:10.1063/1.96937].
- [17] T. Mayr, S. M. Borisov, T. Abel, B. Enko, K. Waich, G. Mistlberger, and I. Klimant, "Light Harvesting as a Simple and Versatile Way to Enhance Brightness of Luminescent Sensors," *Analytical Chemistry* **81**(15), 6541–6545 (2009) [doi:10.1021/ac900662x].
- [18] A. Mills, Q. Chang, and N. McMurray, "Equilibrium studies on colorimetric plastic film sensors for carbon dioxide," *Analytical Chemistry* **64**(13), 1383–1389 (1992).
- [19] C. R. Schröder and I. Klimant, "The influence of the lipophilic base in solid state optical pCO₂ sensors," *Sensors and Actuators, B: Chemical* **107**(2), 572–579 (2005).
- [20] N. Christ, S. W. Kettlitz, S. Züfle, S. Valouch, and U. Lemmer, "Nanosecond response of organic solar cells and photodiodes: Role of trap states," *Phys. Rev. B* **83**(19), 195211 (2011) [doi:10.1103/PhysRevB.83.195211].
- [21] S. R. Cowan, A. Roy, and A. J. Heeger, "Recombination in polymer-fullerene bulk heterojunction solar cells," *Phys. Rev. B* **82**(24), 245207 (2010) [doi:10.1103/PhysRevB.82.245207].
- [22] S. M. Borisov and I. Klimant, "Ultrabright Oxygen Optodes Based on Cyclometalated Iridium(III) Coumarin Complexes," *Anal. Chem.* **79**(19), 7501–7509 (2007).

7 Fluorescent materials for pH sensing and imaging based on novel 1,4-diketopyrrolo-[3,4-c]pyrrole dyes

Daniel Aigner ^a, Birgit Ungerböck ^a, Torsten Mayr ^a, Robert Saf ^b, Ingo Klimant ^a and Sergey M Borisov ^a

Published by the Royal Society of Chemistry in Journal of Materials Chemistry C, September 2013, Volume 1, pp 5685-5693

DOI: 10.1039/C3TC31130A

Abstract New optical pH-sensors relying on 1,4-diketopyrrolo-[3,4-c]pyrroles (DPPs) as fluorescent pH-indicators are presented. Different polymer hydrogels are useful as immobilization matrices, achieving excellent sensitivity and good brightness in the resulting sensor. The operational pH can be tuned over a wide range (pH 5 – 12) by selecting the fine structure of the indicator and the matrix. A ratiometric sensor in the form of nanoparticles is also presented. It is suitable for RGB camera readout, and its practical applicability for fluorescence imaging in microfluidic systems is demonstrated.

The indicators are available starting from the commercially available DPP pigments by a straightforward concept employing chlorosulfonation and subsequent reaction with amines. Their sensitivity derives from two distinct mechanisms. At high pH (> 9), they exhibit a remarkable alteration of both absorption and fluorescence spectra due to deprotonation of the lactam nitrogen atoms. If a phenolic group is introduced, highly effective fluorescence quenching at near-neutral pH occurs due to photoinduced electron transfer (PET) involving the phenolate form.

7.1 Introduction

pH is one of the key parameters in medical, environmental and life sciences. Despite the strong performance of electrochemical pH-sensors, optical pH-sensors have proved invaluable in numerous important applications. They possess numerous advantages including for example greater ease of miniaturization and the possibility of contactless measurement. Moreover, optical probes enable imaging applications¹⁻⁵. These features are particularly attractive in high-throughput screening and for probing small samples such as living cells or sub-cellular structures^{6,7}.

Optical pH-sensors typically consist of a pH-sensitive dye (*i.e.* a pH-indicator) immobilized in a polymer matrix which has to provide suitable mechanical and adhesive properties, together with sufficient water uptake. Although most optical pH-indicators are essentially (de)protonable chromophores⁸⁻¹⁰, those with proton receptors separated from the chromophore have also found numerous applications. They are the most flexible in terms of rational dye design since the chromophore and the receptor can be selected independently. Most frequently, they take advantage of the photoinduced electron transfer (PET)¹¹⁻¹³ process. Though PET is an extensively investigated effect, in most publications it is introduced by amine functionalities¹⁴⁻¹⁷, while phenolic groups have attracted comparatively little attention. In 1997, Gareis et al.¹⁸ presented a boron-dipyrromethene (BODIPY) pH-indicator with a phenolic proton receptor. Most comparable systems have relied on the BODIPY chromophore since then¹⁹⁻²¹.

Derivatives of 1,4-diketo-3,6-diphenylpyrrolo[3,4-c]pyrrole, often referred to as DPPs, are chemically stable, brightly fluorescent²² molecules that have found a variety of applications. While the parent compounds are commonly used pigments, the attachment of suitable substituents yields readily soluble fluorescent dyes. Alkylation of the lactam nitrogen atoms is most effective in this regard since hydrogen bonding interactions are suppressed. DPP-based dyes and pigments have been used as high-performance colorants in prints and inks, as components of solid-state dye lasers²³⁻²⁷ and more recently in the field of organic optoelectronics. Particularly, DPP-containing conjugated polymers²⁸⁻³⁰ and small molecules³¹ have found extensive use in Organic Field Effect Transistors (OFETs)^{32,33} and Organic Solar Cells^{34,35}. DPP dyes are also particularly promising for the design of two-photon excitable fluorophores^{36,37}. A few DPP-based fluorescent probes and sensors for fluoride³⁸, cyanide³⁹, thiols⁴⁰ and molecular hydrogen⁴¹ have been developed. The DPP-based probe presented by Yamagata et al.⁴² is suited for detecting strong acids in organic solvents, rather than measuring near-neutral pH in aqueous solution. Recently, we presented carbon dioxide sensors that exploit the deprotonation of the lactam nitrogen atoms in DPPs⁴³. The same mechanism is useful for the determination of comparatively high pH (> 9), as will be demonstrated in this work. Furthermore, we present – to the best of our knowledge for the first time – DPP-based pH-sensors that operate at near-neutral pH. They rely on PET from phenolate groups to the chromophore.

7.2 Results and discussion

The preparation of the new pH-indicators and sensors is shown in fig. 1. The indicators **2** and **3** feature phenolic PET groups. **4** carries a morpholino group for solubilization and is an example of a DPP pH-indicator relying on deprotonation of the lactam nitrogen.

7.2.1 Indicator syntheses

The indicators **2 - 4** can be easily prepared in a single step starting from commercially available 1,4-diketo-3,6-diphenylpyrrolo[3,4-c]pyrrole. Notably, the reaction conditions applied afforded only monosulfonated products. Doubly sulfonated products are formed under harsher reaction conditions⁴³. The intermediate, a sulfonyl chloride, can yield a large variety of sulfonamides, depending on the amine it is reacted with. The synthetic concept employed is simple and versatile as it is applicable for any class of chromophore that can withstand chlorosulfonation. It is useful for tagging a large variety of structures and is not limited to the preparation of pH-indicators, which has been the main focus of this work.

The modest yields (13 - 22%) are due to difficulties in purifying the products by column chromatography. They strongly bind to the stationary phase and are hard to elute completely. Nevertheless, all products could be easily isolated in sufficient amounts starting from the cheap commercial pigment.

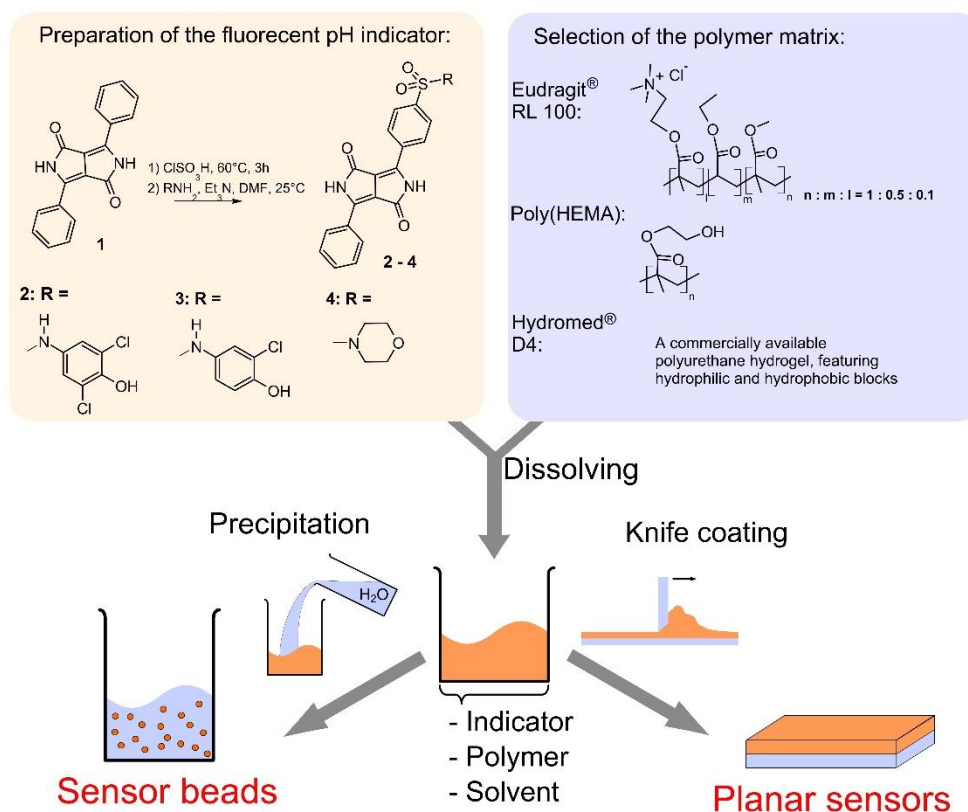


Figure 7.1. Scheme for the preparation of the fluorescence pH-sensors in this work.

7.2.2 Indicator properties

Spectral properties of the DPP sulfonamides **2 - 4** in comparison to the starting material are listed in table 1. The attachment of a sulfonamide group results in bathochromically shifted and less structured absorption bands, while the Stokes shifts are significantly enlarged. Despite that **2 - 4** are not *N*-substituted their solubilities exceed 2 g / l in *N,N*-dimethylformamide and tetrahydrofuran. This is dramatically higher than for pigment **1** which is virtually insoluble in these solvents at 25 °C. Note that for the majority of applications requiring soluble DPPs, *N*-

substituted derivatives are used. However, our preliminary experiments indicated that chlorosulfonation of a *N,N'*-dialkylated DPP (*N,N'*-di(2-ethylhexyl)-1,4-diketo-3,6-diphenylpyrrolo[3,4-c]pyrrole) and subsequent reaction with 4-amino-2,6-dichlorophenol did not yield a pH-indicator.

Table 1: Spectral properties of the DPP dyes in tetrahydrofuran: λ_{\max} abs - wavelengths of the absorption maxima; ϵ - molar absorption coefficients; λ_{\max} em - wavelengths of the fluorescence emission maxima; Φ_F - relative fluorescence quantum yield; n.d. - not determined; n.m. - not measureable (2 and 3 are virtually non-fluorescent in the phenolate form). Acidic/basic denotes 0.1% (V/V) trifluoroacetic acid / 1 mM tetrabutylammonium hydroxide.

Dye	λ_{\max} abs ($\epsilon \cdot 10^{-4}$) / nm ($M^{-1} \cdot cm^{-1}$) acidic / basic	λ_{\max} em / nm acidic / basic	Φ_F acidic/basic
1	468(2.95), 502(3.91)	514, 552	n.d.
2	509(2.23), 543(2.40) / 575(1.88), 606(2.16)^a	580 / n.m.	0.70 / n.m.
3	508(1.74), 541(1.86) / 575(1.60), 606(1.86)^a	577 / n.m.	0.66 / n.m.
4	509(2.02), 541(2.14) / 391(0.95), 584(1.89), 619(2.39)	576 / 679	0.71 / 0.08

^aThe bathochromically shifted spectra correspond to the dianionic form (both phenol and lactam are deprotonated). The absorption of the monoanionic form (only phenol is deprotonated) is not shifted with respect to the acidic form (Figure 7.3).

The pH-sensitivity of the DPP indicators is associated with two distinct mechanisms, as illustrated in Figure 7.2. **2** and **3** are subject to photoinduced electron transfer (PET) when the phenolic group is deprotonated. The result is fluorescence quenching around the pKa of the phenolic group (that is, pH 5.9 – 9.3, table 2). No alteration of the absorption spectra at all is observed (Figure 7.3), indicating that the effect is solely PET. Importantly, the quenching is extremely efficient (virtually no fluorescence from the deprotonated form is detected) which indicates that phenolates are suitable proton receptor groups for designing fluorescent pH-indicators. Thus they represent a very promising alternative to the much more common amino-based receptors.

Fluorescence quenching of **4** occurs at higher pH (9.7 – 11.6) and is clearly accompanied by a bathochromic shift in absorption and fluorescence spectra. This effect is caused by deprotonation of the lactam nitrogen within the chromophore⁴³. Similar changes in the absorption spectra can also be observed for **2** and **3** at higher pH. The absorption spectra shown in Figure 7.2C correspond to the neutral and the monoanionic form of **4**. Note that the monoanion exhibits weaker but clearly detectable fluorescence. Under more basic conditions, a further bathochromic shift is observable, which originates from partial deprotonation of the second lactam nitrogen, resulting in the dianion.

Notably, the sulfonamide moiety itself can also undergo deprotonation. Typical pKa values would be in the range 8 – 11 for structures comparable to **2** and **3**^{44,45}. Such a deprotonation mechanism may contribute to their pH-sensitivity to some extent. The anion formed, a sulfonimide, is in protolytic equilibrium with the phenolate form shown in Figure 7.2. Note that the sulfonamide group in **4** cannot be deprotonated and its pH-sensitivity is thus related exclusively to lactam deprotonation.

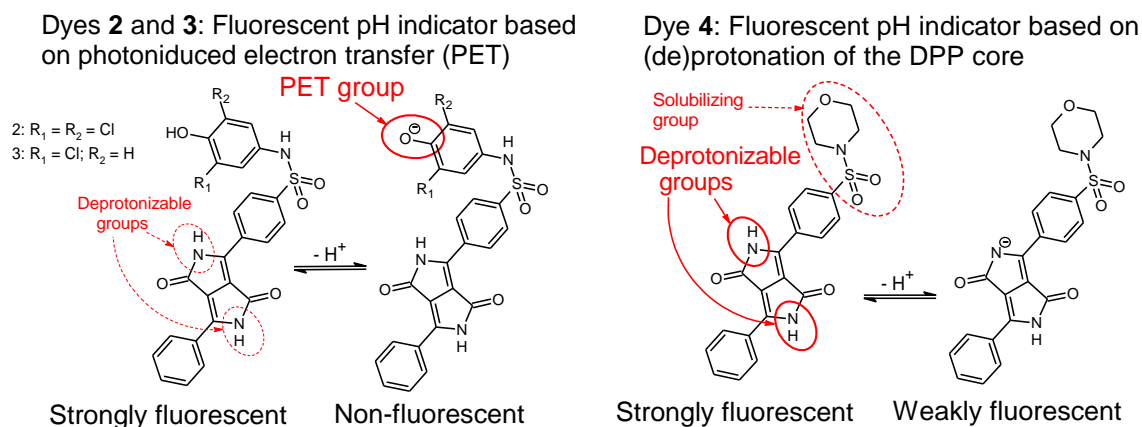


Figure 7.2. Mechanisms causing pH-sensitivity in the DPP-based indicators.

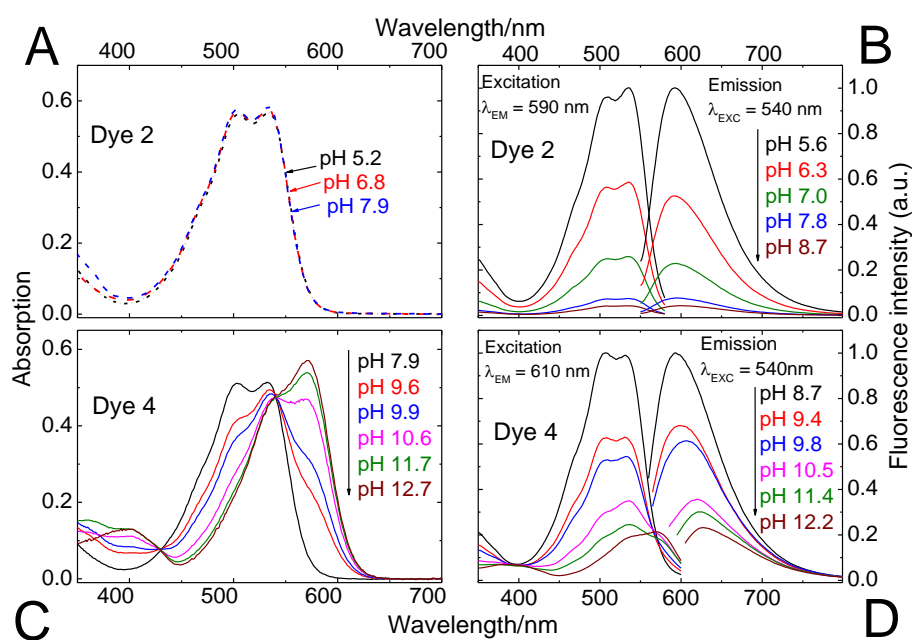


Figure 7.3. pH-dependent absorption (A, C) and fluorescence (B, D) spectra of the DPPs 2 and 4. Since 2 and 3 feature virtually identical spectral properties and differ only by their sensitive pH ranges, 3 has been included in the electronic supplementary information (ESI; fig. S1) only. Spectra were recorded in ethanol/aqueous buffer (ionic strength 100 mM) solution 1:1 (V/V). pH values are those of the aqueous buffer used. DPP concentration was 20 μM for absorption and 4 μM for fluorescence measurements.

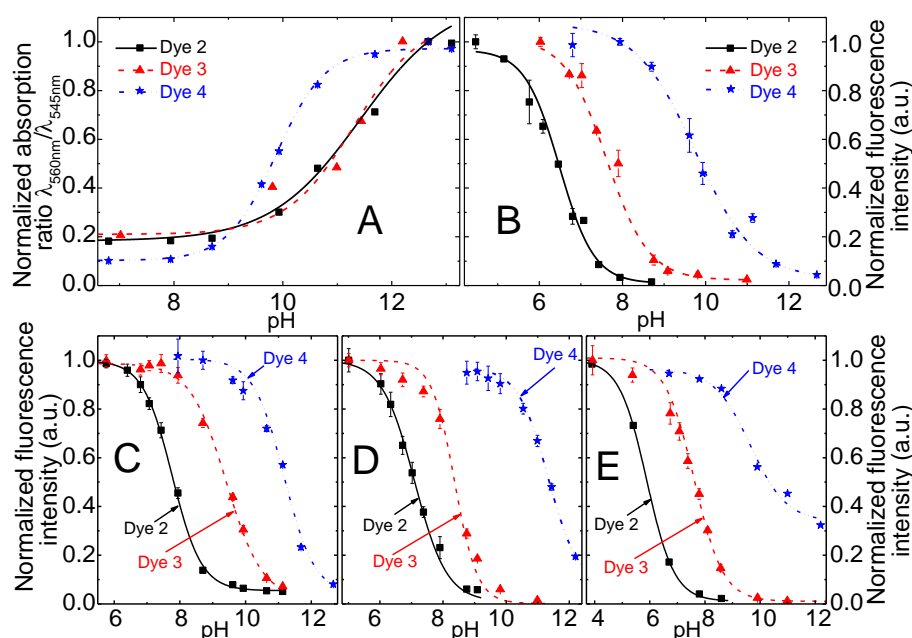


Figure 7.4. A: pH calibration curves of the DPP indicators in ethanol/aqueous buffer (ionic strength 100 mM) solution 1:1 (V/V); pH values are those of the aqueous buffer used. B: Corresponding fluorescence calibration curves for the solution ($\lambda_{\text{exc}} = 540 \text{ nm}$, observed at 595 nm); C, D: pH calibration curves based on fluorescence in planar sensors (dye content 0.25%; C in D4[®] hydrogel; D in poly(2-hydroxyethyl-methacrylate), E: Calibration curves in RL100 sensors beads dispersed in aqueous buffer (dye content 0.5% (w/w), bead concentration 0.2 mg / ml).

Table 2: $\text{pH}_{1/2}$, the pH values at which half of the pH-dependent signal change is effective, based on absorption (Abs.) and fluorescence (Fluo.), corresponding to the calibration curves in figure 4. n.d. denotes not determined.

Dye	EtOH/H ₂ O 1:1 (V/V)		D4		poly(HEMA)	RL100
	$\text{pH}_{1/2}$ (Fluo.)	$\text{pH}_{1/2}$ (Abs.)	$\text{pH}_{1/2}$ (Fluo.)	$\text{pH}_{1/2}$ (Abs.)	$\text{pH}_{1/2}$ (Fluo.)	$\text{pH}_{1/2}$ (Fluo.)
2	6.49 ^a	11.3 ^b	7.76 ^a	n.d. ^c	7.08 ^a	5.88 ^a
3	7.63 ^a	11.3 ^b	9.34 ^a	n.d. ^c	8.36 ^a	7.62 ^a
4	9.75 ^b	9.88 ^b	11.1 ^b	11.6 ^b	11.1 ^b	9.65 ^b

^a corresponds to deprotonation of the phenolic PET group

^b corresponds to deprotonation of the lactam nitrogen

^c The doubly charged basic form is quickly leached out of the sensor

The photostability of the DPPs has been investigated and compared to reference dyes which represent two of the most commonly used types of pH-indicators. It is vastly superior to that of fluorescein octadecyl ester (fig. 5). Compared to HPTS (8-hydroxypyrene-1,3,6-trisulfonate), a highly photostable pH-indicator, DPPs are degraded 3 – 4 times faster under the same illumination conditions. Photostability is greatly increased (dye degraded > 20 times slower) in deoxygenated samples which implies an oxidative photo-degradation pathway or may involve photosensitized singlet oxygen. No degradation at all was observed for the phenolate form of 2. That could be because PET causes fast quenching, leaving little time for degradation in the excited state.

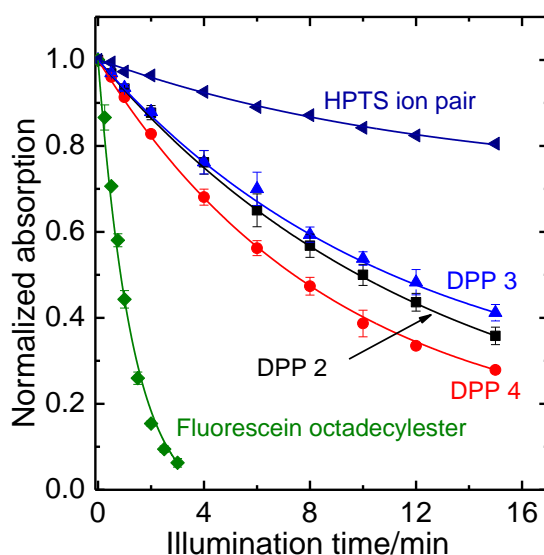


Figure 7.5. Photodegradation profiles of the DPP dyes, compared to fluorescein octadecyl ester and 1-hydroxypyrene-3,6,8-trisulfonate (HPTS) in the form of an ion pair with tetraoctylammonium. The solutions in tetrahydrofuran (for HPTS, 0.02 mM tetraoctylammonium hydroxide in the form of a 1 M methanolic solution was added) were illuminated with a 458 nm high-power LED array. The decay rates compared to 2 are 0.92 for 3, 1.12 for 4, 0.31 for HPTS ion pair and 6.1 for FODE.

7.2.3 pH-sensing materials

The pH-indicators have been immobilized in polymer matrices to obtain pH-sensors. The host materials are Hydromed[®]D4 (a commercially available polyurethane-based hydrogel) and poly(2-hydroxyethylmethacrylate) (p(HEMA)) in the form of planar sensors and Eudragit[®] RL100 (a positively charged acrylate polymer) in the form of sensor nanobeads (typical average size 30 nm). The sensors are promising not only due to their high brightness and sensitivity, but in particular because their sensitive range can be tuned by selecting the indicator structure and the matrix (table 2, Figure 7.4). The PET-based indicators **2** and **3** can tackle pH 5 – 10. Monochlorinated **3** covers higher pH than dichlorinated **2**. The basic form of the indicator is negatively charged and thus most effectively stabilized by the cationic RL100 matrix and least effectively stabilized by the comparatively hydrophobic D4; this results in $\text{pH}_{1/2}$ values increasing in the same order. The pH-range covered by **2** and **3** in those matrices meets the one of interest to the most relevant applications for pH-sensors, namely medical applications (physiological pH 7 – 7.5), marine science (optimal pH 7.5 – 8.5) and biotechnological process monitoring (pH 5 – 7, depending on the process). **4** enables measurement at pH 9 – 12, a range that is more seldomly addressed but is of importance to applications such as concrete quality testing. In this pH-range, the choice of already available pH-indicators is rather limited.

In practical applications, not only the sensitive range of a fluorescence sensor is of importance but also referencing possibilities. Referencing can make the signal independent on the optical path length, the efficiency of the light source and the guidance of light to the detector. Therefore, a ratiometric pH-sensor employing the commercially available coumarin Macrolex Yellow (3-(5-chloro-2-benzoxazolyl)-7-(diethylamino)-2H-1-benzopyran-2-one) as a reference dye has been developed. In this approach, the reference dye is excited, its excitation energy is partially transferred to the DPP pH-indicator dye by Förster resonance energy transfer (FRET) and the

emission ratio between both dyes is detected. The referenced system is particularly promising since it can be read out with a simple RGB-CCD camera (fig. S2 in the electronic supplementary information, ESI). Imaging with RGB cameras is becoming increasingly popular⁴⁶⁻⁴⁸. Its sensitive range is very similar to the non-referenced analog, as demonstrated in fig. S3.

7.2.3.1 Planar sensors.

The usefulness of the planar ratiometric sensors is demonstrated in Figure 7.6– fluorescence imaging was successfully performed over an application time of > 0.5 h. However, limitations were revealed when the long-term performance of the planar sensors was examined in a fiber-optic measurement setup with a LED light source. A significant decrease of the indicator signal is observable if a sensor based on **2** or **4** is measured over several hours (6% per hour for **2**, 14% per hour for **4**; visualized in the ESI, fig. S4 and S5, respectively). This signal drift is also present in the ratiometric system. It is strongly intensified when measurement is carried out under continuous illumination and it is accompanied by a diminishment in the DPP absorption band. That implies photo-degradation is an important factor for the signal drift. However, no significant dependence on illumination time was found if that time is generally short (a fraction of < 1% of the overall measurement time) and minimal emission intensity of the light source is applied. That suggests that other effects like dye aggregation or migration can also cause unwanted signal drift and become dominant at lower light intensities. Consequently, the DPP-based pH-sensors in the planar format are limited to applications requiring short times and low light densities.

7.2.3.2 Sensor beads.

In contrast to planar sensors which are static, sensor beads can be dispersed in the sample. Therefore, in all fluidic applications the beads are continuously renewed. When the residence time of each individual nanosensor is short, signal drifts within the sensor do not become noticeable even if the actual application time is long. As a result, photodegradation can be negligible in the case of sensor beads, while the same sensing materials used as planar sensors suffer from a signal drift. An example for this is given by Figure 7.7A where the performances of DPP-based ratio-

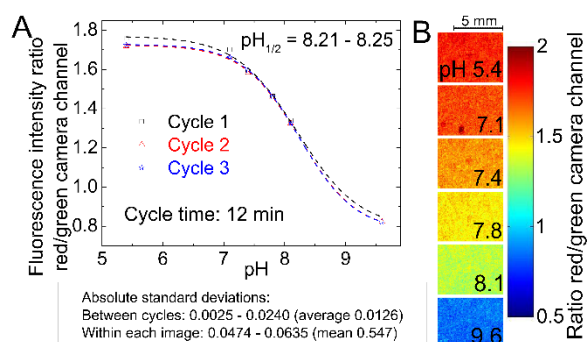


Figure 7.6. Fluorescence imaging with a planar ratiometric pH-sensor (7 μm thick) containing Macrolex yellow (1.5% (w/w)) and pH-indicator **2** (0.5% (w/w)), read out with a RGB-CCD camera. The sensor was placed in a home-made flow-through cell and buffer solutions (ionic strength 100 mM) were applied (flow rate 1 ml / min, 2 min for each buffer). A blue (458 nm) LED array in combination with a Schott BG 12 bandpass filter (350 - 465 nm) was used for excitation. Excitation light was excluded from the camera employing a Schott OG515 nm long-pass filter. **A:** Calibration curve, based on the ratio between red and green color channel; **B:** Corresponding false color images.

metric pH-sensors in both formats are compared using a fluorescence microscope. Owing to the high light density typical for fluorescence microscopy, the signal of the planar sensor is dramatically affected by photo-bleaching and measurement is rendered essentially impossible. On the other hand, the performance of the RL100 sensor beads in a fluidic system remains unperturbed over the whole measurement time. Consequently, while the DPP-based planar sensors and sensor beads can both be useful for macroscopic fluorescence imaging (Figure 7.6), the use of beads is imperative in fluorescence microscopy. Figure 7.7 also demonstrates the applicability of the sensor beads in a microfluidic system. Note that imaging in microfluidic systems enables high-throughput measurements, for instance in medical applications. RGB cameras are generally simple readout systems available at low cost and were demonstrated to be suitable for pH-imaging in microfluidics⁴⁹. To underline the suitability of the DPP-based sensor beads in this regard, they were used in a microfluidic system that allows parallelization (Figure 7.8).

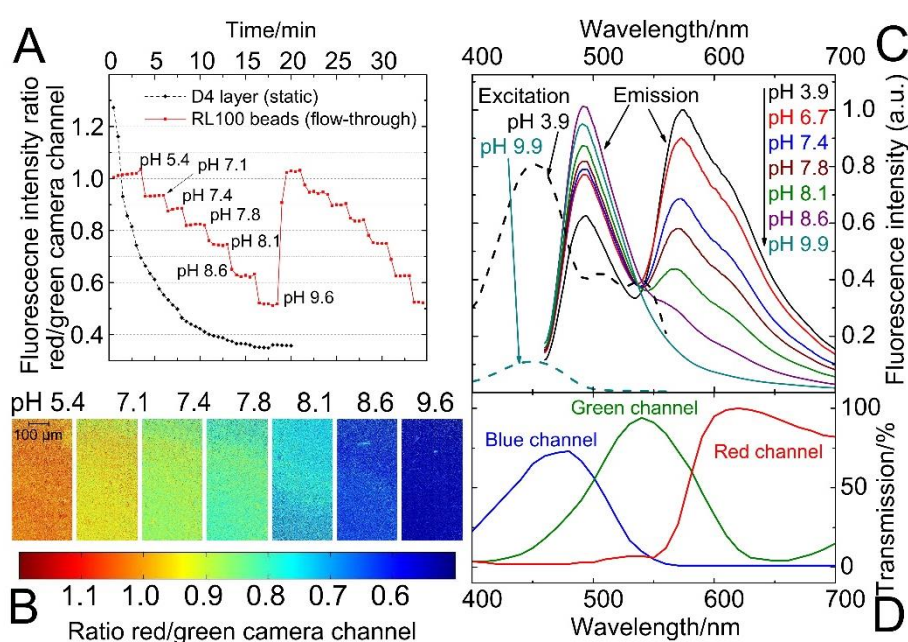


Figure 7.7. pH-imaging in a microfluidic system using a fluorescence microscope, employing ratiometric pH-nanosensor beads containing indicator 3 (1% w/w) and Macrolex® yellow (1.25% w/w) in RL100 polymer. The sensors were read out employing a RGB-CCD camera; **A:** Response curve of the bead suspensions, each measurement point was recorded illuminating for 2 s (the corresponding calibration curve can be found in fig. S6 in the ESI). They are compared to the performance of a planar sensor (static, placed on a microscope slide; composition as specified in Figure 7.6) under the same measurement conditions; **B:** Images of the sensor bead suspensions corresponding to measurement A (cycle 1) - the ratio between red and green channel is visualized; **C:** pH-dependent fluorescence spectra (excitation at 450 nm; emission observed at 570 nm) of the sensor beads; **D:** Spectral characteristics of the RGB-CCD camera.

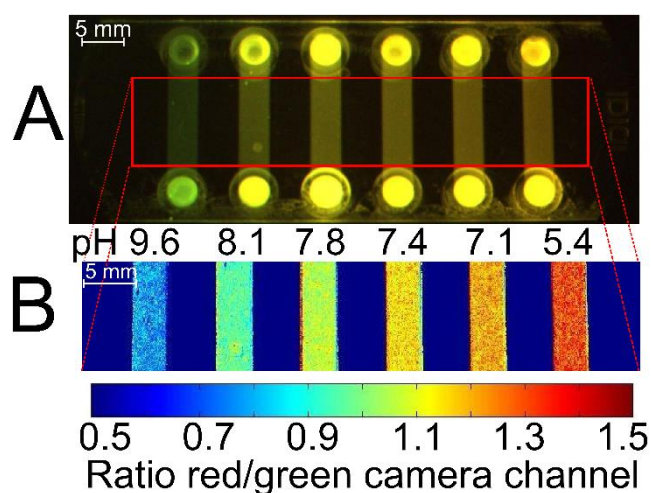


Figure 7.8. Example for a possible application of the DPP-based ratiometric pH-nanosensor beads in high-throughput measurement, using pH-imaging in a microfluidic system. pH can be determined simultaneously in every chip compartment. The pH-sensor beads (as specified near Figure 7.7) in aqueous buffer of defined pH were read out employing a RGB-CCD camera. Excitation source and filters were the same as in fig. 6.

A: Photographic image; B: False color image of the chip. At the channel inlets, locally higher optical pathlengths cause deviations in fluorescence measurement due to overexposure. When red and green color channels exhibit maximum intensities, the ratio of these channels is 1. For the sake of clarity, the inlets are not shown in B.

7.3 Conclusion

In conclusion, new pH-sensors have been presented that exclusively rely on fluorescent dyes and host polymers which are either commercially available or can be prepared from commercially available compounds in a single, simple reaction step. By properly selecting the sensor components, one can tune the sensitive pH-range of the material to cover a broad region (pH 5 - 12). This pH-region meets the requirements of a vast majority of pH-sensor applications. While sensors in the planar format are limited to short-time applications, sensitive nanobeads in Eudragit® RL100 polymer are most promising for practical applications in (micro)fluidic systems and even for fluorescence imaging and microscopy. By taking advantage of a ratiometric approach, good compatibility with a simple RGB camera for readout is accomplished.

Beyond the presented new pH-sensors, this work highlighted the usefulness of the tools employed for rational dye design. The phenolate proton receptors have been demonstrated to be very efficient quenchers operating via Photoinduced Electron Transfer and represent a promising alternative to the more commonly used amino-receptors. They can be used in combination with other fluorophores in order to match the requirements of a particular application considering spectral properties or indicator stability. The receptors have been attached by a simple concept, *i.e.* chlorosulfonation and subsequent reaction with amines. Following this concept, a variety of functionalities can be tagged to DPPs, making them suitable for probing analytes other than pH or targeting particular biomolecular structures.

7.4 Experimental

7.4.1 Materials and Methods

1,4-Diketo-3,6-diphenylpyrrolo[3,4-c]pyrrole (Irgazin Scarlet) was purchased from Kremer Pigmente (<http://kremer-pigmente.de/en>), Macrolex Fluorescent Yellow from Simon and Werner GmbH (www.simon-und-werner.de). 4-Amino-2-chlorophenol was from TCI Europe (www.tcichemicals.com), 4-amino-2,6-dichlorophenol from ABCR (www.abcr.de). Solvents used for work-up and purification (synthesis grade) as well as buffer salts were supplied by Carl Roth (www.roth.de). Deuterated solvents were obtained from Eurisotop (www.eurisotop.com), silica gel from Acros (www.fishersci.com). Polyurethane hydrogel D4[®] was from CardioTech (www.cardiotech-inc.com), poly(2-hydroxyethylmethacrylate) (MW = 150000 g / mol), from Polysciences Inc. (www.polysciences.com), Eudragit[®] RL100 from Evonik Industries (<http://corporate.evonik.de>). All other chemicals were from Sigma-Aldrich (www.sigmaaldrich.com). Poly(ethylene glycol terephthalate) support (Mylar[®]) was from Goodfellow (www.goodfellow.com).

NMR spectra were recorded on a 300 MHz instrument (Bruker) with TMS as a standard. MALDI-TOF mass spectra were taken on a Micromass ToFSpec 2E in reflectron mode at an accelerating voltage of +20 kV. Absorption measurements were performed on a Cary 50 UV-VIS spectrophotometer from Varian (www.varianinc.com). Fluorescence spectra were recorded on a Hitachi F-7000 spectrofluorimeter (www.hitachi.com). Relative fluorescence quantum yields were determined at 25 °C using rhodamine 101 ($\Phi_F = 0.98$ in ethanol⁵⁰) as a standard. Photostability measurements were performed by irradiating the samples with the light of a 458 nm high-power LED array (10W input power, www.led-tech.de) focused through a lens purchased from Edmund optics. The photodegradation profiles were obtained by monitoring the absorption spectra.

pH-imaging was performed using a RGB-CCD camera (Marlin F201C, Allied Vision Technologies, <http://www.stemmer-imaging.de>) equipped with a Xenoplan 1.4/23 objective lens (<http://www.schneiderkreuznach.com>). For images taken on the fluorescence microscope (Zeiss Axiovert 25 CFL, <http://corporate.zeiss.com>), a blue ultrabright LED with emission maximum at $\lambda = 450$ nm (Luxeon lambert emitter, blue, 5 W) was applied as the excitation light source and combined with a filter set-up consisting of Linos DT blue/Linos DC blue/Schott OG 515 (LINOS Photonics, Göttingen, Germany; Schott, www.schott.com) as the excitation filter/dichromatic mirror/barrier filter, respectively. Image acquisition was performed with the software AVT SmartView (<http://www.alliedvisiontec.com>). Matlab R2008a (www.mathworks.com) was used for image processing. The color channels of the obtained images were separated and the ratiometric images were obtained by dividing the red by the green channel.

Microfluidic flow-through experiments were performed using a custom made flow cell or a 6 channel μ -Slide (ibidi μ -Slide VI^{0.4}, <http://ibidi.com>), which was connected to a syringe pump (model 540060, TSE systems, www.tse-systems.com).

The pH of the buffer solutions was controlled by a digital pH-meter (InoLab pH/ion, WTW GmbH & Co. KG, www.wtw.com) calibrated at 25 °C with standard buffers of pH 7.0 and 4.0. The buffers were adjusted to a constant ionic strength of 100 mM using sodium chloride as the background electrolyte.

7.4.2 Indicator synthesis

7.4.2.1 1,4-Diketo-3-((4-[N-(3,5-dichloro-4-hydroxyphenyl)amino]sulfonyl)phenyl)-6-phenylpyrrolo[3,4-c]pyrrole (2)

1,4-Diketo-3,6-diphenylpyrrolo[3,4-c]pyrrole (500 mg, 1.73 mmol) was heated in chlorosulfuric acid (3 ml) to 60 °C. After 3 h, the mixture was allowed to cool to RT and was added dropwise onto ice cubes. The deep orange precipitate was filtered using a Büchner funnel, rinsed with cold H₂O (0 °C) until pH was neutral and dried by applying a rotary vane pump for 0.5 h. The obtained sulfonyl chloride was dissolved in dry *N,N*-dimethylformamide (30 ml) and 4-amino-2,6-dichlorophenol (1.25 g, 7.02 mmol, 4 equiv.) and triethylamine (1.94 ml, 13.9 mmol) were added. The mixture was stirred for 2.5 h at RT, then 1 M aqueous HCl (150 ml) was added. The precipitate was washed with water, dried and purified by column chromatography (silica gel, 40 – 63 μm) with ethyl acetate / chloroform 75 / 25 as eluent, yield 188 mg (21%). Mp.: Decomposition at > 260 °C. UV/VIS absorption: λ_{max}(tetrahydrofuran)/nm 246 (ε/dm³ mol⁻¹ cm⁻¹ 37 000), 291 (32 100), 509 (22 300) and 543 (24 000). IR absorption:

$\nu_{\max}/\text{cm}^{-1}$ 3426 and 3320 (NH), 3222 (OH), 3030-3160 and 2800-2980 (CH), 1676, 1630 and 1595 (CO), 1555, 1488, 1395, 1331, 1283, 1219, 1156, 1088, 986, 893, 843, 811, 757, 726, 701, 645, 605, 552, 470. NMR (300 MHz, DMSO-*d*₆, TMS): δ_H = 11.47 (1 H, s, Ar-H), 10.44 (1 H, s, ArOH), 10.11 (1 H, s, SO₂NH), 8.3 - 8.7 (2 H, br s, CONH), 8.33 (3 H, d, J = 8.4 Hz, Ar-H), 8.26 (1 H, dd, J₁ = 7.7 Hz, J₂ = 1.1 Hz, Ar-H), 7.70 - 7.86 (4 H, m, Ar-H), 7.09 (2 H, s, Ar-H). δ_C = 175.67, 166.14 (C=O); 147.20, 146.29, 139.39, 139.02, 135.80, 133.54, 132.49, 131.34, 130.49, 130.16, 129.17, 127.65, 126.25, 124.73, 122.64, 120.99, 110.81, 100.35 (aromatic). MALDI-TOF: m/z [MH⁺] 528.0190 found, 528.0188 calcd.

7.4.2.2 1,4-Diketo-3-((4-[N-(3-chloro-4-hydroxyphenyl)amino]sulfonyl)phenyl)-6-phenylpyrrolo[3,4-c]pyrrole (3)

3 was prepared according to the same procedure as **2**, 4-amino-2-chlorophenol (4 equiv.) was reacted with the sulfonyl chloride. Column chromatography was performed with ethyl acetate / ethanol / 25% aqueous NH₃ 93 / 7 / 0.33 as eluent, yield 116 mg (14%). Mp.: Decomposition at > 270 °C. UV/VIS absorption: λ_{max}(tetrahydrofuran)/nm 245 (ε/dm³ mol⁻¹ cm⁻¹ 27 200), 291 (23 800), 508 (17 400) and 541 (18 600). $\nu_{\max}/\text{cm}^{-1}$ 3407 and 3314 (NH), 3225 (OH), 3030-3160 and 2800-2980 (CH), 2360, 2339, 1677, 1635 and 1593 (CO), 1557, 1507, 1487, 1405, 1332, 1287, 1202, 1156, 1088, 1053, 953, 895, 843, 820, 757, 726, 701, 614, 597, 544, 496. NMR (300 MHz, DMSO-*d*₆, TMS): δ_H = 11.45 (1 H, s, Ar-H), 10.10 (2 H, d, ArOH, SO₂NH), 8.3 - 8.7 (2 H, br s, CONH), 8.31 (3 H, dd, J₁ = 8.1 Hz, J₂ = 2.1 Hz, Ar-H), 8.26 (1 H, dd, J₁ = 7.7 Hz, J₂ = 1.4 Hz, Ar-H), 7.70 - 7.86 (4 H, m, Ar-H), 7.06 (1 H, d, J = 2.3 Hz, Ar-H), 6.89 (1 H, dd, J₁ = 8.7 Hz, J₂ = 2.4 Hz, Ar-H), 6.85 (1 H, d, J = 8.5 Hz, Ar-H). δ_C = 175.64, 166.15 (C=O); 150.50, 147.15, 139.79, 139.16, 135.81, 133.26, 132.46, 131.31, 130.48, 129.24, 128.99, 127.65, 126.67, 124.71, 123.23, 121.78, 119.54, 116.90, 110.75, 100.36 (aromatic). MALDI-TOF: m/z [MH⁺] 494.0600 found, 494.0577 calcd.

7.4.2.3 1,4-Diketo-3-((4-(1-morpholinyl)sulfonyl)phenyl)-6-phenylpyrrolo[3,4-c]pyrrole (4)

1,4-Diketo-3,6-diphenylpyrrolo[3,4-c]pyrrole (300 mg, 1.04 mmol) was heated in chlorosulfuric acid (3 ml) to 60 °C. After 3 h, the mixture was allowed to cool to RT and added dropwise onto morpholine (10 ml). The deep red mixture was stirred for 10 min and H₂O (80 ml) was added. The

precipitate formed was thoroughly washed with water, dried and purified by column chromatography (silica gel, 40 – 63 μm) with methanol / chloroform 95 / 5 as eluent, yield 170 mg (22 %). Mp. > 300 °C. UV/VIS absorption: λ_{max} (tetrahydrofuran)/nm 247 ($\epsilon/\text{dm}^3 \text{ mol}^{-1} \text{ cm}^{-1}$ 28 000), 292 (27 900), 509 (20 000) and 541 (21 400). IR absorption: $\nu_{\text{max}}/\text{cm}^{-1}$ 3419 and 3309 (NH), 3030-3170 and 2780-2980 (CH), 2368, 2339, 1665, 1627 and 1597 (CO), 1554, 1486, 1449, 1436, 1340, 1325, 1284, 1260, 1161, 1114, 1095, 938, 839, 747, 701, 668, 612, 595, 536, 469. NMR (300 MHz, DMSO- d_6 , TMS): δ_{H} = 11.58 (1 H, s, Ar-H), 8.3 - 8.8 (2 H, CONH), 8.50 (2 H, d, J = 8.7 Hz, Ar-H), 8.36 (1 H, d, J = 7.8 Hz, Ar-H), 8.30 (1 H, dd, J_1 = 7.8 Hz, J_2 = 1.1 Hz, Ar-H), 7.85 (3 H, dt, J_1 = 8.4 Hz, J_2 = 1.9 Hz, Ar-H), 7.77 (1 H, t, J = 7.5 Hz, Ar-H), 3.67 (4 H, t, J = 4.2 Hz, OCH₂), 2.95 (4 H, t, J = 4.1 Hz, ArNCH₂). δ_{C} = 175.71, 166.19 (C=O); 147.27, 138.99, 135.81, 135.01, 133.76, 132.49, 131.34, 130.48, 129.15, 127.66, 127.26, 124.73, 110.90, 100.41 (aromatic); 65.29 (C-O); 45.92 (C-N). MALDI-TOF: m/z [MH⁺] 438.10 found, 438.11 calcd.

7.4.3 Preparation of planar sensors

A “cocktail” containing indicator dye (0.16 mg), hydrogel D4 / p(HEMA) (41 mg) and ethanol / water 9:1 (V/V) (500 μl) was knife-coated on a dust-free Mylar support to obtain a \approx 7 μm thick layer after solvent evaporation. Ratiometric sensors were prepared in analogy, using 0.2 mg of **2**, 0.6 mg of Macrolex Yellow and tetrahydrofuran (461 μl) as a solvent.

7.4.4 Preparation of sensor nanoparticles

Eudragit RL100 (100 mg) was dissolved in acetone (50 ml), indicator dye (1 mg) and Macrolex yellow (1.25 mg) were added. Water (300 ml) was added quickly (5 s). Acetone was removed on a rotary evaporator and the particle suspension was concentrated to a volume of 50 ml.

7.5 Acknowledgements

Financial support from the Austrian Science Fund FWF (project P 21192-N17) is gratefully acknowledged. We thank Martin Thonhofer, Institute of Organic Chemistry, and Stefan Müller, Institute of Inorganic Chemistry, for their support in measuring melting points and IR spectra.

7.6 Notes and References

^aInstitute of Analytical Chemistry and Food Chemistry, Graz University of Technology, Stremayrgasse 9, Graz, Austria. Tel: +43 316 873 32516; E-mail: sergey.borisov@tugraz

^bInstitute for Chemistry and Technology of Materials, Graz University of Technology, Stremayrgasse 9, A-8010 Graz, Austria

† Electronic Supplementary Information (ESI) available: NMR and MS spectra, further sensor characteristics and sensor long-time performance. See DOI: 10.1039/c3tc31130a

1. M. Schäferling, *Angew. Chem., Int. Ed.*, 2012, **51**, 3532–3554.
2. M. Kühn and L. Polerecky, *Aquat. Microb. Ecol.*, 2008, **53**, 99–118.
3. H. Stahl, A. Glud, C. R. Schröder, I. Klimant, A. Tengberg, and R. N. Glud, *Limnol. Oceanogr.: Meth.*, 2006, **4**, 336–345.
4. G. Liebsch, I. Klimant, C. Krause, and O. S. Wolfbeis, *Anal. Chem.*, 2001, **73**, 4354–4363.
5. S. Hulth, R. C. Aller, P. Engström, and E. Selander, *Limnol. Oceanogr.*, 2002, **47**, 212–220.
6. J. Han and K. Burgess, *Chem. Rev.*, 2010, **110**, 2709–2728.
7. A. Almutairi, S. J. Guillaudeu, M. Y. Berezin, S. Achilefu, and J. M. J. Fréchet, *J. Am. Chem. Soc.*, 2008, **130**, 444–445.
8. C. Munkholm, D. R. Walt, F. P. Milanovich, and S. M. Klainer, *Anal. Chem.*, 1986, **58**, 1427–1430.

9. N. Strömberg, E. Mattsson, and A. Hakonen, *Anal. Chim. Acta*, 2009, **636**, 89–94.
10. J. E. Whitaker, R. P. Haugland, and F. G. Prendergast, *Anal. Biochem.*, 1991, **194**, 330–344.
11. A. P. de Silva, T. Gunnlaugsson, and T. E. Rice, *Analyst*, 1996, **121**, 1759–1762.
12. A. P. de Silva, T. P. Vance, M. E. S. West, and G. D. Wright, *Org. Biomol. Chem.*, 2008, **6**, 2468–2480.
13. R. A. Bissell, A. P. de Silva, H. Q. N. Gunaratne, P. L. M. Lynch, G. E. M. Maguire, and K. R. A. S. Sandanayake, *Chem. Soc. Rev.*, 1992, **21**, 187–195.
14. R. A. Bissell, E. Calle, A. P. de Silva, S. A. de Silva, H. Q. N. Gunaratne, J.-L. Habib-Jiwan, S. L. A. Peiris, R. A. D. D. Rupasinghe, T. K. Shantha, D. Samarasinghe, K. R. A. S. Sandanayake, and J.-P. Soumillion, *J. Chem. Soc., Perkin Trans. 2*, 1992, 1559–1564.
15. K. Zhou, Y. Wang, X. Huang, K. Luby-Phelps, B. D. Sumer, and J. Gao, *Angew. Chem.*, 2011, **50**, 6109–6114.
16. N. Saleh, Y. A. Al-Soud, and W. M. Nau, *Spectrochim. Acta Part A*, 2008, **71**, 818–822.
17. T. Werner, C. Huber, S. Heinl, M. Kollmannsberger, J. Daub, and O. S. Wolfbeis, *Fresenius' J. Anal. Chem.*, 1997, **359**, 150–154.
18. T. Gareis, C. Huber, O. S. Wolfbeis, and J. Daub, *Chem. Commun.*, 1997, 1717–1718.
19. M. Baruah, W. Qin, N. Basarić, W. M. De Borggraeve, and N. Boens, *J. Org. Chem.*, 2005, **70**, 4152–4157.
20. N. Boens, V. Leen, and W. Dehaen, *Chem. Soc. Rev.*, 2012, **41**, 1130–1172.
21. C. N. Baki and E. U. Akkaya, *J. Org. Chem.*, 2001, **66**, 1512–1513.
22. T. Potrawa and H. Langhals, *Chem. Ber.*, 1987, **120**, 1075–1078.
23. W. Herbst and K. Hunger, *Industrial Organic Pigments*, third ed., WILEY-VCH, Weinheim, 2004, pp. 487–494.
24. Z. Hao and A. Iqbal, *Chem. Soc. Rev.*, 1997, **26**, 203–213.
25. S. Luňák Jr., M. Vala, J. Vyňuchal, I. Ouzzane, P. Horáková, P. Možišková, Z. Eliáš, and M. Weiter, *Dyes and Pigm.*, 2011, **91**, 269–278.
26. S. Luňák Jr., J. Vyňuchal, M. Vala, L. Havel, and R. Hrdina, *Dyes and Pigm.*, 2009, **82**, 102–108.
27. J. S. Zambounis, Z. Hao, and A. Iqbal, *Nature*, 1997, **388**, 131–132.
28. J. C. Bijleveld, A. P. Zoombelt, S. G. J. Mathijssen, M. M. Wienk, M. Turbiez, D. M. de Leeuw, and R. A. J. Janssen, *J. Am. Chem. Soc.*, 2009, **131**, 16616–16617.
29. Y. Zhu, A. R. Rabindranath, T. Beyerlein, and B. Tieke, *Macromolecules*, 2007, **40**, 6981–6989.
30. K. Zhang and B. Tieke, *Macromolecules*, 2008, **41**, 7287–7295.
31. B. Walker, A. B. Tamayo, X.-D. Dang, P. Zalar, J. H. Seo, A. Garcia, M. Tantiwiwat, and T.-Q. Nguyen, *Adv. Funct. Mater.*, 2009, **19**, 3063–3069.
32. M. Tantiwiwat, A. Tamayo, N. Luu, X.-D. Dang, and T.-Q. Nguyen, *J. Phys. Chem. C*, 2008, **112**, 17402–17407.
33. L. Bürgi, M. Turbiez, R. Pfeiffer, F. Bienewald, H.-J. Kirner, and C. Winnewisser, *Adv. Mater.*, 2008, **20**, 2217–2224.
34. M. M. Wienk, M. Turbiez, J. Gilot, and R. A. J. Janssen, *Adv. Mater.*, 2008, **20**, 2556–2560.
35. Y. Zou, D. Gendron, R. Badrou-Aïch, A. Najari, Y. Tao, and M. Leclerc, *Macromolecules*, 2009, **42**, 2891–2894.
36. Y. Jiang, Y. Wang, J. Hua, S. Qu, S. Qian, and H. Tian, *J. Polym. Sci. A: Polym. Chem.*, 2009, **47**, 4400–4408.
37. E. Q. Guo, P. H. Ren, Y. L. Zhang, H. C. Zhang, and W. J. Yang, *Chem. Commun.*, 2009, 5859–5861.
38. Y. Qu, J. Hua, and H. Tian, *Org. Lett.*, 2010, **12**, 3320–3323.
39. Y.-H. Jeong, C.-H. Lee, and W.-D. Jang, *Chem. Asian J.*, 2012, **7**, 1562–1566.
40. L. Deng, W. Wu, H. Guo, J. Zhao, S. Ji, X. Zhang, X. Yuan, and C. Zhang, *J. Org. Chem.*, 2011, **76**, 9294–9304.
41. J. Mizuguchi, T. Imoda, H. Takahashi, and H. Yamakami, *Dyes Pigm.*, 2006, **68**, 47–52.
42. T. Yamagata, J. Kuwabara, and T. Kanbara, *Tetrahedron Lett.*, 2010, **51**, 1596–1599.
43. S. Schutting, S. M. Borisov, and I. Klimant, *Anal. Chem.*, 2013, **85**, 3271–3279.
44. M. Thakur, A. Thakur, P. V. Khadikar and C. T. Supuran, *Bioorg. Med. Chem. Lett.*, 2005, **15**, 203–209.
45. C. Caltagirone, G. W. Bates, P. A. Gale and M. E. Light, *Chem. Commun.*, 2008, 61–63.
46. M. Larsen, S. M. Borisov, B. Grunwald, I. Klimant, and R. N. Glud, *Limnol. Oceanogr.: Meth.*, 2011, **9**, 348–360.
47. R. J. Meier, L. H. Fischer, O. S. Wolfbeis, and M. Schäferling, *Sens. Actuators B: Chemical*, 2013, **177**, 500–506.

48. X. Wang, H. H. Gorris, J. A. Stolwijk, R. J. Meier, D. B. M. Groegel, J. Wegener, and O. S. Wolfbeis, *Chem. Sci.*, 2011, **2**, 901.
49. S. Jezierski, D. Belder, and S. Nagl, *Chem. Commun.*, 2013, **49**, 904–906.
50. R. F. Kubin and A. N. Fletcher, *J. Luminescence*, 1982, **27**, 455–462.

7.7 Electronic Supplementary Information

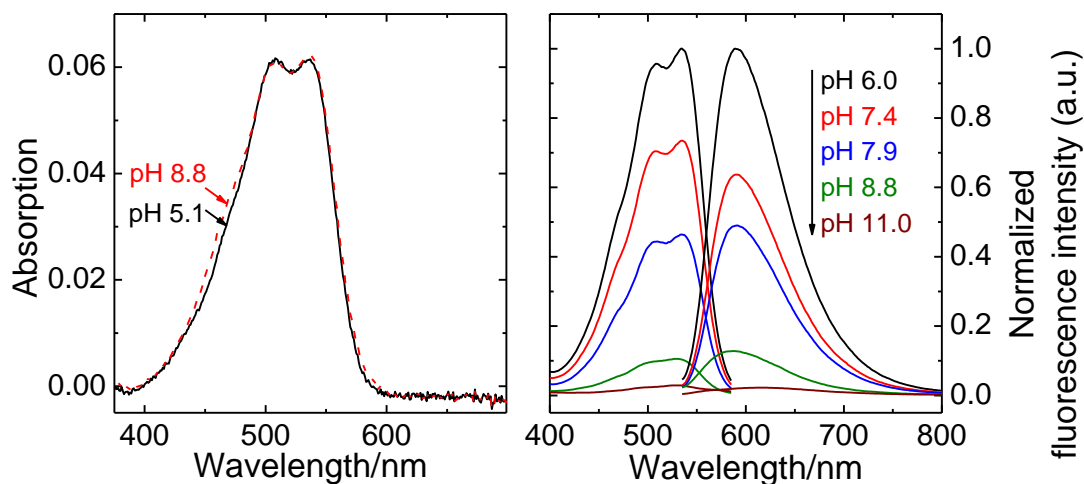


Figure S1. pH-dependent absorption and fluorescence spectra of **3**. Spectra were recorded in ethanol/aqueous buffer (ionic strength 100 mM) solution 1:1 (V/V). pH values are those of the aqueous buffer used. DPP concentration was 20 μ M for absorption and 4 μ M for fluorescence measurements.

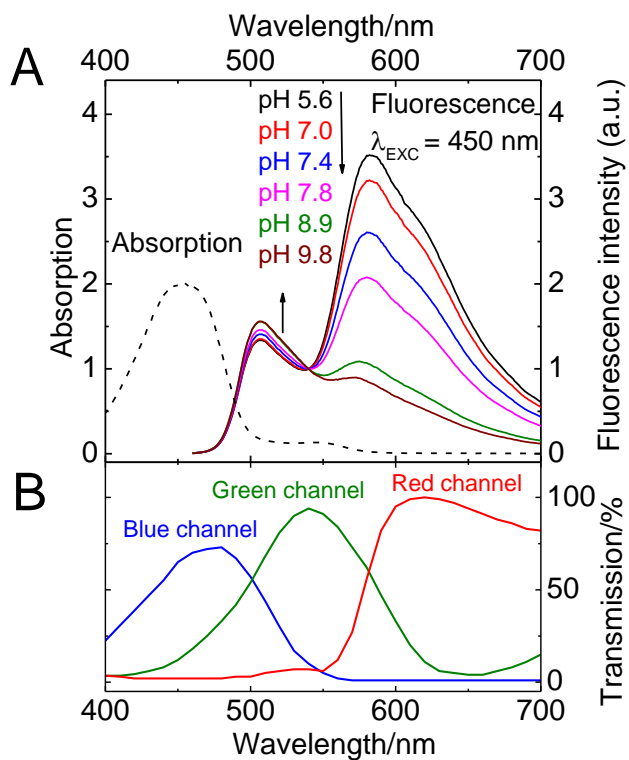


Figure S2. A: pH-dependent fluorescence spectra a planar ratiometric sensor containing Macrolex Yellow (1.5% (w/w)) and DPP pH-indicator **2** (0.5% (w/w)). B: Spectral characteristics of the RGB CCD camera.

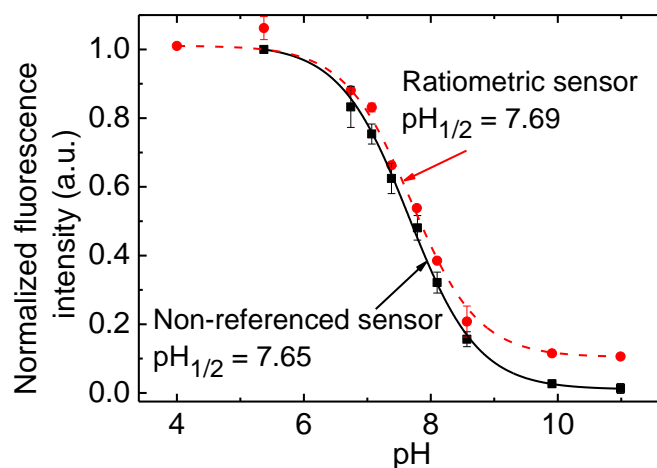


Figure S3. pH calibration curve of the ratiometric sensor beads, *i.e.* dye 3 (1% w/w) and Macrolex Yellow (reference dye; 1.25% w/w) in RL100 (bead content 2 mg / ml in aqueous buffer of ionic strength 100 mM), compared to beads containing only 3 (0.5% w/w) - this non-referenced system is also included into Figure 2.1 (main text).

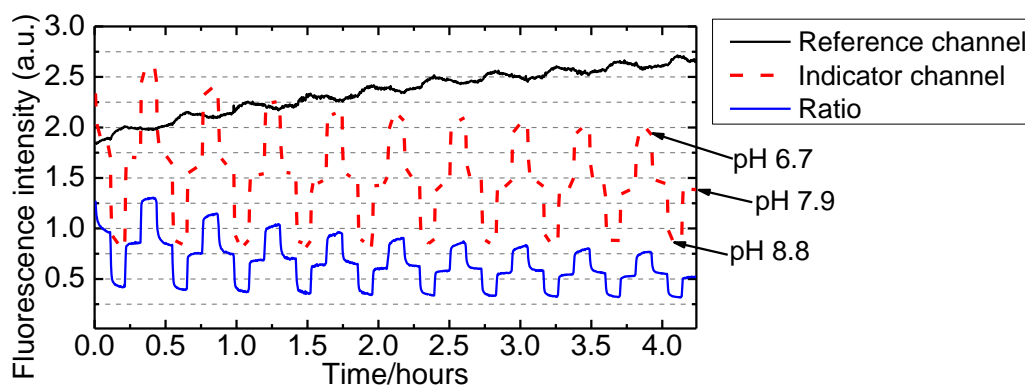


Figure S4. Long-time performance of a planar ratiometric sensor containing Indicator 2 (0.5% w/w) and Macrolex Yellow (1.5% w/w) in D4 hydrogel, excited with a 450 nm LED (Roithner, www.roithner-laser.com) combined with a Schott BG 12 bandpass filter (350 - 465 nm). The reference channel was equipped with 520 / 40 nm bandpass filter, the indicator channel with a 600 / 50 nm bandpass filter (both from Edmund optics, www.edmundoptics.de). Both channels were equipped with separate PMT detectors, *i.e.* do not represent absolute brightness ratios. The planar sensor was placed in a home-made flow-through cell and 100 mM buffer was passed through the cell, flow rate 1ml / min. Cell temperature was kept constant at 25 °C. The sensors were interrogated with a two-phase lock-in amplifier (SR830, Stanford Research Inc., www.thinksrs.com) equipped with a PMT detector (H5701-02, Hamamatsu, www.sales.hamamatsu.com). Illumination time was 1% of the measurement time.

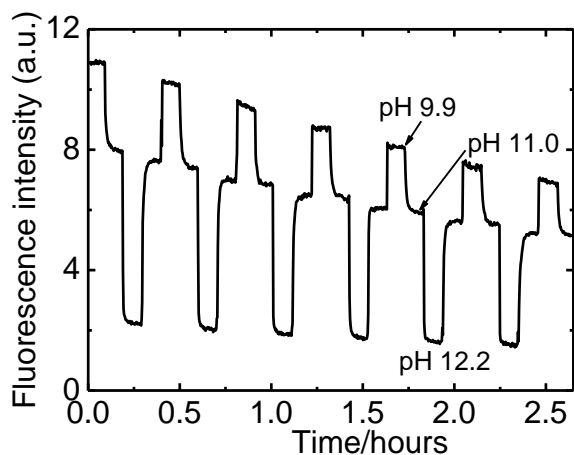


Figure S5. Long-time performance of a planar sensor containing **4** (0.4% w/w) in D4 hydrogel, excited with a 525 nm LED combined with a 520 / 40 nm bandpass filter (Edmund Optics) and a Schott OG 550 nm longpass filter before the detector. Measurement was carried out as stated near fig. S3.

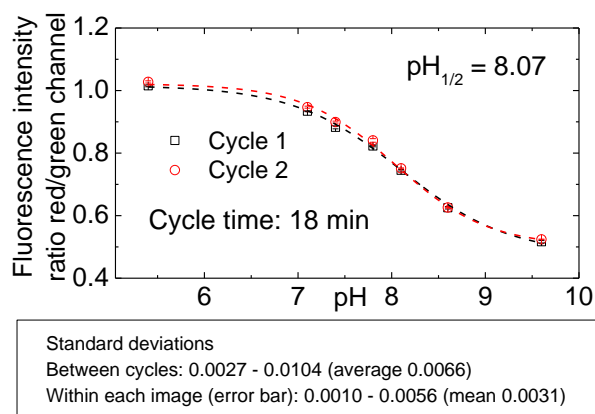


Figure S6. pH-calibration curve of pH-nanosensor beads containing dye **3** (1% w/w) and Macrolex yellow (reference dye; 1.25% w/w) in RL100 polymer. The beads were read out under the fluorescence microscope employing a RGB-CCD camera. Response curve and images are shown in Figure 7.7.

NMR spectra

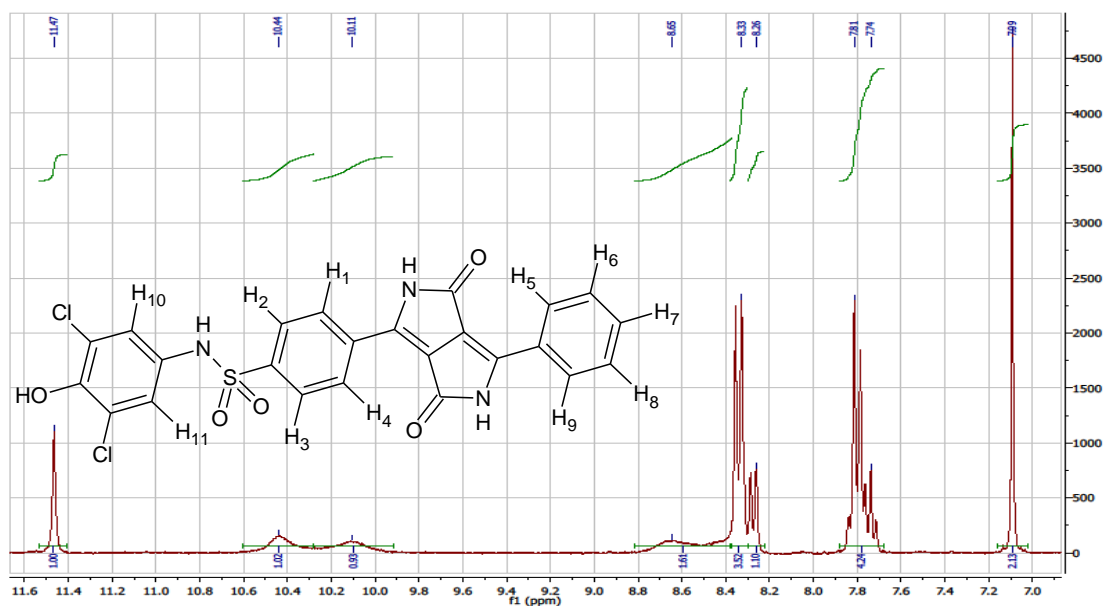


Figure S7: ¹H-NMR spectrum of 2 (300 MHz, DMSO-d₆, TMS): δ H = 11.47 (1 H, s, Ar-H(9)), 10.44 (1 H, s, ArOH), 10.11 (1 H, s, SO₂NH), 8.3 - 8.7 (2 H, CONH), 8.33 (3 H, d, J = 8.4 Hz, Ar-H(2,3,5)), 8.26 (1 H, dd, J₁ = 7.7 Hz, J₂ = 1.1 Hz, Ar-H(8)), 7.70 - 7.86 (4 H, m, Ar-H(1,4,6,7)), 7.09 (2 H, s, Ar-H(10,11)).

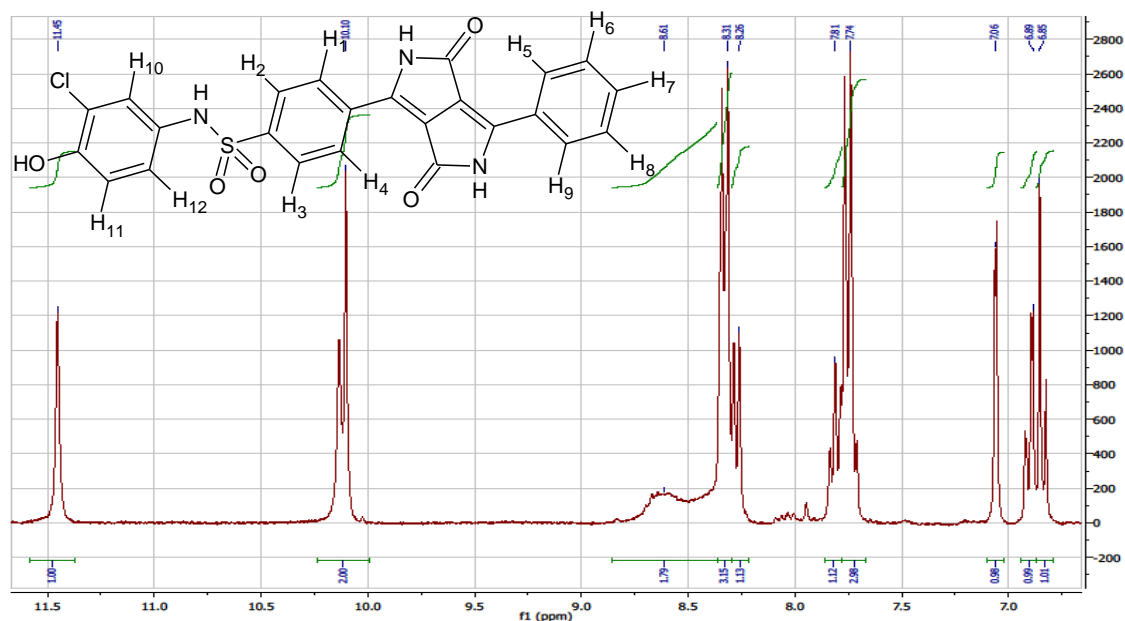


Figure S8. ¹H-NMR spectrum of 3 (300 MHz, DMSO-d₆, TMS): δ H = 11.45 (1 H, s, Ar-H(9)), 10.10 (2 H, d, ArOH, SO₂NH), 8.3 - 8.7 (2 H, CONH), 8.31 (3 H, dd, J₁ = 8.1 Hz, J₂ = 2.1 Hz, Ar-H(2,3,5)), 8.26 (1 H, dd, J₁ = 7.7 Hz, J₂ = 1.4 Hz, Ar-H(8)), 7.70 - 7.86 (4 H, m, Ar-H(1,4,6,7)), 7.06 (1 H, d, J = 2.3 Hz, Ar-H(10)), 6.89 (1 H, dd, J₁ = 8.7 Hz, J₂ = 2.4 Hz, Ar-H(12)), 6.85 (1 H, d, J = 8.5 Hz, Ar-H(11)).

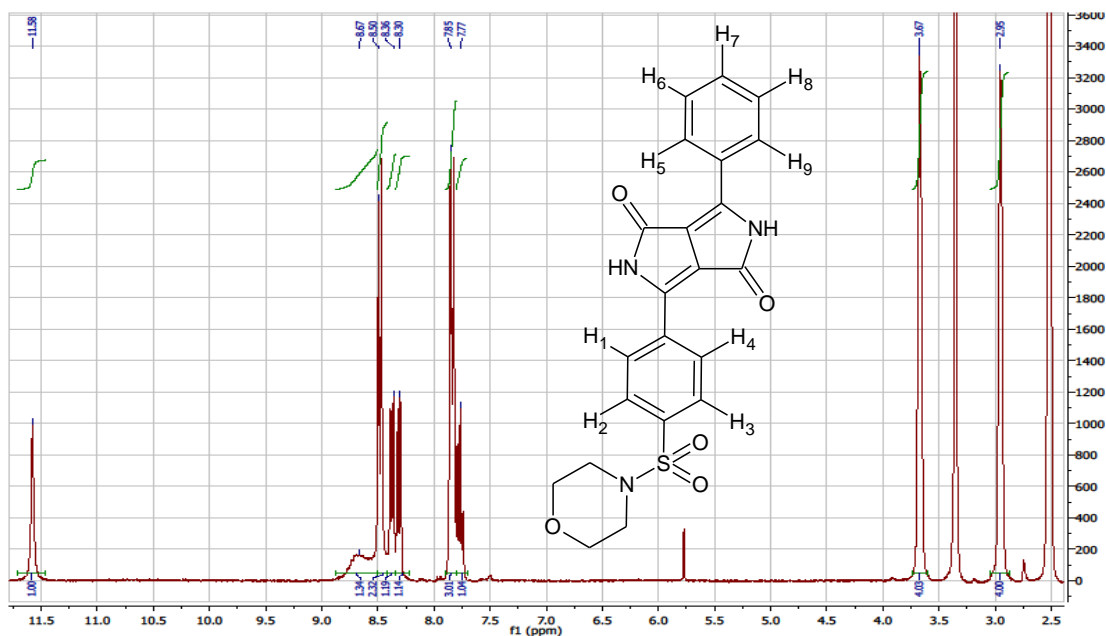


Figure S9. $^1\text{H-NMR}$ spectrum of **4** (300 MHz, DMSO-d_6 , TMS): $\delta_{\text{H}} = 11.58$ (1 H, s, Ar-H(9)), 8.3 - 8.8 (2 H, CONH), 8.50 (2 H, d, $J = 8.7$ Hz, Ar-H(2,3)), 8.36 (1 H, d, $J = 7.8$ Hz, Ar-H(5)), 8.30 (1 H, dd, $J_1 = 7.8$ Hz, $J_2 = 1.1$ Hz, Ar-H(8)), 7.85 (3 H, dt, $J_1 = 8.4$ Hz, $J_2 = 1.9$ Hz, Ar-H(1,4,6)), 7.77 (1 H, t, $J = 7.5$ Hz, Ar-H(7)), 3.67 (4 H, t, $J = 4.2$ Hz, OCH₂), 2.95 (4 H, t, $J = 4.1$ Hz, ArNCH₂).

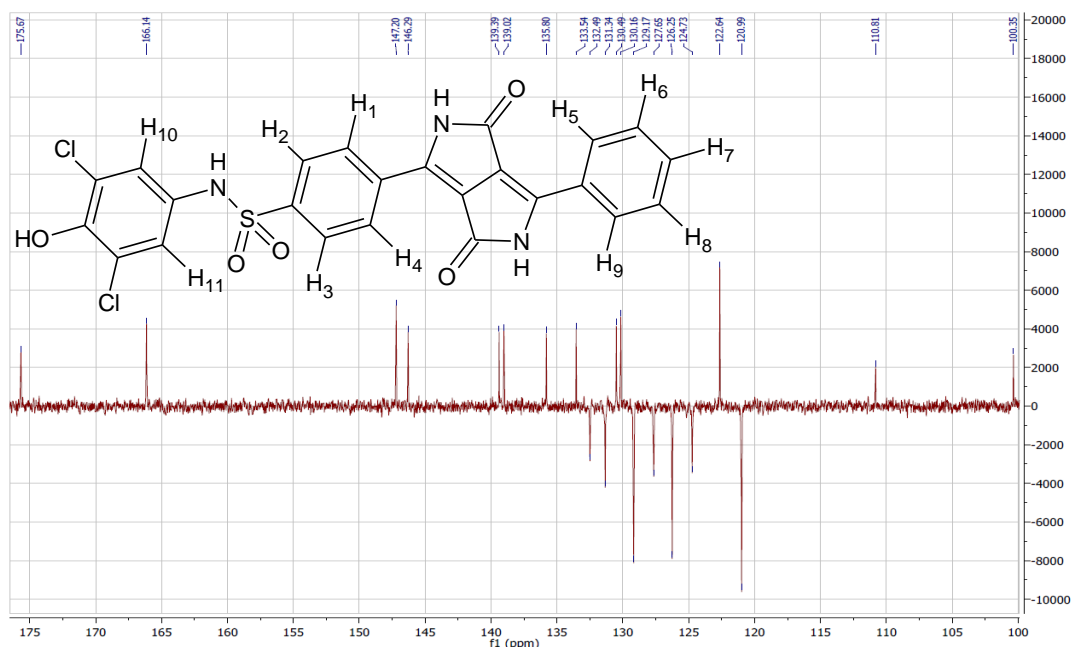


Figure S10. $^{13}\text{C-APT-NMR}$ spectrum of **2** (300 MHz, DMSO-d_6 , TMS): $\delta_{\text{C}} = 175.67, 166.14$ (C=O); 147.20, 146.29, 139.39, 139.02, 135.80, 133.54 (C_{Ar}); 132.49 ($\text{C}_{\text{Ar-H6}}$), 131.34 ($\text{C}_{\text{Ar-H7}}$); 130.49, 130.16 (C_{Ar}); 129.17 (2C, $\text{C}_{\text{Ar-H2}}$, $\text{C}_{\text{Ar-H3}}$), 127.65 ($\text{C}_{\text{Ar-H8}}$), 126.25 (2C, $\text{C}_{\text{Ar-H1}}$, $\text{C}_{\text{Ar-H4}}$), 124.73 ($\text{C}_{\text{Ar-H5}}$); 122.64 (2C, C_{Ar}); 120.99 (2C, $\text{C}_{\text{Ar-H10}}$, $\text{C}_{\text{Ar-H11}}$); 110.81, 100.35 (C_{Ar}).

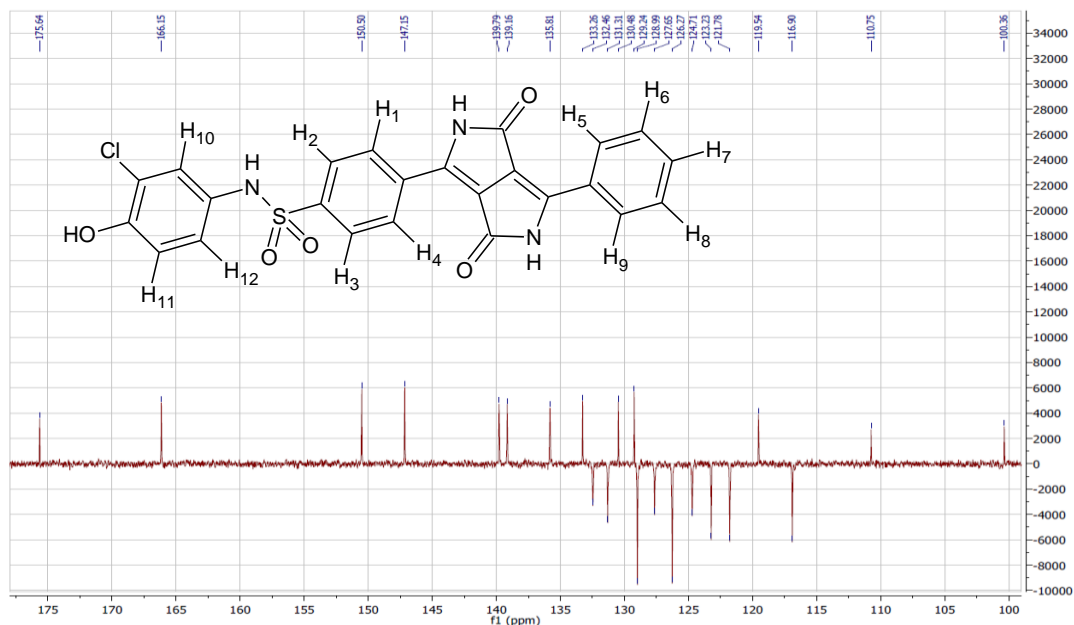


Figure S11. ^{13}C -APT-NMR spectrum of **3** (300 MHz, $\text{DMSO-}d_6$, TMS): δ_{C} = 175.64, 166.15 (C=O); 150.50, 147.15, 139.79, 139.16, 135.81, 133.26 (C_{Ar}); 132.46 ($\text{C}_{\text{Ar-H6}}$), 131.31 ($\text{C}_{\text{Ar-H7}}$); 130.48, 129.24 (C_{Ar}); 128.99 (2C, $\text{C}_{\text{Ar-H2}}$, $\text{C}_{\text{Ar-H3}}$), 127.65 ($\text{C}_{\text{Ar-H8}}$), 126.67 (2C, $\text{C}_{\text{Ar-H1}}$, $\text{C}_{\text{Ar-H4}}$), 124.71 ($\text{C}_{\text{Ar-H5}}$), 123.23 ($\text{C}_{\text{Ar-H10}}$), 121.78 ($\text{C}_{\text{Ar-H12}}$); 119.54 (C_{Ar}); 116.90 ($\text{C}_{\text{Ar-H11}}$); 110.75, 100.36 (C_{Ar}).

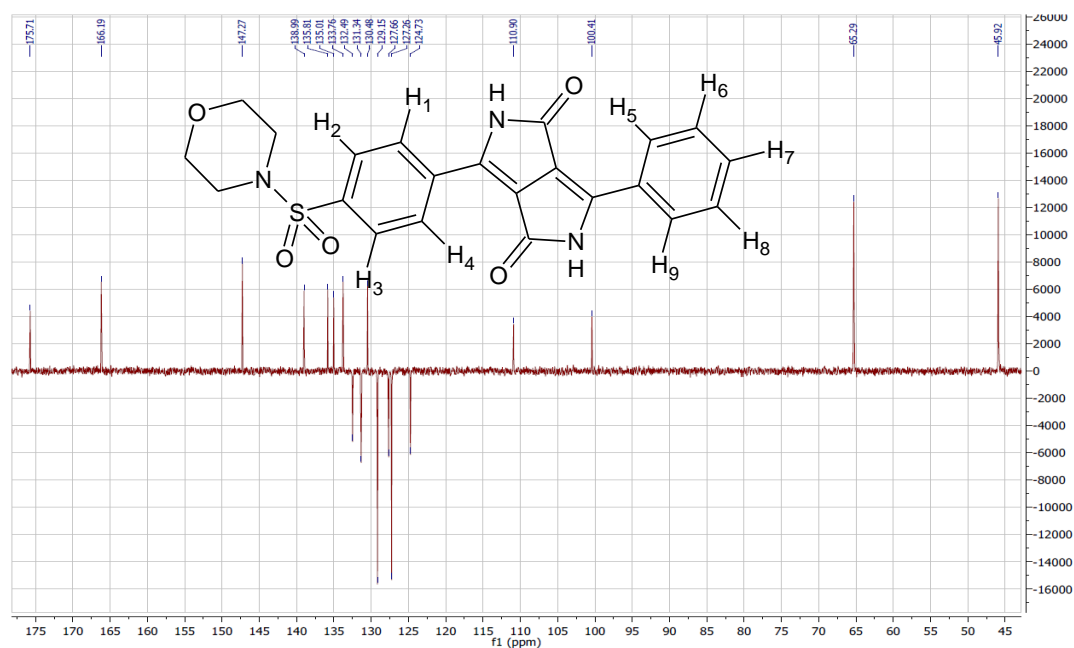


Figure S12: ^{13}C -APT-NMR spectrum of **4** (300 MHz, $\text{DMSO-}d_6$, TMS): δ_{C} = 175.71, 166.19 (C=O); 147.27, 138.99, 138.81, 135.01, 133.76 (C_{Ar}); 132.49 ($\text{C}_{\text{Ar-H6}}$), 131.34 ($\text{C}_{\text{Ar-H7}}$); 130.48, (C_{Ar}); 129.15 (2C, $\text{C}_{\text{Ar-H2}}$, $\text{C}_{\text{Ar-H3}}$), 127.66 ($\text{C}_{\text{Ar-H8}}$), 127.26 (2C, $\text{C}_{\text{Ar-H1}}$, $\text{C}_{\text{Ar-H4}}$), 124.73 ($\text{C}_{\text{Ar-H5}}$); 110.90, 100.41 (C_{Ar}); 65.29 (C-O); 45.92 (C-N).

MALDI-TOF spectra:

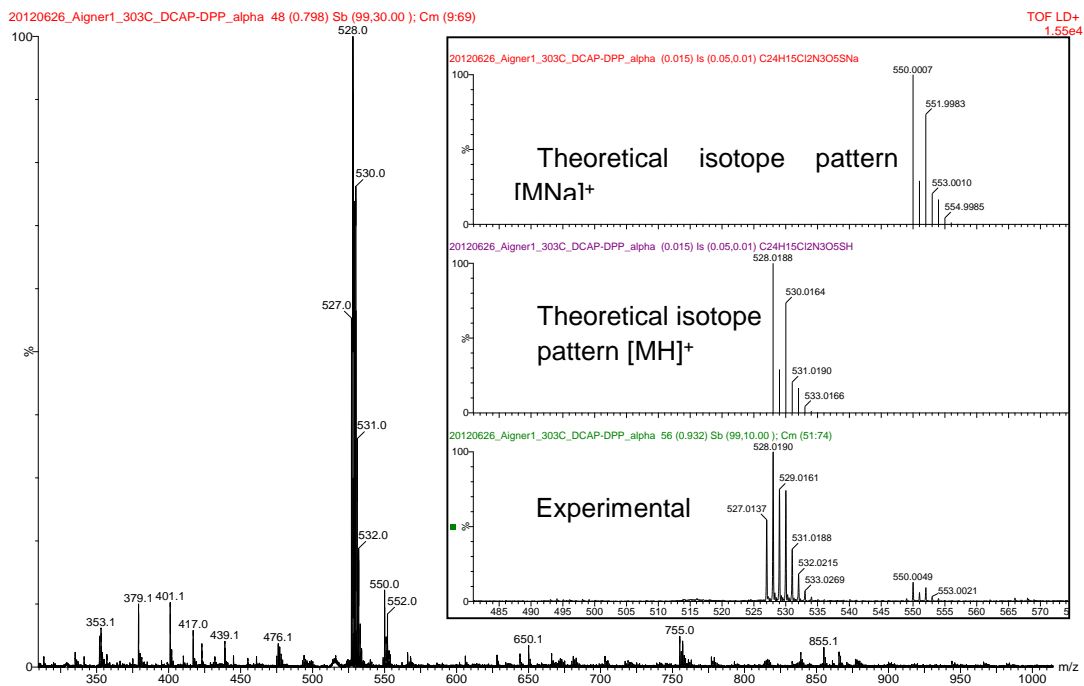


Figure S13. MALDI-TOF spectrum of 2

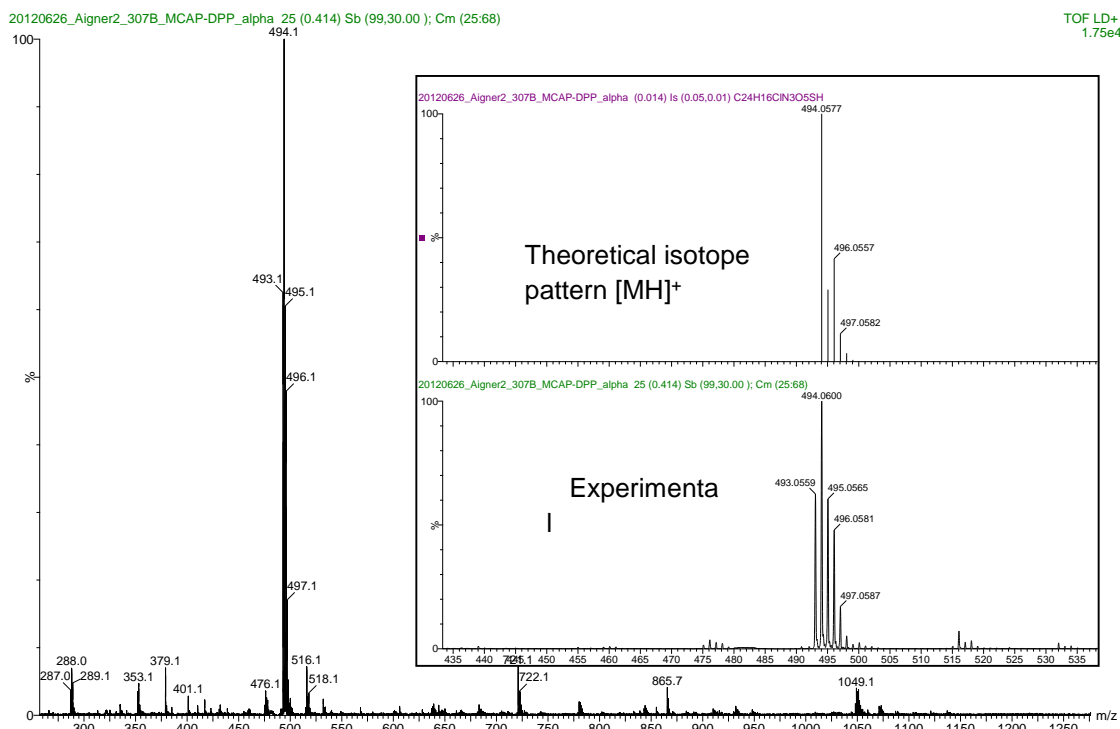


Figure S14. MALDI-TOF spectrum of 3

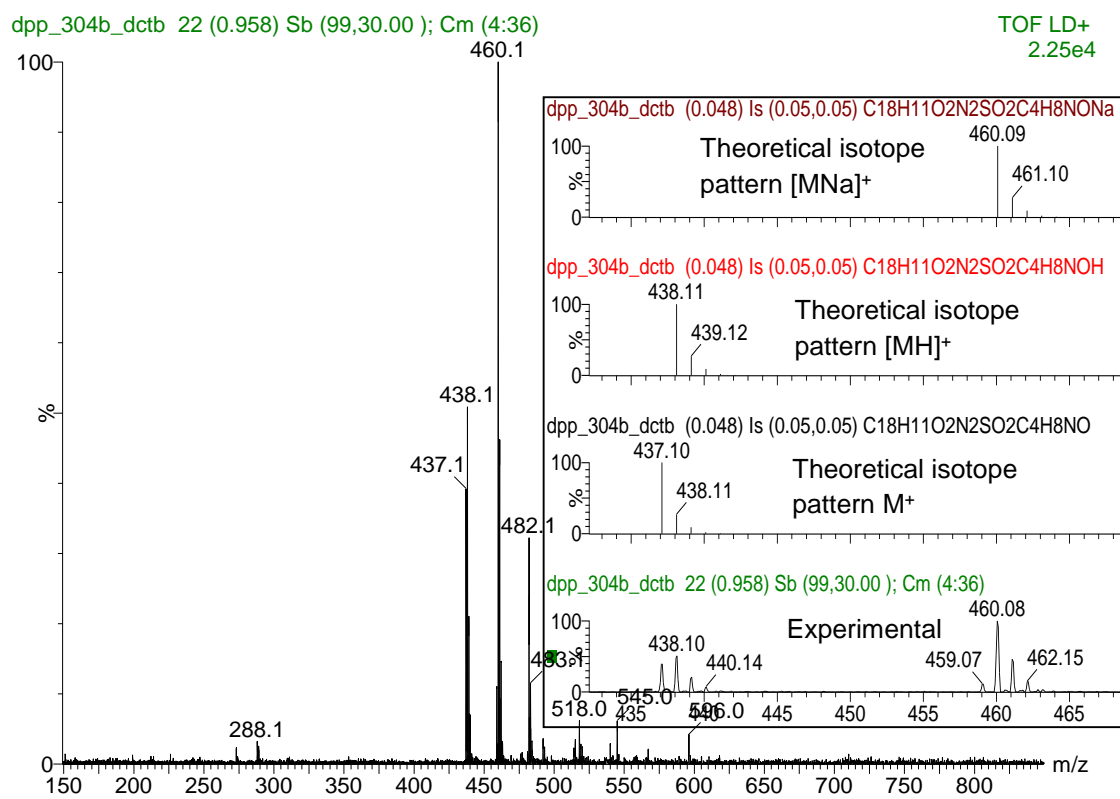


Figure S15. MALDI-TOF spectrum of 4

Full UV/VIS absorption spectra (230 – 1000 nm):

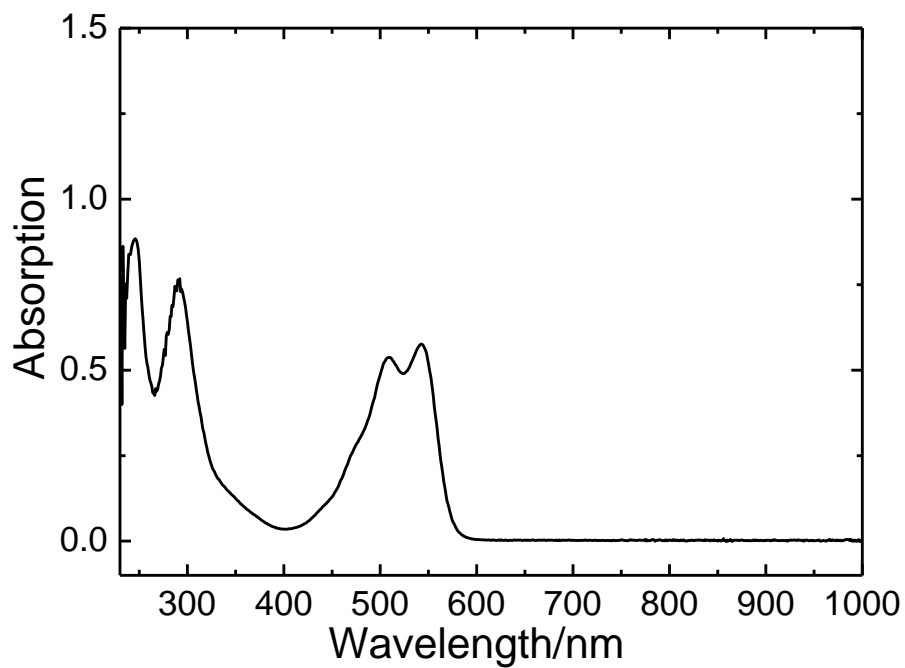


Figure S16. UV/VIS absorption spectrum of 2 in tetrahydrofuran

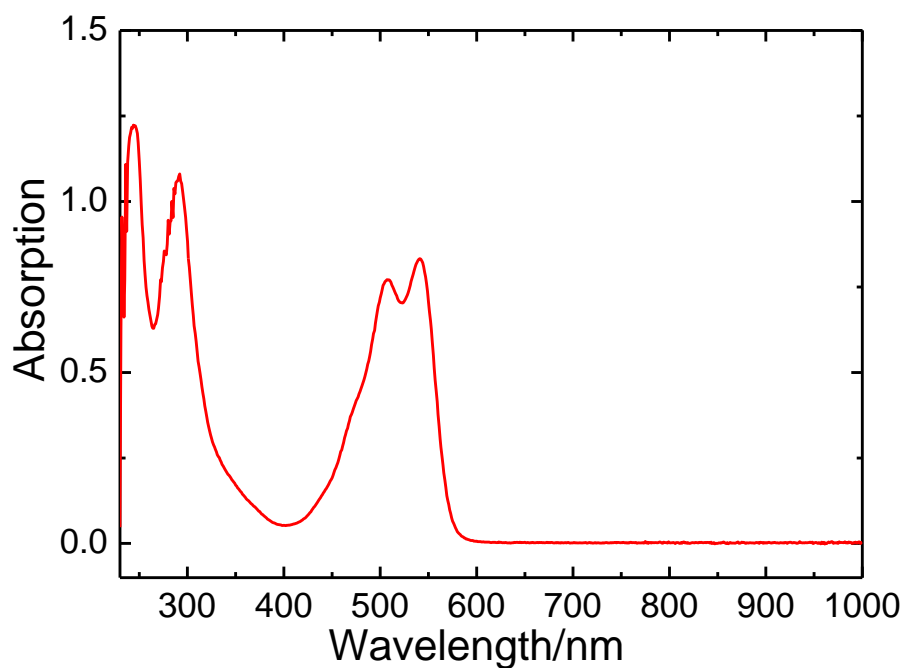


Figure S17. UV/VIS absorption spectrum of 3 in tetrahydrofuran

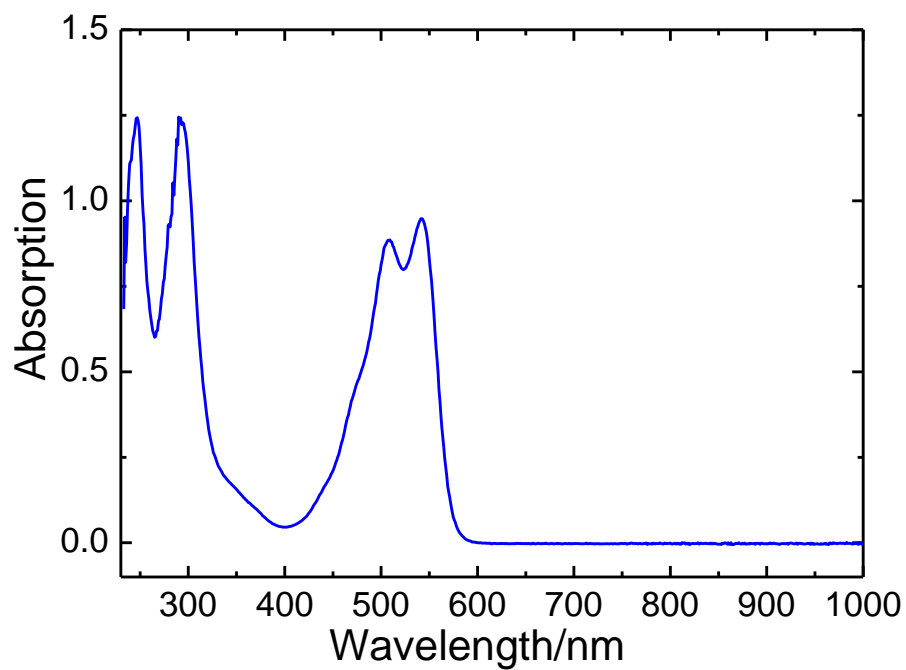


Figure S18. UV/VIS absorption spectrum of 4 in tetrahydrofuran

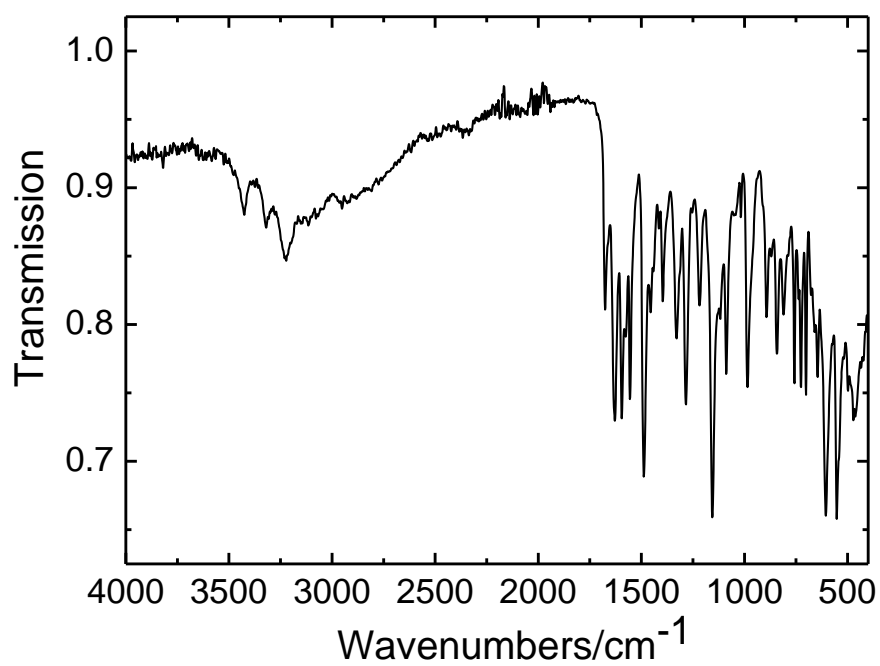


Figure S19: ATR-IR spectrum of 2

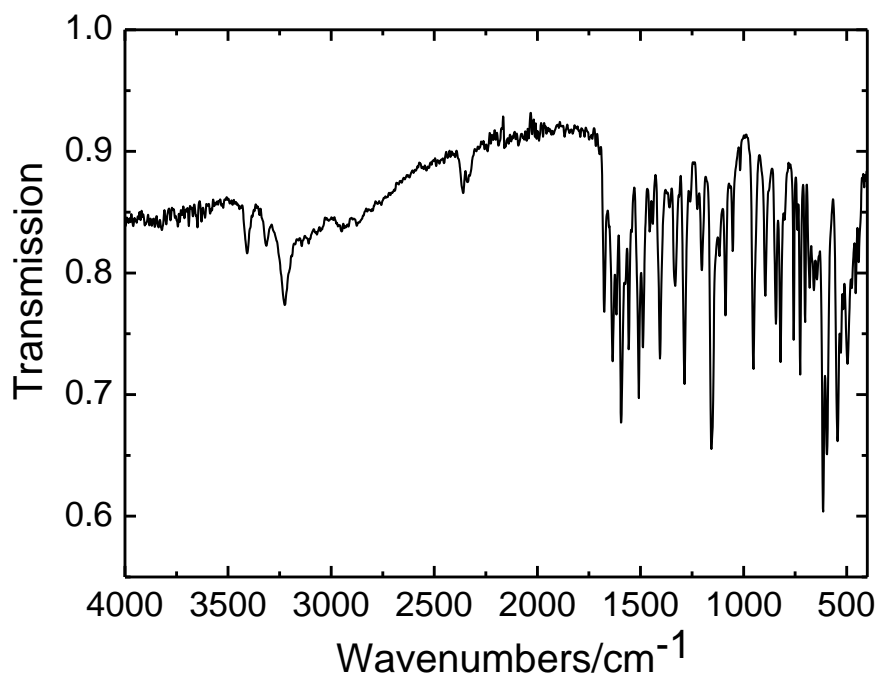


Figure S20. ATR-IR spectrum of 3

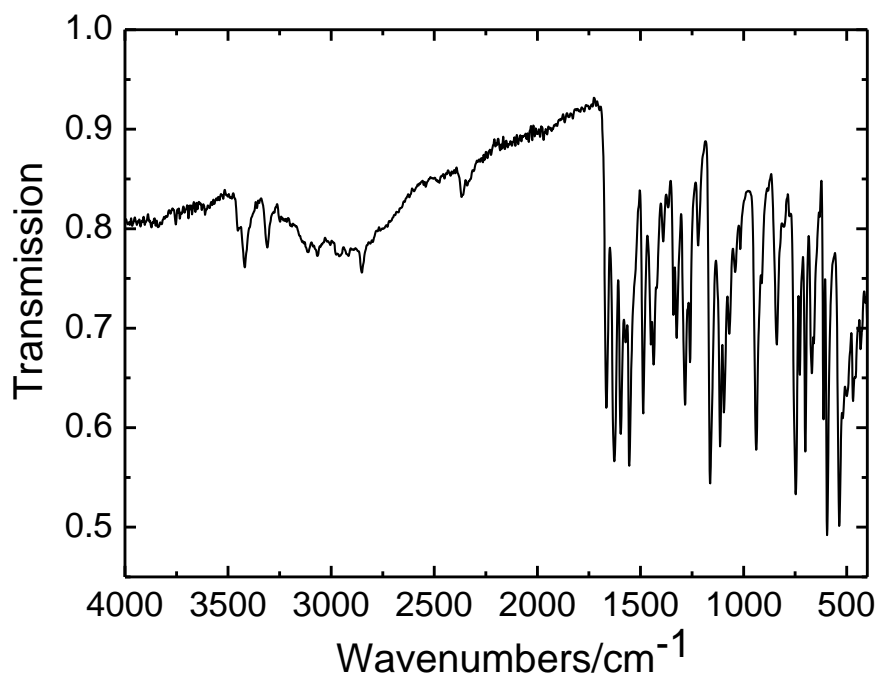


Figure S21: ATR-IR spectrum of 4

8 Summary and Conclusion

The integration of analytical tools into miniaturized devices is a challenging scientific task due to several reasons: the need of the sensing device to be scalable to smaller dimensions, the importance of overall costs of microfluidic devices and a reduced analysis volume and consequentially a small number of analyte molecules. Optical on-chip sensors, and especially luminescent sensors, provide a range of interesting features to handle the above-mentioned challenges: they are easy to miniaturize, highly sensitive, do generally not consume the analyte under investigation and are relatively low-cost devices.

In summary, various articles on the successful integration and application of oxygen and pH sensors in miniaturized devices were published in the course of this thesis. The number of accepted peer-reviewed publications and the promising results reveal that microfluidic systems with integrated luminescent sensors provide a powerful tool, particularly for biological applications such as monitoring of cell cultures or (bio-)catalytic process optimization. The information obtained through all these sensor applications might help to gain a deeper understanding of cellular behavior and general microfluidic processes.

However, microfluidic sensing with luminescent sensors remains an especially challenging task and sensing devices have to be adapted to these new challenges. Further sensor material development regarding highly photostable luminescent indicators with increased brightness, sterilizable and stable sensing matrices, new application procedures of sensor cocktails, and simple and cheap measurement systems will help to advance useful applications of luminescent sensors in microfluidics.

9 Appendix

9.1 Curriculum Vitae

DI Birgit Ungerböck

Address: Bürgergasse 13, 8010 Graz, Österreich

Date of birth: 25th March 1983

Email: birgit.ungerboeck@tugraz.at

Mobile: +43 650 9819592



Profile

My educational and professional background lies in the area of optical sensor development. My fields of expertise comprise oxygen and pH imaging including image analysis and integration of optical oxygen and pH sensors into microfluidic devices. Moreover I have experience in project management and supervision of students.

Education and Qualification

Educational Background

March 2010 – to date

PhD candidate, Graz University of Technology, Austria

PhD on “Integration of Optical Chemical Sensors into Miniaturized Devices”, working group “Applied Sensors”, estimated graduation in June 2014

March 2009 - March 2010

Master thesis, Graz University of Technology, Austria

“Application of Optical Sensor Materials to Microfluidic Devices (Lab on a Chip)”, A graded

October 2002 -March 2010

Diploma studies, Graz University of Technology, Austria

Technical Chemistry, passed with distinction

Professional Training

- Participation in ASCOS 2011 – Optical Sensors for Life Sciences, Cork, Ireland
- Seminars in “Effective Scientific Writing in English”, “Project management” and “Competence training for Teaching Assistants”

Professional Activities

- Organization of DocDays 2012 – PhD-conference of Doctoral School Chemistry
- Student representative for PhDs in Senate of Graz University of Technology (2011 -2013)

Teaching Experience

- Lab Course Analytical Chemistry (Bachelor level)
- Supervision of several bachelor thesis and bachelor and master projects

Relevant work experience

August 2012 – January 2014

University project assistant, Graz University of Technology, Austria

Biointense – Mastering bioprocess integration and intensification across scales

July 2011 -July 2012

University project assistant, Graz University of Technology, Austria

NAES – Micro structured substrates for Amplification of Optical Sensor Signal Intensity

March 2010 -June 2011

University project assistant, Graz University of Technology, Austria

ISOTEC – Integrated Organic Sensor and Optoelectronics Technologies

April 2008 – September 2008

Part-time project assistant, Joanneuch Research, Austria

Research activities in waste water recycling of industrial processes

Activities and Interests

- Hiking, travelling, socialising with friends
- Volunteer work and independent initiatives, such as the project “Science, Technology and Society” or assistant for social policy (student union)

Additional Information

- Native Speaker German
Excellent in written and spoken English
Basic level of French
- Computing Skills: Proficient in Microsoft Office, Origin, Inkscape
Programming and Web: Matlab (Image Analysis and Data processing), TYPO3 (basic)
- Full driving license

Awards

Best Poster Award – DocDays 2011

Best Poster Award – IMTB 2013 – Implementation of Microreactor Technology in Biotechnology

9.2 List of publications

Publications in peer-reviewed journals

Birgit Ungerböck, Siegfried Fellingner, Philipp Sulzer, Tobias Abel and Torsten Mayr

Magnetic Optical Sensor Particles: A Flexible Analytical Tool for Microfluidics

Analyst, **2014**, 139, 2551-2559; 10.1039/C4AN00169A

Birgit Ungerböck, Andrej Pohar, Torsten Mayr, Igor Plazl

Online oxygen measurements inside a microreactor with modeling of transport phenomena

Microfluidics and nanofluidics, **2013**, 14, 565 -574; DOI: 10.1007/s10404-012-1074-8

Birgit Ungerböck, Verena Charwat, Peter Ertl, Torsten Mayr

Microfluidic Oxygen Imaging using Integrated Optical Sensor Layers and a Color Camera

Lab on a chip -miniaturisation for chemistry and biology, **2013**, 13, 1593 -1601; DOI: 10.1039/C3LC41315B

Daniel Aigner, Birgit Ungerböck, Torsten Mayr, Robert Saf, Ingo Klimant, Sergey Borisov

Fluorescent materials for pH sensing and imaging based on novel 1,4-diketopyrrolo-[3,4-c]pyrrole dyes

Journal of materials chemistry / C, **2013**, 1, 5685 -5693; DOI: 10.1039/c3tc31130a

Torsten Mayr, Birgit Ungerböck, Günter Mistlberger, Sergey Borisov, Ingo Klimant

A simple method to reduce optical cross-talk effects in chemical imaging with planar optodes

Limnology and oceanography, **2012**, 10, 101-109; DOI: 10.4319/lom.2012.10.101

Tobias Abel, Birgit Ungerböck, Ingo Klimant, Torsten Mayr

Fast responsive, optical trace level ammonia sensor for environmental monitoring

Chemistry central journal [Elektronische Ressource], **2012**, 6, 124 -133; DOI: 10.1186/1752-153X-6-124

Tobias Abel, Martin Sagmeister, Bernhard Lamprecht, Elke Kraker, Stefan Köstler, Birgit Ungerböck, Torsten Mayr

Filter-free integrated sensor array based on luminescence and absorbance measurements using ring-shaped organic photodiodes

Analytical and Bioanalytical Chemistry, **2012**, 10, 2841 – 2849; DOI: 10.1007/s00216-012-6175-4

Bernhard Lamprecht, Elke Kraker, Stefan Köstler, Martin Sagmeister, Harald Dietlbacher, Nicole Galler, Birgit Ungerböck, Tobias Abel, Torsten Mayr

Integrated waveguide sensor utilizing organic photodiodes

Physica status solidi / Rapid research letters, **2011**, 9, 344 - 346; DOI: 10.1002/pssr.201105300

Conference Proceedings

Torsten Mayr, Tobias Abel, Birgit Ungerböck, Martin Sagmeister, Bernd Lamprecht

Opto-chemical sensors based on integrated ring-shaped organic photodiodes: Progress and Applications

SPIE Optics + Photonics -Organic Semiconductors in Sensors and Bioelectronics V. San Diego, 12.08.2012

Bernhard Lamprecht, Birgit Ungerböck, Tobias Abel, Martin Sagmeister, Elke Kraker, Paul Hartmann, Georg Kajopic, Stefan Köstler, Nicole Galler, Harald Dietlbacher, Joachim Krenn, Torsten Mayr

Integrated waveguide sensor platform utilizing organic photodiodes

SPIE - Plasmonics in Biology and Medicine IX V., San Francisco, 22.01. – 24.07.2012

Birgit Ungerböck, Günter Mistlberger, Verena Charwat, Peter Ertl, Torsten Mayr

Oxygen Imaging in Microfluidic Devices with Optical Sensors Applying Color Cameras

Eurosensors, Linz, 05.09.2010 – 08.09.2010

Presentations

Magnetic Sensor Particles: A Valuable Tool for Application in Microfluidics*

Implementation of Microreactor Technology in Biotechnology -IMTB 2013, Cavtat, 05.05.2013

Opto-chemical sensors based on integrated ring-shaped organic photodiodes: Progress and Applications

SPIE Optics + Photonics - Organic Semiconductors in Sensors and Bioelectronics V, San Diego, 12.08.2012

Spatially resolved measurement of oxygen transfer through natural and synthetic bottle closures

Vino Analytica Scientia, Graz, 21.07.2011

Oxygen Imaging in Microfluidic Devices with Optical Sensors Applying Color Cameras*

Eurosensors XXIV, Johannes Kepler Universität, Linz, 05.09.10

Optical sensors for microfluidic devices

Implementation of Microreactortechnology into Biotechnology, Ljubljana, 29.09.2010

Optical sensors for bioprocess monitoring in microfluidic devices

International Graz Congress for Pharmaceutical Engineering, Graz, 17.09.2009

Optical Sensor for Microscale Devices

Society for General Microbiology - Meeting, Edinburgh, 07.09.2009

*Some presentations only as co-author, own presentations are marked with **

Poster contributions

Validation of a Diffusion-and-Convection Model for Microfluidics by Oxygen Imaging

Implementation of Microreactor Technology in Biotechnology - IMTB 2013, Cavtat, Croatia, 05.05.2013

Microfluidic Oxygen Imaging using Color CCD-Cameras

Implementation of Microreactor Technology in Biotechnology - IMTB 2013, Cavtat, Croatia, 05.05.2013

Magnetic Sensor Particles: a new Tool for the Determination of Oxygen in Microfluidics

MICROTAS - 17th International Conference on Miniaturized Systems for Chemistry and Life Sciences, Freiburg, 27.10.2013

Microfluidic Oxygen Imaging using Color CCD-Cameras

Österreichische Chemietage, Graz, 23.09.2013

Oxygen Lifetime Imaging with a new class of phosphorescent indicators - A smartphone application

Eurotrode XI. Barcelona, Spain, 01.04.2012

Applying Oxygen Imaging for Validation of a Diffusion-and-Convection Model for Microfluidics

Eurotrode XI. Barcelona, Spain, 01.04.2012

Oxygen Imaging in Microfluidic Devices with Integrated Sensors Applying Color Cameras

Eurotrode X. Prague, Czech Republic am: 28.03.2010

Biofilm Monitoring in Microfluidic Devices with Optical Chemical Sensors

Lab-on-a-Chip European Congress. Ireland, Dublin am: 25.05.2010